# Remotely Sensed, Geophysical and Geochemical Data as Aids to Mineral Exploration in Bahia State, Brazil

## Thesis

# REMOTELY SENSED, GEOPHYSICAL AND GEOCHEMICAL DATA AS AIDS TO MINERAL EXPLORATION IN BAHIA STATE, BRAZIL

A Thesis presented

for the degree of

Doctor of Philosophy

by

**Ardemirio de Barros Silva**

*MSc (University College of London)*

*BSc (Universidade Federal de Pernambuco, Brazil)*



August 1991

Department of Earth Sciences

The Open University



ProQuest LLC.
789 East Eisenhower Parkway
P.O. Box 1346
Ann Arbor, MI 48106 – 1346

# REMOTELY SENSED, GEOPHYSICAL AND GEOCHEMICAL DATA AS AIDS TO MINERAL EXPLORATION IN BAHIA STATE, BRAZIL

## TABLE OF CONTENTS

# LIST OF FIGURES

## Chapter 4



## Chapter 5

## Chapter 7

## Chapter 8

## Chapter 9

# LIST OF TABLES

## Chapter 6



## Chapter 7

## Chapter 8

## Chapter 9

# Acknowledgments

I wish to thank the Department of Earth Sciences of the Open University for accepting me to carry out this research project.

I thank the Brazilian Conselho Nacional de Desenvolvimento Cientifico e Tecnologico - CNPq for the financial support.

This Thesis would never been completed without the help of the following people:

Dr. Steve A. Drury, a supervisor and a half. You have been both a good supervisor and a good friend. I would heartily recommend you to any prospective student. Thank you very much.

Clive Oppenheimer many thanks for cosy accommodation, mega-meals, encouragement, discussions and many more. You have been treating me not like a friend, but as a brother.

Dick Carlton who provided me the majority of assistance with some computing involved in the production of this Thesis, Thank you.

Jill Eyers for the revisions and discussions. Thanks.

Dr. Alvaro P. Crosta who, from Brazil, gave me so much help and encouragement. Thank you.

Dr. Dave Rothery for discussions and criticisms. Thank you.

Ranjit Makwana who gave me so much help in the UNIX world. Thank you.

My Mom and Dad who have given me every encouragement in my endeavour. I know that you will feel as much achievement from the completion of this Thesis as I do myself,

Last, but not least, I dedicate this Thesis to my beloved daughters CRISTINA, ANA and JULIA. You will no longer have to share me with my work.

# Abstract

This thesis aims to establish methodological procedures to implement Geographical Information System (GIS) techniques applied to mineral exploration, in particular gold associated with an Archaean greenstone belt located in a semi-arid climate: - the Contendas-Mirante greenstone belt which is located in the southeastern part of Bahia State in northeastern Brazil.

To achieve this goal a systematic approach was formulated. It begins with the correlation between Brazil and Africa. The geographical position of adjacent age-provinces, the coincidence of structural trends, their continuity in a pre-drift reconstruction and the similarities in the geochronological patterns, all indicate their correlation.

A particular Brazilian portion of the South America Platform, termed the Sao Francisco craton, (SFC) became stabilised in the late Proterozoic (1800 Ma). In this crustal block the Archaean rocks include medium-grade (Gaviao Block) and high-

grade (Jequie Block) terrains which form the infrastructure for a number of volcano-sedimentary or sedimentary sequences.

One of these volcano-sedimentary sequences, the Contendas-Mirante belt (CMB), is located along the junction between the Gaviao and Jequie Blocks. It is divided into Lower Unit (mainly volcanogenic) and Upper Unit (essentially clastic). In the CMB the plutonic granitoid associations exhibit geochemical characteristics compatible with a continent-continent collision.

The available data set for this area includes topographic and geological maps, stream sediment survey, Landsat TM and radar data, and airborne magnetic and radiometric surveys. The most suitable way for dealing with this enormous amount of data leading to mineral exploration exploration, is via GIS.

Gold deposits can be distinguished according to depositional and genetic models. In this work I concentrat on the depositional model which can be divided according to the structural setting and lithological associations.

From the available data set, the use of the Landsat TM data in lithological mapping was restricted by the vegetation and soil cover. However, TM data provided useful information on regional structures. Radar data were valuable for structural information and as ancillary data combined with radiometric data for lithological discrimination. The stream sediment reconnaissance was interpreted via a raster model. Several sets of very well correlated elements were defined: Fe-Cu-Co-As, Fe-As-Cr-V-Ba-Cu, Fe-Ni-Cu, Fe-Mg-Ti-Cu, Fe-Cu-As-Pb and Fe-Ba-As-Pb.

From these element associations anomalous areas were defined.

The magnetic data were useful for both the selection of zones with high magnetic fields and the detection of magnetic lineaments. The radiometric data in both small and large scale were valuable for lithological discrimination.

The selected and diversified GIS functions generated a final product, called data fusion, which is far more sophisticated than data integration. The four selected areas for gold, which represent 12% of the total study area, and due to the convergent geological factors, have good potential for gold.

# PREFACE

This study is the first attempt to apply Geographical Information System (GIS) techniques to mineral exploration in Brazil. It was based on a variety of data, such as geological maps, geophysical and geochemical surveys, Landsat TM and radar imagery and topographic information.

The study area forms part of a well known volcano-sedimentary sequence in Brazilian Precambrian geology, the Contendas-Mirante belt. It is located in the southeastern part of Bahia State in northeastern Brazil. Because of several mineral occurrences in the region, the area has been the subject of several exploration projects on both regional and detailed scales.

An enormous amount of field data are now available. These data resulted in the identification of a series of deformation events and associated igneous intrusions and metamorphism. However, a more comprehensive integration using GIS techniques was needed to give a better understanding of the potential for

gold in that segment of the Brazilian shield.

Although each data set is independent, a common factor is that every set covers approximately the same geographical area. Furthermore, each data set has its own built-in resolution. The geochemical stream sediment reconnaissance was undertaken using irregularly spaced points whereas airborne geophysical data are from densely sampled flight lines.

GIS requires resampling each data set to a common grid. Extensive use of interpolation methods, data reformatting, Landsat and radar interpretation were carried out. As in all sciences data have little intrinsic value until analysed.

Thus, the main objectives of this thesis are:
a)to characterize known gold occurrences in the volcano-sedimentary sequence located in the northeastern part of Brazil;
b)to provide new information on the geology of the Contendas-Mirante belt on the basis of data fusion, thus updating its geology;
c)to establish a methodological procedure for implementing GIS for gold exploration;
d)to target other areas in this belt with potential for gold exploration.

Although the emphasis of this thesis is gold mineralisation, the data from this study can also be used to evaluate other potential economic mineral deposits and strategic mineral resources.

To accomplish these aims a methodological procedure was framed. It all begins with an overview of the geology

of the Pan-African and Brasiliano Belts, their links and similarities, and introduces the concept of the Archaean Sao Francisco Craton (Chapter 1).

Chapter 2 discusses at some length the Sao Francisco Craton, its geotectonic entities, geochronology and evolution. A particular volcano-sedimentary sequence termed Contendas-Mirante belt is introduced.

The Contendas-Mirante belt is described in terms of its lithological units, structure, chemistry, metamorphism, intrusions and mineral occurrences in Chapter 3.

The available information is derived from different sources, had different scales when gathered, and was collected in different years from several authors. The generation of a data set which includes topographical information, geological maps, geochemical reconnaissance (stream sediment), geophysical surveys (airborne magnetic and radiometric surveys), remote sensed imagery (radar and Landsat TM data) is discussed in detail in Chapter 4.

This variety of data is almost impossible to analyse without computer facilities and an adequate software environment. Chapter 5 presents the importance of GIS in mineral exploration and define the main characteristics of the decision model for targetting gold.

The next step is the extraction of relevant information from each data set. Chapter 6 shows the interpretation of the remotely sensed data and presents a final product which will be integrated with other data sets. Chapter 7 presents the results of the interpretation of the magnetic images and

Chapter 8 presents the geochemical behaviour of elements which are common in gold deposits.

Chapter 9 presents the fusion of all data set used in this study, and via sophisticated operations target areas for gold were defined.

Chapter 10 contains a summary of conclusions which may include minor discussions and recommendations.

Finally, the list of references cited throughout the text is given in the end along with appendixes which refer to the abbreviations used in this study, and programs to convert particular ASCII files into GRASS format files.

# CHAPTER 1: GEOLOGICAL SYNTHESIS

## 1.1 Introduction

Undoubtedly, one of the most spectacular mountain-building events on Earth is represented by the Upper Proterozoic Pan-African belts of Africa and Brasiliano belts of South America. Much detailed work was undertaken on many of these belts in the 1970s, and several geodynamic models, such as ensialic and ensimalic development have been put forward for consideration. It is important to emphasise that the relationships among individual belts are far from being well understood.

Since 1964, diverse evidence from palaeomagnetism, oceanography, marine geophysics, geochronology and other fields has demonstrated conclusively the separation of continental masses with concomitant formation of ocean basins. With respect to radiometric ages from many Precambrian areas in Brazil, it is also important to note that, although a considerable number of radiometric determinations are now available, the data are based on few and widely separated samples. However, despite this reservation, the geochronological data, where available for the Precambrian

domains, are included here to give an indication of the probable age range of these domains.

The starting point for the development of the Pan-African belt system was probably the continental rifting (*Porada*,1989). Thus the related belts of eastern Brazil described by *Torquato* and *Cordani* (1981), will be described in this work under the continental rifting model. Continental rifting is a process that cuts across time planes in an individual rift system. Consequently, the processes involved operated in different places at different times and with different rates. For instance, convergence and tectogenesis could be operating at one place, while elsewhere rifting was still going on.

It is a challenge to find a systematic relationship between individual structural trends, because their relationships may be rather complex. On this basis the review of the geological links between Africa and Brazil presented in this chapter remains speculative but serves to show the study area in global context. In this chapter I also present the main geological characteristics of the Sao Francisco Craton of Bahia State Brazil, in which the study area is located, based on available literature and on data collected from geological traverses in the field as part of this study.

## 1.2 Correlation of the Brasiliano/Pan-African Belts across the Atlantic

Several papers have been published in the last few years dealing with the mechanism of Mesozoic separation of South America and Africa, within the context of plate tectonics (*Sial* et al, 1976; *Cordani*, 1975; *Asmus*, 1975). In these papers, geological phenomena related to the origin of the

South Atlantic were described on the basis of evidence collected along the continental margins of both continents and/or the ocean floor. The pre-drift "fit" of the two continents is now well agreed, allowing older events to be correlated across the rift system.

The present knowledge of these terrains varies considerably with their geographical position, outcrop quality and geological data. Along the southern Atlantic coasts of Brazil and Africa, a terrain with ancient rocks, mainly gneisses, migmatites, granulites and granites, predominates. In Africa these rocks occur from Gabon down to 13° latitude. In Brazil, the belt is much wider (> 300 km) and gneisses, migmatites and granites are the most common rocks, although several nuclei of granulitic rocks have been described. Figure 1.1 matches the geologic and geochronologic provinces for the South Atlantic as interpreted by *Torquato* (1975).

Two main aspects suggested by *Torquato* and *Cordani* (1981), indicate the correlations between Brazil and Africa:

a) the geographical position of adjacent age provinces, the coincidence of structural trends, their continuity in a pre-drift reconstruction, and

b) similarities in the geochronological patterns observed in adjacent regions, on both sides of the South Atlantic.

The most important evidence for correlation between these continents lies in the geological features of the Lower Precambrian. In South America and Africa, there are large cratonic areas of granulitic terrains from which ages in the 2600 - 2900 Ma range have been obtained. In Brazil, these rocks make up the Jequie Complex located in the northeastern

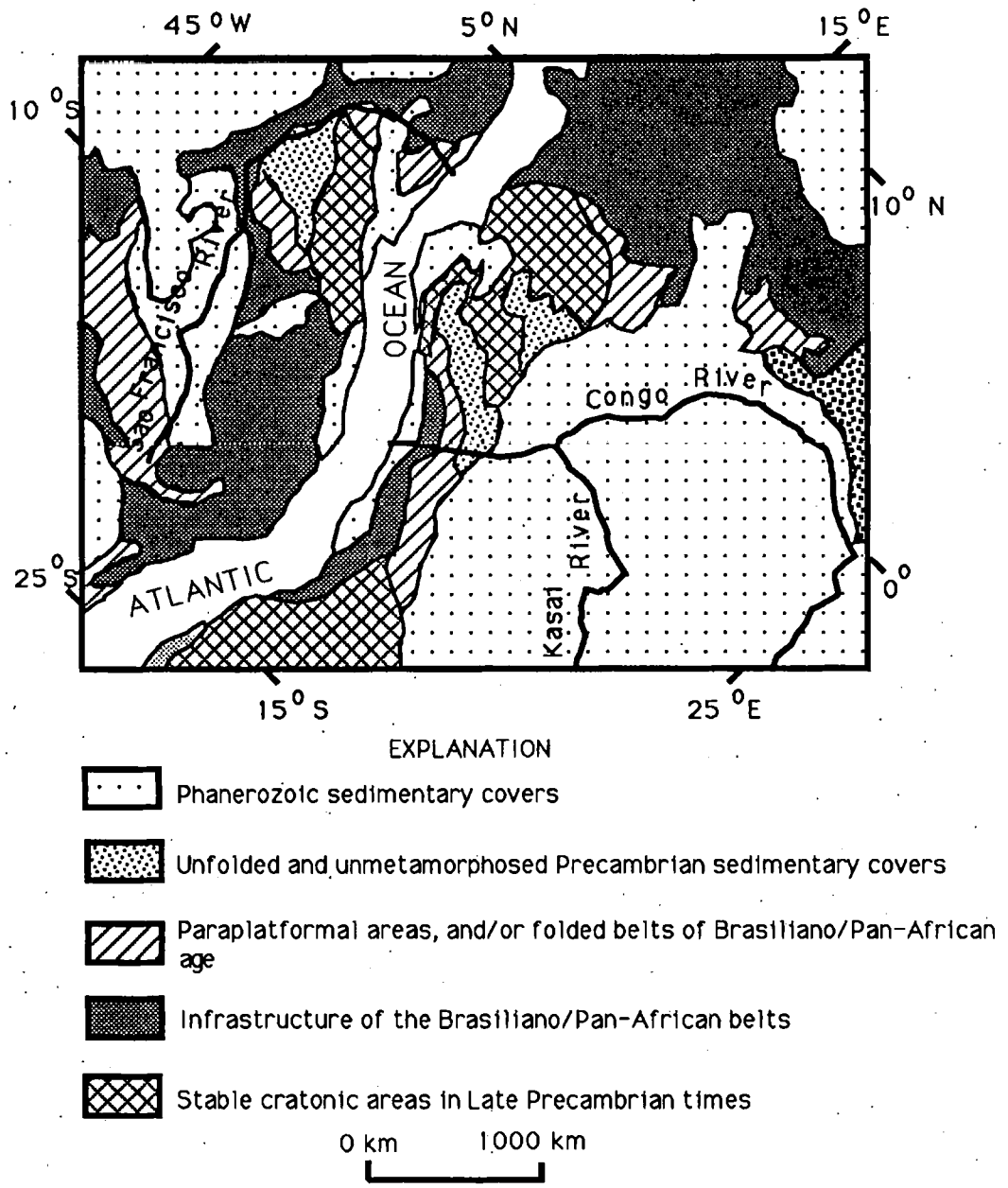


Figure 1.1: *Correlation among the geotectonic units of eastern South America and western Africa (modified from Cordani, 1973)*

part of Brazil (see Figure 1.1), whereas in Africa they can be found in a very large area from the Kasai shield to the Atlantic coast, most probably underlying the cratonic sedimentary cover of the Congo Basin (see Figure 1.1)

*Kroner* (1976, 1977) employed the existence of a very large granulitic-charnockitic region in Africa, to suggest that an old and extensive sialic crust existed since Archaean times. In the pre-drift reconstruction, this area became still larger, including the eastern part of Brazil.

Radiometric pre-Pan-African ages have been obtained in several places, however extensive metamorphism and granitization took place in Late Precambrian times (*Cordani*, 1973; *Torquato*, 1977). Many granites and migmatites were formed in close association with regional metamorphism, almost everywhere at amphibolite facies. According to *Torquato* et al (1981), the last regional cooling on both continents, as revealed by K-Ar and Rb-Sr radiometric ages on micas, occurred at about 450 Ma.

### 1.2.1 The Pan-African Belt System

*Kennedy* (1964) defined the Pan-African tectonic episode as a major tectono-thermal event at ±500 Ma. The individual Pan-African belts have been recognised as belonging to an interrelated system which surrounds and traverses the African continent and partly extends into South America, Antarctica and Australia, and probably parts of India (*Porada*, 1989).

The late Precambrian thermotectonic episodes related to the Brasiliano/Pan-African events were very important in the formation and stabilisation of the Gondwana crust, either as a single continent as postulated by *Piper* (1982), or two major continental fragments named East Gondwana (Australia, India

and Antarctica) and West Gondwana (Africa and South America) as suggested by *McWilliams* (1981). According to *Almeida et al* (1973), there are indications for continental accretion encroaching on an old oceanic basin, which would have existed in the place now occupied by the South Atlantic ocean. *Piper et al* (1973) have suggested from palaeomagnetic data a relative stability for some of the major cratonic regions of Africa during a large part of the Precambrian.

If we consider, as suggested by *Porada* (1989) for the period preceding latest Precambrian times, the two major continental fragments of West and East Gondwana, (Figure 1.2), it is possible that the Gondwana supercontinent formed by a subsequent collision between these two continental masses along the Pan-African Mozambique belt. This event implies that the majority of the Pan-African belts must have evolved from early continental rift structures or oceanic basins.

Remnants of oceanic material have been traced at several localities in the belt system: arc-derived sediments and/or sheared oceanic crust have so far been identified in the Pharusian belt (*Leblanc*, 1981), in the Gariep belt of southern Namibia (*Kroner*, 1975) and possibly in the southern Damara belt (*Miller et al.*, 1983).

The bilinear distribution of occurrences of ophiolites, as in the Mozambique belt of Ethiopia (*Kazmin et al*, 1978) and in Kenya (*Shackleton*, 1977), and indicators of subduction processes, suggested that ocean opening, subduction and continental collision took place along the Mozambique-Red Sea fold belt line, along a zone comprising the Atlantic coastal regions of southern to equatorial Africa and Brazil,

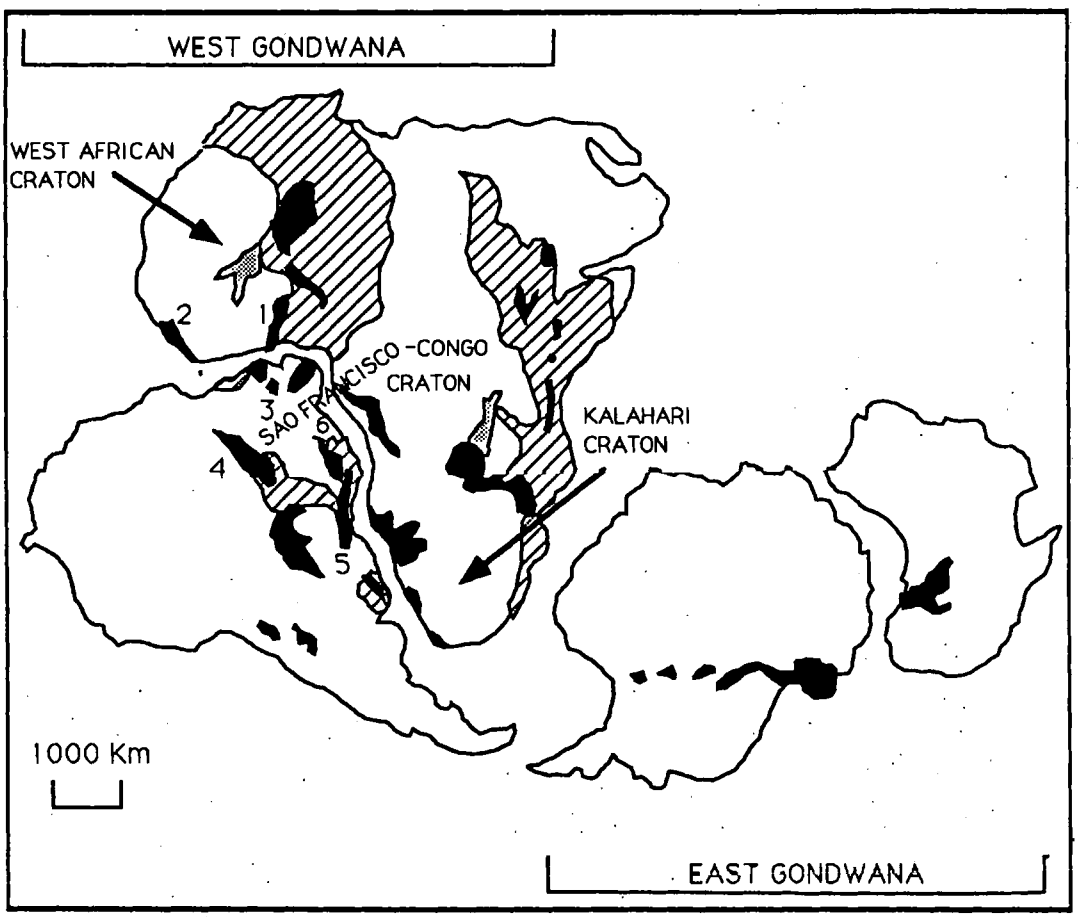


EXPLANATION

Areas of Upper Proterozoic to Lower Palaeozoic tectono-thermal basement rejuvenation

Upper Proterozoic aulacogen deposits

Upper Proterozoic 'geosynclinal' deposits

1 - Dahomeyan belt; 2 - Rokelide belt; 3 - Northeastern fold belt;
4 - Araguaia belt; 5 - Ribeira belt; 6 - Mantiqueira belt

Figure 1.2: *Configuration of the Upper Proterozoic Pan-African belt system with extensions into South America, Antarctica and Australia on a pre-drift reassembly (modified from Porada, 1989)*

continuing further north along the eastern border of the West African craton.

The Precambrian palaeomagnetic data from Gondwana further suggest that the older cratons within West Gondwana retained their Palaeozoic configuration back as far as 1000 Ma and perhaps longer. Thus not all Pan-African and older mobile belts mark the sites of major ocean closure, but rather formed without the destruction of vast amounts of oceanic lithosphere (*McWilliams*, 1981)

*Porada* (1989) defined the Sao Francisco-Congo cratonic "bridge" as shown in Figure 1.3, according to the numerous structural, lithological and radiometric links between Brazil and Africa. He emphasised that if the existence of such a bridge is considered then termination of the Pan-African rift structures and shallowing of deposits towards the bridge has to be expected, whereas during convergence development of transcurrent faults for regional adjustment would have been necessary.

### 1.2.2 Upper-Proterozoic Brasiliano Belts of South America

The Brasiliano orogeny which culminated at about 600 Ma, is the counterpart of the Pan-African cycle in South America. Orogenic belts formed during the Brasiliano event have passed through a history similar to that of the Pan-African belts and are both genetically and geometrically connected with these.

This is valid for the Northeastern fold belt of Brazil (no 3 on Figure 1.2) which is intimately linked with the Dahomeyan belt (no 1 on Figure 1.2). In both regions a strong orogenic episode during the late Precambrian produced metasedimentary

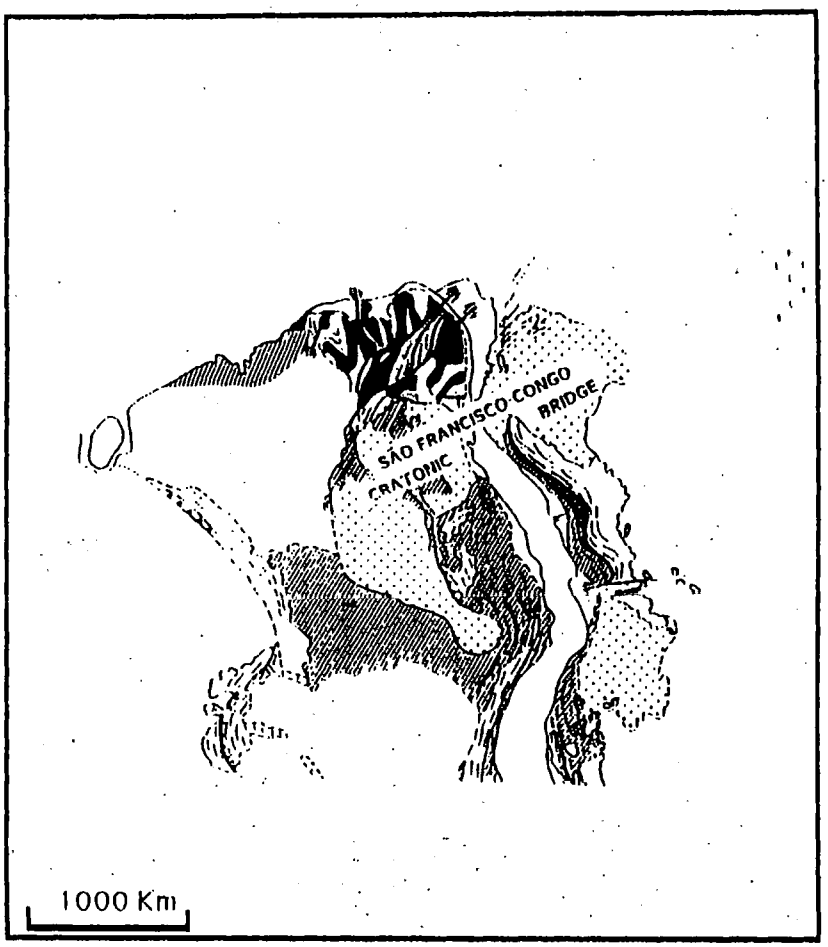


EXPLANATION

- Undifferentiated rocks of Sao Francisco and Congo cratons
- Basement rocks affected by Pan-African and Brasiliano orogenies
- Basement inlier in Upper Proterozoic belt
- Rocks of Kibaran age or overprinted during Kibaran cycle
- Upper Proterozoic deposits
- Undifferentiated Precambrian to Recent rocks
- Transcurrent sheer zone
- Major thrust

Figure 1.3: *Selective geological map of Equatorial and Southern Africa and eastern South America (modified from Porada, 1989)*

rocks, induced granitization and the formation of granitic rocks of different types, and rejuvenated crustal rocks of pre-Brasiliano and pre-Pan-African age as suggested by *Almeida* (1967). Another connection can be recognised for the Araguaia Belt (no 4 on Figure 1.2) which in the pre-drift reconstruction is in direct continuation with the Rokelide Belt of the western Africa (no 4 on Figure 1.2), as well as the Ribeira Belt (no 5 on Figure 1.2), trending along the eastern coast of Uruguay and Brazil, has been interpreted as an integral part of the Damara-Ribeira orogen (*Porada*, 1979).

According to *Porada* (1989), the opening of an Upper Proterozoic ocean, roughly coinciding with the present South Atlantic margins, followed by continental collision, had occurred to the east of the Ribeira Belt. Relicts of ocean floor and continental margin deposits thrust on the African continent in the Gariep Belt, attest to the collisional event which, on the South American side, was accompanied by big intrusions of granitoids between 700 and 500 Ma. Similar relationships appear to have existed between the Mantiqueira Belt of Brazil (no 6 on Figure 1.2) and Kaoko-West Congolian Belts of Africa.

In Africa gneisses and granites occur along the coast from Gabon down to about 13°S latitude. In Brazil, the belt is much wider, about 300 km, and covers large parts of the states of Bahia, Minas Gerais, Espirito Santo and Rio de Janeiro. Also in Brazil, gneisses, migmatites and granites predominate, although several nuclei of granulitic rocks have been described in these regions.

### 1.2.3 Development of the Brasiliano Rift System

Most of the better exposed Upper Proterozoic Brasiliano belts of South America are confined to the eastern part of Brazil and Uruguay. They include two geologically different types of Precambrian terrain: the mobile belt systems and the almost unmetamorphosed sedimentary platform sequences. Both are mainly covered by younger sediments and therefore their geological features remain rather obscure.

There are two hypothesis for continental rifting, which will be briefly described here. According to *Burke et al* (1981) the hypothesis of active mantle rifting implies that continental rifting starts from rrr-type triple junctions above mantle plumes ("hot spots"). Usually, at two of the three arms rifting proceeds until eventually continental rupture may occur, while for geometrical reasons, the third arm becomes a aborted rift or, after orogeny, an aulacogen. The two active rifts propagate away from the triple junction and into the continent, and may link up with other rifts originating from other triple junctions. In this manner, a long continuous rift may extend across a continent and eventually split it into two plates. These continental rifts are believed to occur mainly in plates that are fixed with respect to the underlying mantle. The hypothesis of passive mantle rifting suggests that continental rifts may form instantaneously in response to a regional extensional stress field which causes stretching and thinning of the lithosphere. As a consequence, the asthenosphere rises passively to replace part of the thinned lithosphere. Passive continental rifting is believed to be related to horizontal movements of plates and their interaction.

According to *Porada* (1985) the main Pan-African rifting was caused by crustal stretching in terms of passive mantle rifting, whereas for a precursory period of continental rifting the active mantle hypothesis might have been applicable.

The same author in 1989, suggested the similarities between Mesozoic North Atlantic opening and Pan-African rifting, in relation to size and distribution of individuals rifts and extension of the entire system.The available data suggest that rifting in all Pan-African and Brasiliano belts started between 1100 and 1000 Ma.

The same author suggested that in the Pan-African-Brasiliano rift system, sea-floor spreading occurred most probably along a north-south oriented main line of rifting and led to the opening of a proto-South Atlantic ocean. Possibly, the ocean terminated in the north at the Sao Francisco-Congo cratonic bridge between northeastern Brazil and Gabon-Cameroom.

## 1.3 Previous studies and geological framework of the Sao Francisco craton

*Almeida et al* (1981) divided the Brazilian portion of the South-America Platform into ten structural provinces, six corresponding to Precambrian terrains and four to Phanerozoic platform cover terrains. One Precambrian province is particularly important in this work; it is the Sao Francisco Province (Figure 1.4) which is a cratonic area and has been recognised in the general area of the Sao Francisco river for about 40 years.

In current Brazilian usage, the term "craton" is often applied to crustal blocks which became stabilised in the late

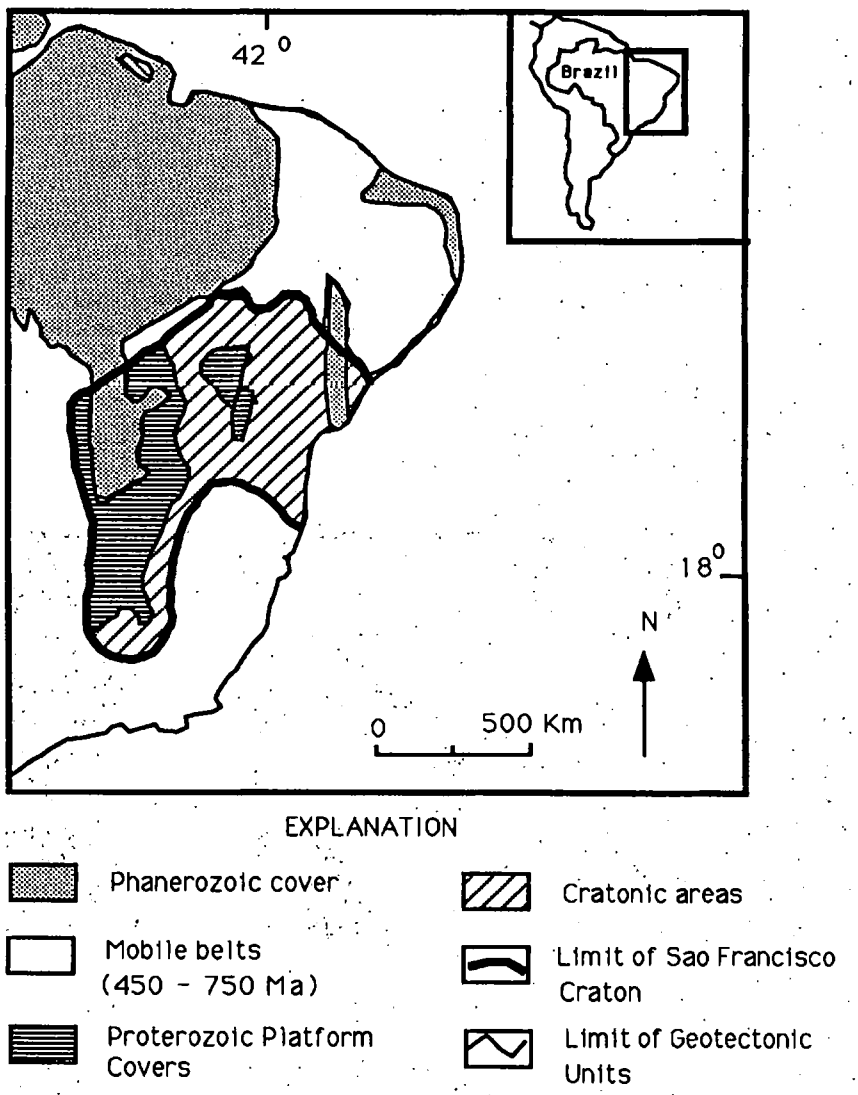


Figure 1.4: *Situation of the Sao Francisco Craton in the Brazilian Shield (modified from Shobbenhaus et al, 1984)*

Proterozoic and were not subject to deformation during the Brasiliano event (Table 1.1)

| Ma | Tectonic Events |
|---|---|
| 450 - 700 | Brasiliano |
| 1000 - 1300 | Espinhaco |
| ±2000 | Transamazonico |
| 2600 - 2700 | Jequie |

**Table 1.1**: *Tectonic events on Sao Francisco Craton (from Shobbenhaus and Campos, 1984)*

This nucleus was identified by *Guimaraes* (1951) as "Arqui-Brasil" ("Ancient-Brazil"), which he thought had a larger extension towards the north. *Pflug* (1965) used the name "Macico do Sao Francisco" for an area west of the Espinhaco ridge, in Minas Gerais State. *Barbosa* (1966) proposed the name "Craton Franciscano" for an area in the Sao Francisco hydrographic basin, that had reached stability in the Archaean. The term Sao Francisco craton was introduced by *Almeida* (1967), to indicate a fairly large (up to $5x10^5$ $km^2$), ancient and tectonically stable geotectonic unit, surrounded by late Proterozoic mobile belts of the Brasiliano event. *Pflug et al* (1969) limited the name "craton Sao Franciscano" to the western part of the area currently designated by the term Sao Francisco craton and proposed a smaller craton, named Lencois, in the east separated by the Minas Gerais Geosyncline.

During the 1970s *Cordani* (1973) and *Hasui* (1975) suggested the separation of the Sao Francisco craton into two parts, the Sao Francisco craton to the west, and the Salvador craton to the east, that could have taken place at 500 Ma. Geological evidence and Rb-Sr data weigh strongly against this hypothesis. According to *Jardim de Sa* *et al* (1978), the assumed Late-Precambrian structural trends (NNW) do not cut across some supracrustal sequences as would be expected in the event of collision. The latest regional metamorphic event took place at 2600 Ma. The 500 Ma event must essentially reflect the closure of K-Ar systems at shallow crustal levels, perhaps involving some hydrothermal phenomena. In view of this evidence, the concept of *Almeida* (1967) for the Sao Francisco Craton (SFC) will be adopted in this work.

The SFC is a tableland, in the inner part of which elevations attain between 500 and 1000 m, and which drains into the Sao Francisco river, and then to the Atlantic Ocean. North of the river, the relief is table-form with altitudes not greater than 900 m, but in the east the tableland has a mountainous aspect with local elevations of nearly 1800 m in the extreme south.

The complex and diverse basement of the SFC (Figure 1.5), is well exposed in the State of Bahia. Some of the limits are still imprecisely defined, and the western (Brasilia) and the southeastern (Aracuai) belts appear to have had a long late Proterozoic evolution culminating with folding and plutonism. On the other hand the northeastern belts have substantial supracrustal and granite intrusions (*Sabate* *et al*, 1982).

Large portions of the SFC are covered by platform sequences of

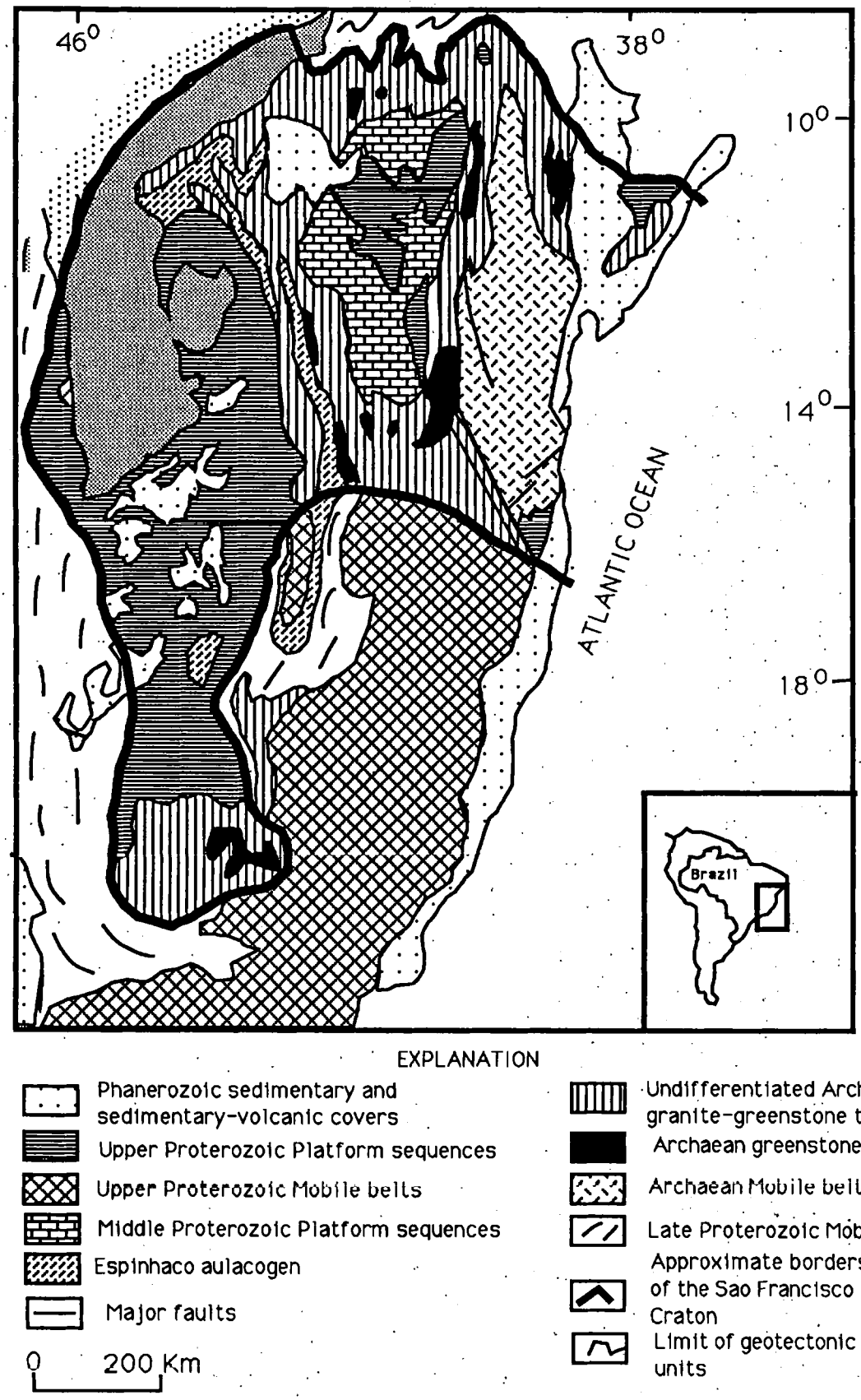


Figure 1.5 : *Simplified geology of the Sao Francisco craton (modified from Bernasconi, 1987)*

Upper Proterozoic age, termed the Sao Francisco Supergroup. They are slightly to strongly deformed at the borders of the SFC. These sediments also overlay part of the Espinhaco Supergroup, which represents and elongated intracratonic unit of Middle-Upper Proterozoic age. Another cratonic cover, named Chapada Diamantina Group, of the same age, also overlays the SFC (*Brito Neves et al* , 1980; *Cordani* and *Brito Neves*, 1982).

In the SFC, the basement is assumed to consist of products of Late-Archaean events (2700 Ma), although a few old isolated nuclei possibly as old as 3200 Ma can be found. The Archaean rocks are conventionally separated into complexes based on criteria such as lithological composition and metamorphic grade. However, contacts are often inter-digitating or transitional, and correlations between areas separated by Late-Archaean or Lower Proterozoic fold belts are difficult. Although the chronological subdivision of well exposed and well studied cratonic areas, such as Central and Southern Africa and Australia is based on major tectonic events for which there is ample evidence, and has been made on the basis of stratigraphic principles, the Precambrian areas in Brazil are still divided in generalised tectonogenetic cycles.

*Almeida et al* (1967), using geochronological data and geological information, identified the influence or participation of diverse orogenic cycles and/or thermotectonic and/or tectonomagmatic events and/or episodes, some of them having continental importance and some having only local significance, in the geologic evolution of the Precambrian areas in Brazil. Usually the orogenic cycles were defined by radiometric ages (Rb-Sr whole rock), which indicated the main geological activities (metamorphism, tectonism or magmatism).

Using this methodology, they proposed a conventional division with which most Brazilian geologists agree. In the Precambrian areas they defined four main geotectonic events or cycles: Jequie (2900 - 2600 Ma), Transamazonico (2100 - 1800 Ma), Urucuano (1300 - 1100 Ma) and Brasiliano (700 - 450 Ma) (*Almeida et al* 1981). Apart from a few exceptions, the initial evolution of the orogenic cycles is ill defined.

The SFC achieved its cratonic condition by the end of the Transamazonico (1800 Ma), when about 80% of the present Brazilian crust in shield areas was formed (*Cordani et al*, 1988). The Jequie event is characterised by intense reworking of older Archaean crust and generation of ensialic mobile belts. The Transamazonico event is defined by extensive reworking of Archaean crust, intense magmatism and deformation of Lower Proterozoic sequences. Between the Transamazonico and Brasiliano events, the SFC experienced a major extensional episode of Urucuano age, now represented by the Espinhaco aulacogen (*Costa* and *Inda*, 1982), and which led to extrusion of K-rich acid volcanics in some places (*Sa*, 1981), deposition of continental shallow clastic sediments and subsequent deformation (*Sa*, 1981). Mafic dyke swarms associated with this extensional episode are known in the craton (*Sa*, 1981).

There are some differences between the northern and southern parts of the Archaean in the SFC. In the northern part the supracrustal sequences are conformably interleaved with acid gneisses and migmatites, probably as a result of major deformation, in a situation broadly similar to that described by *Bridgewater et al* (1973) for the 3100 Ma Nuk gneisses and older Malene supracrustals in West Greenland. On the other hand, the observed transition between the two parts, could be

explained by coeval evolution and vertical zonation between the northern part (as the upper section), and the southern part (as the lower section), in a relationship analogous to the one proposed by *Glikson* and *Lambert* (1976) for the Pilbara and Yilgarn Blocks in Australia. *Jardim de Sa et al* (1973), on the basis of available radiometric ages, have suggested that this would imply a north-west tilting of the eastern part of the SFC, with shallow levels exposed to the north or buried below the Chapada Diamantina group. In fact, greenstone belts are known from this region, while supracrustal remnants within the gneiss-migmatitic rocks are quite common. High angle faults with vertical displacement at the east and southeast border of the granulite belt, described by *Mascarenhas* (1973), may have been associated with such a general tilting.

Archaean rocks form the Gaviao and Jequie Blocks, which will be described in the next chapter. They represent medium-grade and high-grade terrains, respectively, and they form the infrastructure for a number of volcanic-sedimentary or sedimentary sequences, whose ages are ill defined.

# CHAPTER 2: ARCHAEAN TO PROTEROZOIC FEATURES OF THE SAO FRANCISCO CRATON IN BAHIA STATE

## 2.1 Introduction

One of the most impressive landmarks in Earth evolution is the transition from Archaean to Proterozoic. Some remarkable changes occurred, such as typical Archaean bimodal associations of mafic rocks (predominantly komatiites) and tonalitic-trondjhemitic-granodioritic plutonic suites giving way to more differentiated volcanic rocks and massive production of K-rich granitoids at the end of Archaean. The first major production of K-rich granitoids might have been related to a sudden change of global continent composition (*Taylor* and *McLennan*, 1985). Some problems are still debated, *Taylor* and *McLennan* believe that this chemical change is real and due to crustal differentiation by internal melting, whereas, *Gibbs* (1986) advocates that this chemical change is fictitious and it is due to differences in tectonic setting under which crustal differentiation took place.

In Bahia State, the Sao Francisco Craton (SFC) is a favourable area to give good constraints on crust-forming events during Lower-Middle Proterozoic age.

The area studied is essentially composed of three domains elongated north-south. Figure 2.1 shows, from east to west, a mobile belt made of igneous and supracrustal series, metamorphosed in the granulite facies (Jequie Block), a low to medium-grade sedimentary and volcano-sedimentary belt (Contendas-Mirante) and the gneiss-migmatitic and granitic basement enclosing it (Gaviao Block).

In this Chapter, the geological characteristics of the Jequie and Gaviao Blocks will be presented. Although detailed discussions of petrological, structural, stratigraphic and geochronological features are beyond the scope of this work, geological units are discussed on the basis of available literature, my previous work in this region and on data collected in the field as part of this study. Geological nomenclature, which will be referred to in later Chapters is also introduced here.

## 2.2 The high-grade terrain: Jequie Block

Metamorphic rocks at granulite grade and high amphibolite facies are well developed in the Jequie Block (Figure 2.2) which constitutes one the largest outcropping granulite complexes in the world. It includes granulitized plutonic igneous rocks, volcano-sedimentary rocks and migmatites (*Cordani*, 1973) situated within the basement of the SFC.

Geochronological investigations of different areas within the granulitic terrain were carried out mainly by whole-rock Rb-Sr isotopic measurements by *Cordani* and *Yier* (1979), *Brito Neves*

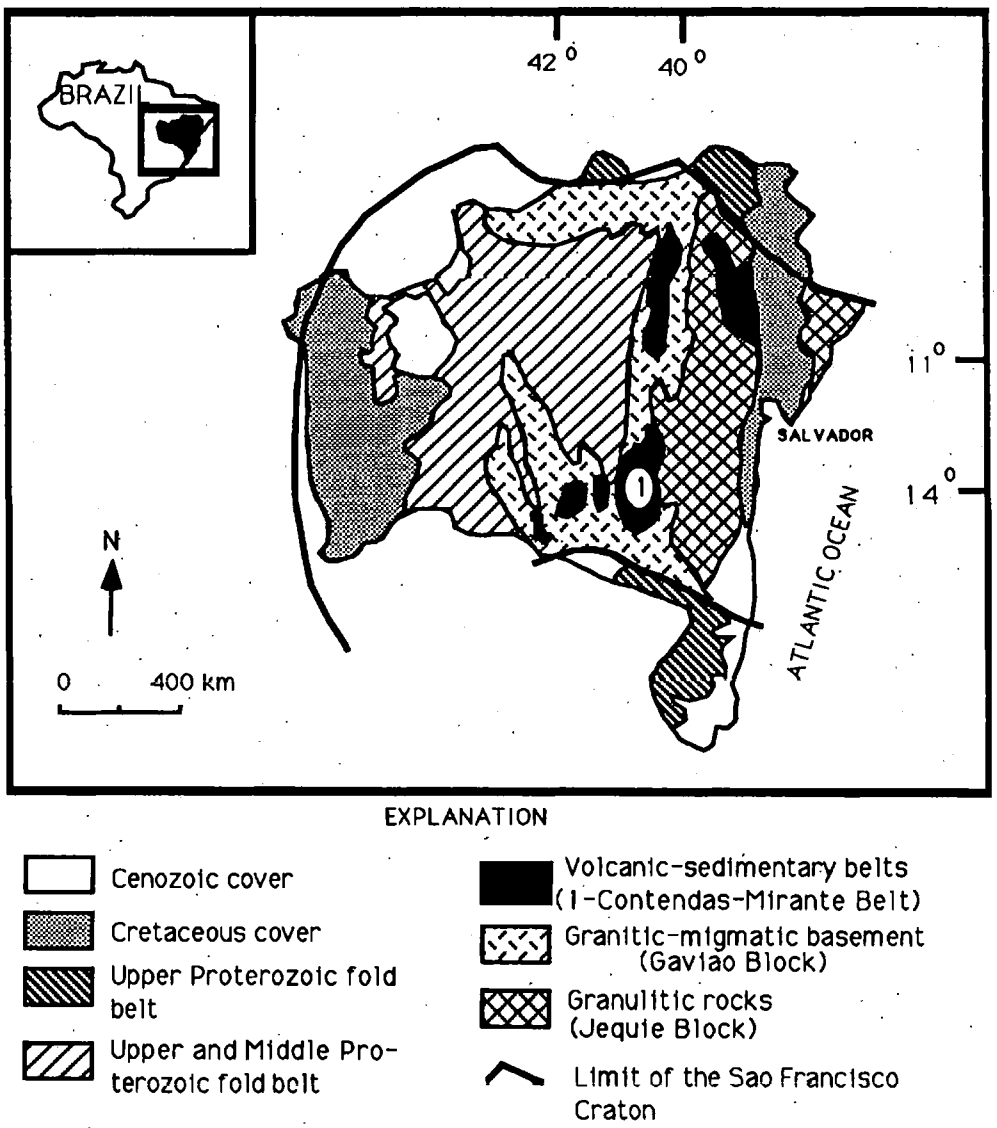


Figure 2.1: *General geological map of the State of Bahia (modified from Mascarenhas, 1978)*

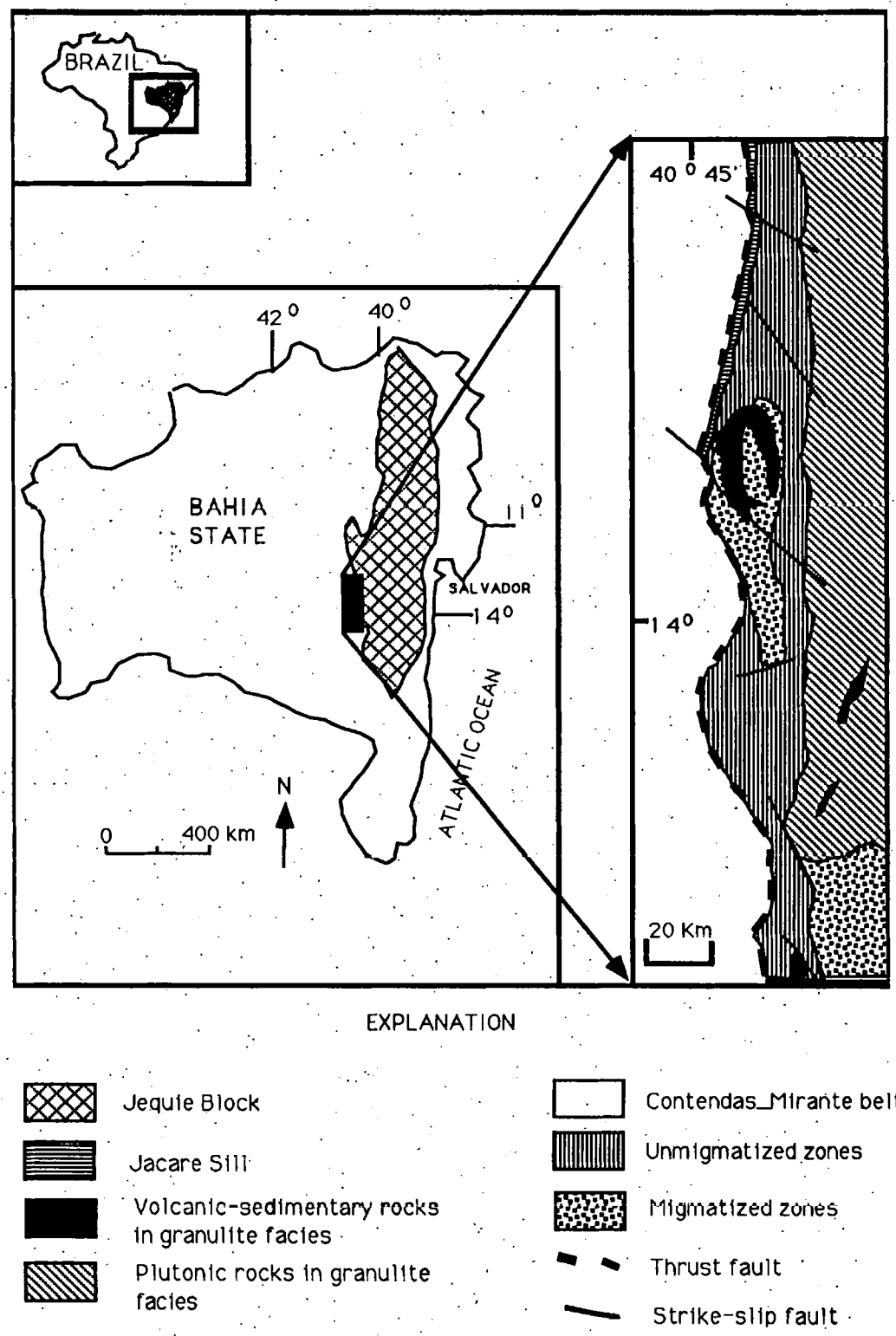


Figure 2.2: *The Jequie Block and the form of the contact between Jequie Block and the Contendas-Mirante belt (modified from Mascarenhas, 1980)*

*et al* (1980) and *Cordani* (1985). The contribution of these studies are undeniable, but they did not succeed in clearly distinguishing specific geological events, due to the unsatisfactory geological and petrochemical knowledge of the granulites, and lack of quantitative data on the physical and chemical conditions which governed their deformation and metamorphism.

Recent work by *Wilson* (1987) and *Wilson et al* (1988), on the cogenetic enderbitic-charnockitic suite and on the granulitic supracrustal sequences, has made a great contribution to understanding the geology of the SFC. They selectively sampled these rocks and dated them by combined Rb-Sr whole rock, Sm-Nd model and Pb/Pb whole-rock methods. For the enderbite-charnockitic rocks ages of 2932±124 Ma and 3100-2900 Ma, using Rb-Sr whole rock and Sm-Nd model respectively, were found, whereas Pb/Pb whole rock method produced ages of 3432±48 Ma. *Wilson* (1987) using Pb-isotope modelling demonstrated that the enderbitic-charnockitic suite had suffered a later episode of U-depletion. *Vignol* (1987) dated an intrusion of gabbro-norite in this suite, finding an Sm-Nd isochron of 2920±490 Ma.

According to *Barbosa* (1989), the granulite supracrustal sequence from the Jequie Complex gave ages of 1970±136 Ma (Pb/Pb whole rock) and 2085±222 Ma (Rb-Sr whole rock). The 2900 Ma and 2600 Ma (Sm-Nd model age) determined, using the same rocks, indicates that the protoliths are much older than 2000 Ma.

Structurally, the granulite sequence is very complex. *Barbosa* (1989) has suggested that this suite was affected by at least four phases of ductile deformation. The first event (F1) is

quite rarely noted and the only features of possible F1 nature are recumbent folds with southeastern vergence, enclosed in the subvertical limbs of isoclinal folds of the third phase. The second event (F2) is characterised by recumbent folds with northwestern vergence. The third event (F3) is marked by subvertical folds with their limbs always strongly transposed. The fourth event (F4) produced east-west striking folds of small amplitude and large wavelength

### 2.2.1 Plutonic rocks in granulite facies

The plutonic rocks comprise intensely deformated enderbite, charno-enderbite and charnockite (*Costa* and *Mascarenhas* , 1986). They retain remnants of mesoperthite and perthite phenocrysts in a mylonitic matrix of quartz, plagioclase, orthopyroxene and minor amounts of clinopyroxene, hornblende and biotite. Generally, they are banded with light-green feldspathic and dark-green ferromagnesian-rich bands.

No doubt remains about the plutonic character of these rocks, and it is reinforced by the presence of euhedral chlorine-rich hornblende, by the occurrence of Ti-rich biotite inclusions in plagioclase (*Barbosa*, 1989) and by the presence of aggregates of clinopyroxene-orthopyroxene with typical magmatic composition (*Barbosa* et al, 1988).

According to *Barbosa* (1989), these plutonic rocks appear to form a calc-alkaline suite, and the K/Rb ratio and relations involving CaO, $Na_2O$ and several other major and trace elements, including rare earths, suggest that they are co-magmatic. *Barbosa* and *Fonteilles* (1989) have suggested that there was no apparent gross modification in their chemistry during the granulite facies metamorphism.

Granulite facies gabbro-norite-anorthositic bodies are very restricted in the study area, and they are geochemically distinct from the enderbitic-charnockitic rocks, having a tholeiitic character (*Cruz*, 1989).

### 2.2.2 Volcanic-sedimentary rocks in granulite facies

This domain was divided by *Barbosa* (1989) into unmigmatized and migmatized zones. The unmigmatized zone is mainly composed of mafic and felsic bands, generally up to a couple of meters thick and with abrupt contacts, including restricted intercalation of kinzigites, garnetiferous quartzites and banded iron-formation.

The mafic bands are rich in pyroxene and plagioclase. *Barbosa* (1989) has demonstrated that these rocks exhibit relatively flat rare earth elements patterns, high Fe, Ti and Cr contents and low abundance of $K_2O$, $Al_2O_3$ and $P_2O_5$. These chemical features suggest that they might originally have been basalts and/or gabbros from ocean-floor or back-arc basins (*Pearce et al*, 1975).

The felsic bands of the felsic granulites are generally quartzo-feldspathic assemblages. Due to the absence of original textures it is very difficult to petrographically establish the original nature of the material. The thickness of these bands ranges from a few centimetres to few metres. *Barbosa* (1989) has shown that these bands have remarkably uniform chemical composition, continuous over distances up to 300 metres. Their compositions fall within the sedimentary field (*Garrels* and *Mackenzie*, 1971), resembling feldspathic arkoses (*Barbosa*, 1986). However, due to regular spatial disposition it is possible to suggest an alternative origin.

arkoses (*Barbosa*, 1986). However, due to regular spatial disposition it is possible to suggest an alternative origin. They could be volcanogenic in origin, possibly tuffs, as suggested by *Barbosa* (1986). The kinzigites form bands intercalated with felsic granulite bands. Using *Garrels* and *Mackenzie*'s criteria (1971), these rocks plot in the sedimentary field and are probably metapelites (*Barbosa*, 1989). The garnetiferous quartzites also plot in the same sedimentary field, and *Barbosa* (1989) suggested that they were impure siliceous sediments.

The migmatized zones probably formed when when fluid pressure and granulite facies temperature were sufficient to cause partial fusion, accompanied by remobilization and K-metasomatism. They are characterized by biotitized mafic bands, charnockite neosome, quartzo-feldspathic veins and leuco-granites. The mafic bands are rich in horblende and biotite and show chemical similarities to tholeiitic basalts and/or gabbros from ocean floor or back-arc basins (*Barbosa*, 1989). The charnockite neosomes are heterogeneous in compositiom depending on the degree of anatexis and metasomatism. Quartz-feldspathic veins occur randomly, cross-cutting the neosomes and the mafic bands.

The leucogranites form irregular bodies of variable sizes, their diameters ranging from metres to tens of metres, and they are generally very little deformed. Their S-type chemical characteristics suggest an origin by anatexis of a possibly kinzigitic source material at granulite facies (*Barbosa*, 1989).

## 2.3 Geology of the Gaviao Block

A number of authors have described the granite-migmatitic-gneissic terrains of the Gaviao Block (*Pedreira et al*, 1975; *Marinho et al*, 1979,1980; *Silveira et al* 1980; *Mascarenhas*, 1979, 1982; *Moraes et al* 1981; *Lima et al* 1981; *Pedreira* and *Marinho*, 1981;). Correlation difficulties, mostly derived from the lack of outcrops and the extreme complexity, result sometimes in divergent interpretation for the evolution of this terrain.

The Gaviao Block is located in the western part of the SFC (Figure 2.3) and comprises diverse lithologies. There are four distinct groups: the gneissic-migmatitic basement, the supracrustal sequences, the plutonic rocks and the paraplatform sequences.

*Cordani* and *Sato* (1985) have produced a large number of age determinations from the Contendas-Mirante belt using K-Ar mineral ages, whole-rock Rb-Sr and Pb-Pb methods.

The K-Ar determinations on mica and hornblende have defined the area affected by late Proterozoic heating and deformation, and K-Ar cooling ages of 1700 -1800±45 Ma are attributed to the final episodes of the Transamazonico event.

The Rb-Sr results on granitoid rocks, have defined a reference line of 3243±81 Ma with an initial $^{87}Sr/^{86}Sr$ ratio of 0.7026±0.0016, indicating the probable existence of early Archaean continental crust. The Pb isotopic analysis from the same samples, defined a line having MSWD of 53 and yields an age of 2470±270 Ma. In general terms, the complex geochronological pattern suggests the existence of terrains formed prior to 3000 Ma which were affected by later events,

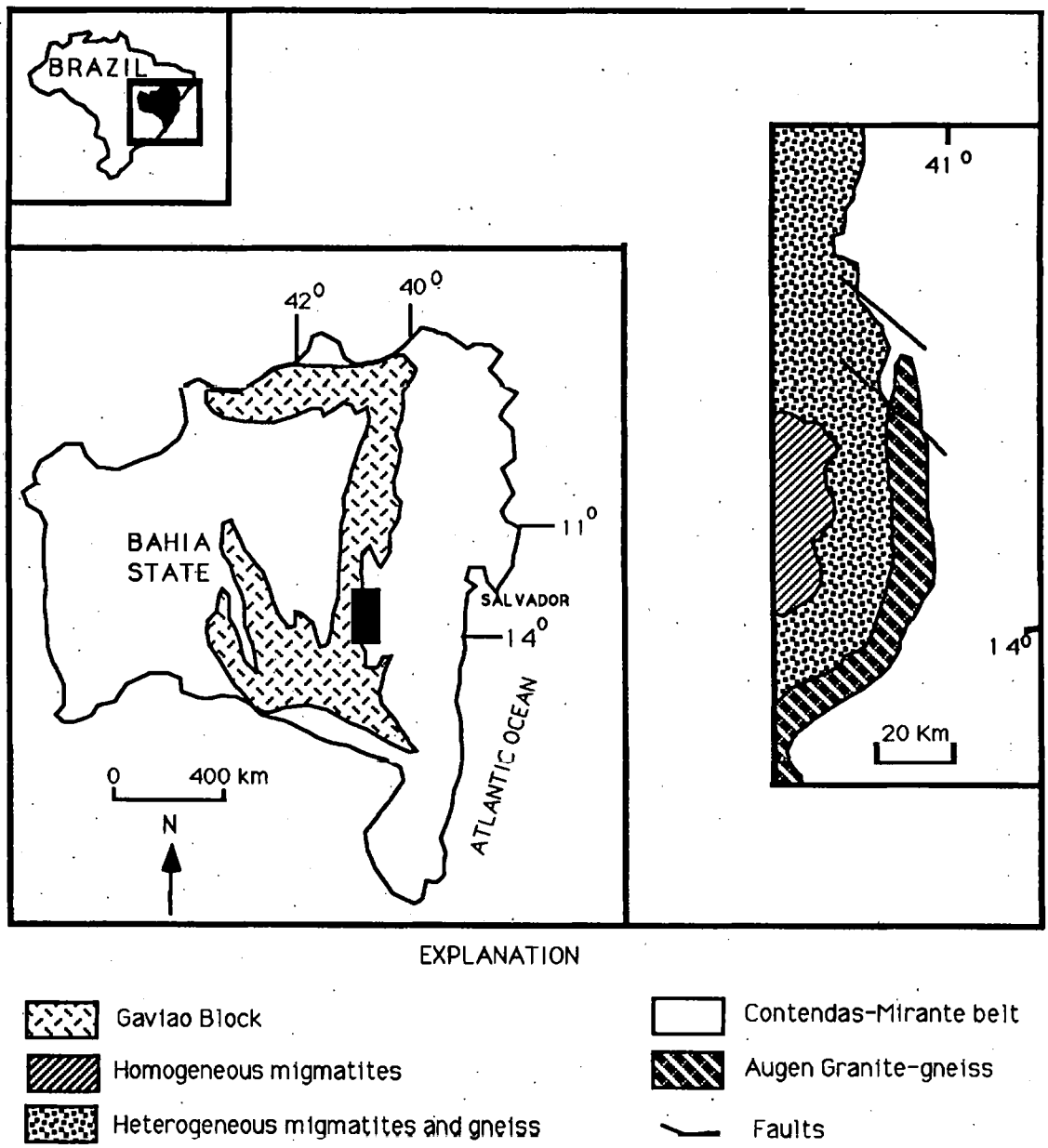


Figure 2.3: *The Gavlao Block and the appearance of the contact between the Gavlao Block and the Contendas-Mirante belt (modified from Mascarenhas, 1980)*

one around Late Archaean, the last one in the Middle Proterozoic.

Structurally, the rocks are polydeformed by Archaean and Proterozoic tectonics. The latter is marked by a mainly east-west shortening with westward thrusting and crustal thickening related to the last migmatitic processes (*Sabate et al*, 1988).

### 2.3.1 The gneissic-migmatitic complex

The gneissic-migmatitic complex comprises gneiss-amphibolite associations, which suffered anatexis and/or migmatization. Parts of the gneiss units show some features which indicate they are derived from sedimentary rocks, but most of the gneiss-leptite-amphibolite piles are considered as volcanic, volcanoclastic or volcanic-sedimentary sequences (*Marinho et al*, 1979, 1980)

The migmatites and gneisses are divided into homogeneous and heterogeneous varieties and augen granite-gneisses. The homogeneous migmatites correspond to an advanced anatectic and/or metasomatic transformation stage and have schlieren and nebulitic structures. They have granitic, tonalitic or granodioritic composition and granoblastic textures predominate.

The heterogeneous migmatites and gneisses, include banded rocks with a penetrative regional foliation which, in the majority of cases, are associated with patches of granite-pegmatite, frequently surrounded by biotite-rich rims. The patches adopt various patterns, forming migmatites with frequent stromatic and folded structures. The palaeosomes are usually tonalitic with textures which are almost always granoblastic.

The principal paragenesis of the gneisses and migmatites is quartz, microcline, plagioclase, biotite and horblende which reflects medium-grade metamorphism (amphibolite facies). *Marinho et al* (1978) have suggested that the migmatites were derived from huge amounts of igneous rocks and small amounts of sedimentary sequences.

The augen granite-gneisses show the effect of an important cataclastic event, and the petrographic features of intense K-feldspathization. They are well foliated and the most characteristic feature is the presence of centimetric K-feldspar megacrysts. The augen granite-gneisses have isotropic centres which contrasts with the foliated borders, where stromatic structures are developed. In these margins, planar and linear elements are parallel to the components of the Contendas-Mirante belt. The transition between augen granite-gneisses and migmatites is almost always transitional, with progressive development of K-feldspar megacrysts. Locally, the feldspathization appears to have been selective, following an original lithologic-compositional control, and on the basis of field observations, it is possible to correlate the feldspathization with the intrusion of the pegmatites.

### 2.3.2 The supracrustal sequences

Several Archaean supracrustal sequences affected by Transamazonico deformation are found in close association with the medium-grade terrains, forming what appear to be a typical granite-greenstone terrain (Figure 2.4). The supracrustal rocks are found as relicts within gneissic-migmatitic country rocks or areas with coherent volcano-sedimentary sequences. They were metamorphosed at greenschist to amphibolite facies

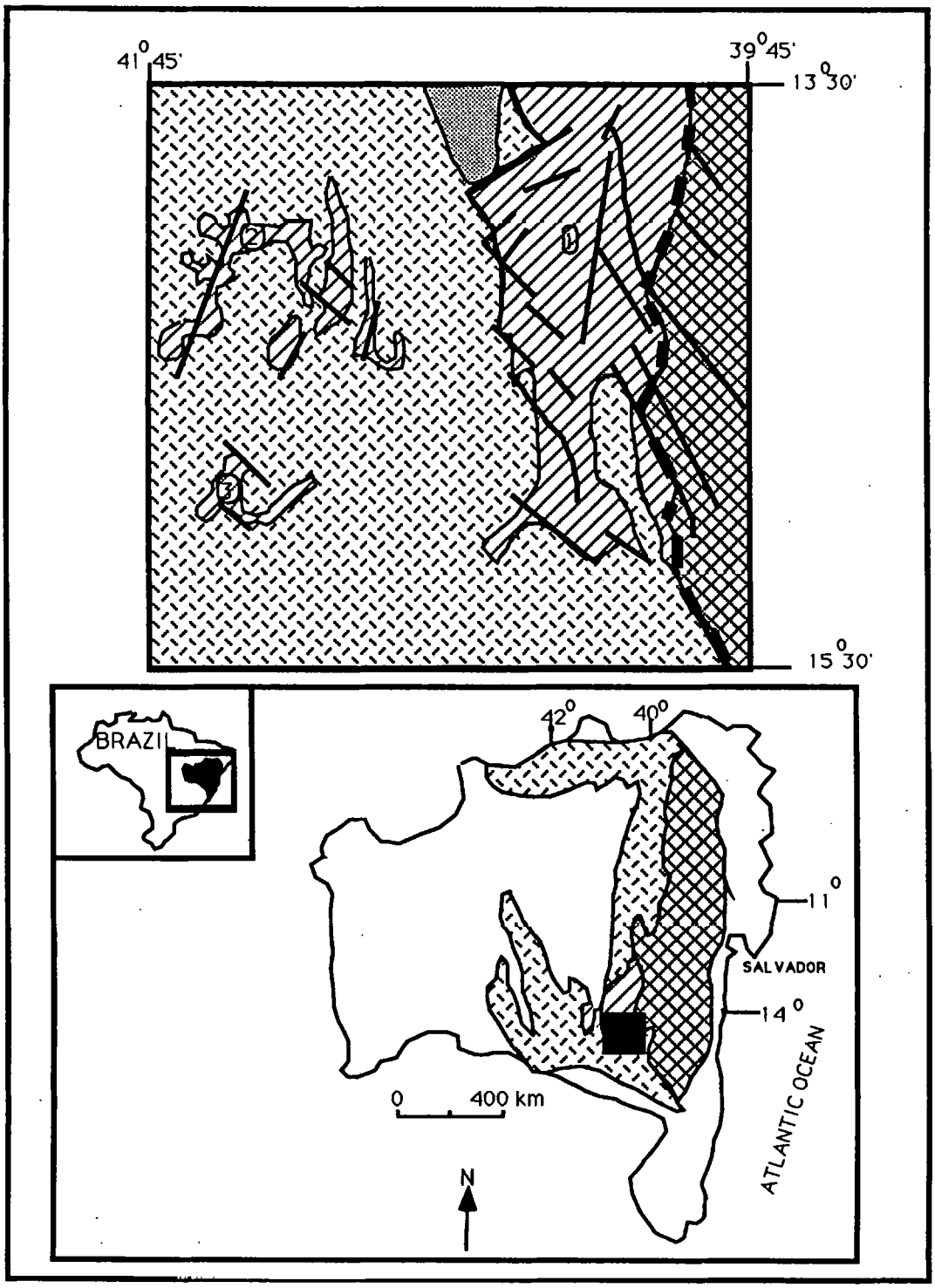


Figure 2.4: *Location of the supracrustal sequences (modified from Mascarenhas, 1980)*

and were subjected to polyphase deformation. In general terms, they comprise a lower unit and an upper unit. The lower unit includes ultramafic rocks, such as tremolite and actinolite schists, felsic to mafic metavolcanic rocks and chemical sediments. The upper unit consists mainly of clastic sediments.

The most representative supracrustal sequence, the Contendas-Mirante belt (CMB), is localized along the junction between the two Archaean blocks; it will be described in detail in Chapter 3. Some remnants of sequences somewhat analogous to the CMB are recognised well within the Gaviao Block, such as Umburanas-Brumado and Guajeru belts (Figure 2.4).

The Umburanas-Brumado belt is a volcano-sedimentary sequence of complex lithological composition, overlain by a carbonate-quartzite sedimentary pile. The metavolcanic nature of the rocks was defined by *Silveira et al* (1981). The belt is divided into two units, the lower and upper units. The lower unit includes a basal ultramafic assemblage occupying the external parts of the belt and comprises sepentinites, amphibole-schists, cherts, banded iron-formation, metabasalts and felsic metavolcanics. The upper unit consists of a succession of weakly metamorphosed sediments with dolomites at the base and includes a >400 m thick magnesite. The pile is capped by tectonically superposed quartzites and iron formations.

The Guajeru belt named by *Lima et al* (1981), corresponds to a weakly metamorphosed volcano-sedimentary sequence. The basal segment is composed by meta-ultramafics such as serpentinite, hornblendite, actinolite and chlorite-talc schists. In the

upper segment and intercalated with these lithologies, occur carbonates, cherts and banded iron-formation.

Although not radiometrically dated, these volcano-sedimentary sequences show numerous affinities with Archaean greenstone belts from other cratons.

### 2.3.3 The mafic and ultramafic intrusions

Mafic to ultramafic intrusions occupy the basal parts of the supracrustal sequences, in direct contact with migmatites of the neighbouring crustal blocks. Pyroxenites, gabbros, tremolite-schists, actinolite-schists, serpentinites and amphibolites can be recognised. They are massive or foliated, sometimes schistose with folds and crenulation and in some places they appear weakly chloritized or talcified, having fine to medium grain-size, although there are textural and compositional variations.

The most important of these bodies is the Rio Jacare sill (Figure 2.2), which is a remarkably linear sheet-like structure, trending north-south, composed of pyroxenites and gabbros. It has been divided into two zones by *Brito* (1981).

The lower zone consists of massive coarse-grained gabbro with anorthosite. These rocks show conspicuous cumulate textures, with the orthopyroxene and plagioclase being the cumulus phase, and the clinopyroxene being the post-cumulus phase. The anorthosites occur as lenses and also discontinuous and irregular shaped bodies.

The upper zone is divided into four distinct members, probably representing separate phases of differentiation. It is a 80% gabbroic unit with intercalation of pyroxenites, tonalites and

magnetitites. The magnetitites are a very important unit, and mark the base of each member.

The lower member consists of medium-grained and well layered gabbro with rhythmic banding. It also grades laterally into coarse-grained gabbro. The central member consists of thin bands of pyroxenites which grade into melanogabbro. Although uralitization of the pyroxenes has been almost complete, the cumulate nature of these rocks can still be identified. The upper part is composed of layered cycles with two main members of magnetite-gabbro with rhythmic banding of alternatively fine, medium and coarse-grained gabbro. A tonalite component comprises lenses of granophyric tonalitic rocks which occur throughout the layered zone. These more acid rocks are considered to be the late stage felsic product of the differentiation and do not have a definite stratigraphic position in the sill.

### 2.3.4 Plutonic granites

In the region, more than fifteen granitic bodies can be recognised which intrude both basement and the CMB. Most of these granitic bodies are elongated parallel to the major thrust planes, their magmatic foliation parallels ductile shear zones generally developed within the plutons at their margins and is parallel to the foliation of the enclosing metamorphic rocks (Figure 2.5). This suggest that the granites were emplaced during or at a late stage of the Transamazonico event, which affected both basement and the CMB.

The granitic bodies are generally equigranular, fine to medium grained (1 to 5 mm) and rarely porphyritic. Enclaves have been

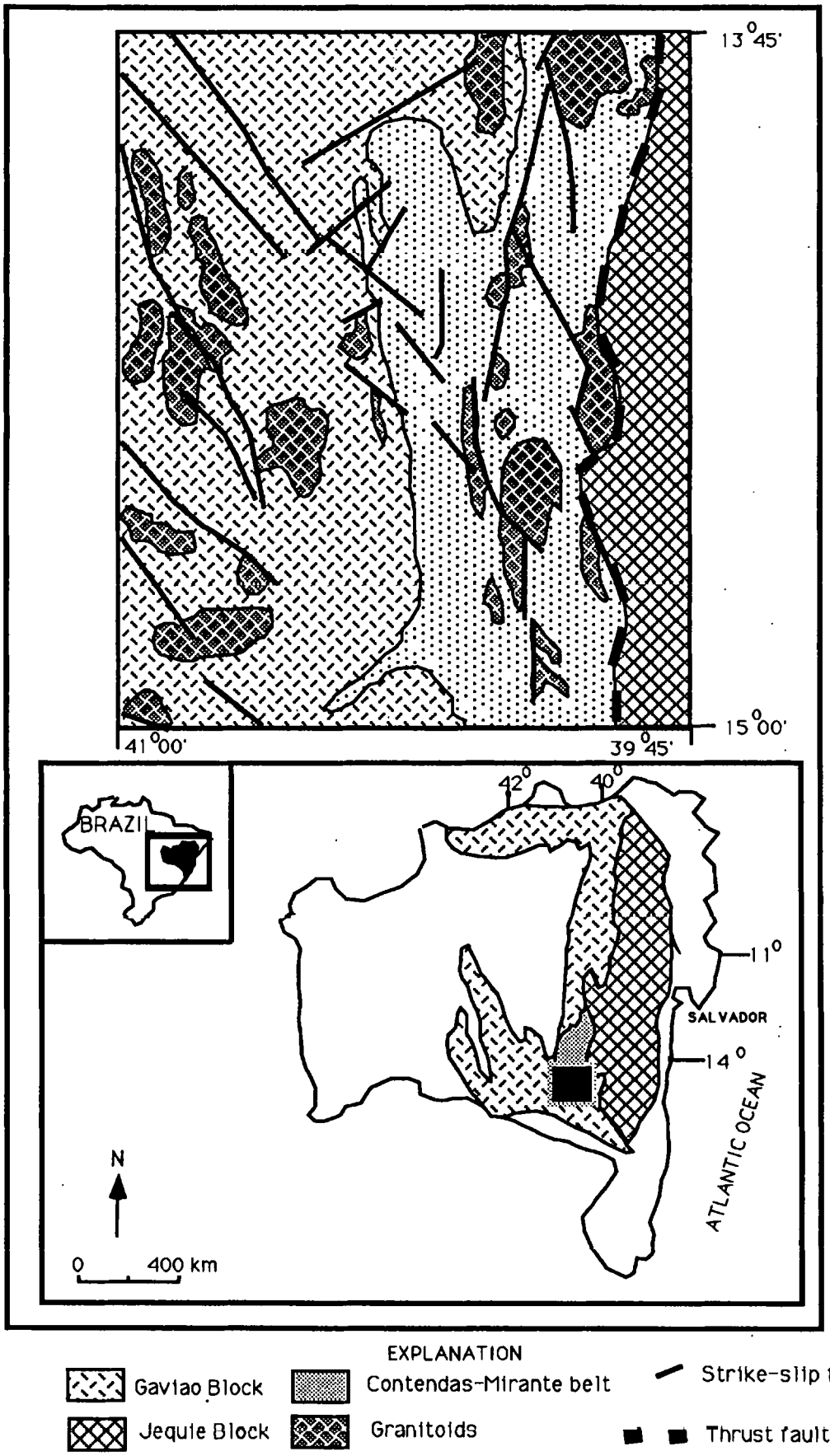


Figure 2.5: *Granitoids of the Contendas-Mirante region (modified from Mascarenhas, 1980)*

recognised and three different types can be described by *Marinho et al* (1979):

(a) enclaves of the enclosing metamorphic rocks mostly located in the vicinity of the contact, but also as roof pendants;
(b) centimetric to decimetric biotite-rich layered enclaves;
(c) enclaves of early emplaced granites in later intrusions.

The mineralogy of the granites was defined by *Cunney et al* (1989). The main variation between the different granitic plutons is the basicity of plagioclase and its proportion relative to K-feldspar. In these granites, the biotite content is always less than 7%. Muscovite content varies from 1 to 14%. Tourmaline is frequent in the pegmatites and quartz veins. Chloritization is common in most of the granites, but its development is generally very limited. Magnetite is the main iron oxide. Apatite, zircon, allanite and epidote have been observed in most of the leucogranites.

Most of the leucogranites show an evolutionary trend similar to that of Hercynian peraluminous leucogranites, i.e. a strong increase of the peraluminous index with decreasing mafic mineral content. Although on average the leucogranites of the study area are less peraluminous than their Hercynian or Himalayan equivalents (*Marinho et al*, 1989), the characteristics of the source material from which these granites derive may explain these features. Highly peraluminous sediments are less abundant in Archaean crust, therefore the main source material consists of meta-igneous plutonic or volcanic formations (*Marinho et al*, 1989).

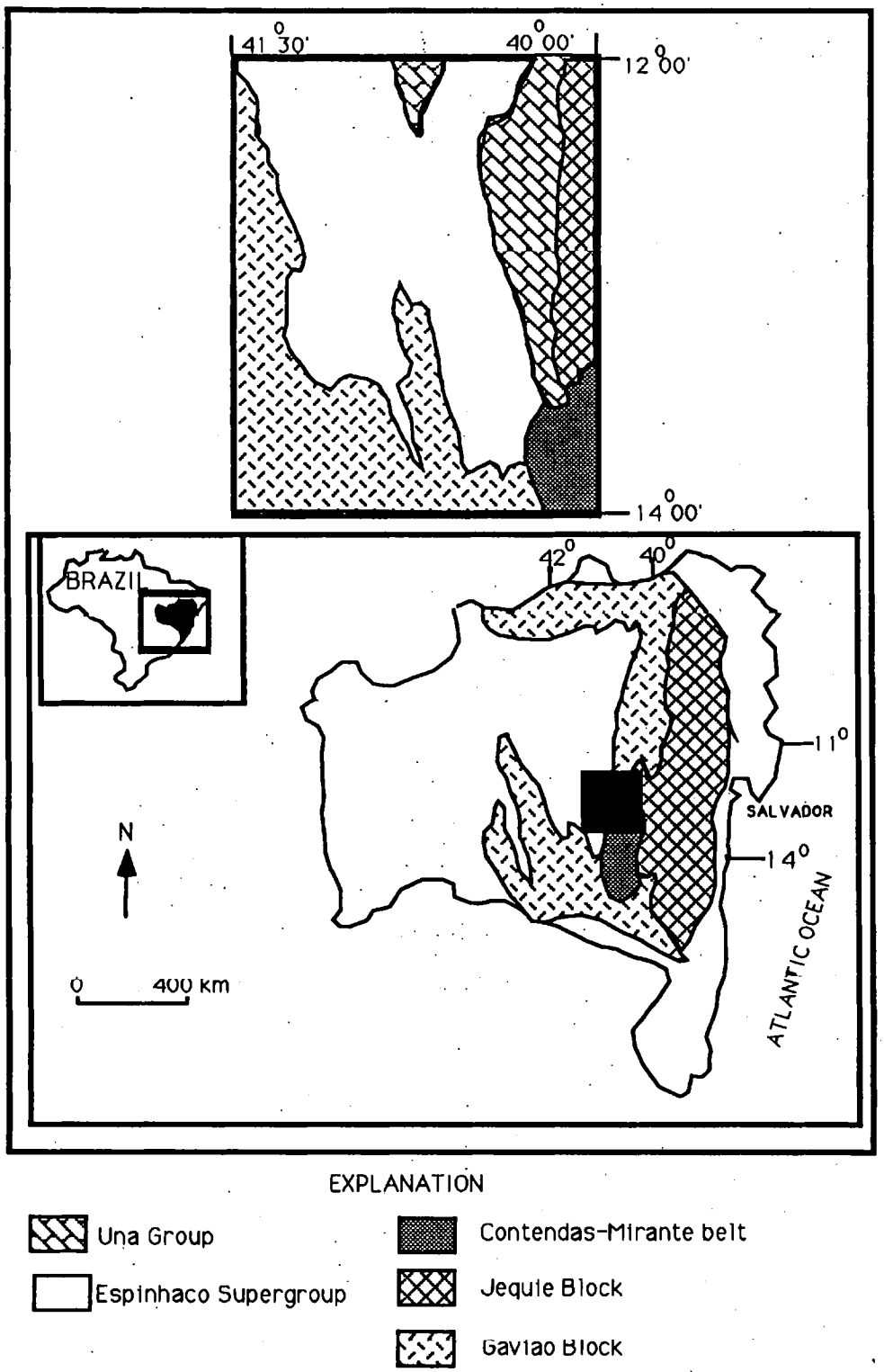


Figure 2.6: *Situation of the Paraplatform sequences in the Contendas-Mirante region (modified from Shobbenhaus, 1973)*

### 2.3.5 The paraplatform sequences

The Archaean terrains are discordantly covered by two platform assemblages of both Middle and Upper Proterozoic age (Figure 2.6). The Middle Proterozoic cover corresponds to the essentially clastic formations of the Espinhaco Supergroup (*Pedreira et al*, 1975). Its age is still open to debate, and it consists of supracrustal units metamorphosed at low grade, that were submitted to successive deformation. *Inda* and *Barbosa* (1978) has suggested a mid-Proterozoic age of 1700 Ma for the initial acid volcanism of the sequence, and 1200 Ma for the first regional metamorphism.

From the base to top, three groups of deposits can be recognised in the Espinhaco Supergroup:

(a) The Rio dos Remedios Group, composed of subaerial felsic volcanics with quartzite intercalations;
(b) the Paraguassu Group composed of impure sandstones metasiltstones and polymict conglomerates, over which were deposited arkosic quartzites with metasiltstones and slate intercalations, and an uppermost sequence of impure red quartzites associated with metasiltstones and shales;
(c) the Chapada Diamantina Group that oversteps onto the basement, and is composed of grey and pink metasandstones with a central section of friable quartzites and a thicker upper sequence of metasandstones with metasiltsone intercalations.

The clastic material was provided by intense erosion which followed the cratonic stabilization at the end of the Transamazonico event. The detrital members were deposited in a extensive intra-cratonic basin associated with volcanic

products. Both sedimentation and tectonic evolution have a distinct aulacogenic character.

The Upper-Proterozoic cover is represented in the region by the sediments of the Una Group. Two sequences can be distinguished:

(a) a basal one which comprises continental sediments, with conglomeratic horizons with evidence of glacial contribution, and

(b) a sequence essentially composed of carbonate, mainly limestone, dolomites, marls and calcareous argillites.

The sedimentation proceeded in a continental margin environment. (*Mascarenhas et al*, 1982) strongly influenced by cyclic variations of the rates of subsidence and sedimentation. These variations reflect the oscillatory movements which has affected the continent during the upper Proterozoic (*Sabate* and *Marinho*, 1982).

According to *Jardim de Sa et al* (1978), the Chapada Diamantina and Espinhaco metasediments show analogies with the Kibaran tectonics elements in Africa.

# CHAPTER 3: GEOLOGY OF THE STUDY AREA

## 3.1 Introduction

The Contendas-Mirante belt constitutes what many authors term a greenstone-granite terrain of probably Archaean age. Archaean greenstone belts constitute the most ancient volcano-sedimentary basins, where evidence for primitive crustal conditions can be found. Many well-studied Archaean cratons contain greenstone belts that formed in two distinct episodes: an older (3500 - 3300 Ma) and a younger (3000 - 2700 Ma) set. In general the older set is dominated by ultrabasic-basic komatiitic lavas and chemogenic sediments and the younger set by tholeiitic suites with rare ultramafic volcanics, minor chemogenic sediments and a late basin fill dominated by turbidites. Sometimes platform sediments dominate late Archaean basin fills (*Viljoen*, 1982; *Groves* and *Batt*, 1984; *Foster* and *Wilson*, 1984; *Gee* et al, 1986; *Corfu* and *Andrews*, 1987; *Groves* et al, 1987; and *Marmont* and *Corfu*, 1988).

According to *Groves* and *Batt* (1984), the diversity and intensity of metallogenetic associations in Archaean

greenstone belts is heterogeneous in both space and time. On the scale of a single greenstone basin, parameters such as intensity of faulting, rapidity of burial, former water depth and extent of eruption of komatiitic and felsic magma appear to have controlled the nature and intensity of the mineralisation. These inter-related parameters apparently depended on the degree of extension during basin development. Older greenstones which formed in shallow water contain metallogenetic associations such as evaporite baryte, small Pb and sulphide-rich volcanogenic massive sulphides and porphyry style Mo-Cu deposits (*Barley*, 1982). Younger greenstones which formed in deeper water basins have more conventional metallogenetic associations. The volcanogenic massive sulphides, komatiite-associated Ni-Cu deposits and gold mineralisations are normally spatially restricted, and the greenstone belts themselves have a relatively low intensity of mineralisation.

Greenstone metallogenesis peaked in the late Archaean (2800 - 2700 Ma) in association with the development of major linear rift zones, probably related to increasing crustal thinning. The rift phase of greenstone basin development may be represented in the older terrains by more limited, dominantly sediment-filled, grabens which are poorly mineralized relative to younger rift zones. This appears to be the major reason for the temporal contrasts in the nature of metallogenetic associations relating largely to the anomalous, very shallow water environments at the platform stage in the older basins (*Groves* and *Batt*, 1984).

The probable existence of a volcano-sedimentary sequence in the southeastern part of the Bahia State, with peculiar

characteristics akin to Archaean greenstone belts, led the "Secretaria das Minas e Energia" (SME) (Secretariat of Mining and Energy) to initiate geophysical, geological and geochemical surveys of the region in 1976. Since then, mineral exploration aimed at targetting base metal sulphides and gold have been carried out by several companies, though most of the data remain unpublished and confidential.

In this chapter, the main geological characteristics of the largest greenstone association, the Contendas-Mirante belt (CMB) will be presented, based on the available literature, and my own work in the region. The data integration for this particular supracrustal sequence, using a Geographical Information System (GIS), will be described in Chapter 5.

## 3.2 Geology of the volcano-sedimentary sequence of Contendas-Mirante

The CMB is defined by an approximately north-south synclinorium, about 200 km long and 65 km wide, situated very close to the contact between the Gaviao and Jequie Blocks (Figure 3.1). To the north and south, it branches into smaller belts interdigitated with granite-migmatite-gneiss lithologies. To the northwest, the belt is partially covered by Middle- and Upper-Proterozoic platform sediments. Metamorphic mineral associations in the belt are typical of greenschist facies, with the exception of areas near to granite plutons, or at the margins of the belt, which are in amphibolite facies.

The sharp contact between the volcano-sedimentary sequence and granulitic sequences of the Jequie Block relates to shearing along a regional steep reverse fault, the Jequie Block having

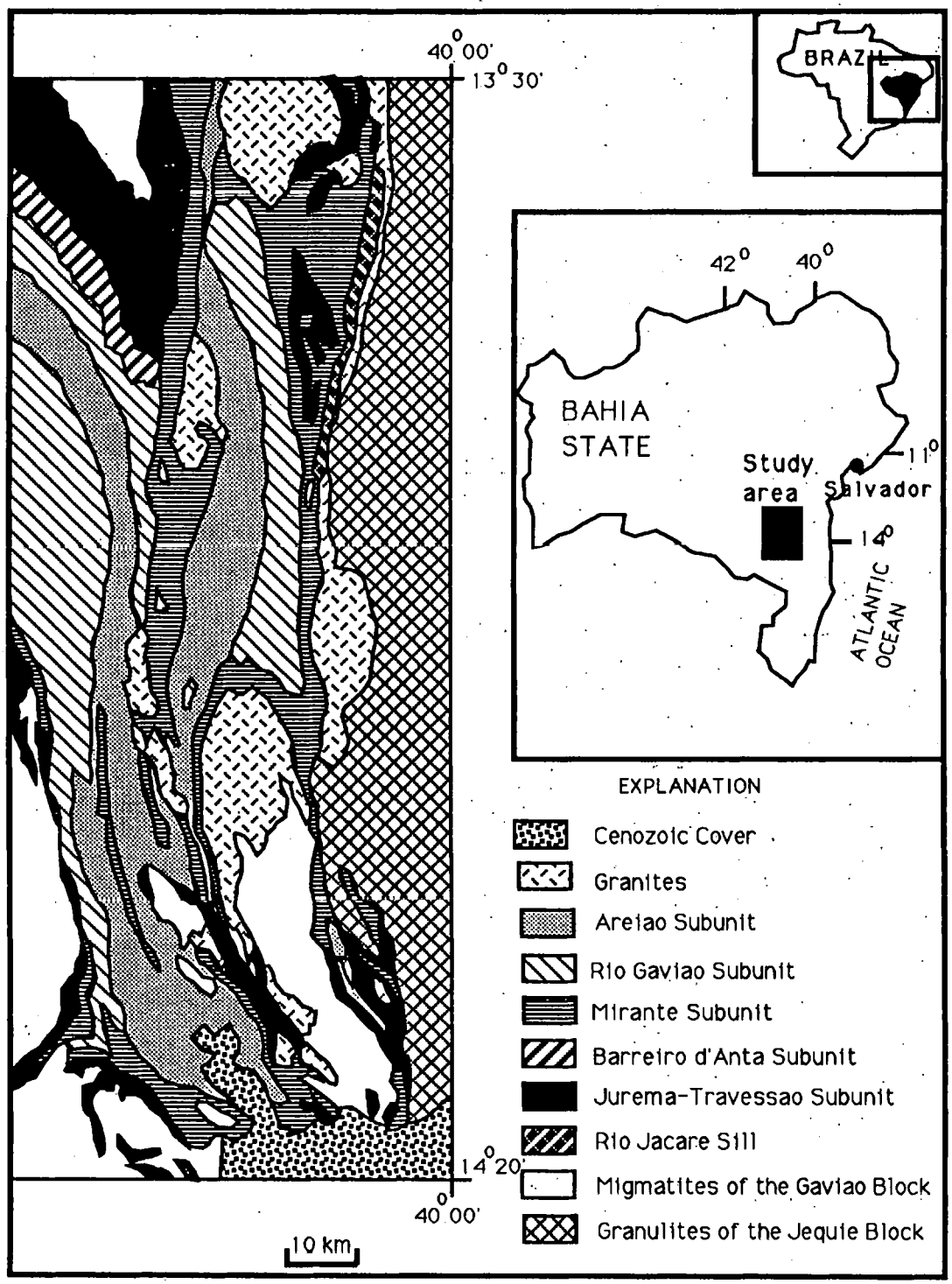


Figure 3.1 : *Simplified map of part of the Contendas Mirante belt (modified from Mascarenhas, 1982)*

been thrust over the Gaviao Block. In a similar fashion, there is a sharp, probably faulted, contact between the CMB and granitic-migmatitic Gaviao Block. The contacts of the CMB are, in all cases, parallel to the structures of the cratonic blocks and no unconformity can be detected. The available Rb-Sr and K/Ar radiometric dating of the Gaviao Block suggest the existence of a continental crust between 3400 and 3100 Ma.

The CMB was divided into two distinct units by *Marinho et al*, (1979, 1980): a mainly volcanogenic Lower Unit consisting of the Jurema-Travessao and Barreiro d'Anta Subunits, and an essentially clastic Upper Unit that includes the Mirante, Rio Gaviao and Areiao Subunits. The complex folding and ductile deformation makes estimation of thickness very difficult.

A large number of typical syn-kinematic to late kinematic peraluminous leucogranite plutons have been recognized in the area of the CMB.

### 3.2.1 The Jurema-Travessao Subunit

The Jurema-Travessao Subunit (JTS) forms the borders of the CMB, and is in contact with the basement (Figure 3.1). It also outcrops in an extensive axial zone as a result of regional anticlinal folding. The JTS comprises mafic to felsic metavolcanic rocks, volcanoclastic sediments, chemical metasediments and numerous minor masses of ultramafic and mafic rocks.

The mafic metavolcanic rocks are represented by two different types of basalt:

(a) the massive variety has fine grain size, sometimes exhibits pillow structure, is frequently schistose and is invariably cut by microveins of quartz and calcite. It has

granolepidoblastic, blastoporphyritic and blastointersetal textures. Original igneous features are preserved where the basalt is little deformed including microphenocrysts or microlites of plagioclase. The matrix is formed by very small prisms of tremolite-actinolite and/or horblende, plagioclase and small flakes of biotite, almost always impregnated with iron oxides. Coarser types could be the result of recrystallization giving them a gabbro-diorite appearance, but could could reflect parental basaltic intrusives.

(b)the amygdaloidal variety is aphanitic, dark green in colour and schistose. It has a very fine matrix which is composed of plagioclase in lath-like microlites which rarely shows preferred orientation. Fine prisms of actinolite and hornblende are situated between the plagioclases. The amygdales are polygonal aggregates of calcite, chlorite, epidote and alkali-feldspar in radial concentric structures.

The intermediate and acid lavas do not outcrop over wide areas. They are grey to greenish in colour, schistose and sometimes cataclastic. Generally they have millimetric phenocrysts. Their textures are blastoporphyritic, blastointersetal or sometimes granolepidoblastic, when the blastesis is more intensely developed. The plagioclase phenocrysts are tabular and idiomorphic and most are corroded, fragmented and saussuritized. Quartz phenocrysts are smaller but are rounded and equally corroded. The matrix has microlaths of plagioclase, sometimes oriented, which occur with quartz and small plates of mica impregnated with iron oxides produced during the blastesis.

The chemical sediments include intimate associations of metachert, banded iron-formation (BIF) and metacarbonates. They form discontinuous horizons or belts of variable thickness up to 10 metres intercalated with the volcanogenic components. The metacherts are massive or banded, and are extremely fine grained. They are always recrystallized and cataclastic, appearing as quartzites. The colour varies with the composition, being light to dark grey, greenish or reddish. Quartz is accompanied by subsidiary biotite, chlorite and hematite.

The BIF consists predominantly of alternations of millimetre-to-centimetre bands of magnetite and amphibole (grunerite) with pyrrhotitic chert. They are dense, fine-grained rocks with an oriented granoblastic texture.

The metacarbonates are represented by marble and calc-silicates. The calc-silicate units form thin discontinuous levels and are fine to coarse grained, light greenish-grey to dark green in colour, and commonly contain tight disharmonic folds. They form a series of moderately high ridges. The rocks are rather quartzose and have high diopside, tremolite-actinolite and epidote contents, and are generally foliated with granoblastic to granolepidoblastic textures. The marble contains variable quantities of goethite, quartz, sericite, albite, talc and tremolite as well as calcite.

The volcanoclastic rocks comprise mainly metatuffs. Their appearance in outcrop varies according to the amount of clastic-size fragments. Stretched lithic fragments of aphanitic material of a generally basic composition, elongated aggregates of quartz, or isolated crystals of plagioclase may

be present and indicate a pervasive ductile deformation. Locally microfolds can be observed. Detailed mapping has shown that is possible to separate lithic-poor metatuffs from discontinuous belts of fine-grained, mafic to intermediate lithic metatuffs and belts of coarse-grained intermediate to acid volcanoclastics, which grade locally into true ignimbrites. Basaltic breccias appear sporadically amongst the amygdaloidal basalts and lithic metatuffs. They are characterized by angular basaltic fragments in a fine, schistose matrix of basaltic composition. The fragments have an extremely wide size-range, from millimetric grains to centimetric blocks.

Throughout the JTS ultramafic and mafic rocks form narrow, discontinuous belts associated with practically any of the other lithologies of the subunit. They often occupy the basal parts of the supracrustal sequence in direct contact with migmatites and augen-granitoids of the neighbouring blocks. They are massive or foliated, sometimes schistose with folds and crenulations. Grain size is fine to medium, although there are textural and compositional variations. Tremolite, actinolite and hornblende schists, amphibolites and serpentinites can be recognized. The tremolite and actinolite schists sometimes have radial agglomerates of amphibole crystals. The hornblende schists are composed of xenoblasts or hypidioblasts of green hornblende. Quartz grains form ill-defined bands or are included within the hornblende. Prisms of chlorite, epidote and some carbonate comprise the accessories. The serpentinite contains chlorite and antigorite. An incipient foliation is locally present and they are sometimes talcified. Magnetite is present as grains, filaments or

dispersed patches. The amphibolites are represented by several varieties characterized by different mineral associations. The variety of paragenesis is due to small differences of metamorphic evolution and reflects as well the subtle variations of the original compositions (*Marinho* and *Sabate*, 1982) The ultramafic and mafic rocks due to high content in Cr (>1000 ppm) could possibly correspond to small intrusions.

### 3.2.2 The Barreiro d'Anta Subunit

The Barreiro d'Anta Subunit (BAS) is distributed along the western flank of a vast imbricated antiform (Figure 3.1) controlling high ground. *Cunha et al* (1981), defined the BAS as an undivided mixed assemblage of pyroclastic rocks, chemical and detrital sediments.

Pyroclastic rocks predominate at all stratigraphic levels of the subunit, and are mixed with the other components. They comprise microfolded, fine grained schistose metatuffs of essentially acid composition. The matrix, frequently micaceous, contains millimetric globular quartz or iron oxide crystals and angular fragments (up to 4mm) of plagioclase and quartz.

The chemical sediments are represented by BIFs which are centimetric-to-metric beds, intercalated with the pyroclastic schists. They are similar in all aspects to those in the JTS.

The detrital components of the BAS comprise metagraywackes, metapelites and schists. The metagraywackes are very monotonous. Their primary greenish grey colour is weathered to yellowish or reddish. Microfolded argillaceous levels are intercalated with silty-arenaceous levels in which very small medium-sand size angular to slightly rounded quartz or rock

fragments stand out. The quartz fragments show corrosion typical of a volcanic origin, and the source rocks for these fragments were probably acid tuffs. The metapelitic horizons are distinguished by the predominance of fine silty phyllites and schists. Their composition differs from the metagraywackes due to the presence of biotite. The schists are highly folded, dark to greenish. Quartz, magnetite and similarly-oriented hematite flakes form the granoblastic components. The phyllitic minerals are chlorite and sericite. Some fine-grained chlorite schists are rich in ilmenite.

### 3.2.3 The Mirante Subunit

The Mirante Subunit (MS) (Figure 3.1) is composed of fine to medium grained, grey-green schistose metapelites, which are strongly foliated, crenulated and folded. Some include numerous narrow intercalations of very fine-grained feldspathic metasandstones, sometimes containing large quantities of anhedral magnetite crystals. Milky quartz segregations follow the principal foliation, in some places having pinch-and-swell structures or penetrative rodding. The MS is characterized by the pervasive presence of biotite. The schists form two different varieties: the nodular and gneissified schists.

The nodular schists are found in contact aureoles, and contain nodules of high temperature and low pressure minerals. The few aluminous bands contain andalusite, and the others cordierite. The cordierite pophyroblasts are spongy and include quartz, plagioclase, biotite, muscovite, opaque minerals and sometimes tourmaline. Close to the granites, the nodules are stretched within the principal foliation planes which appear "moulded"

around the intrusive body suggesting syn-kinematic intrusion. Away from the intrusions, there is a reduction in the quantity and the size of the nodules and also the mica flakes. The metamorphic transitions clearly result from an increase in the thermal gradient close to the intrusion. This gradient was superimposed on and accompanied the regional metamorphism which generated the foliation. The feldspathic metasandstone intercalations are less affected by thermal metamorphism and composed mainly of plagioclase, quartz and lesser quantities of microcline and biotite.

The gneissified schists occur nearby granitoid intrusions, are of metasomatic origin (*Marinho et al*, 1980) and are composed of mica, quartz and/or albite-oligoclase. The granular minerals form elongated granoblastic aggregates alternating with micaceous lenses. Chlorite, silimanite and garnet may be present, and microcline is rare.

The components of the MS suffered intense deformation, which produced tight, usually isoclinal folds as well as quite frequent convolute folds and crenulations. Sometimes, very strong transpositions are observed. These factors make attempts at estimating the thickness of the AS very difficult.

### 3.2.4 The Rio Gaviao Subunit

The metasediments which comprise the Rio Gaviao Subunit (RGS) (Figure 3.1) are phyllites, metasiltites and a few schists . Abundant thin bands of light grey fine-grained feldspathic metasandstones and rare lenses of coarse, sometimes conglomeratic metasandstone with cross bedding are intercalated in the metapelites. The clastic are predominantly quartz and quartzites. The distinction between the RGS and MS

lies in their different metamorphic grade. The biotite isograde is not attained in the RGS where sericite, chlorite and muscovite are important minerals. Locally, a few porphyroblasts of cordierite are a sign of nearby intrusions. Apart from biotite, the mineralogical compositions of RGS and MS are similar. According to *Sabate* and *Marinho* (1982), the RGS was probably deposited in a deltaic environment. A reasonable hypothesis is to consider the RGS and MS the same unit.

### 3.2.5 The Areiao Subunit

The clastic assemblage which forms the Areiao Subunit (AS) (Figure 3.1), occupies the top of the CMB. *Marinho et al* (1980) found a progressive upward transition from the metapelites of the RGS. This transition zone, however could be the result of tectonic repetition by folding and/or imbrication of different facies of the AS and RGS. This would follow the structural style of the belt, and also would be compatible with the existence of a probable erosional discordance, suggested by the presence of grey phyllite pebbles. The sediments of the AS are composed of impure quartzose metasandstones, sometimes feldspathic but predominantly psammitic. Well developed cross-stratification at metric to decametric scale is often present. The beds are usually thin and made prominent by the alternation of layers rich in magnetite, hematite and quartz. More or less consistent conglomerate levels, with elongated or rounded centimetric pebbles of quartz or grey quartzite are also found. The AS underwent low grade metamorphism to chlorite-sericite facies (*Marinho et al*, 1980). The effect of deformation was weak, resulting in tenuous schistosities,

sometimes imperceptible in the outcrops. The mineralogical composition is dominated by quartz, altered albite-oligoclase, sericite-muscovite with chlorite along cleavage plans, opaques as disperse grains, and subordinate microcline.

The thickness of the AS was estimated by *Menezes* (1980) at approximately 2,000 m. This author also demonstrated the fluvio-continental to fluvio-deltaic origin.

The poor outcrop and structural complexity of the CMB means that this stratigraphy is provisional and needs more detailed structural and stratigraphic analysis.

## 3.3 Volcanic geochemistry of the Contendas-Mirante Belt

Usually, the magmatic nature of rocks is evident from field relations and petrography. Volcanoclastic and clearly sedimentary formations can also be recognised from field relations and petrography. However, because the rocks from the CMB have suffered metamorphism, their classification cannot be made by petrographic methods alone. Even when the recrystallization is not complete, and we can recognize fragments of magmatic minerals or relicts of volcanic textures, it is still difficult to identify in the recrystallized matrix the proportion of primary minerals.

*Sabate et al* (1982), used the different behaviour of Na, K, and Al during magmatic and sedimentary processes (*La Roche*, 1968) to separate the various petrographic groups. The metamorphic rocks were separated into magmatic, volcano-sedimentary and sedimentary groups. The same authors demonstrated the overall affinities of the metavolcanic rocks on AFM diagrams (Figure 3.2.a). *Sabate* and *Marinho* (1982)

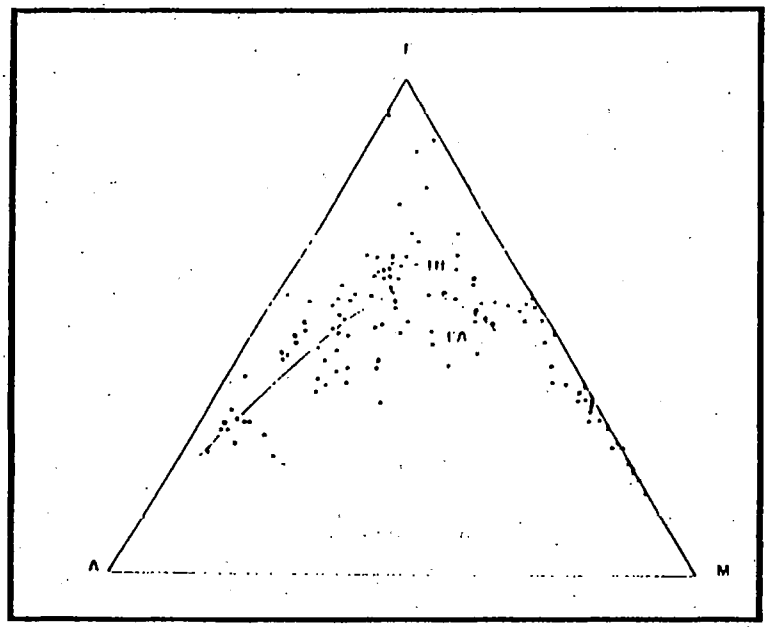


Figure 3.2.a : *Distribution of the magmatic rocks in the AFM diagram (A = $K_2O$ + $Na_2O$, F = Feo + 0.9*$Fe_2O_3$), M = MgO) (from Sabate et al, 1982)*

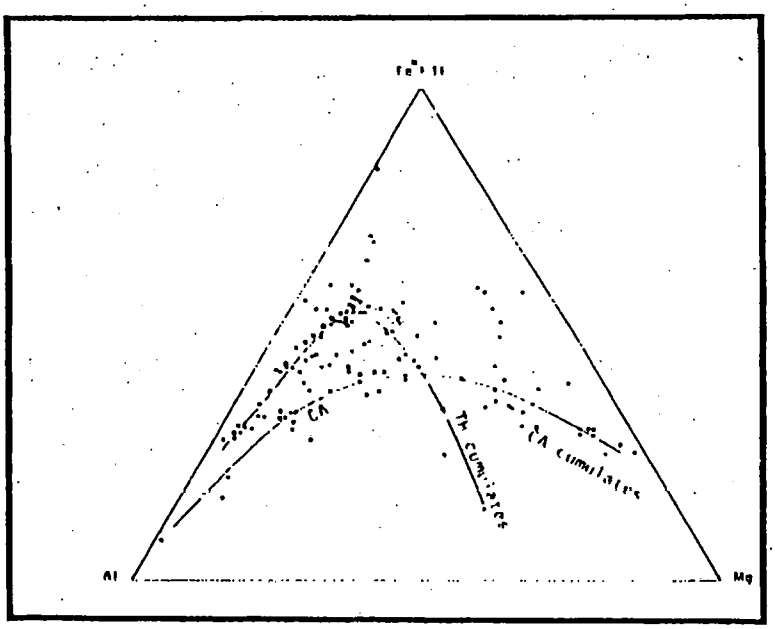


Figure 3.2.b: *Distinction between the two magmatic suites and their respective cumulates as a fuction of the contrasting behaviour of Al, Fe total and Mg. (from Sabate et al, 1982)*

have shown a typical Archaean bimodal association by comparing the contents of Al, Fe and Mg for these two magmatic suites. According to these authors, the suites show two kinds of distribution: one marked by a strong enrichment in Fe and Al, characteristic of tholeiitic evolution, and the other a trend of increasing alkalis and $SiO_2$ practically devoid of Fe-enrichment, more consistent with calc-alkaline differentiation (Figure 3.2.b). This contrast is similar to that observed in modern magmatic suites (*Pearce et al*, 1977), and common in other Late-Archaean volcanic terrains.

Variations in the content of Al, Fe, Mg and Ti in ultramafic rocks of the Jurema-Travessao Subunit confirmed that they are cumulates separated from primitive liquids and are responsible for the generation of the calc-alkaline and tholeitic trends, respectively (*Sabate et al*, 1982). According to *Marinho* and *Sabate* (1982) in some chemical aspects the composition of eight samples collected from the ultramafic rocks may be chemically related to that of komatiites (MgO=9%-20%, $SiO_2$=50%-56%, $TiO_2$ and $K_2O$<0.9% and $CaO/Al_2O_3$>1). Nevertheless none of the structural or textural features, such as spinifex texture, typical of komatiites have been found so far.

The behaviour of K, Rb and Ba suggests important post-magmatic transformations which are explained essentially by hydrothermal phenomena. Thus the ultramafic rocks are strongly depleted in K and Sr and the metavolcanics have increased their content in Rb and Ba (*Marinho* and *Sabate*, 1982).

## 3.4 The structural framework

The CMB is composed of several narrow strips clearly parallel to the contact between the Gaviao and Jequie Blocks. The

strips are bounded by faults and shear zones which also form the contacts between the subunits. The result is an imbricate interleaving, is made more complex by earlier plastic deformation. On a large scale, the lithological units form a vast elongated synclinorium, with wide superimposed antiforms: a northern axial antiform, in which the lowermost JTS and BAS are exposed, and a second contiguous eastern antiform, separated by a narrow zone of pinching of the synform. This structure hosts, in its axial zone, the Gameleira granitic intrusion and a third southeastern antiform determined by the insertion of the crustal blocks.

Two phases of plastic deformation can be recognized. The first phase (P1) manifests itself in the form of tight isoclinal folds often deformed by later minor folds. This phase developed a cleavage (S1) marked generally by crystallization of sericite and chlorite. In many rock types such as phyllites and metasiltites, the transposition of the original layering to S1 is complete. The dips and strikes of S1 are variable, the attitude being controlled by the second phase. The second phase is generally expressed as a constant schistosity (S2) trending approximately north-south and dipping steeply. The juxtaposition of the two schistosities S1 and S2 is common in outcrop. Regional scale structures are repeated at the scale of outcrop and show different styles at different locations within the belt. At the margins, especially close to the Gaviao Block, P2 in the Lower Unit is represented by tight isoclinal folds of decimetric wavelength. The antiform flanks have metric to decimetric kink folds in formations of the Upper Unit. In the axial zone of the belt, cylindrical folds

are found, and in the synforms similar folds are also observed.

*Sabate* and *Marinho* (1982), and *Silva* (1984, 1985) have carried out a structural analysis of several outcrops of the belt, and they concluded that the two phases are almost co-axial but with distinct axial planes.

Later brittle deformation in the form of discrete faults and fractures will be discussed in chapter 6 on the basis of the interpretation of processed TM and radar data.

## 3.5 The intrusive granites: peraluminous magmatism

Thickening continental crust typically allows the generation of large amounts of crustal melt without the direct involvement of mantle material. Peraluminous leucogranites represent the most characteristic magmatic products generated during continental collision, resulting from a low degree of melting of metasedimentary material.(*Pichavant et al*, 1988a) Associated intermediate to basic plutonic members are typically absent. In the Hercynian and Himalayan belts, peraluminous leucogranites form relatively narrow belts elongated over several hundreds of kilometres parallel to the major thrust plane (*Pichavan et al*, 1988b).

In the CMB, six plutonic granitoid associations can be recognized in the same tectonic alignment: the Gameleira, Riacho das Pedras, Caetano-Alianca, Sete Volta, Lagoa Grande and Lagoinha granites (Figure 3.3). They cross-cut most of the CMB structures, and represent late to post-tectonic granitic bodies.

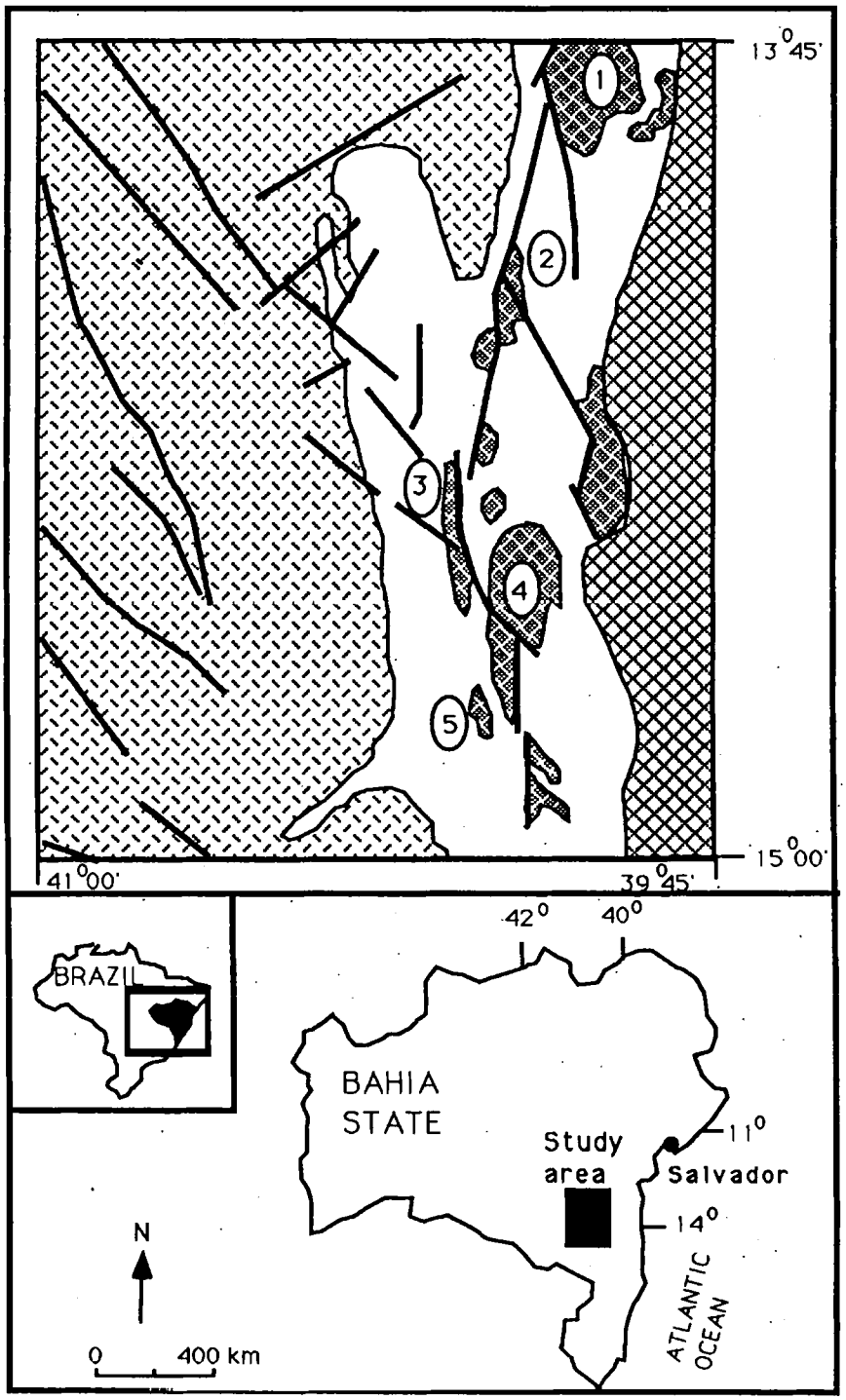


Figure 3.3 : *Granitoids of the Contendas-Mirante region (modified from Mascarenhas, 1980)*

The Gameleira granite induced a thermal metamorphism in the host rocks, with the formation of cordierite and andalusite in the MS. Its emplacement is synchronous with the important late overprinting and folding phase, whose corresponding shortening is related to thrusting (*Sabate et al*, 1980). The overall composition is granodioritic, with a variable quartz, oligoclase-andesine, microcline assemblage.

The Riacho das Pedras granite is late tectonic and is associated with a network of aplite and pegmatite dykes which crosscut the supracrustal sequence. A crustal origin is assumed on the basis of the peraluminous and semi-potassic paragenesis (*Marinho* and *Sabate*, 1982).

The Caetano-Alianca granites form an elongated 20 km north-south belt and are only separated by a small isthmus of CMB. Biotite-garnet schlieren and muscovite-biotite-garnet-tourmaline pegmatites are common. A syn-tectonic emplacement is indicated by the second phase foliation which tends to cut across the pegmatites.

The Sete Voltas body occupies the core of a structural dome and is composed of banded grey gneiss with incipient anatexis, and weakly deformed porphyritic granites. The granites represent the central and major part of the dome and have a more homogeneous mineralogical composition.

The Lagoa Grande intrusion is poor in muscovite and very homogeneous. The existing foliation is underlined by biotite and garnet schlierens and mylonitic textures are reached at the eastern margin of the body.

The Lagoinha granitoid is one the southernmost leucogranite body intruding the CMB. The presence of biotite- and/or muscovite-rich schlierens are widespread.

Possible differences among these granites are returned to later, in the context of their radiometric signatures.

### 3.5.1 Isotopic studies

Strontium and neodymium isotopic compositions have been obtained by *Cunney et al* (1989). The result from Rb-Sr isochrons are summarised in Table 3.1.

| Granitic body | Age (Ma) | ISR $^{86}Sr/^{87}Sr$ |
|---|---|---|
| Gameleira | 1947±47 | 0.7072±0.0030 |
| Riacho das Pedras | 1979±19 | 0.7648±0.0151 |

**Table 3.1**: *Rb-Sr isotopic data for some Bahia State granitoids (from Sabate et al,1990)*

A basic uncertainty of this approach is that although the Sr isotope geochemistry indicates that all granitoids possess a crustal signature, the exact characteristics of their sources are impossible to deduce by Rb-Sr since various sources, different in age, and Rb-Sr ratios can produce magmas which have the same Sr isotopic compositions (*Sabate et al*, 1990).

The Sm-Nd method has been applied to these granites and the data collected by *Sabate et al* (1990) are reported in Table 3.2

| Granitoids | Sm (ppm) | Nd (ppm) | $^{147}Sm/^{144}Nd$ | $^{143}Sm/^{144}Nd$ | $\varepsilon_T$ | $T_{CHUR}$ (Ma) | $T_{DM}$ (Ma) |
|---|---|---|---|---|---|---|---|
| Gameleira | 4.1 | 27.2 | 0.09111 | .51087 | -8.8 | 2586 | 2600 |
| Riacho das Pedras | 0.55 | 2.02 | 0.1646 | .51191 | -6.2 | 3410 | 3165 |

**Table 3.2**: *Sm-Nd isotopic data for some Bahia State granitoids $T_{CHUR}$ refers to chondritic mantle and $T_{DM}$ depleted mantle (from Sabate et al,1990)*

The granitoids seem to originate from a late-Archaean Jequie-type source rather than from an older source or from the Contendas-Mirante Upper Unit which, according to the available Nd data has a Lower Proterozoic age (*Marinho* pers. comm.).

### 3.5.2 Major and trace elements

With respect to major elements, *Cunney et al* (1989) used the A-B diagram (Figure 3.3.a) of *Debon* and *Le Fort* (1982), and demonstrated clearly that all these granites are peraluminous, although the peraluminous index varies widely between and within the different granitic plutons. In the Sete Voltas plutonic rocks, the most leucocratic samples are the most peraluminous. The porphyritic facies is weakly peraluminous. The Riacho das Pedras granite is very leucocratic and presents a large variation in the peraluminous index without any significant variation of its biotite content. Two sub-groups can be distinguished in the A-B diagram: a first one presenting a low and rather constant peraluminous index and the second one with high and variable peraluminous index.

*Cunney et al* (1989) show that the Rare Earth Element spectrum(REE) of the Sete Voltas granite is similar to Archaean trondjhemitic-granite suites. The Gameleira samples show a REE pattern very similar to the most trondjhemitic

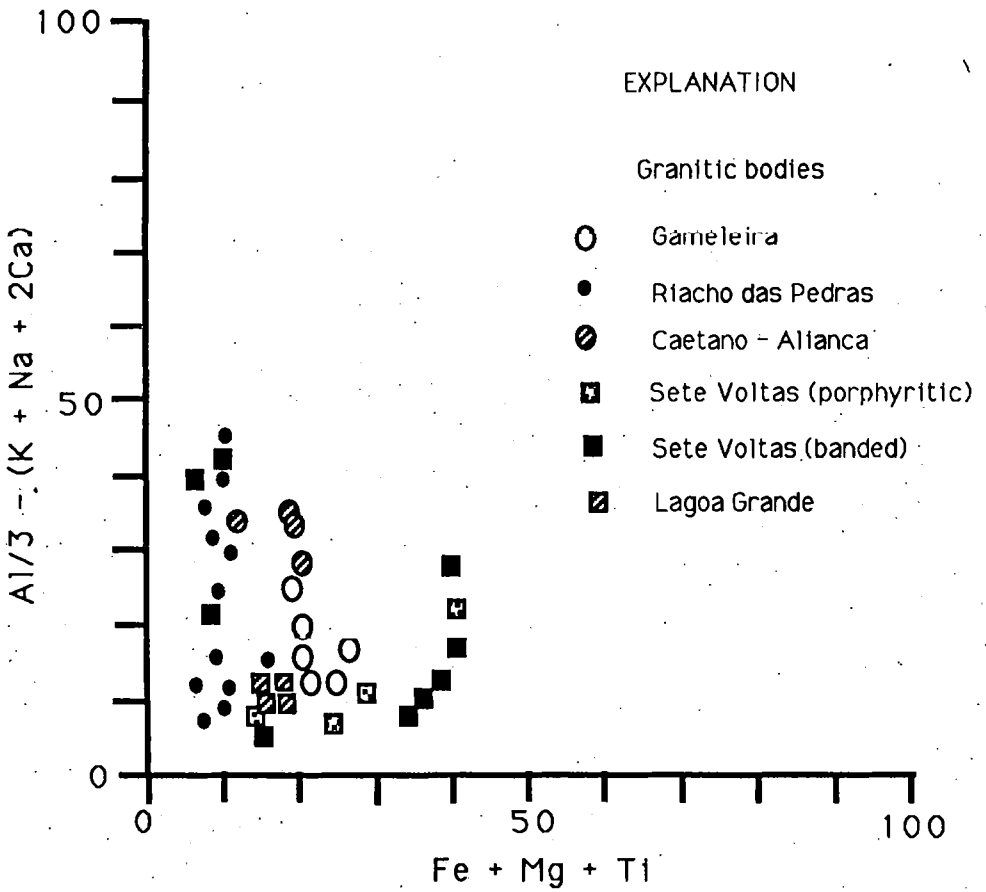


Figure 3.3.a : *The A - B diagram (from Cunney et al, 1989)*

sample of the Sete Voltas dome. The Riacho das Pedras and Alianca plutons display very low REE contents and the strongest positive europium anomaly.

The chemical signature supports the idea that the Archaean TTG suites may represent a possible source material for the Transamazonico leucogranites (*Cunney et al*, 1989).

## 3.6 Mineral occurrences

Baryte has been exploited in the CMB since 1950. In the 1980s, the region increased in importance following the discovery of an important mafic-ultramafic intrusion with a Ti-V-PGE association and a gold-bearing banded iron-formation. From 1985, as a result of intense geological survey, many occurrences of base metals have been found in this area (Figure 3.4)

The baryte ore field represents 48% of the total reserve of Bahia State. Although baryte can be found in the CMB, the majority of the ore bodies are related to the metavolcanic rocks of dacitic composition in the Rio dos Remedios group (Espinhaco Supergroup) (*Marinho et al*, 1979). Two types of ore bodies can be recognised:

(a) related to metamorphic-migmatitic complex near the contact between this complex and Rio dos Remedios group, and
(b) the orebodies related to the Paraguassu group, in the contact between this unit and the metavolcanics of the Rio dos Remedios group. Generally, the orebodies are structurally controlled and are associated with lineaments. Their grain size varies from fine to coarse. Their length varies from 250 m to 2500 m, and thickness from 1 m to 4 m.

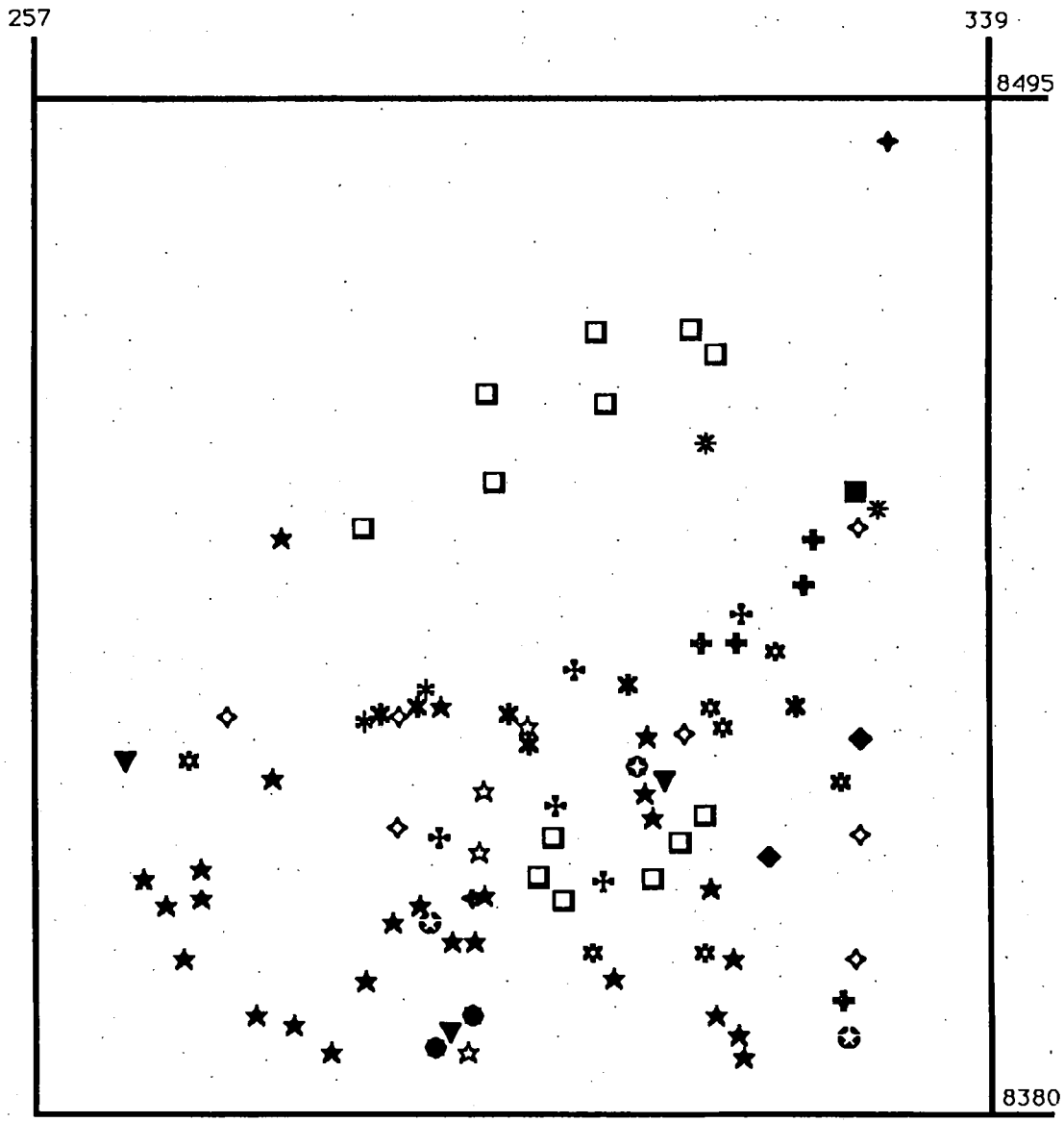


Figure 3.4 : *Mineral occurrence locations of the study area (★talc, (✦titanium, (✲vermiculite, (✚quartz, (☆beryllium, (✳manganese, ( ◇asbestos (✱baryte, (✪kyanite, (✣copper, (✪calcite, ( ▼)iron, (◆graphite, ( ●emerald, (□gold, (✳)lead, (■corundum*

The V-Ti-Platinum group elements (PGE) deposits related to the Rio Jacare Sill are in a pipe-like body, hosted in pyroxenites. It comprises a zoned plug made up of diallageite pegmatoid, similar to that which occurs in Kennedy's Vale at Magnet Height in the Bushveld Complex (*Galvao et al*, 1987). A reserve of 70,000 tons of $V_2O_5$ was determined, with a cut off of 0.6% $V_2O_5$. Vanadium-rich magnetite occurs as disseminations in the pyroxenite and as stratiform massive ore. The thickness of the layer varies from a few centimetres to 12 metres. The $V_2O_5$ content of the massive ore is fairly variable, reaching as high as 6% in the deepest part of the deposit. The main ore minerals are magnetite and ilmenite. PGE, pyrite and pyrrhotite occur as traces. The Fe/Ti ratio varies from 4 up to 8 and the $P_2O_5$ content is less than 0.02%. The rocks of the Rio Jacare Sill are confined to the tholeitic field (*Galvao et al*, 1987).

Gold-bearing BIF occurs interlayered with felsic to mafic metavolcanic rocks of the JTS. The BIF consists predominantly of alternating millimetre-to-centimetre thick bands of magnetite and chert. This chert, sometimes, contains disseminated pyrrhotite and forms a well defined layer. With respect to the origin of the BIF, *Silva* (1987) has suggested that the volcanic exhalative hypothesis is well supported by the sedimentary rock associations: the sedimentary facies and structures, the cyclic nature of the deposition and the evidence of associated volcanic activity. Two types of gold mineralisation can be found:

(a) confined to the relatively thin BIF, especially those rich in arsenopyrite and other sulphides, and

(b) controlled by structural features such as shear zones and fracturing.

Talc is frequently associated with serpentinized ultramafic bodies, and actinolite-tremolite schists or amphibolites which have been intruded in the metamorphic-migmatitic complex. Few occurrences can be found associated with the JTS. The ore bodies form lenses up to 50 m wide and 120 m in length. The high content of total Fe, MgO, $SiO_2$, $Al_2O_3$, Mn, Pb and As, high pH and moisture of the ore, restrict its industrial application (*Marinho et al*, 1979)

Vermiculite occurs as veins and lenses frequently associated with actinolite and tremolite schists, and biotite gneiss. In the schists the mineralisation is apparently related to hydrothermal fluids, in the gneisses to supergene processes. Vermiculite occurs as small (<1cm) black to green plates. In general terms, there are no technological tests to establish the quality of the ores. One sample has been studied and showed an expansion factor of 84% (*Marinho et al*, 1980).

Beryl is related to zoned pegmatites which intrude highly deformed ultramafic rocks of the JTS and metasandstone of the AS. Beryl occurs as dark green anhedral crystals, disseminated throughout the pegmatites (*Marinho et al*, 1979).

Manganese is related to volcano-sedimentary rocks at different metamorphic grades. Ore bodies related to greenschist metavolcanic rocks comprise carbonate rocks with high iron content, and they are structurally concordant with the host rocks. Ore bodies associated with granulitic rocks correspond to supergene alteration of Mn-rich supracrustal sediments,

which subsequently suffered high metamorphism (*Marinho et al*, 1979)

Asbestos is related to serpentinized ultramafic rocks mainly intruded into the enderbites of the Jequie Block, but also into the migmatites of the Gaviao Block and the JTS. The ore bodies are classified as cross fibre and slip fibre, and occur as lenses up to 5 cm in length (*Cunha et al* 1981).

Kyanite occurs disseminated within quartz-veins which are hosted by granulitic and migmatitic rocks. Colluvial concentrations are less important. The crystals are light green varying in length from 1 mm to 13 cm and are associated with sericite, biotite and feldspar (*Cunha et al* 1981).

Secondary copper minerals such as malachite and azurite are found associated with fault zones which cross mafic and ultramafic rocks and mafic metavolvanics of the JTS. Primary copper minerals, mainly chalcopyrite, can be found associated with the baryte veins (*Cunha et al* 1981).

Graphite occurs as concordant centimetric veins hosted in the granulitic rocks. Its economic importance is not yet evaluated (*Cunha et al* 1981).

Emerald and beryl occur in the contact between ultramafic schists and granitoids. The contact is characterized by tightened folds and shear zones, and the presence of pegmatites which are homogeneous and structurally concordant (*Cunha et al* 1981).

## 3.7 Climatic setting

Climate plays an important role in geological remote sensing. The climatic conditions found in the study area are relatively

uniform. According to the classification of *Koppen* (in *Silva*, 1987), which is based on average temperatures and on rainfall, the study area falls into the category BS, equivalent to semi-arid or steppe. Within this category three subdivision can be found:

a) BSx'h' - very hot, average annual temperature and average of the coldest month both greater than 18°C; irregular rainfall;
b) BSwh' - similar to BSx'h' but with high rainfall during the summer;
c) BSsh' - similar to BSx'h' but with high rainfall during the winter.

Generally speaking the climatic setting of the study area is characterised by a dry winter (June, July and August) and a wet summer (November, December and January). The total rainfall index varies from 450 mm to 700 mm per year and the annual temperature from 24°C to 27°C.

### 3.7.1 Vegetation aspects

In the study area, agriculture is not widespread due to climate. Nevertheless part of the 'original vegetation' cover was removed for cattle settlement. The term 'original vegetation' as used here indicates areas where natural primary flora still predominate over secondary flora. Four main types of vegetation cover can be found: a region characterized by thorny, stunted vegetation called caatinga, grassland, cultivated land and forest.

The vegetation maps presented in Figures 3.5.(a) and (b) represent part of the study area and are based on information collected from reports generated by the "Companhia Baiana de

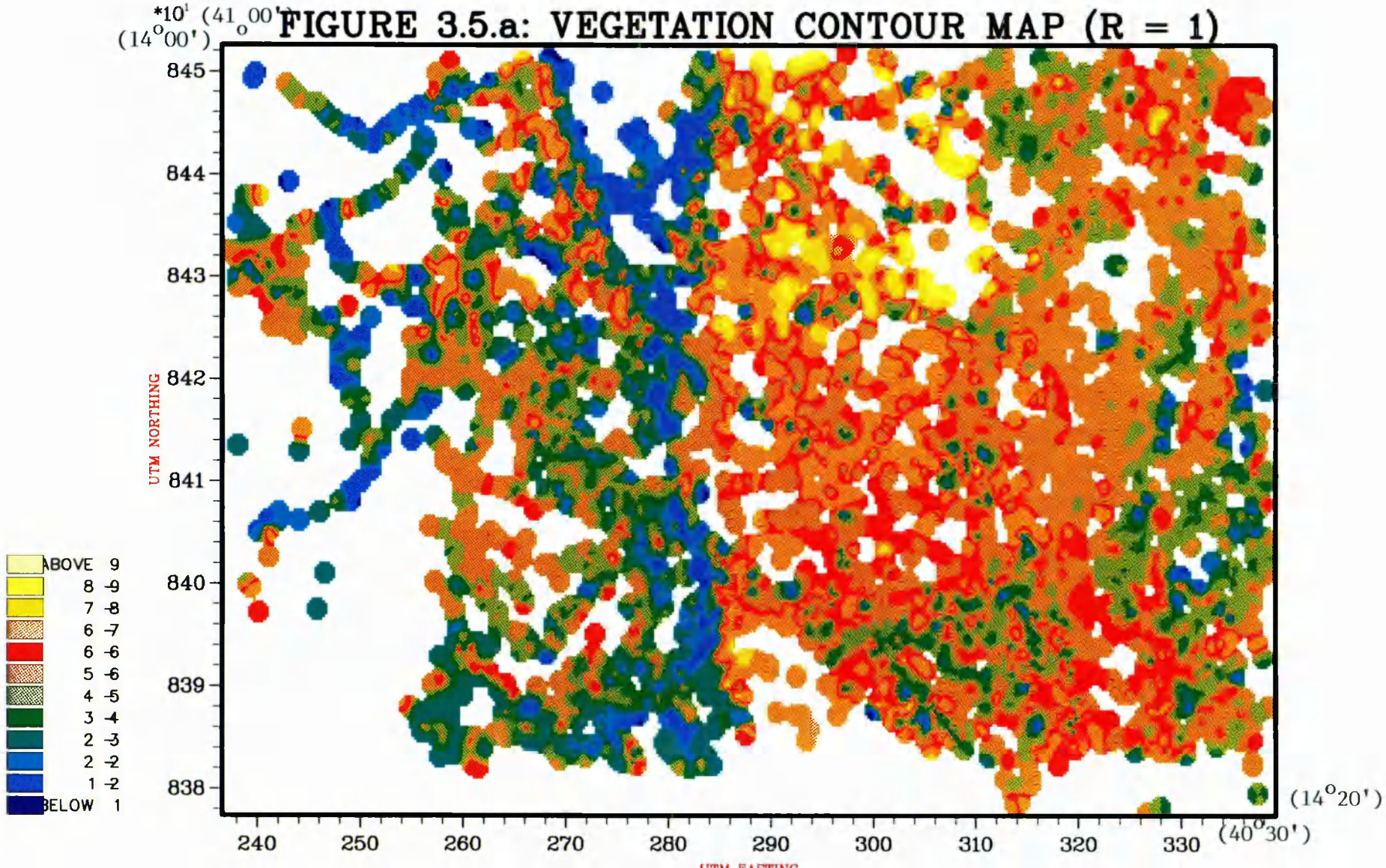


FIGURE 3.5.a: VEGETATION CONTOUR MAP (R = 1)

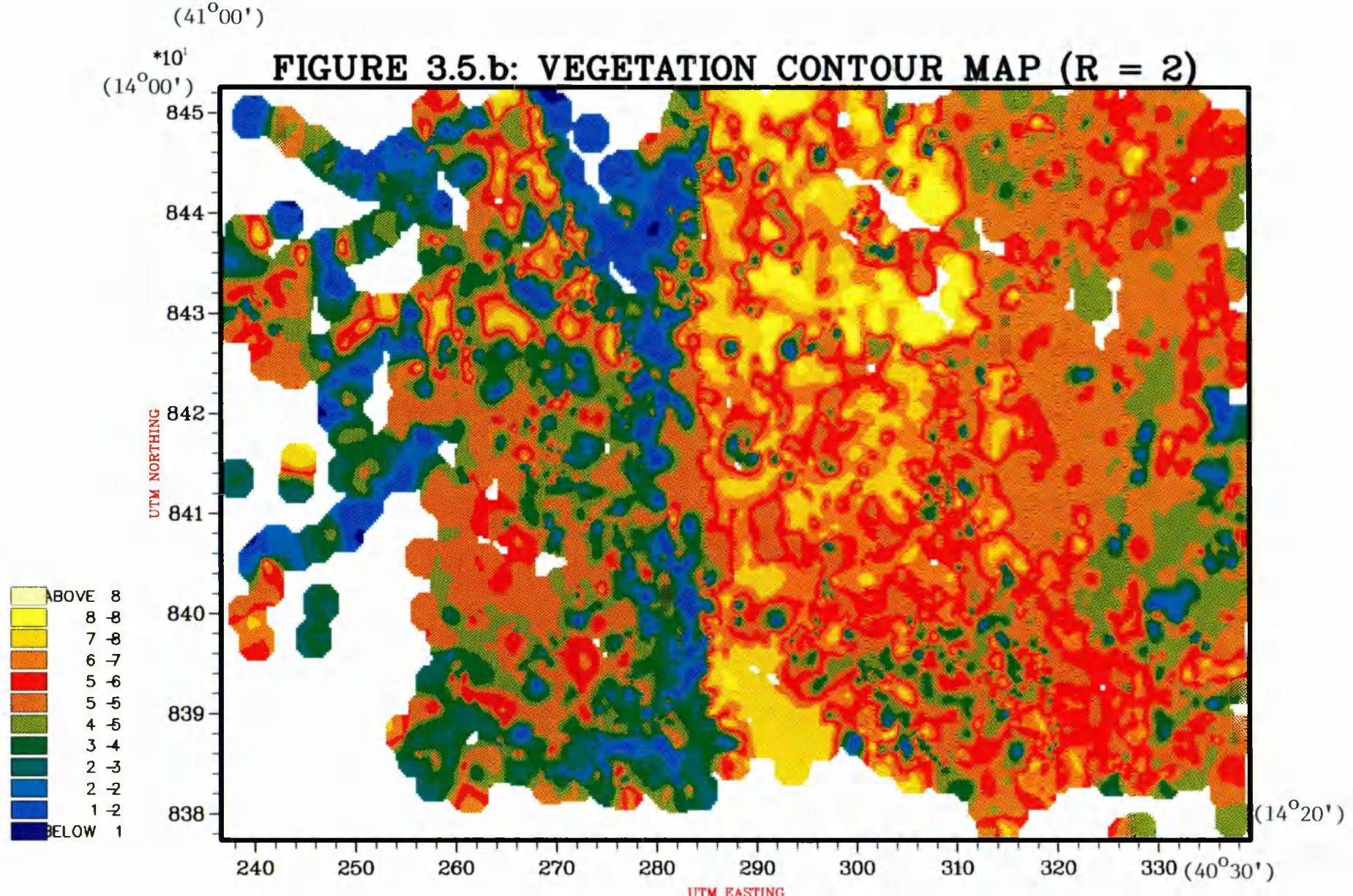
FIGURE 3.5.b: VEGETATION CONTOUR MAP (R = 2)
(41°00')
*10⁵
(14°00')
845
844
843
842
841
840
839
838
UTM NORTHING
ABOVE 8
8 -8
7 -8
6 -7
5 -6
5 -5
4 -5
3 -4
2 -3
2 -2
1 -2
BELOW 1
240
250
260
270
280
290
300
310
320
330
(40°30')
(14°20')
UTM EASTING

Pesquisa Mineral - CBPM"( Bahian Company for Mineral Resources) and field work. Although with artifacts, which are a function of the chosen radius (R) that is used to set in user units around each grid node to search for data points affecting it, the resultant maps show a strong contrast between vegetation in the central to the west part of the study area. This boundary corresponds to the contact between migmatites and gneisses and the Contendas-Mirante belt. To the east forest (classes: 1 to 3) and dense caatinga predominate (classes: 4 to 6) and to the west scarce caatinga (classes: 6 to 8) and cultivated areas (class: above 8) predominate.

Caatinga dominates in the study area. According to the density of the trees, two subdivision are proposed: scarce caatinga and dense caatinga. The scarce caatinga corresponds to open arboreal areas comprising small to medium weight trees (2 m to 4 m) while dense caatinga comprises small to medium weight (2 m to 4 m) and some high trees (over 4 metres).

Grasslands correspond to areas used for cattle grazing and are developed on soils derived from rocks of granitic composition and metasediments. The grass is very sensitive to drought and during dry seasons it becomes sparse exposing the soil.

Cultivated areas include mainly maize crops. Maize fields are seasonally cleared after harvest and this may leave the soils exposed for some time. There is no strong correlation between planted vegetation and particular rock unit. Forests are found in scattered patches and are mostly of deciduous trees. Forest is often found along the drainage channels. They are easily seen in remotely sensed images but obscure the water beneath.

FIGURE 3.6: SOIL MAP OBTAINED BY POINT KRIGING TO GRID CELLS

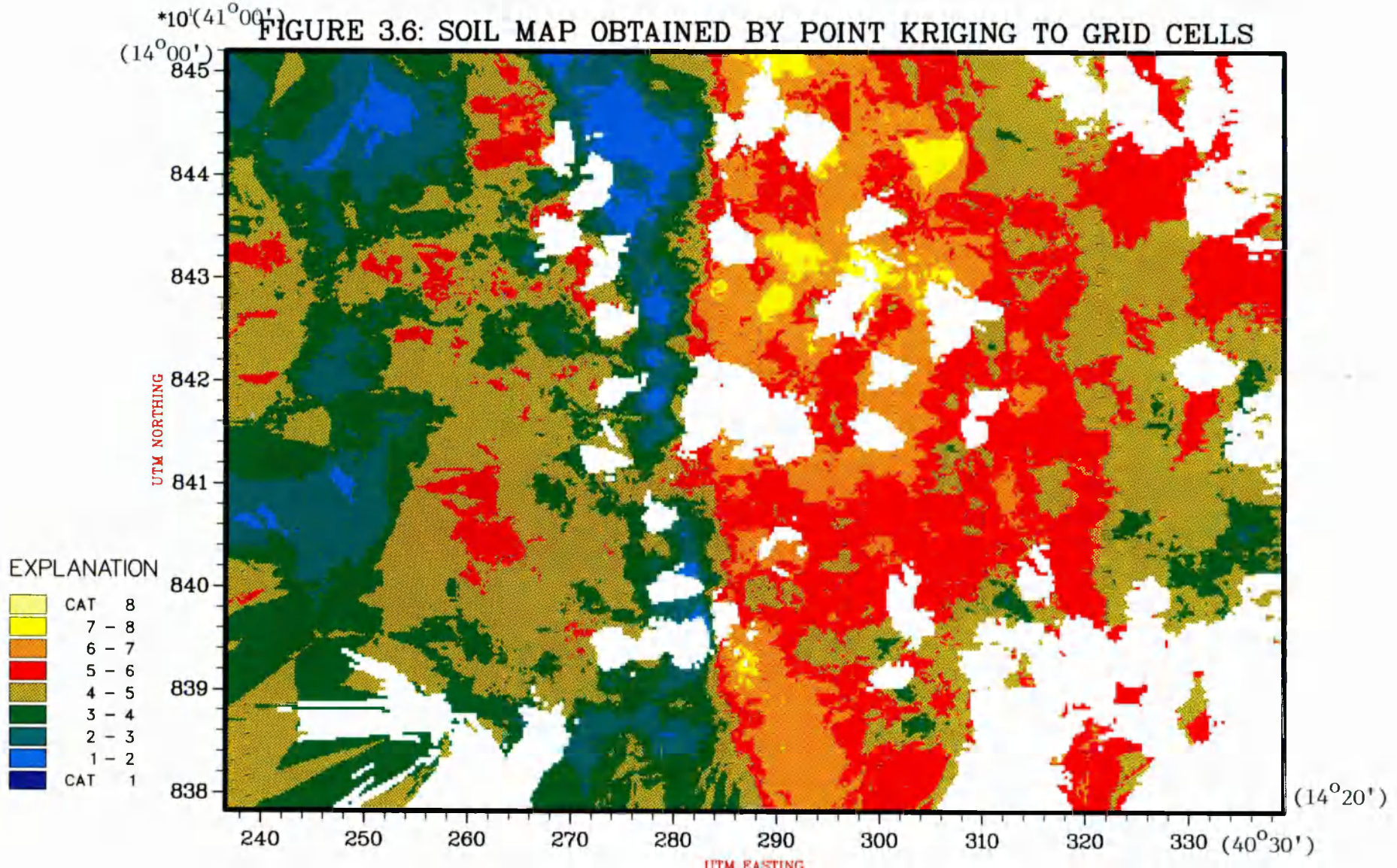


3. 24. A

### 3.7.2 Rock weathering and soil cover

Under the climatic conditions described above, the weathering processes are dependent on geomorphic factors. In regional terms the soils are classified according to the nomenclature proposed by the Brazilian System of Soil Classification (SNLCS).

The soil map of the study area was generated using kriging technique (Figure 3.6). The data were collected at field sites from the Contendas-Mirante Project, Anage-Caldeirao Project, Triunfo-Contendas Project and during my field work in December 89 to February 90. A soil map to conventional standards has never been produced, but the soil classification at field sites, in ASCII form, enables a rough guide to soil distribution to be produced by computer interpolation. It was produced using UNIRAS (UNIversal RASter system). Briefly UNIMAP 2000 is part of the UNIRAS package, a technical mapping system that can capture, model and analyse data in 2D or 3D. Its built-in analysis functions allow the computation of surface models from sparse data points, and it can perform relatively complex mathematical calculations on multiple surfaces simultaneously. UNIMAP operates by using the processes of either triangulation or rectangular gridding.

In general terms in the study area it is possible to separate the area into three subareas. Subarea A occupying approximately 50% of the total area is located in the western part. In this subarea categories 1 to 4 (white and yellow latosols, red luvisol and white regosol) predominate. Subarea B which occupies the central part has approximately 20% of the total area, categories 5 and 6(red regosol and yellow regosol)

predominates. Subarea C corresponds to the eastern part of the area, and represents approximately 30% of the total area. In this subarea categories 4 and 5 (white regosol and yellow regosol) predominate. In general terms, Subareas A, B and C correspond approximately to migmatites and gneisses, Contendas-Mirante belt and Granulites domains, respectively.

Red, yellow and white latosols are well developed in the study area. They are deep soils with a well developed drainage and a clayey texture and are related to granulites and schists, migmatites and metavolcanics, and ultramafic rocks, respectively. Luvisols are restricted in the study area. They are deep soils and fairly developed on mafic ultramafic rocks. Regosols are typical of the lowland zone. They are moderately well drained with a depth of few metres. Geologically there is some coincidence between their occurrence and rocks of granitic composition (yellow) and metasediments (white). Lithosols are related to quartzites and migmatites. They have a depth of a few decimetres and are not used for agricultural purposes. Alluvial soils are associated with rivers and are developed from recent deposits, and consist predominantly of sand, clay and silt with frequent conglomeratic levels.

## 3.8 Geomorphological features

The study area forms part of the Rio de Contas hydrographic basin and *King* (1956) attributes the landform to three denudation cycles: Sul-Americano, Velhas and Paraguassu which took place during the Eotertiary, Neotertiary and Quaternary, respectively.

The processes acting on the land depend on lithological and structural factors, climatic conditions and vegetation cover.

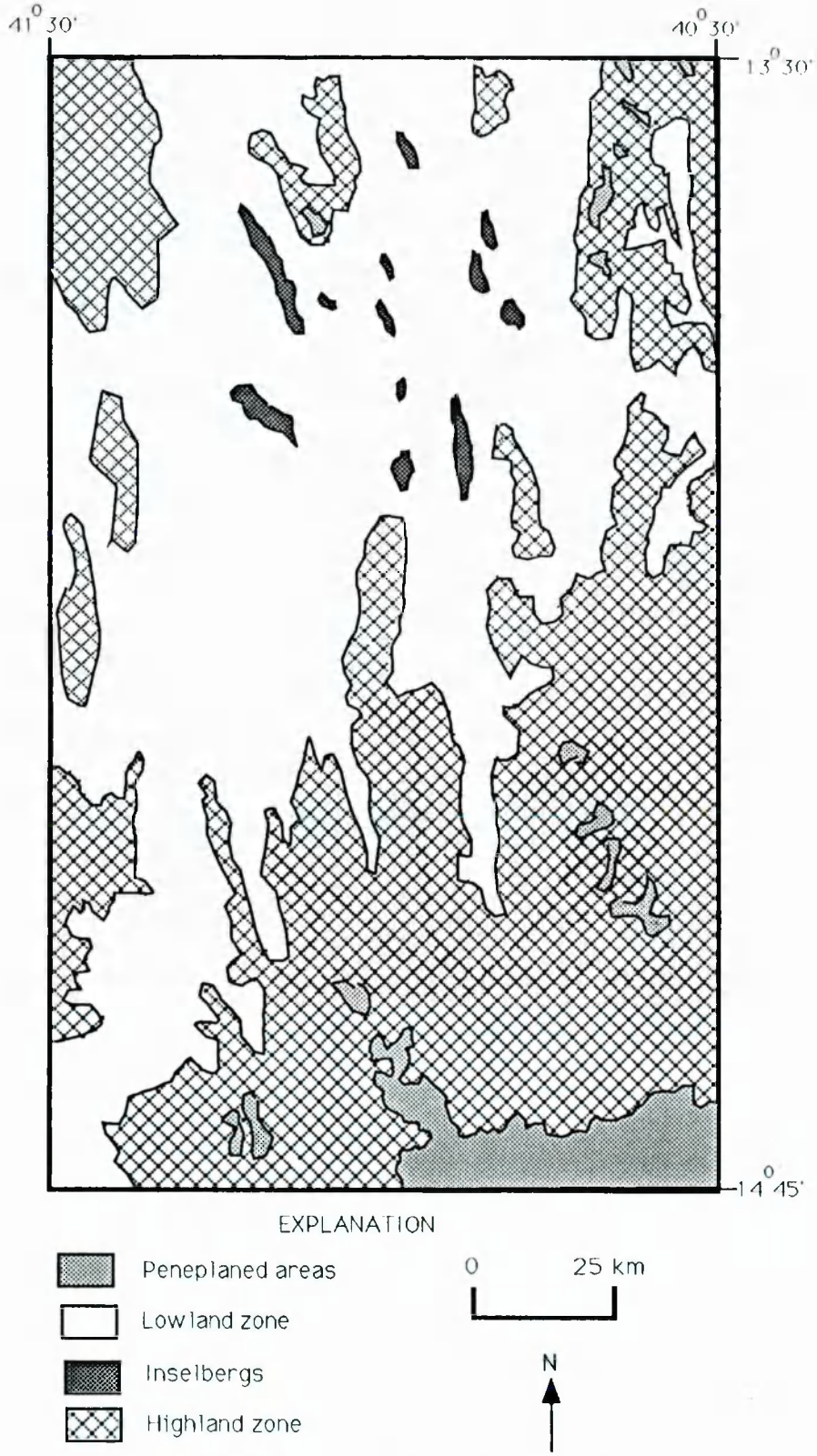


Figure 3.7 : *The geomorphological map of the study area*

As a result three major morphological units: peneplaned areas, highland zone and lowland zone can be recognised in the study area

The peneplaned areas are related to the Sul-Americano cycle and are characterized by small plateaux with a maximum height of 750 m, and covered by sandy, sometimes conglomeratic sediments (Figure 3.7). The highland zone generally correlates with granulite complexes, and is characterised by deep valleys and N-S ridges with an average height of 800 m. The drainage pattern is dendritic and relatively dense The lowland zone occupies large portions of the study areas. It comprises areas below 550 m above sea level, and most is developed on the volcano-sedimentary sequence. The landscape was formed largely during the Paraguassu cycle. Two subdivisions can be recognised: a denuded area ranging from 240 m to 500 m above sea level, and an area characterised by moderate relief and gently rolling hills with conspicuously NNW-SSE orientated inselbergs of quartzites and meta-arkoses (Figure 3.15).

# CHAPTER 4: DATA SETS OF THE STUDY AREA

## 4.1 Introduction

Until the end of 1960s, the ancient terrains in the central southeastern part of the State of Bahia remained geologically unknown. The requirement for geological information linked to the start of exploration for base metal deposits, compelled several Brazilian Government agencies to begin geological mapping, geochemical and geophysical surveys. As a result of such efforts, typical geotectonic features that had already been extensively described in the geological literature from other areas of same age, began to be identified in what had been formerly refered to in general terms as the "crystalline basement".

The study area forms part of this region and is situated in this southeastern portion of the Sao Francisco craton (SFC) in the State of Bahia, within a rectangle bounded by the parallels 13°30' and 14°45' south and by the meridians 40°30' and 41°15' west (Figure 4.1).

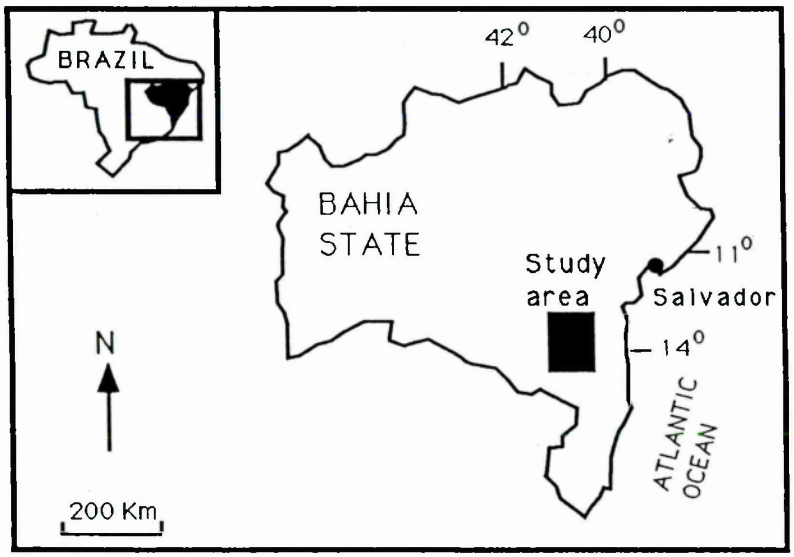


Figure 4.1 : *Location of the study area in the Bahia State of northeastern Brazil*

This chapter will describe:

(a)the level of detail on published geological and topographic available maps;

b)the geochemical and geophysical data derived from diverse surveys;

(c)the remotely-sensed imagery used for lithological discrimination and structural analysis;

## 4.2 Data acquisition

The geological data used in this work are derived both from Brazilian Government agencies, and from field work as part of this study. The starting point was the "Projeto Rochas Basicas-Ultrabasicas" (Basic-Ultrabasic Rocks Project - BURP). This project was carried out by the "Companhia Baiana de Pesquisa Mineral - CBPM" (Bahian Company for Mineral Research) in 1974, which aimed by geophysical techniques to identify new occurrences of chromite-bearing basic-ultrabasic bodies. Since basic-ultrabasic rocks could be related to magnetic anomalies due to their content of magnetite and ilmenite, the chosen method was an aeromagnetic survey. In addition, a complementary airborne gamma-radiometric survey was undertaken as an aid to geological interpretation. The area covered by this survey is within a rectangle bounded by the parallels 14°00' and 15°00' south, and by the meridians 40°00' and 42°00' west, and the study area forms part of this project (Figure 4.2).

In 1976 an extensive geophysical survey was carried out by the CPRM named "Itaberaba-Belmonte Project - IBP", covering an area of 72000 $km^2$. The study area also forms part of this project. The methods used in this survey were aeromagnetic and

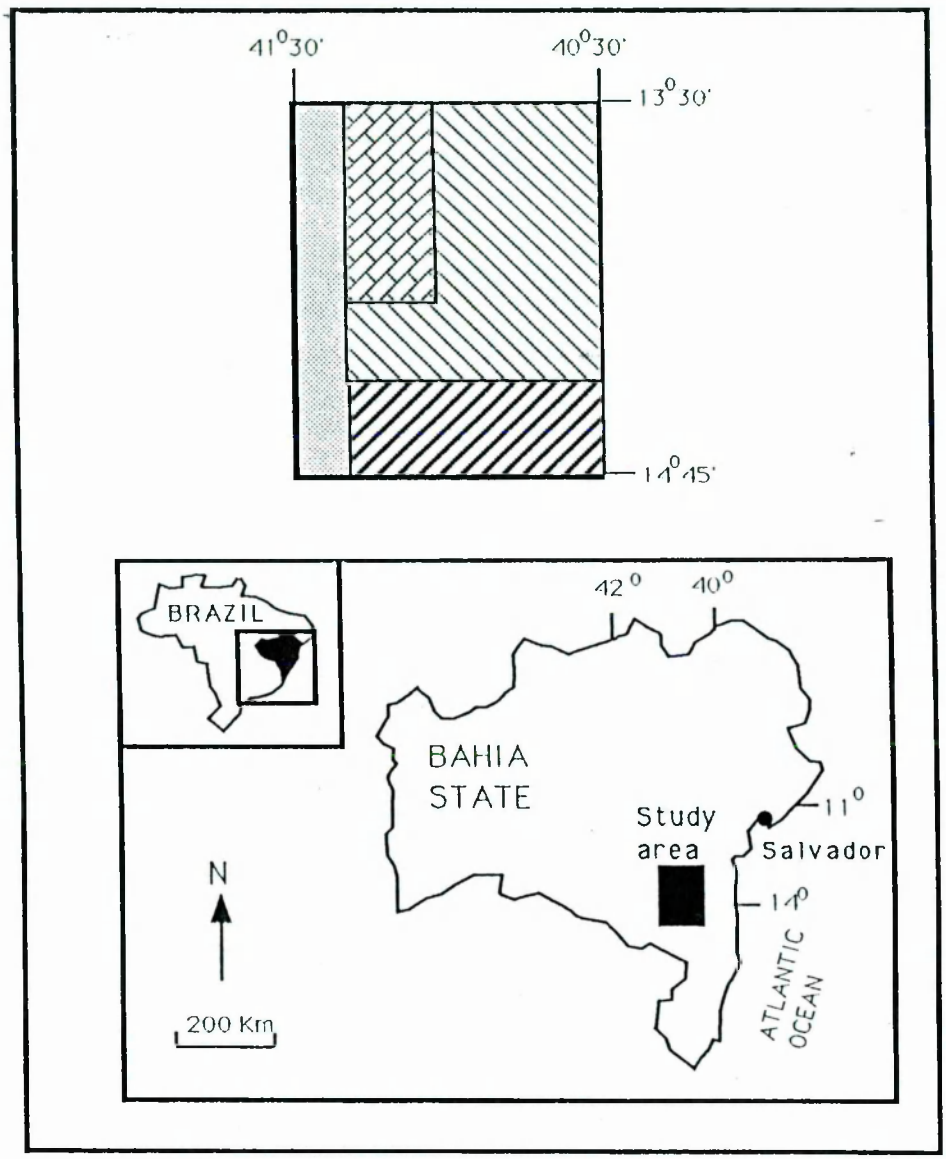


EXPLANATION

BASIC-ULTRABASIC ROCKS PROJECT (BURP)

TRIUNFO-CONTENDAS PROJECT (TCP)

ANAGE-CALDEIRAO PROJECT (ACP)

CONTENDAS-MIRANTE PROJECT (CMP)

Figure 4.2: *The available geological data in the study area*

aeroradiometric, and aimed to discriminate geological features not well marked on radar images or aerial photographs, and to correlate structural patterns with magnetic and radiometric anomalies.

The possible existence of volcano-sedimentary sequences, sharing characteristics of typical greenstone belts located in the southeastern part of Bahia State, led the "Secretaria de Minas e Energia - SME" (Secretariat of Mining and Energy) to initiate a programme of geological mapping and evaluation of mineral resources in part of this region in 1976. The program was termed the Contendas-Mirante Project (CMP) and covered an area of 5250 $km^2$ located within a rectangle bounded by the parallels 13°30' and 14°15' south and by the meridians 40°30' and 41°15' west (Figure 4.2). This project aimed to discriminate the diverse geological units by field mapping and interpretation of airphotos. At the same time an intensive geochemical survey of stream sediments was undertaken.

As a result of the mineral occurrences and expressive geochemical anomalies revealed by the CMP, the SME decided to continue the investigations in the southern part of the volcano-sedimentary sequence. In 1979 a project termed the Anage-Caldeirao Project (ACP) was carried out in this region covering an area of 4500 $km^2$, within a rectangle bounded by the parallels 14°15' and 14°45' south and by the meridians 40°30' and 41°15' west (Figure 4.2). This project involved geological mapping to identify stratigraphic units, and a geochemical survey of stream sediments carried out at the same time, with aim of delimiting target areas for further exploration.

In 1987, based on the results obtained from both the CMP and ACP, the SME decided to intensify the geological investigation of the volcano-sedimentary sequence. An area of 1500 $km^2$ was selected within a rectangle bounded by the parallels 13°30' and 14°00' south and by the meridians 41°00' and 41°15' west (Figure 4.2). The project was called the Triunfo-Contendas Project (TCP) and aimed to identify new targets for mineral exploration. To achieve this goal, an intensive stream-sediment geochemical survey and geological mapping were carried out.

### 4.2.1 The geological information

The geological maps have a cartographic base produced photogrammetrically from airphotos at 1:108000 scale, using Universal Traverse Mercator (UTM) coordinates. Classification of rock types and different concepts from several authors were used: for migmatitic rocks (*Menhert*, 1971), for cataclastic rocks (*Higgins*, 1971), for sedimentary rocks (*Pettijohn*, 1975) and for igneous rocks (*Streickeisen*, 1976).

The geological maps produced by the CMP were derived from photogeological interpretation using airphotos at 1:60000 scale and field geology. 3140 outcrops were described in the field, an average of 1 outcrop per 1.9 $km^2$, 1024 thin sections were studied and 36 mineral occurrences were visited.

The area studied by the ACP generated geological maps derived from interpretation of airphotos at 1:60000 scale and intensive field geology. 4100 outcrops were described in the field, an average of 1 outcrop per 1.5 $km^2$, 899 thin sections were studied and 21 different mineral occurrences were classified.

The geological maps produced by the TCP were derived from photogeological interpretation using airphotos at 1:60000 scale and field geology. In the course of fieldwork 434 outcrops were described, an average of 1 outcrop per 3.9 $km^2$ and 117 thin sections were studied.

I organised all the geological data into four files: geological maps, mine locations, mineral occurrences and outcrop locations. The 42 geological maps were manually digitised using an Altek Datatab 36 x 48 inch Digitizer and Sigma T5670 Monochrome Graphics Terminal. The program used for capture and handling of positional information was written by Steve Daniels (Open University) and is called PICT (Positional Information Capture and Tagging) it is designed to be modifiable to suit different systems, devices and graphics libraries.

The mine sites were organised into an ASCII file and comprise the location of barytes (21 mines), Ti-V-PGE (1 mine), magnesite (2 mines), diatomite (1 mine), talc (2 mines) and asbestos (1 mine). The mineral occurrences were also organised into an ASCII file and corresponds to the location of amethyst (5), asbestos (10), beryllium (4), calcite (4), kyanite (11), chromium (1), copper (8), corundum (1), diatomite (2), emerald (5), gold (12), graphite (2), iron (12), lead (4), magnesite (3), mica (4), nickel (2), quartz (11), talc (8), titanium (1), tourmaline(3), tungsten(1), vermiculite(16) and zinc (3).

The 6500 outcrops were classified into seven categories: granulites, granite-migmatites, granites, mafic-ultramafics, metavolcanic, chemical-exhalative sediments and metasediments and organised into an ASCII file.

### 4.2.2 The geochemical stream sediment survey

The geochemical information was derived from reconnaissance stream-sediment surveys. Diverse geochemical surveys were undertaken in the study area for distinct purposes. Essentially, they aimed to discover base-metals related to greenstone belt terrains. The stream-sediment samples were collected from small channels draining catchment areas typically in the range of 2 to 5 $km^2$.

The data available from the CMP comprise 1686 samples. These samples were analysed by three different methods: Optical Emission Spectrography (Fe, Mg, Ca, Ti, Mn, Ag, As, Au, B, Ba, Be, Bi, Cd, Co, Cr, Cu, La, Mo, Nb, Ni, Pb, Sb, Se, Sn, Sr, V, W, Y, and Zr) corresponding to 50580 determinations; Atomic Absorption Spectrophotometry (Cu, Pb, Ag, Cd and Mo) corresponding to 10116 determinations and Colorimetry (As) corresponding to 1686 determinations.

In the stream sediment survey undertaken by the ACP, 2024 samples were collected and analysed again by Optical Emission Spectrography (Fe, Ti, Mg, Ag, B, Ba, Be, Bi, Co, Cr, Cu, Mo, Nb, Ni, Pb, Sn, Sr, V, Zr) corresponding to 38456 determinations; Atomic Absorption Spectrophotometry (Cu, Ni, Co, and Pb) corresponding to 10120 determinations and Colorimetry (As and W) corresponding to 4048 determinations.

The stream sediment survey carried out by the TCP, 382 samples were collected and were analysed by only: Optical Emission Spectrography (Ba and Mo) corresponding to 764 determinations and Atomic Absorption Spectophotometry (Cu, Ni, Ag, Co, V, Pb, Zn, Fe, Mn, As and Cr) corresponding to 4202 determinations.

### 4.2.3 The geophysical data

In areas of poor outcrop airborne geophysical methods are useful. However, for them to be successful requires a contrast in some measurable physical property throughout the area and especially between the country rocks and the body under investigation. Airborne geophysics is cheaper per unit area surveyed than almost all other methods of exploration except remote sensing. According to *Reeves* (1985) the global production of aeromagnetic surveys amounts to more than 2.5 million line-kilometres of data per year.

The main advantages of airborne geophysical surveys, which include magnetic, electromagnetic and gamma-ray spectometry are:

a) surveys can be undertaken with equal speed regardless of the surface terrain. Swamps, lakes, rivers, dense bush, forest, deserts, glacial drift, and seas can obscure the surface geology from direct inspection, but generally make little difference to airborne surveys. There is an exception to this. The gamma rays detected in airborne spectrometry are absorbed totally by water, and to a greater or lesser degree by vegetation, depending on its density, and moisture content

b) the magnetic method, in particular, is capable of detecting the contrast in the magnetic susceptibilities of rocks at all depths down to the Curie-point isotherm (20 km or more); However, the deeper the source and the higher the altitude flown, the lower the contrast in the resulting signal

c) several different geophysical systems may be mounted in the aircraft and operate simultaneously without any reduction in the rate of coverage.

With respect to this work, only airborne magnetic and gamma-ray spectometer methods concern us. These data are collected as a profile from a succession of parallel flight paths. The collected data differ from remotely sensed data, such as TM and radar, because the former are recorded as point data, and the latter are gathered as continuous images.

Another important difference is that the TM and radar imagery collect information directly from the surface (vegetation, soil, water and rock) whereas the magnetic method contains information from the subsurface and deep-seated magnetic sources, while the radiometric method measures gamma radiation emitted by the top 100 cm of ground surface (*Richards* and *Walraven*, 1975).

The available geophysical data from BURP include an aeromagnetic survey (Figure 4.3), in which two aircraft (Britten Norman Islanders) were used. The photographic system in the aircraft PT-JZN was a continuous strip camera (Eymo 35 mm). A proton magnetometer (Geometrics, model G-803) and a Hewlett-Packard registrator with two channels (model 712 8A) were used. In order to cover the whole area, 217 N-S flight lines and 7 E-W control lines were defined. The N-S flight-line spacing was 1 km, the E-W control-line spacing was 22 km, the aircraft was flown at 220±22 km/h, at an altitude of 150±15 m above the ground.

The available geophysical data from the IBP consist of aeromagnetic and aeroradiometric surveys which cover 30% of the study area. In these surveys two aircraft (Britten Norman Islanders) were used. The equipment used for the aeromagnetic survey was the same as described above.

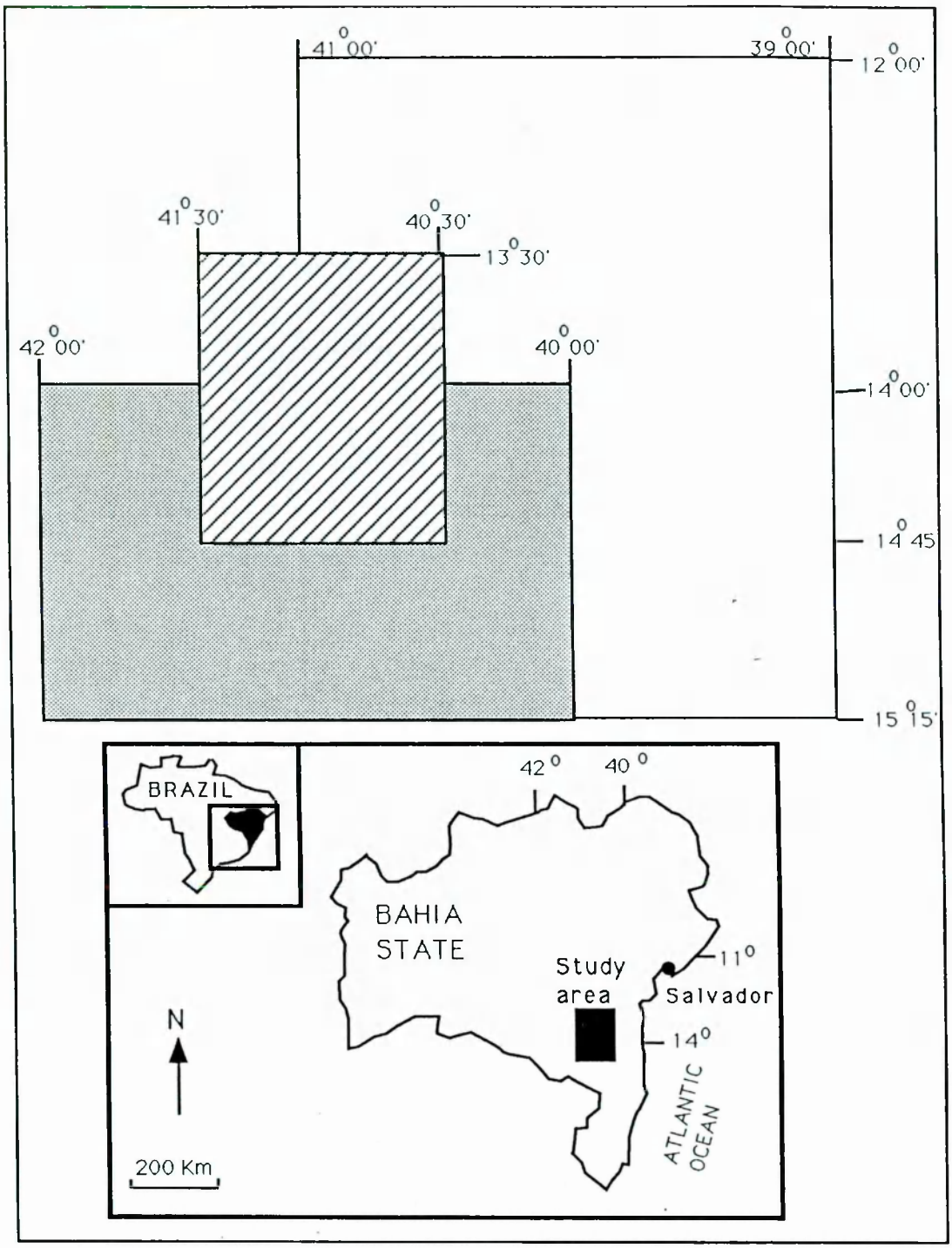


Figure 4.3: *The availabe geophysical data of the study area*

The aeroradiometric equipment consisted of a photographic system (Hulcher 105S), a Gamma-ray spectrometer (Exploranium Mars DIGRS 300L) and an Analogical Registrator (Exploranium Mars 6). The N-S flight-line spacing was 1 km, the E-W control-line spacing was 20 km and the aircraft's altitude was 150 m above surface. All the data were recorded on magnetic tape.

The interpretation of magnetic and radiometric data was until recently based exclusively on contour maps and profiles, and there is no doubt that this procedure has limitations and can result in loss of important information. Contouring deliberately sets out to simplify a continuum to a small number of steps in the field intensity.

Image processing techniques to produce pictures of geophysical data have many advantages stemming from the potential to display a greater dynamic range and exploiting the ability of the eye to recognise subtle patterns. Furthermore, data in image form are easier to integrate with similar products from remote sensing systems and also allow the assembly and presentation of a very large data set with minimal loss of detail (*Tucker et al*, 1985).

Ideally, production of raster format files of geophysical data should begin with "raw data" from flight lines and/or ground stations such as the data from IBP which consists of ASCII files recorded on magnetic tapes. Since the data from BURP were not available as magnetic tapes, twelve maps having 10 gamma contour intervals and at 1:50000 scale were digitised. A total of 27 radiometric maps at 1:50000 scale presented as

profiles were converted into scattered data points, then gridded.

Both magnetic and radiometric maps were digitised along flight lines using an Altek Datatab 36 x 48 inch Digitizer and Sigma T5670 Monochrome Graphics Terminal. The next step was to convert these vector format files into raster files.

### 4.2.4 The remotely sensed data

Remote sensing in general is the acquisition of data and derivative information about objects or materials located at or beneath the Earth's surface or in its atmosphere from a distant platform. It uses sensors to measure interactions between Earth materials and the electromagnetic (EM) radiation, certain force fields (e.g. magnetic) and even mechanical waves (e.g. sonic). Many authors restrict the term remote sensing to EM wavelength-intensity information about the immediate surface which needs to be decoded before the message can be fully understood.

For many decades, remote sensing has been used for geological applications and began with black and white aerial photography. Modern remote sensing was initiated in 1972 with the launch of ERTS-1 (Earth Resources Technology Satellite, subsequently renamed Landsat 1). The Landsat series afford a view of a large area of the Earth's surface (34000 $km^2$) but the fields of view are small enough (11° for Landsat 1-3, 15° for Landsat 4-5) that the entire image appears uniformly illuminated (*Goetz* and *Rock*, 1973).

The family of Landsat satellites has proved to be an invaluable component to locating, monitoring, and managing many natural and man-made resources. Landsats 1-3 covered only

the visible and very-near infrared (VNIR) in four broad bands (Table 4.1). The platform employed for these first generation Landsats was a modified Nimbus type. It consisted of two main parts: the lower sensor ring which carried the instruments and the upper solar array panels which collected solar energy to power those instruments. The remote sensing payload of Landsat 1 consisted of a Return Beam Vidicon (RBV) camera and a Multispectral Scanner (MSS). The near polar orbit (99°) and the altitude (913 km) of these first generation gave an orbit pattern which each area on the Earth's surface was flown over once every eighteen days. The ground instantaneous field of view (IFOV) or pixel size was 79m x 79m (*Harris*, 1987)

| Satellite | Launch date | End of Operation | Band | Wavelength range |
|---|---|---|---|---|
| Landsat 1 | 23.07.1972 | 06.01.78 | 4 | 0.5 - 0.6 |
| Landsat 2 | 22.01.1975 | 27.07.83* | 5 | 0.6 - 0.7 |
| Landsat 3 | 05.03.1978 | 07.09.83** | 6 | 0.7 - 0.8 |
| | | | 7 | 0.8 - 1.1 |

* Interruption in 1979-80; ** Standby mode from 31.03.1983

**Table 4.1** : *Operation periods and wavebands of the Landsat 1-3 satellites (from Harris, 1987)*

The second generation of the Landsat programme began with the launch of Landsat 4 and continued with the launch of Landsat 5. For this second generation of Landsat a lower orbit of 700 km was chosen and a shorter revisit cycle was achieved (once every sixteen days). Landsats 4-5 carry an MSS of the same design as the early Landsats, except the ground pixel size is 82m x 82m, and the band numbering is changed from 4, 5, 6, 7 to 1, 2, 3,4 (Table 4.2). The RBV camera has been

omitted and a new sensor introduced, the Thematic Mapper (TM), with a ground IFOV of 30m (bands 1-5,7) and 120m (band 6).

| Satellite | Launch date | Band | Wavelength range (μm) |
|---|---|---|---|
| Landsat 4 | 16.07.82 | 1 | 0.45 - 0.52 |
| Landsat 5 | 01.03.84 | 2 | 0.52 - 0.60 |
| | | 3 | 0.63 - 0.69 |
| | | 4 | 0.76 - 0.90 |
| | | 5 | 1.55 -1.75 |
| | | 6 | 10.4 - 11.7 |
| | | 7 | 2.08 - 2.35 |

**Table 4.2** : *Launch date and wavebands of Landsat 4 and 5 satellites (from Harris, 1987)*

The products from Landsats 1-3 are more suitable mainly for vegetation monitoring, but include some information on iron minerals in rocks and soils. Iron features include: a) charge-transfer absorptions being responsible for the steep fall off in intensity towards the blue in the visible spectra, and b) the $Fe^{3+}$ crystal field effect around 0.9 μm.

The launch of Landsat 4-5 including sensors in the short-wave infrared (SWIR) directed at $OH^-$ vibrational features, is useful for detecting hydroxylated minerals such as micas, clays, chlorites and serpentines. This advance greatly assisted geological applications of remote sensing.

Radar remote sensing employs EM energy in the microwave part of the spectrum. Because radar wavelength are so long, they are not affected by the relatively small cloud particles. In addition to its wavelength characteristics, radar energy can also be polarised. Polarisation indicates the plane in which the EM energy travels.

Side looking airborne radar (SLAR) uses real aperture radar for imaging applications. A SLAR radar antenna is carried out on board an aircraft and sends out to one side of the aircraft a pulse or beam of EM energy in the wavelength chosen for the radar at right angles to the direction of flight of the aircraft. The amount of energy returned or backscattered to the antenna from the surface depends upon two main factors:
a)the angle of the surface to the incident radar beam. Backscatter will be high from those surfaces at high angles to the beam, low from those surfaces which slope away from the radar beam, and non-existant in those areas hidden from the active illumination of the radar pulse.
b)The physical properties of the surface, primarily its surface roughness and its dielectric constant. Smooth surfaces backscatter little or no radar energy and act as mirror-like surfaces, while rough surfaces backscatter more energy depending upon their surface roughness. The surface dielectric constant is largely determined by water content. Wet soil will have a high dielectric constant and a high backscatter; dry sand will have a low dielectric constant and a lower backscatter (*Harris*, 1987)

Radar images were acquired by a synthetic aperture radar system (Goodyear Aerospace Corporation), operating in the X-band (wavelength ranging from 24mm to 38mm) and provided spatial resolution quoted as better than 20 m. This system, installed in a high-performance twin-jet Caravelle belonging to the Aeroservice Division of Western Geophysical Company, was flown at 700 km/h at an altitude of 11,000 m. In addition aerial photographs were acquired over selected areas (cloud cover conditions permitting) using both a Zeiss mapping camera

with super-wide-angle lens and colour infrared film, and a multispectral camera. These vertical aerial photos at 1:130,000 and 1:73,000 scales respectively, provided auxiliary data to interpret the radar images. They were also very useful in checking the location and linearity of flight lines.

The inertial navigation system of the aircraft was used in combination with position information provided by a network of radio-positional stations throughout the region. During the later phases of the survey, it was observed that the location accuracy for radar images was still very high when north-south flight lines were combined with east-west flight lines. These east-west tie lines were located over distinctive ground features whose geographic coordinates were defined by the TRANSIT system.

A summary of the characteristics of the radar system is given in Table 4.3.

| | |
|---|---|
| Radar system | GEMS 1000, Goodyear Mapping System |
| Band | X (wavelength range=24mm-38mm) |
| Antenna | Synthetic aperture with capability to acquire data from either side of aircraft. Antenna stabilised yaw, roll and pitch of the aircraft |
| Polarisation | HH |
| Depression angle | Near range: 45°. Far range: 13° |
| Ground resolution | 16 m range azimuth directions |
| Image swath | 37 km |
| Data acquisition scale | 1:400,000 |

**Table 4.3** : *Characteristics of the radar system used in the RADAM project*

Both Landsat Thematic Mapper (TM) and radar data were used in this work. The TM images acquired by Landsat 5 were provided by CBPM. The images were recorded by the Brazilian receiving station at Cuiaba (State of Mato Grosso) and processed by the "Instituto de Pesquisas Espaciais - INPE" (Brazilian Space Research Institute). The acquisition details of these images are as follows: path 217, row 70, quads 1,2 and 4, date 4.5.88, bands 1 to 7. In this work, quad 2 was used, which represents the upper right part of the scene.

Acquisition of geological information in the study area has benefited from the use of side-looking airborne radar (SLAR) images. These radar images at 1:250000 scale are on photographic paper and cover the whole study area. This coverage was a result of a Brazilian government initiative started in 1971 known as the RADAM project. The photographic papers were automatically digitized at Joyce-Loebl at 25µm spot size.

Digital analysis and display techniques are based on the development of microprocessors, pixel processors, data storage and hardcopy devices.

The development of more powerful 32 bit microprocessors, makes interactive image processing cost-effective for many applications on desk top workstations. Effective systems provide a multitasking environment and networking into mainframe databases. Specialized pixel processors optimise arithmetic geometry and logical operations on images. Recent developments in memory chip technology show that it is economically attractive to make displays with 1280 pixels by

1024 lines and 24 bits of dynamic range for each pixel (8 bits each for red, green and blue).

Storage of data is always a problem. Nowadays with the advent of optical disks and high-density tapes with gigabyte capacity, the inconvenience of data storage has almost disappeared. For instance, in order to create a data set of images covering the entire surface of Brazil, which is 8.6 millions $km^2$ approximately, at a spatial resolution of 100 m, we would produce a total of 85 gigabytes of monochrome 8-bit data or 85000 scenes of 1 million pixels. This huge amount of data could be stored on 42 optical disks of 2 gigabytes each, and placed in a few shelves.

Hardcopy output devices such as ink-jet and electrostatic plotters produce print outs directly from the raster data sets. Such low cost, high quality hardcopy forms, at present, the most appropriate environment for most interpretation. However some on-line interpretative possibilities are provided by Boolean logic and limited extraction of line features from images.

Image analysis of the study area, was largely achieved using the DIPIX ARIES-II digital image processing and, to a lesser extent, via the GRASS3.1 software. ARIES-II is a system specifically designed to input, store, manipulate, display and output digital images in an efficient manner. It consists of the central processing unit (CPU), video graphics terminal, which provides the interactive communication between the permanent record of messages to the user from the computer subsystem, a read only memory (ROM), which provides a residence for the applications software during images

analysis, and input/output ports for accessing peripheral devices. The image storage node (ISN) contains three logical disks, a system disk which stores all files-11 and non-image files, a library disk with all ARIES software, and an image disk disk for storing all ARIES image files. The image display subsystem (IDS) comprises the dual port interface, video display control computer, image memory, video processor, high-resolution monitor and graphics pad.

The GRASS3.1 (Geographic Resources Analysis Support System) software used in this work has been designed and developed by researchers at the United States Army Construction Engineering Research Laboratory (USACERL).

The available data set are in different formats and need to be put into a comprehensive and common format. Different methodologies were adopted for format conversion and will be discussed in Chapters 5, 6, 7 and 8. The original files contain hidden, new information that has to be extracted in some way by preprocessing to make it readable, and then further data reduction through interpretation is necessary. In some cases, such as remote sensing and geophysics this involves visual interpretation of various themes which are transported to the GIS. In other cases, such as geochemistry, a semi-automated process is possible, based on knowledge of element associations. Finally, some of the data, such as mapped geology and site information can go unchanged direct to the GIS.

# CHAPTER 5 : GEOGRAPHICAL INFORMATION SYSTEMS AND MINERAL EXPLORATION

## 5.1 Introduction

The need to integrate information, to consider a vast range of combinations, to underline different hypotheses and to replace tedious manual techniques, led to the formulation of Geographical Information Systems (GIS).

Analysis for resources management is commonly done by means of map overlay. This procedure has been used for over a half century, and forms the basis of GIS technology, but with maps in digital form.

In 1972, the International Geographical Data Processing and Remote Sensing Group produced an important report that outlined the field and provided the basis for the subsequent efforts to institute GIS technology. *Tomlinson* (1972) emphasised that GIS "is not a field by itself but rather the common ground between information processing and the many fields utilising spatial analysis techniques".

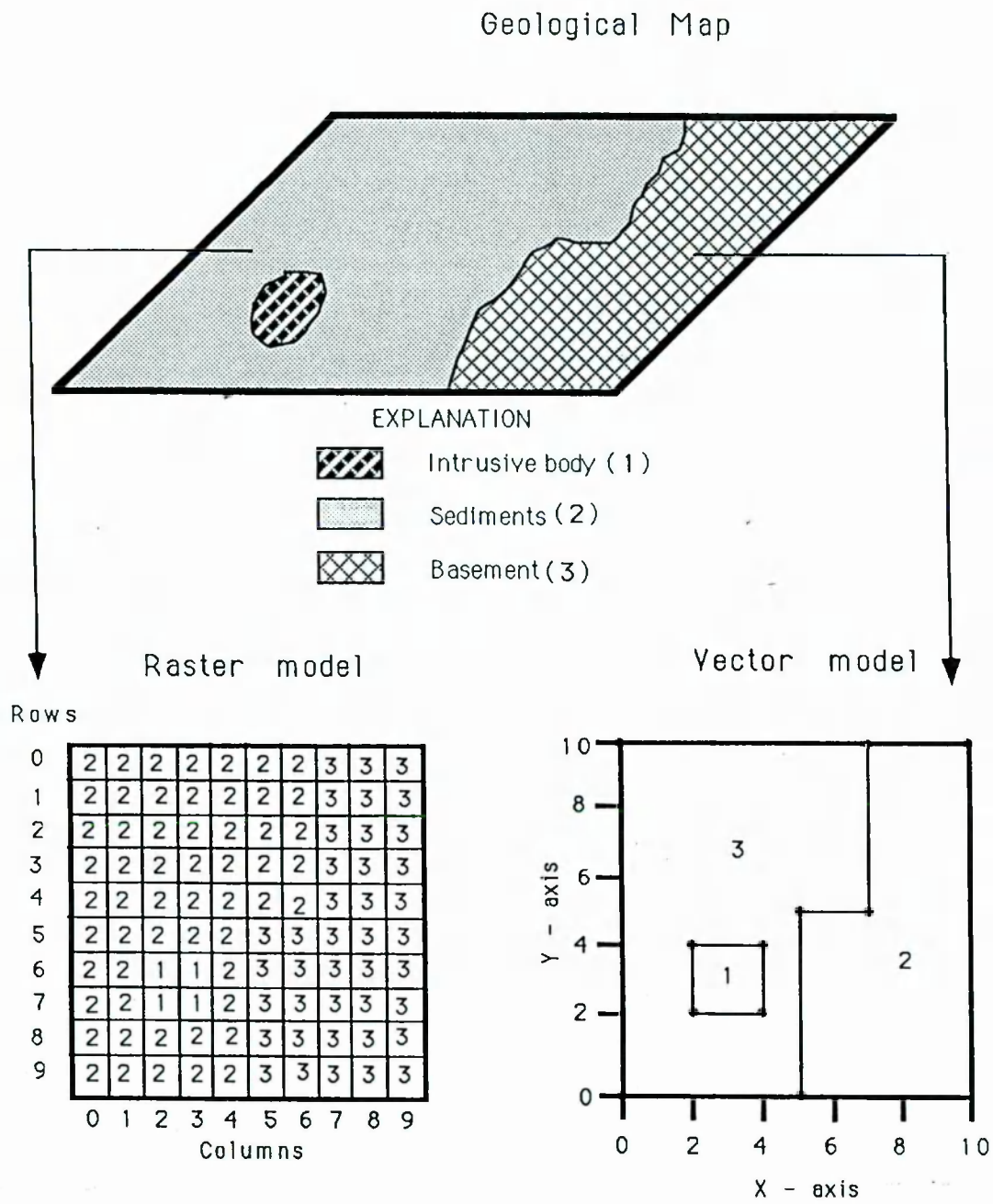


Figure 5.1 : *Data representation by Raster and Vector models*

A GIS is a technology designed to accept a large volume of geographically referenced data, in spatial, non-spatial and temporal form derived from a variety of sources, which are stored, retrieved, manipulated, analysed, reported and displayed according to user-defined specifications (*Clark*, 1986; *Aronoff*, 1989).

GIS has been developed independently for many purposes, including forestry, property and land parcel, transport, agriculture and environment, civil engineering and mineral exploration. The future of GIS will depend on better algorithms and data structures, and continuing improvements in hardware. Also GIS needs research in spatial analysis, pattern recognition, in the development of better methods for manipulating and analysing spatial data, and towards a better understanding of the nature of spatial data themselves through such issues as generalization, accuracy and error.

This chapter reviews the state-of-art of GIS and the methodology adopted in handling the large amount of data described in previous chapters. It also discusses the design and implementation of a mineral-oriented GIS.

## 5.2 Spatial entities

Spatial entities are those that can be individually or collectively referenced to a geographic location. They comprise points, lines and areas. Points represent the place of geographical phenomena at a site. Lines consist of an ordered set of joined points. Areas represent a domain enclosed by lines.

Several coordinate systems (CS) have been developed for precise positioning of measurements. Conversion from one CS to another can be done in most cases via simple mathematical operations.

The basic CS for location on the Earth's surface is latitude and longitude. The coordinates of this system represent location on the surface of a sphere-like solid which closely approximates the shape of the Earth. Through map projection these three dimensional coordinates are transformed into two dimensional coordinates which are suitable for plotting on a flat computer display or map sheet.

Digital representation of spatial entities has developed impressively in recent years. Single pairs of coordinates that represent points produce few problems, but lines and areas are more complicated. Areas correspond to an intersecting sequence of straight lines of different sizes, and lines can be recognized as an ordered sequence of points. These data can be used by the GIS environment in two different formats or models: the vector and raster.

The vector model (VM) represents real objects, facts or conditions by points. Their position is defined in the same way as if they were being drawn on a map (Figure 5.1). The vector assumes that the position of the points is referred to x and y coordinates, termed Cartesian Coordinate System (CCS), which are precisely defined, and the level of accuracy for computer displaying is determined by the number of bits used for representing a single value within the computer. There are

several ways to produce vector data, the most popular are "spaghetti", topological and triangular network models.

The "spaghetti" data model (SDM), shown in Figure 5.2, involves creating files that represent areas by polygons. They are recorded through a closed loop of X and Y coordinates that define its boundary. The common boundary between adjacent polygons must be recorded twice, once for each polygon. The SDM is an efficient model for digitally reproducing maps because information extraneous to the plotting process such as spatial relationships, are not stored (*Peuquet*, 1984). The geological maps of the study area were manually digitised using this model then converted to raster.

The topological data model (TDM) (Figure 5.3) consists of point series, termed arcs which have a starting and ending point. The end of the arc is called a node and can be an intersection point where two or more arcs meet. Thus a polygon can be represented as concatenated arcs which represent its boundaries. The main advantage of this model is that spatial data queries can be processed much more quickly than that by calculation from the coordinate data required for SDM (*Aronoff*, 1989). The structural features, geophysical maps, geochemically anomalous sites, mineral occurrences and outcrop locations of the study area were digitised using this model.

The triangular irregular network model (TINM) is used to represent any surface (*Aronoff*, 1989). A terrain surface for instance, can be represented by a set of interconnected triangles. The vertex of each triangle is defined by X and Y and Z (elevation) coordinates (Figure 5.4). Each triangle is

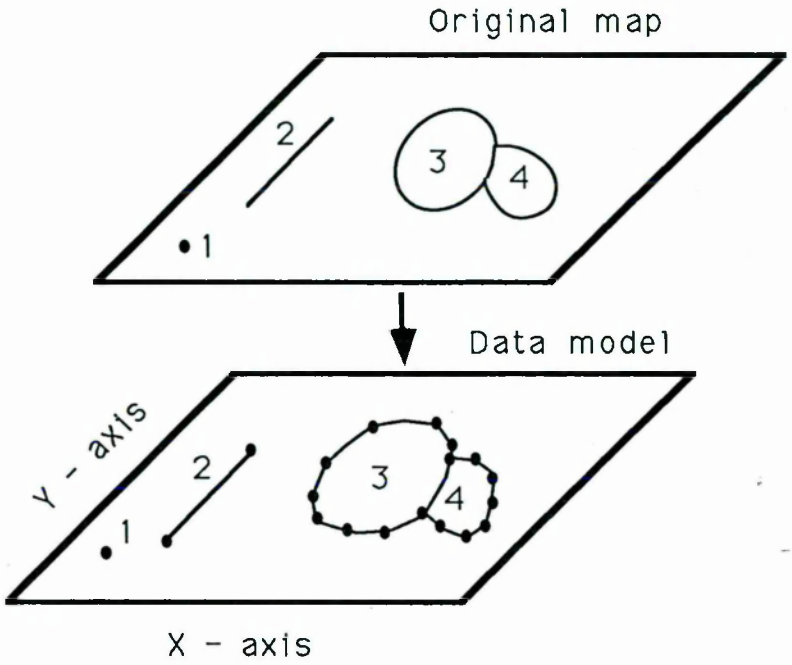


Data structure

| Feature | Number | Representation |
|---|---|---|
| Point | 1 | X,Y (single point) |
| Line | 2 | $X_1Y_1$, $X_2Y_2$ (string) |
| Polygon | 3 | $X_1Y_1$, $X_2Y_2$, .... $X_nY_n$(closed loop) |
| | 4 | $X'_1Y'_1$ , $X'_2Y'_2$, .... $X'_nY'_n$(closed loop) |

Figure 5.2 : *The "spaghetti" data model (adapted from Aronoff, 1989)*

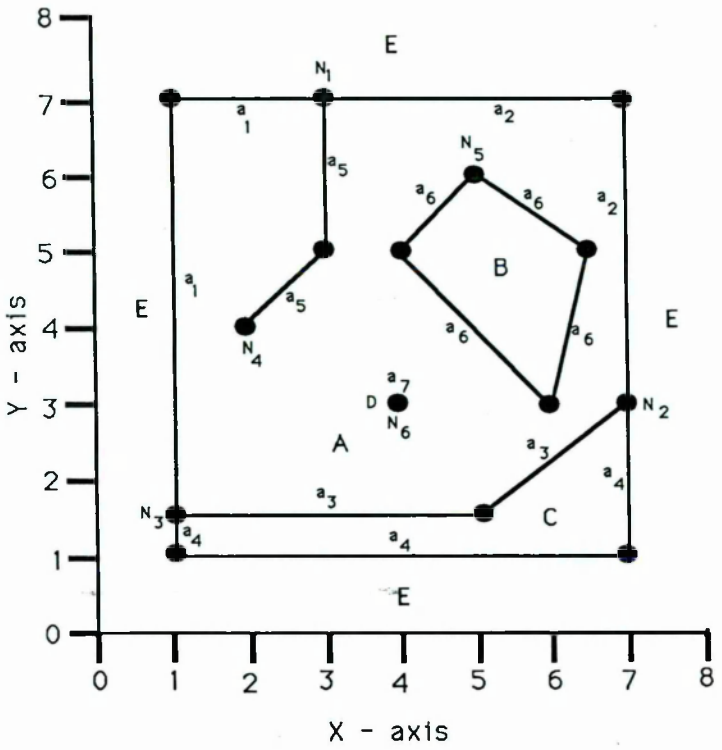


SPATIAL DATA ENCODING

| AREA | TOPOLOGY |
|---|---|
| POLYGON | ARCS |
| A | $a_1$, $a_2$, $a_3$ |
| B | $a_6$ |
| C | $a_3$, $a_4$ |
| D | $a_7$ |
| E | area outside |

| NODE TOPOLOGY | |
|---|---|
| NODE | ARCS |
| $N_1$ | $a_1$, $a_2$, $a_5$ |
| $N_2$ | $a_2$, $a_3$, $a_4$ |
| $N_3$ | $a_1$, $a_4$, $a_3$ |
| $N_4$ | $a_5$ |
| $N_5$ | $a_6$ |
| $N_6$ | $a_7$ |

| ARC TOPOLOGY | | | | | ARC COORDINATE DATA | | | |
|---|---|---|---|---|---|---|---|---|
| ARC | START NODE | END NODE | LEFT POLYGON | RIGHT POLYGON | ARC | START X,Y | INTERMEDIATE | END X,Y |
| $a_1$ | $N_3$ | $N_1$ | E | A | $a_1$ | 1.5,1.5 | 1, 7 | 3, 7 |
| $a_2$ | $N_1$ | $N_2$ | E | A | $a_2$ | 3, 7 | 7, 7 | 7,3 |
| $a_3$ | $N_3$ | $N_2$ | A | C | $a_3$ | 7, 3 | 5, 1.5 | 1, 1.5 |
| $a_4$ | $N_2$ | $N_3$ | E | C | $a_4$ | 7, 3 | 7, 1 | 1, 1.5 |
| $a_5$ | $N_4$ | $N_1$ | A | A | $a_5$ | 2, 4 | 3, 5 | 2, 4 |
| $a_6$ | $N_5$ | $N_5$ | A | B | $a_6$ | 5, 6 | 6.5,5;6,3;4,5 | 5, 6 |
| $a_7$ | $N_6$ | $N_6$ | C | C | $a_7$ | 4, 3 | | 4, 3 |

Figure 5.3: *The topological data model*

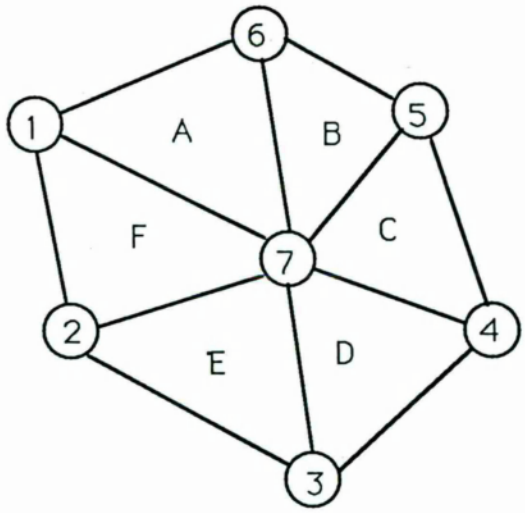


| X-Y COORDINATES | |
|---|---|
| NODE | COORDINATES |
| 1 | $X_1, Y_1$ |
| 2 | $X_2, Y_2$ |
| 3 | $X_3, Y_3$ |
| 4 | $X_4, Y_4$ |
| 5 | $X_5, Y_5$ |
| 6 | $X_6, Y_6$ |
| 7 | $X_7, Y_7$ |

| Z COORDINATES | |
|---|---|
| NODE | Z VALUE |
| 1 | $Z_1$ |
| 2 | $Z_2$ |
| 3 | $Z_3$ |
| 4 | $Z_4$ |
| 5 | $Z_5$ |
| 6 | $Z_6$ |
| 7 | $Z_7$ |

| NODES | |
|---|---|
| △ | NODE |
| A | 1,6,7 |
| B | 6,5,7 |
| C | 5,7,4 |
| D | 4,7,3 |
| E | 3,7,2 |
| F | 2,7,1 |

| EDGES | |
|---|---|
| △ | ADJACENT △ |
| A | B, F |
| B | C, A |
| C | B, D |
| D | C, E |
| E | F, D |
| F | A, E |

Figure 5.4: *The triangular irregular network model (from Aronoff, 1989)*

named by a letter and is defined by three nodes named by numerals. The advantage of the TINM is that extra information can be encoded for areas of complex relief without requiring a large amount of data to be collected, areas of simple relief can be represented by a small amount of data and complex areas of relief can still be represented precisely.(*Aronoff*, 1989).

All these vector formats have some disadvantages. The SDM is very inefficient for most spatial analysis since the spatial relationships must be derived by computation. The TDM presents the unique disadvantage that, when an existing map is changed, it is usually very time-consuming to update topology. The disadvantage of the TINM is that it needs significantly more processing to generate files (*Aronoff*, 1989).

The raster model (RM) is illustrated in Figure 5.1. It consists of a regular grid of square or rectangular cells, named pixels akin to those in a digital image. Each pixel is defined by its column and row numbers, and a value assigned to its quality. The RM in most cases demands an enormous amount of pixels, and many of the pixels in a simple map will have the same qualities. To reduce this redundancy, various methods of representing data in a more compact form can be applied. The most common are run-length, value-point encoding, chain codes and quadtree data models.

The run-length encoding model (RLEM) represents adjacent pixels along a row that have the same value as a group-named run (Figure 5.5). The storage of the data is done for each run together with information about the size and location of the

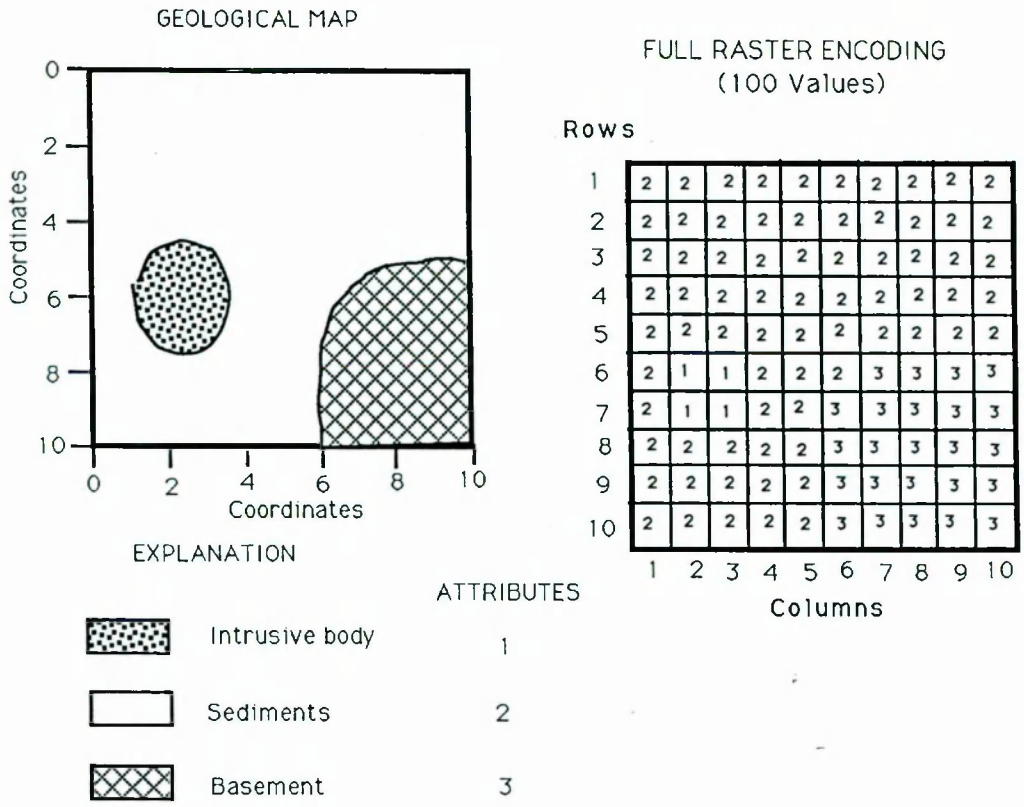


| CHAIN CODES | | | |
|---|---|---|---|
| ROW | COL | ATT | LENGTH |
| 5 | 1 | 2 | $0,^{10}\ 3^{5}\ 2^{10}\ 1^{5}$ |
| 6 | 2 | 2 | $0,3^{2},0^{2},1^{2}\ 0^{3},3\ 2\ 3^{4}\ 2^{5}\ 1^{5}$ |
| 6 | 2 | 1 | $0^{2},\ 3^{2}\ 2^{2}\ 1^{2},$ |
| 6 | 7 | 3 | $0^{4},\ 3^{5},\ 2^{5}\ 1^{4}\ 0,1$ |

| RLE (57 VALUES) | | |
|---|---|---|
| ATTRIBUTES | LENGTH | ROW |
| 2 | 10 | 1 |
| 2 | 10 | 2 |
| 2 | 10 | 3 |
| 2 | 10 | 4 |
| 2 | 10 | 5 |
| 2 | 1 | 6 |
| 1 | 2 | 6 |
| 2 | 3 | 6 |
| 3 | 4 | 6 |
| 2 | 1 | 7 |
| 1 | 2 | 7 |
| 2 | 2 | 7 |
| 3 | 5 | 7 |
| 2 | 5 | 8 |
| 3 | 5 | 8 |
| 2 | 5 | 9 |
| 3 | 5 | 9 |
| 2 | 5 | 10 |
| 3 | 5 | 10 |
| TOTAL=19 | 19 | 19 |

| VPE (28 VALUES) | |
|---|---|
| ATTRIBUTES | POINT |
| 2 | 51 |
| 1 | 53 |
| 2 | 56 |
| 3 | 60 |
| 2 | 61 |
| 1 | 63 |
| 2 | 65 |
| 3 | 70 |
| 2 | 75 |
| 3 | 80 |
| 2 | 85 |
| 3 | 90 |
| 2 | 95 |
| 3 | 100 |
| TOTAL=14 | 14 |

Figure 5.5: *Compression of raster data: Run length (RLE), value point (VPE) encoding and Chain codes (CC)*

run. The raster data of the study area were compressed using this model.

The value-point encoding model (VPEM) assigns the pixel position number starting in the upper left corner, proceeding from the left to right and from the top to the bottom (Figure 5.5).

The chain codes (CC) provide a very compact way of storing a region's representation. The boundary of the region can be given in terms of its origin and a sequence of unit vectors in the cardinal directions. These directions can be numbered such as east=0, north=1, west=2, south=3. Figure 5.5 presents a schematic example of CC. (*Burrough*, 1986).

The quadtree data model (QDM) divides an area into cells of one size, finer subdivisions are then used in those area with finer detail (Figure 5.6). The QDM structure starts from one root from which all other branches expand. These branches, called leaves, are linked to points from which there is no further branching, named nodes (*Aronoff*, 1989). There is a growing interest in the use of quadtrees in GIS (*Mark* and *Lauzon*, 1984; *Samet* *et al*, 1984), and it is clearly an elegant technique that has much to offer.

Although compression reduces storage space, it has some disadvantages. For complex maps RLEM and VPEM become less efficient as the number of edges or transitions increase and greatly enlarge both the size of the files and the processing time. The disadvantages of CC are: (a)the redundancy introduced because all boundaries between regions must be stored twice, and (b)overlay operations are

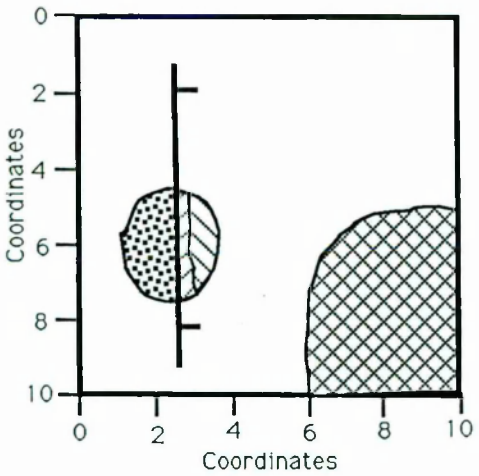


SCHEMATIC REPRESENTATION OF THE QDM

GEOLOGICAL MAP

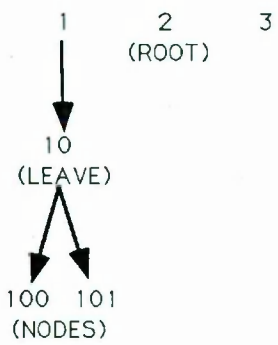


EXPLANATION

- Intrusive body
- Cataclastic Intrusive body
- White altered cataclastic intrusive body
- Yellow altered cataclastic intrusive body
- Sediments
- Basement

QUADTREE REPRESENTATION

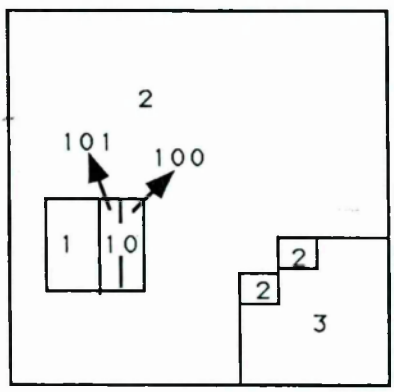


TABLE OF ATTRIBUTES

| QUADTREE LEVELS | | | | | ATTRIBUTES |
|---|---|---|---|---|---|
| 1 | | 2 | 3 | | |
| ROOT | 1 | | | | Intrusive body |
| | 2 | | | | Sediments |
| | 3 | | | | Basement |
| | | LEAVE 10 | | | Cataclastic intrusive body |
| | | | NODES | 100 | White altered cataclastic intrusive body |
| | | | | 101 | Yellow altered cataclastic intrusive body |

Figure 5.6 : *The organisation of data using the qadtree model*

difficult to perform without returning to a full grid representation (*Freeman*, 1974). The inconvenience with the QDM is the time it takes to create and update files. (*Aronoff*, 1989). The choice between raster (RM) and vector models (VM), rests on the nature of the data in a particular area. Advantages and drawbacks of both models are summarised in Tables 5.1 and 5.2.

| Raster model | Vector model |
|---|---|
| 1. It is a simple data structure | 1. It provides a compact data structure |
| 2. Overlay operations are easily and efficiently implemented | 2. It provides efficient encoding of topology and, as a result efficient implementation of operations that require topological information, such as network analysis |
| 3. High spatial variability is efficiently represented | 3. It is better suited to supporting graphics that approximates hand-drawn maps |
| 4. It is more or less suited to efficient manipulation and enhancement of digital images | |

**Table 5.1**: *Comparison of advantages of the raster and vector model (from Aronoff, 1989)*

| Raster model | Vector model |
|---|---|
| 1.The data structure is big | 1. It is a complex data structure |
| 2.Topological relationships are difficult to represent | 2.Overlay operations are more difficult to implement |
| 3.The output of graphics is less aesthetically pleasing | 3.The representation of high spatial data variability is inefficient |
| | 4.Manipulation and ,enhancement of digital images cannot be effectively done in the vector domain |

**Table 5.2**: *Comparison of the disadvantages of the raster and vector models (from Aronoff, 1989)*

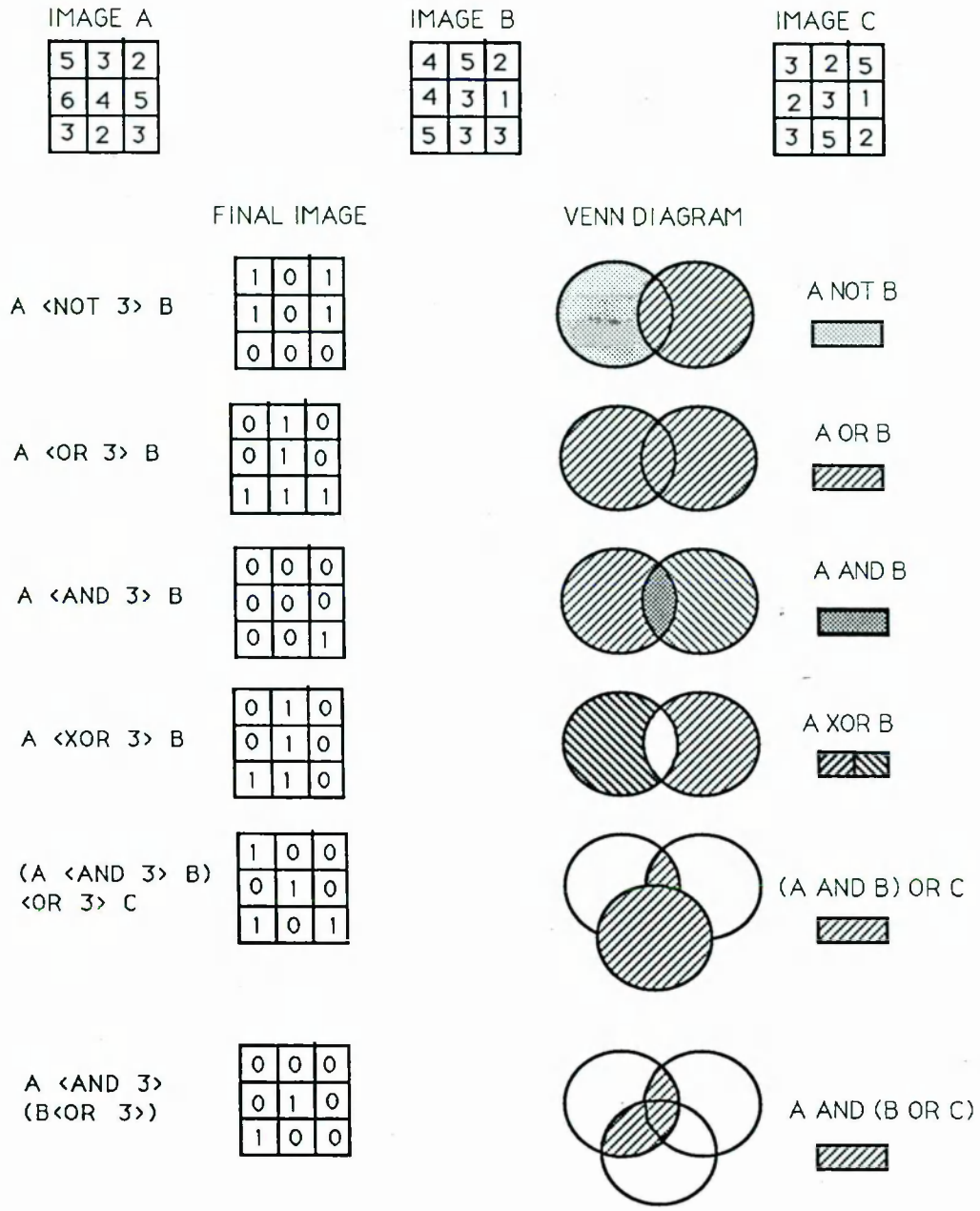


Figure 5.7 : *Schematic diagrams showing the results of applying Boolean Operations*

The raster data (RD) and vector data (VD) for the study area were created according to their relationships and the specific goals of the study. (Table 5.3)

| Raster data | Vector data |
|---|---|
| Geochemical data: As,Ba,Cr,Cu, Co,Fe,Mg,Mo, Ni,Nb,Pb,Sr,Ti,V, Zn and Zr | Geochemical data: As,Ba,Cr,Cu, Co,Fe,Mg,Mo,Ni, Nb,Pb,Sr,Ti,V, Zn and Zr |
| Soil | |
| Vegetation | |
| Geological map | |
| Mineral occurrences | Mineral occurrences |
| Structural features | Structural features |
| Thematic Mapper: Bands 1, 2, 3, 4, 5 and 7 | |
| Radar | |
| Radiometric data: U, Th, K and Total counts | |
| Magnetic data | |

**Table 5.3:** *The spatial entities of the study area*

## 5.3 The non-spatial entities

The non-spatial entities correspond to the information that does not represent location. They can be separated into attributes, spatial relationships and time.

The attributes correspond to a particular characteristic of the geographical data, such as statistical data and descriptive features. Statistical data might comprise a table

with information such as demand and supply, resource quality, cost figures and areas of mutual occurrence. The descriptive features might for example include the amount in parts per million (ppm) of a given chemical element in a stream sediment sample, radiance for remotely-sensed data or the description of the lithological units, types of lineaments and ages of the rock units in a geological survey.

The spatial relationships express the liaison among the geographical features. For example it is not only important to know the location of the lithologies and geochemical anomalies; the potential development of mines depends on what they are near, as well where they are located. Obviously, it is impossible to store information about all the possible relationships. Instead only some of the affinities are explicitly defined in the GIS, and some remainder is either calculated as needed or is not available.

The time consists in knowing when the data were collected. Some data may change with time. For example a hydrographic network may follow the same courses until catastrophic flooding. The water quality may remain healthy for many years, then due to environmental disturbance becomes polluted. Data collected before and after change can be critical. Historical information may also be an important component in the GIS data base. For example, knowing that a given site was a waste dump may restrict its future use.

In this study, the following approach was used for defining the non-spatial entities:

a) The geological maps were simplified, resulting in a set of lithological units that highlighted the geological information required.

b) The structural features were classified on the basis of ductile and brittle deformations.

c) The geochemical elements were evaluated interactively and statistical parameters, such as background (b) and standard deviation (s) were defined in order to establish priorities.

d) The soils were classified according to their mineralogical components.

e) The vegetation cover was classified according to the density, height and type of the trees.

f) The geophysical data were classified on the basis of the intensity of the anomaly.

Table 5.4 presents the summary of the non-spatial entities of the study area.

| | |
|---|---|
| **Geochemical data** | (0) no data(ND); (1)0 to b; (2)b to b+s; (3)b+s to b+2s; (4)>b+2s |
| **Geological map** | (0)ND; (1)Quat.-Ter.sediments; (2)Areiao, (3)Rio Gaviao, (4)Mirante, (5)Barreiro d'Anta, (6)Jurema-Travessao Subunits; (7)Granites; (8)Mafic-ultramafics; (9)Granulites; (10)Migmatites; (11)Espinhaco and (12)Sao Francisco Supergroup |
| **Structural features** | (0)ND; (1)Principal fault; (2)Secondary fault; (3)Antiform axes; (4)Synform axes; (5)Thrust; (6)Fracture |
| **Soil** | (0)ND; (1)Lithosol; (2)red latosol; (3)yellow regosol; (4)white regosol; (5)red luvisol; (6)white latosol; (7)yellow latosol |
| **Geophysical data** | (0)ND; (1)Small anomaly; (2)moderate anomaly; (3)strong anomaly |
| **Vegetation** | (0)ND; (1)scarce caatinga; (2)dense caatinga; (3)grass; (4)cultivated areas; (5)forest |

**Table 5.4:** *Summary of the non-spatial data of the study area*

## 5.4 The data organization

The digital data can be organised using different systems: the computer aided-design (CAD), data base management systems (DBMS), automated mapping and facility management (AM-FM), and GIS.

CAD in essence handles geographical data in the same way as photographic separations are used for the production of topographic maps. Different types of geographical features are placed on different layers that are combined and printed with different colours and line styles to generate the final product. Although the concept is exactly the same, the CAD provides much more versatility in terms of display functions

than their photographic counterpart, and are particularly easy to edit and update.

The DBMS and AM-FM can provide a rudimentary linkage between a database and a graphical display system. In many cases they incorporate large scale statistical analysis programs that provide good interaction between mapping procedures and data manipulation operations. These computer mapping systems also provide very different formats, a wide range of symbolism and publication quality fonts. By combining standard database management operations with automated symbol assignment, the DBMS and AM-FM provide a much better linkage between geographical information and display than doing simple drafting using CAD. However, CAD, DBMS and AM-FM fall far short of the types of capabilities that are now available using GIS.

Table 5.5 illustrates the main disadvantages of CAD, DBMS and AM-FM.

| CAD | DBMS and AM-FM |
|---|---|
| 1. Has severe limitations for analytical tasks | 1. They are restricted to the functions of data, retrieval classification and automatic symbolization |
| 2. Do not generate smooth curves | 2. They are unable to provide appropriate answers to relevant spatial problems |
| 3. Do not force all the lines to join perfectly | |

**Table 5.5**: *Comparative disadvantages of CAD, DBMS and AM-FM (after Cowen, 1983, 1987)*

The unique environment of GIS is most suitable for manipulating the data in this study because I needed to perform overlays and analytical operations, and to generate new spatial data as a result of answering spatial problems. The GIS used here is termed the Geographic Resources Analysis Support System (GRASS) and has been designed and developed by researchers at the United States Army Corps of Engineers Research Laboratory (USACERL).

## 5.5 GIS functions

The GIS software is the heart of the system. The appropriate software should be considered before any special research is initiated. It is the software that determines the activity and utility of a system within the constraints of the hardware system. In terms of data manipulation there are a wide variety on the market and the list is growing rapidly. However, the GIS functions are very well defined. GIS functions can perform both simple operations within individual data planes or layers and complex correlation between layers. The main GIS functions comprise: Boolean combinations, proximity analysis, neighbourhood operations, and region operations.

### 5.5.1 Boolean operations

Boolean operations (BO), in the general case, take two or more images and combine them according to logical rules to produce a new image. Boolean algebra uses the following operators: <NOT>, <AND>, <OR> and <XOR>, to satisfy two basic conditions, true or false, and assign values of 1 and 0, respectively. Figure 5.7 expresses the operators in the form of Venn diagrams.

The <NOT> operator is a simple inversion. The new image derived from this operation contains all DN or attributes of the layer, except those defined by the operator. The <AND> operator produces a new image where both of the defined digital number (DN) or attributes are found. The <XOR> operator yields an image of the difference between the two input images, regardless of where the excess arises. The <OR> operator produces a new image where either or both the same DN or attributes are found.

To take a simple case, suppose we wish to identify the area in the southern part of the study area where granites are covered by red regosol. Figure 5.8.(a) and (b) show the geological and soil map of the southern part of the study area, respectively. Using the BO <NOT> on the two maps generates images including only granites (Figure 5.8.c) and red regosol (Figure 5.8.d). The option <OR> creates a new image (Figure 5.8.e) where red regosol and granites coexist. The option <AND> generates an image where represents the area where red regosol cover granites (Figure 5.8.f).

It is very important to point out that, unlike arithmetic operations, BO are not cumulative. When using three different data sets, for instance geological, soil and vegetation maps, the result of lithosol <AND> granites <OR> caatinga depends on the priority of <AND> with respect to <OR>. The BO should not be thought of as being applicable only for attributes or DN. It can also be applied to the spatial properties. For instance, it may be used to find all granitic bodies that exceed 5 ha in area. More complicated searches may involve the


0) no data
1) Quat.-Ter. Sediments
2) Areiao Submit
3) Rio Gaviao Submit
4) Mirante Submit
5) Barreiro d'Anta Submit
6) Jurema-Travessao Submit
7) Granites
8) Mafic-ultramafics
9) Migmatites
10) Granulites
11) Espinhaco Supergroup
12) Sao Francisco Supergroup
Geological Units
0) no data
1) Yellow latosol
2) White latosol
3) Red luvisol
4) White regosol
5) Yellow regosol
6) Red regosol
7) Lithosol
8) Alluvium
Soil Types

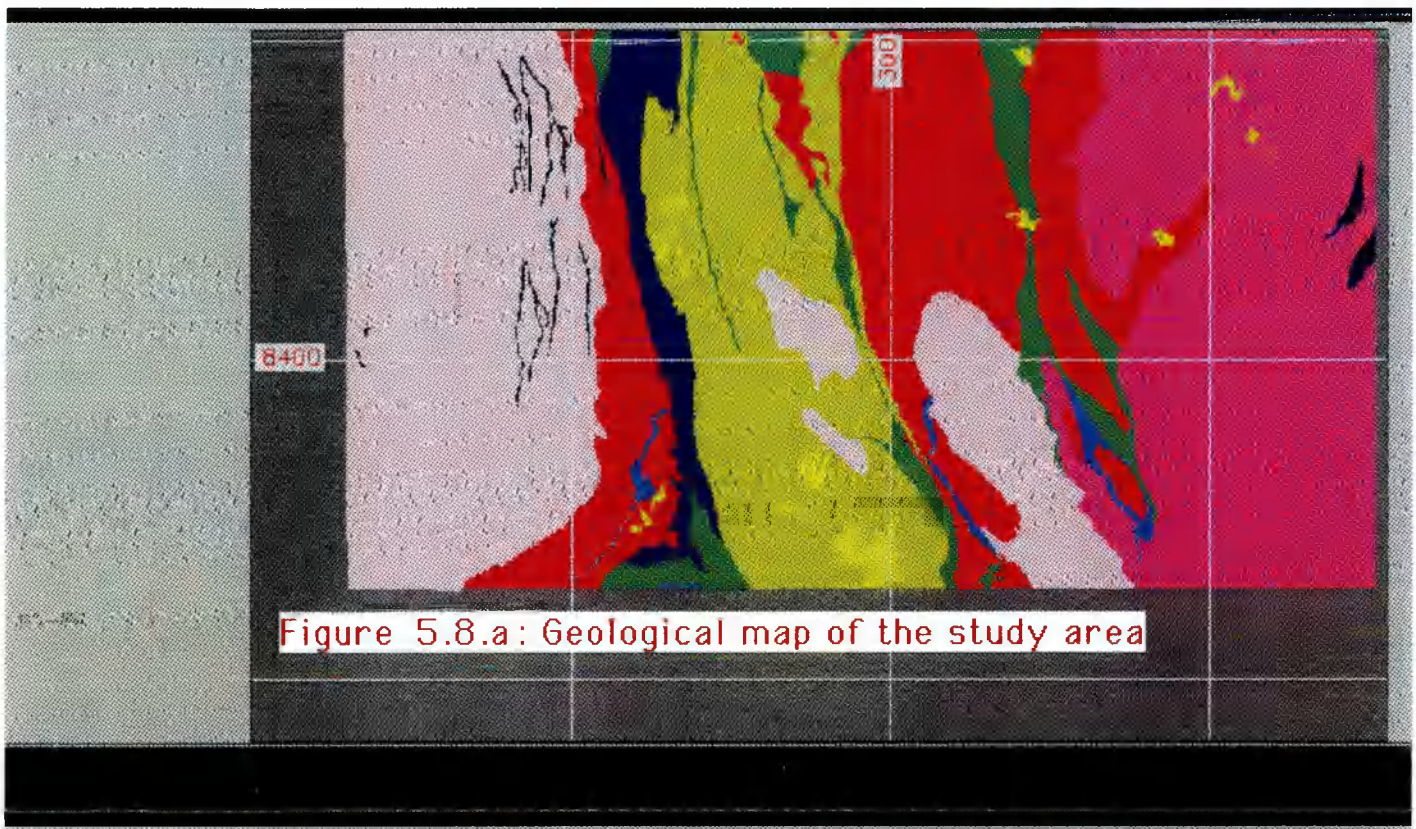


Figure 5.8.a : Geological map of the study area

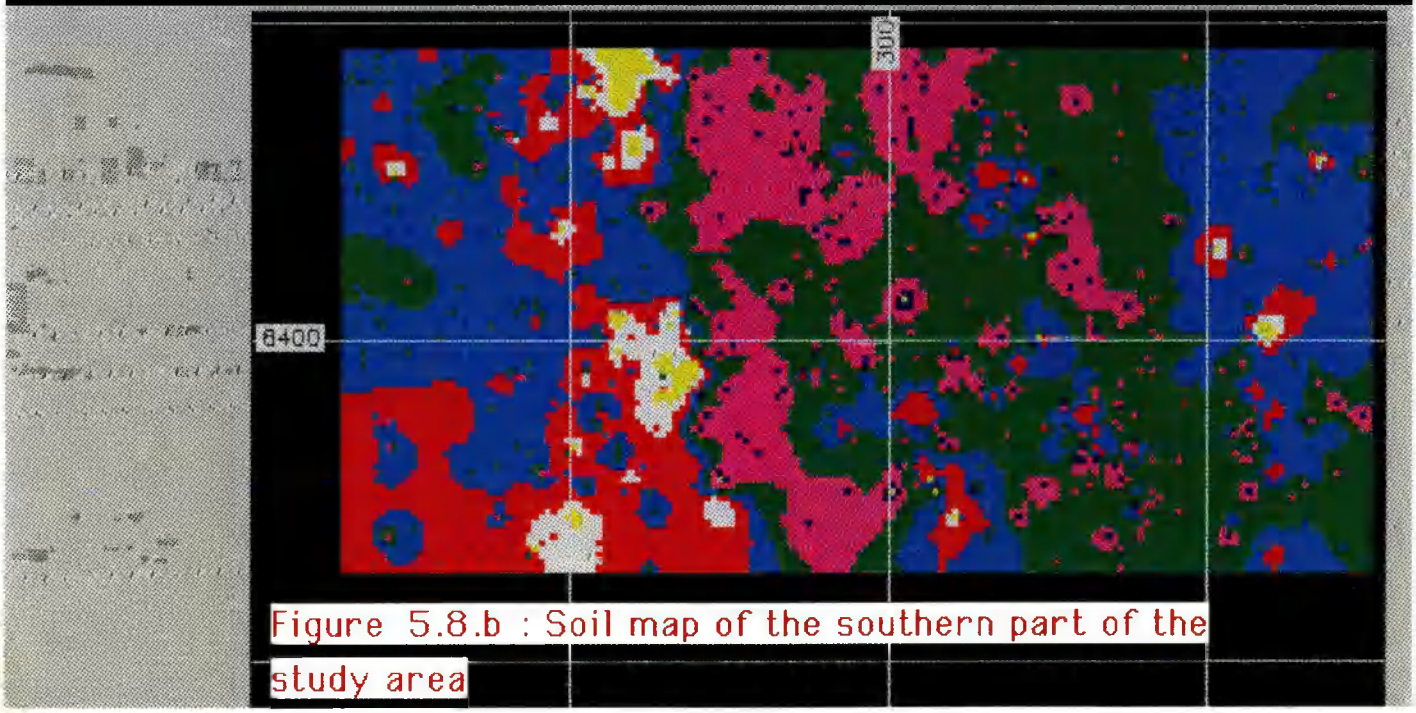


Figure 5.8.b : Soil map of the southern part of the study area

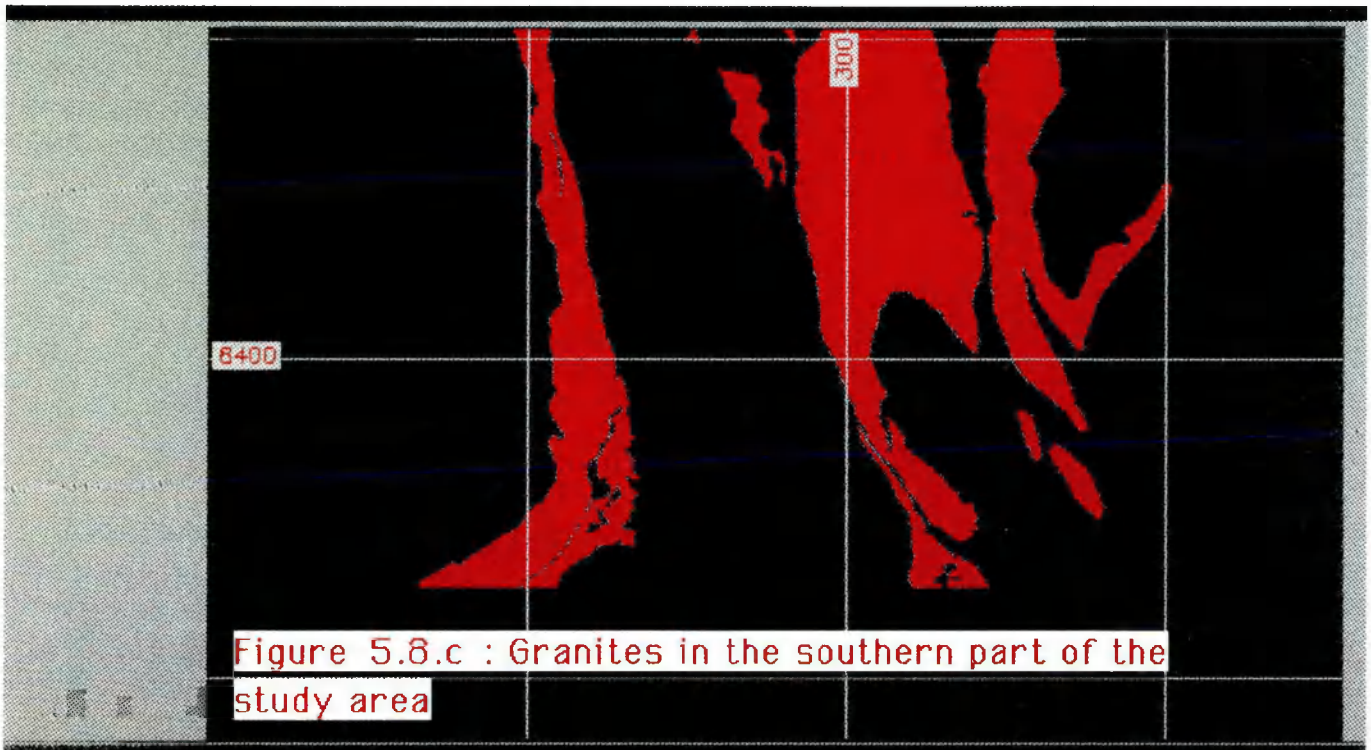


Figure 5.8.c : Granites in the southern part of the study area

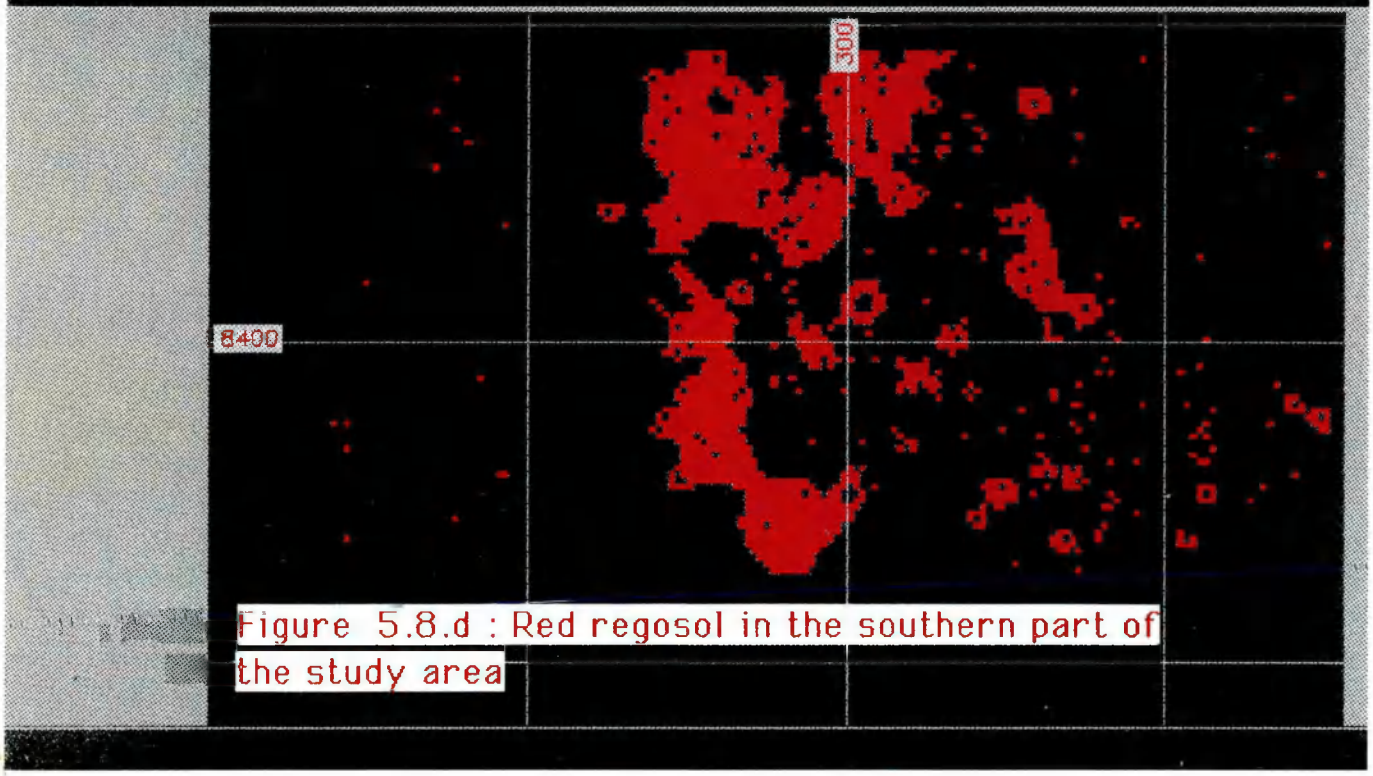


Figure 5.8.d : Red regosol in the southern part of the study area

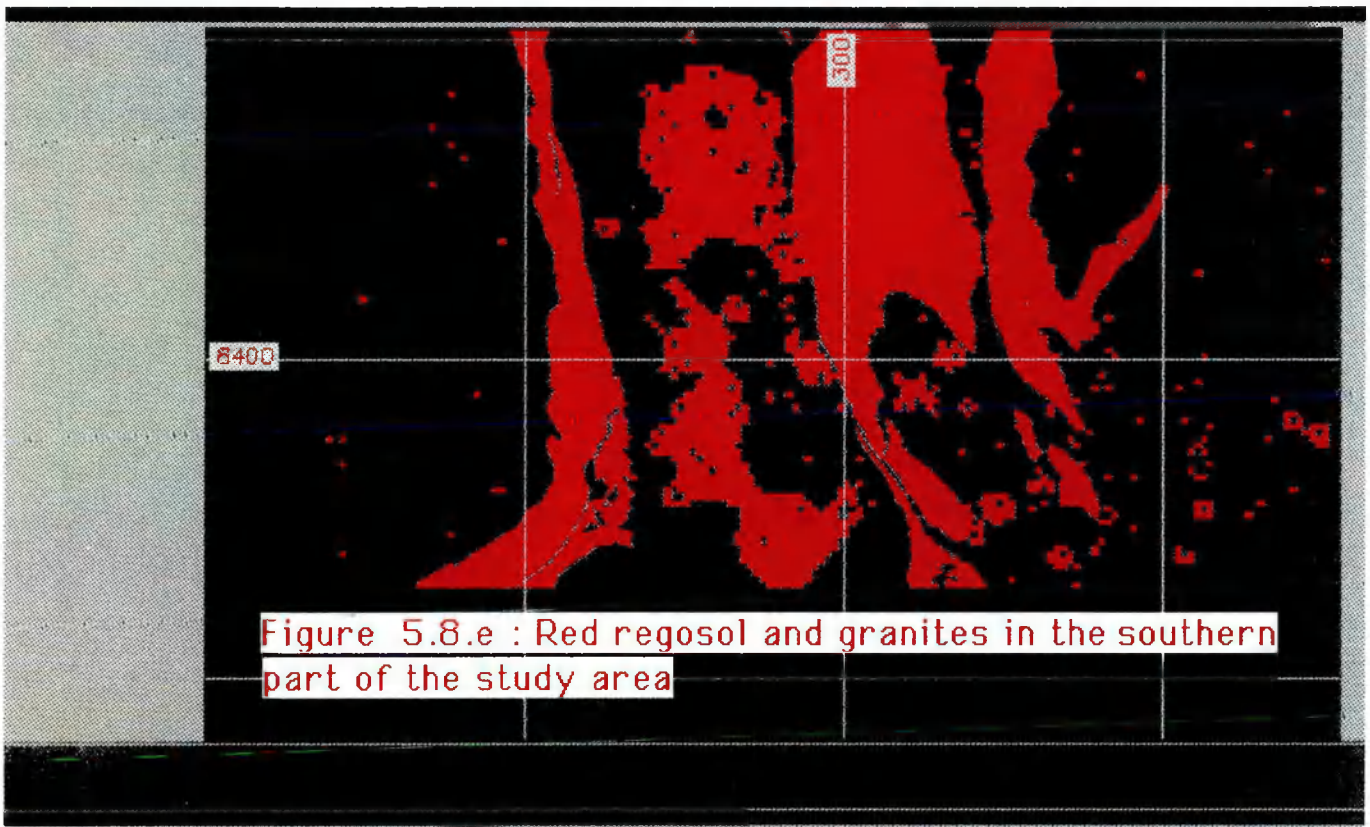


Figure 5.8.e : Red regosol and granites in the southern part of the study area

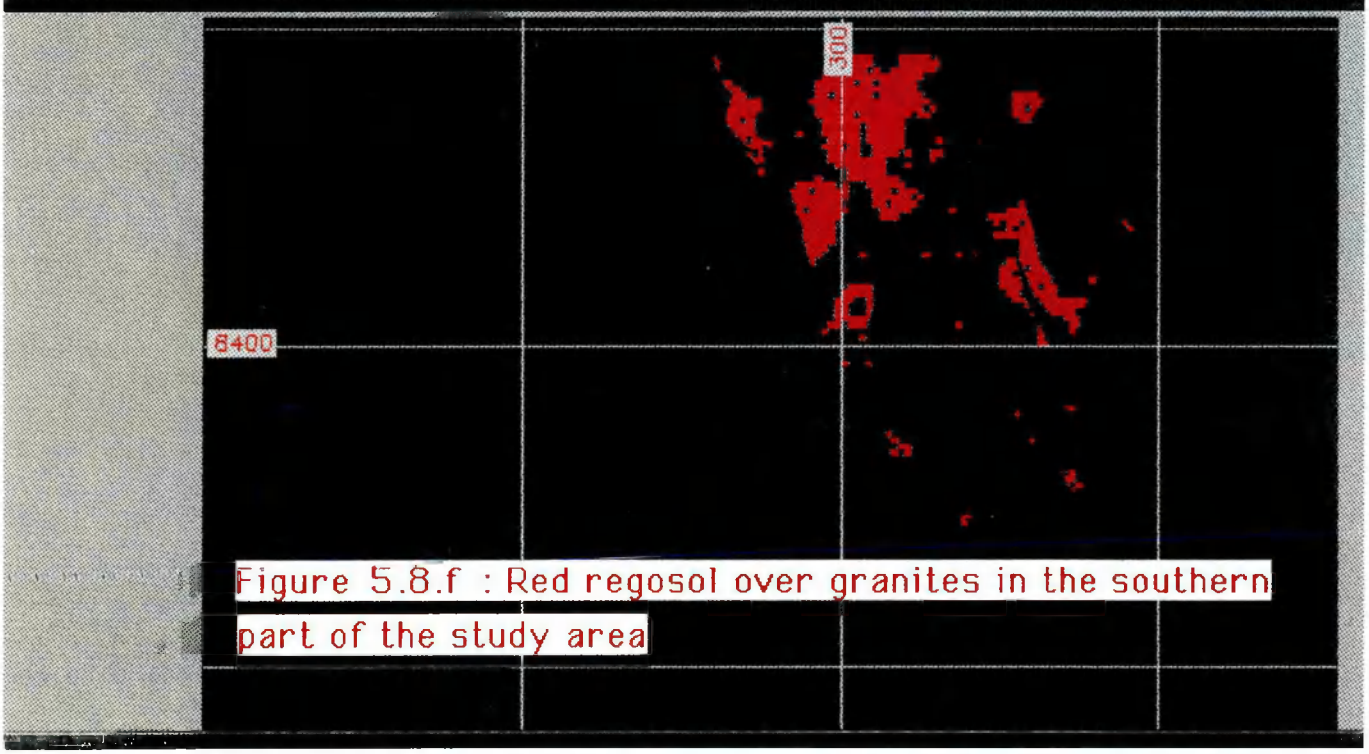


Figure 5.8.f : Red regosol over granites in the southern part of the study area

shape of areas, the properties of boundaries or the properties of neighbouring areas.

### 5.5.2 Proximity analysis

The proximity analysis (PA) is defined by the measure of the distance from a particular point, line or area. Commonly, the chosen unit is length but other units can be selected, such as time or concentration.

To perform the PA, four input parameters must be specified: the target location (e.g. fault planes, fold axes, site sample, boundaries), a unit of measure (e.g. distance in metres), a function to calculate proximity (e.g. straight line distance) and the area to be analysed. The most common technique is often called buffer zone generation. A buffer zone is a user-specified area around one or more map elements. The complexity of the PA is directly related to the number of point locations involved and also the overlay operations associated with multiple data sets.

To take a simple example involving line, point and area, I shall consider part of the study area and the following three hypothetical problems to be solved: (a)a zone of saddle reef, (b)from the threshold, an area having secondary As dispersion and (c)a region where eroded granitic blocks of different size might be found.

The solution of the problem (a) is given from the analysis of the structural pattern of the study area. It is well known that ore deposits are often localised within folded rocks. Saddle reef deposits represent perhaps the most intimate of the associations between folding and mineralisation. Saddle

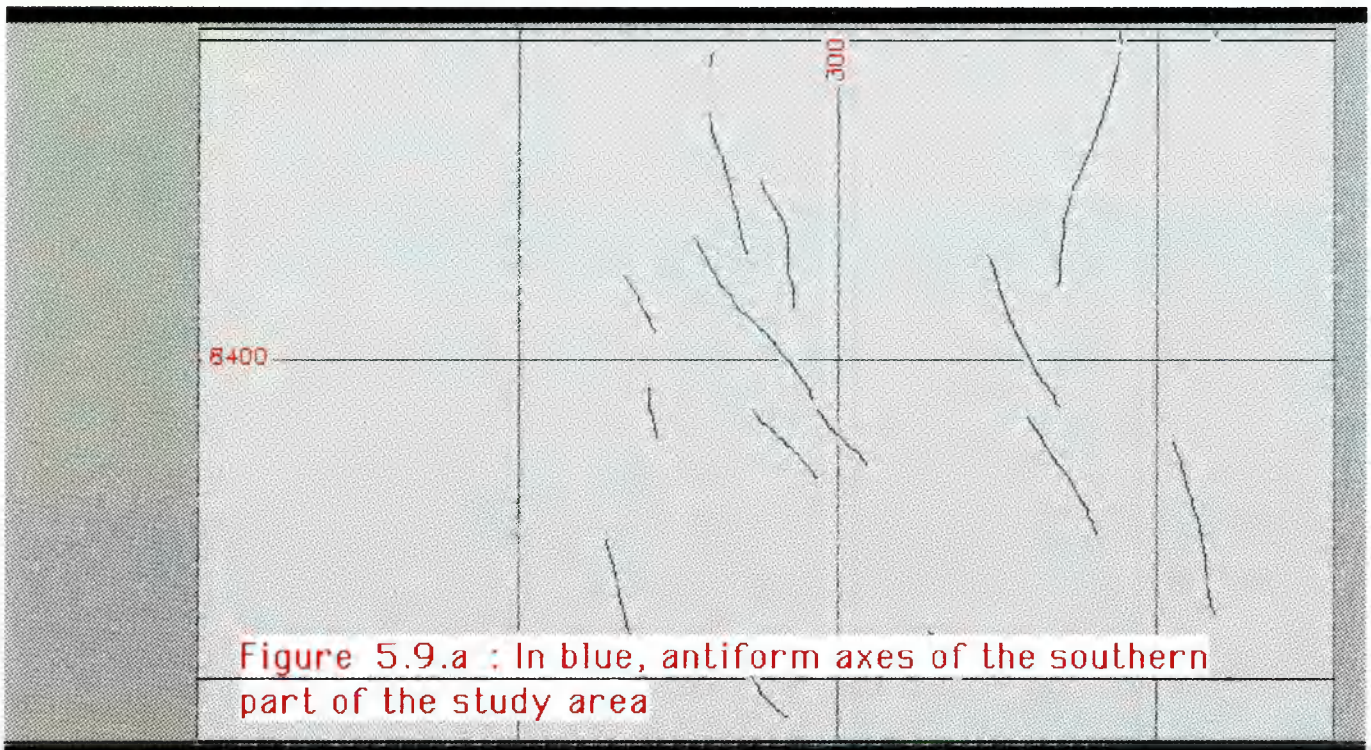


Figure 5.9.a : In blue, antiform axes of the southern part of the study area

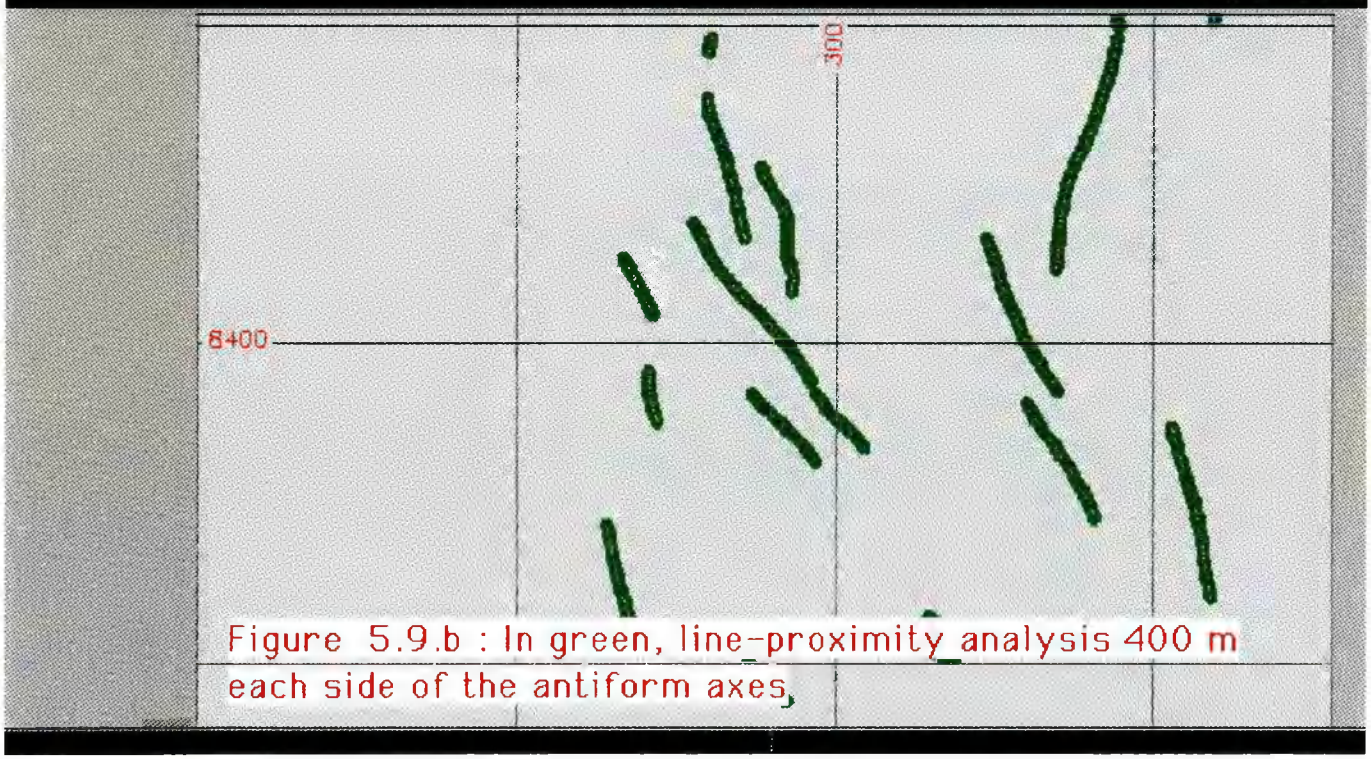


Figure 5.9.b : In green, line-proximity analysis 400 m each side of the antiform axes.

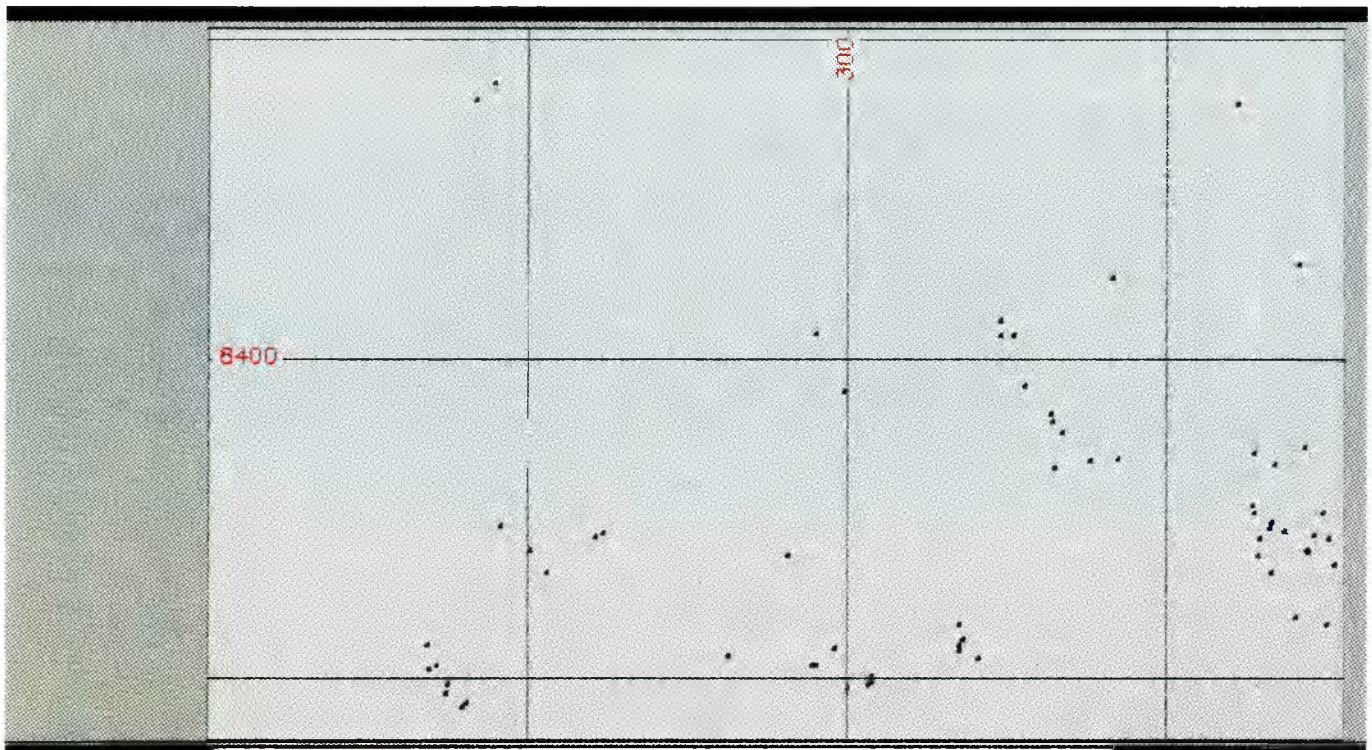


Figure 5.9.c : As sample location (values >b+2s)

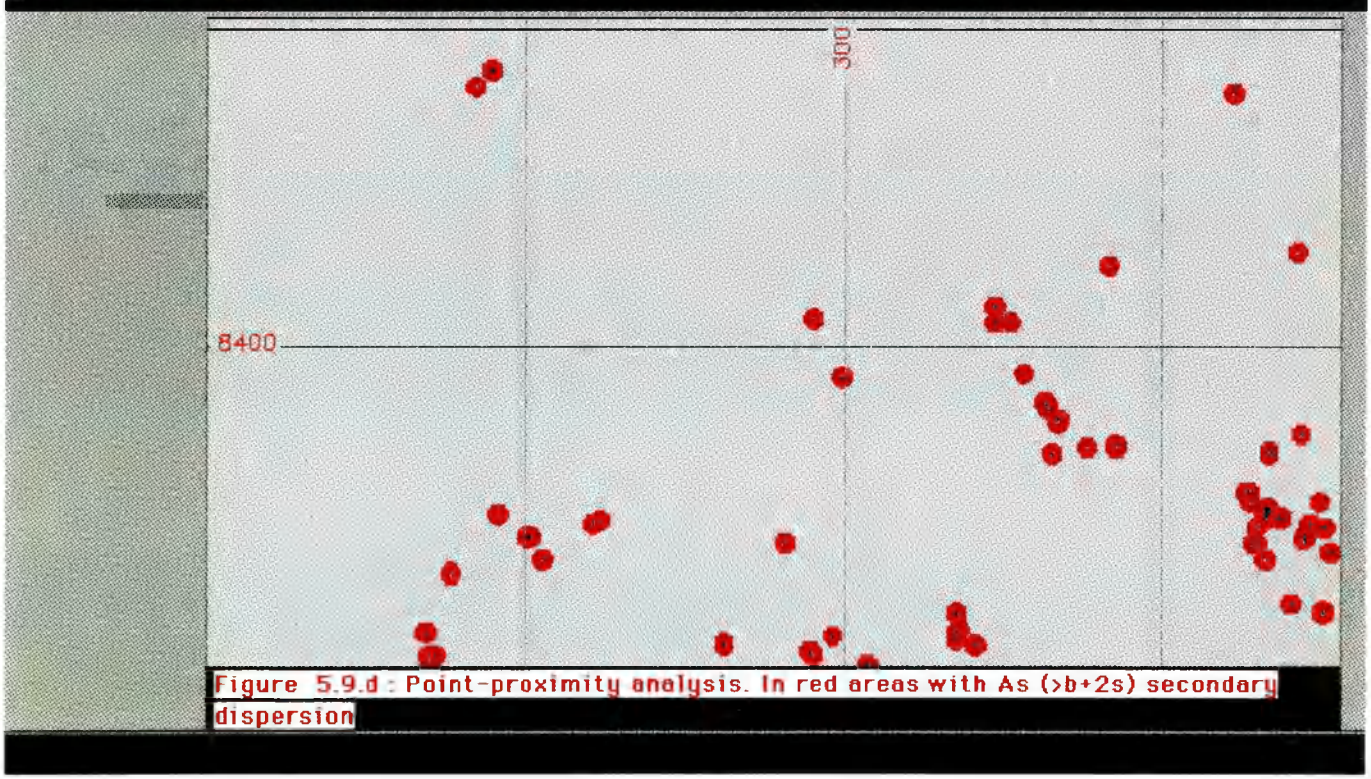


Figure 5.9.d : Point-proximity analysis. In red areas with As (>b+2s) secondary dispersion

reefs are lodes of quartz and precious metals that occupy the core of the folds in openings where bedding and/or foliation has been separated by fold-forming movements. Although saddle shaped in cross-sectional view, they are pipe like in three dimensions, trending parallel to the axis of folding. Figure 5.9.a presents the antiform axes of the part of the study area. I shall consider 400m for each side of the fold axes, because beyond that distance the folds become tight in intensely folded terrains. Figure 5.9.b illustrates the result of the PA, and the area in green represents the potential area for targetting saddle reefs.

Problem (b) is typical of point proximity analysis. Here, I shall consider from each point where the amount of As in stream sediments is equal or greater than the threshold (Figure 5.9.c) and from that point a radius equal to 700 m, as a result of the number of collected stream sediments per $km^2$. Figure 5.9.d illustrates the final result, the red area representing the probable area of As secondary dispersion.

Solution of the problem (c) is achieved from the assumption that the maximum distance over which granitic blocks can be transported by mass wastage is 1500 metres. This information is based on field information. Figure 5.10.a shows the geological map of the area and the result of the PA is shown in Figure 5.10.b. The areas in green represent the probable region where colluvial granitic blocks might be found.

### 5.5.3 Neighbourhood operations

Neighbourhood operations take into consideration the relationship between one point and its neighbourhood. These

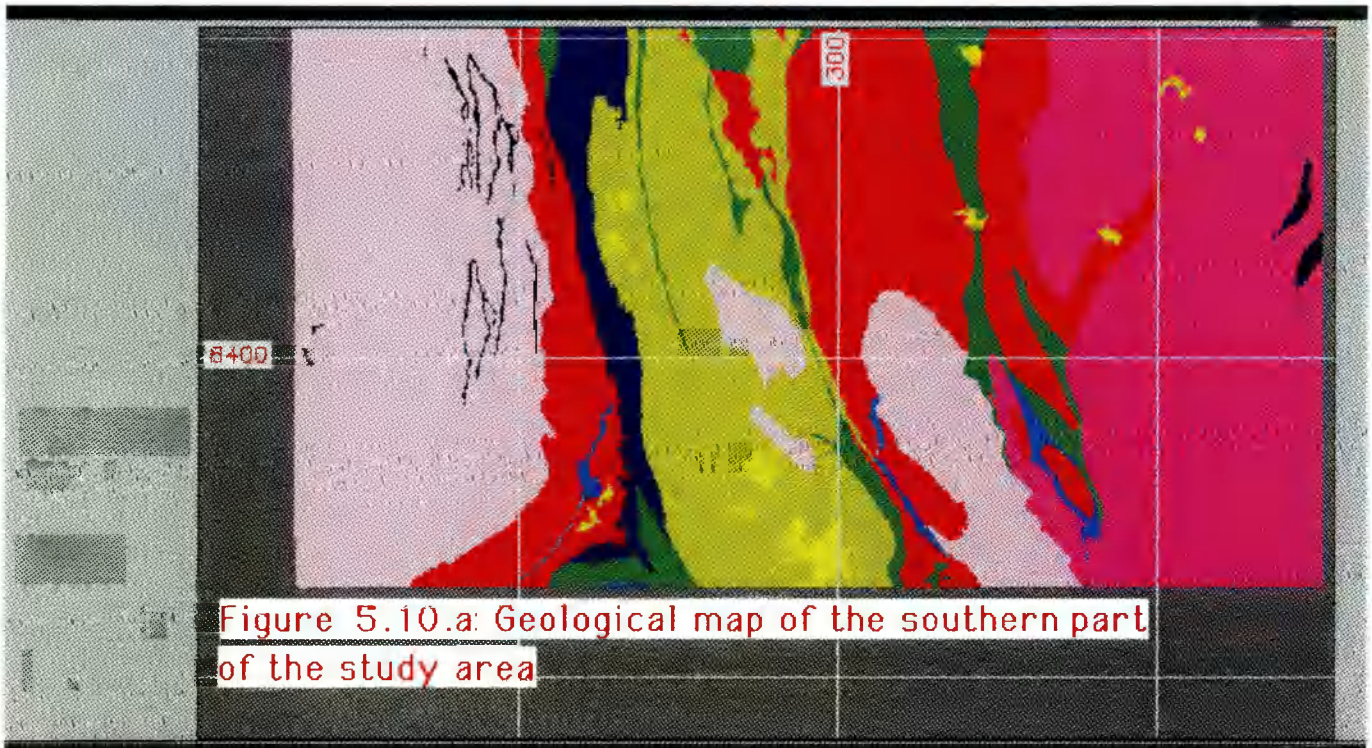


Figure 5.10.a: Geological map of the southern part of the study area

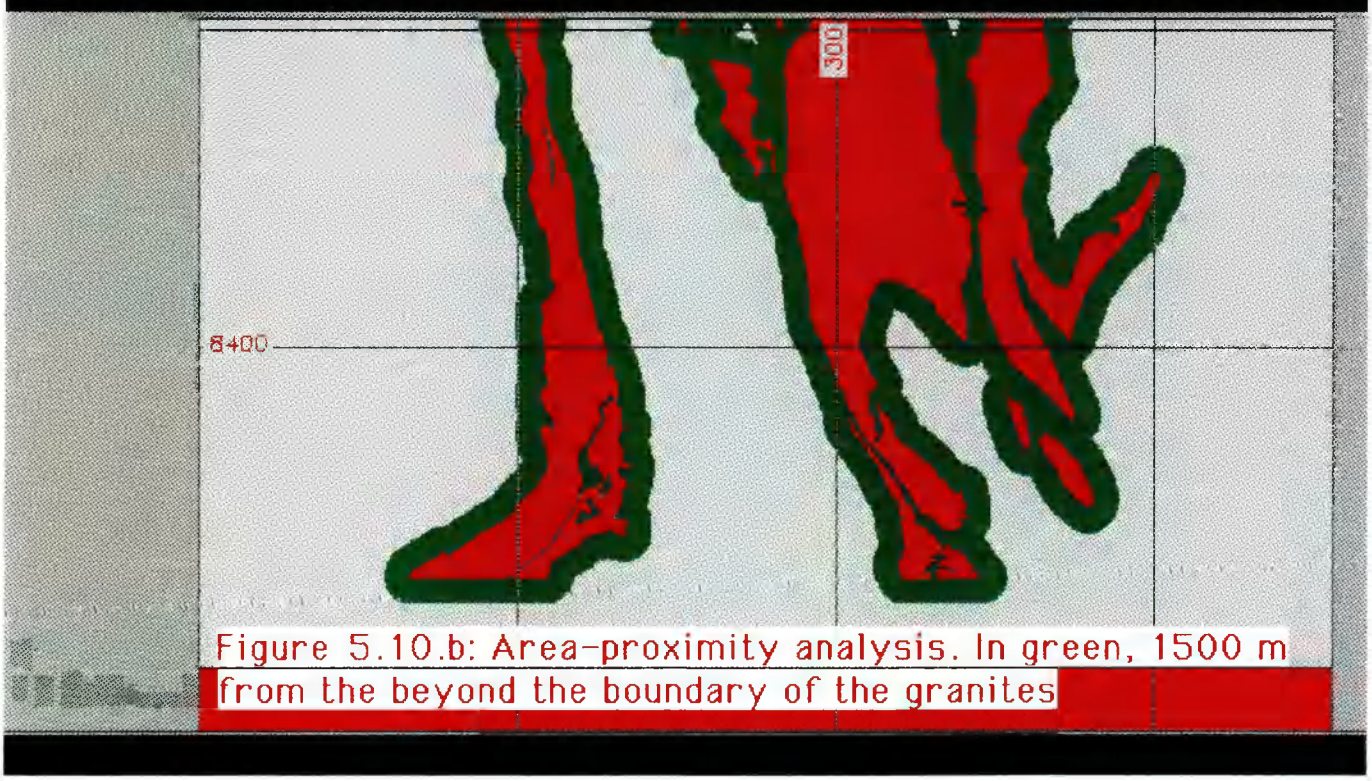


Figure 5.10.b: Area-proximity analysis. In green, 1500 m from the beyond the boundary of the granites

include all functions that make use of some kind of spatial associations aiming to define the value of the new pixel at a determined location. The main neighbourhood operations are:

a)clump:it finds all areas of contiguous pixels in a input image and create a new map by uniquely identifying contiguous groups or "clumps" of units;

b)overlay: it sets mutually contiguous regions associated with a particular area. This can be done by using several layers and the operation can be either opaque or transparent;.

c)convolution: it modifies a data value of one pixel based on the values of its surrounding neighbours;

e)contouring: it performs a grid pixel matrix with interpolated values from a set of irregularly spaced data points using numerical approximation. The final result is a map displaying the distribution of an attributes in terms of lines connecting points of equal value weight, and is called an isopleth map;

f)renumber or reclassify: it permits a new grid pixel map based upon a category reclassification of an existing layer to be created.

### 5.5.4 Region operations

The region operations are related to properties such as length, area perimeter or shape.

The main operations include:

a)cross: it tabulates attribute values of the mutual occurrence or coincident areas from two maps on a point-by-point basis;

b)report: it defines a series of statistical parameters such

as number of pixels in the area of interest and percentage of covered area measures in different units;

c)distribution: it plots the histograms or category-value distribution of the whole overlay or a particular area;

d)analyse: it performs simple statistics or multivariate analysis such as principal component analysis of pixel values on ***n*** overlays;

e)mathematical operation: it performs summation, subtraction, multiplication, division, exponentiation, and trigonometric and logarithmic functions.

## 5.6 Data quality

It is vital to know the quality of the data in order to decide the applications for which they are suitable. It is also crucial to know the cost of assessing data quality which varies enormously. The costs comprise the expenses of performing quality testing and the delays between the production process and actual testing. It is also important to point out that data may be used in ways not anticipated by their producers and by the users in the initial stages. Unfortunately, the quality of geographical data is often examined only after incorrect decisions have been made and financial losses or even personal injury have occurred. To avoid these hasty and nasty circumstances, the data quality standards should be appropriately defined, tested and reported.

The characteristics that affect the reliability of the data can be divided into three categories: microlevel, macrolevel and usage components (*Aronoff*, 1989).

The **microlevel** components consist of factors that belong to the individual data. They comprise positional and attribute accuracy, logical consistency and resolution.

The positional accuracy is the expected deviance in the geographic location of an object in the data set from its true ground position. Two parameters should be calculated: bias and precision. Bias represents the systematic discordancies between the represented and the true position and it is measured by the mean or average position error of the points. Precision is related to the dispersion of the positional errors of the data elements and is estimated by calculating the standard deviation of the selected points. Ideally the bias should be zero and the standard deviation very low. Concerning the data of the study area the results of overlay operations show good correlation between the represented and true position.

*Accuracy* corresponds to ordered categories where the order indicates the hierarchy of the attribute. These categories may be continuous, like the magnetic fields or represent a finite number of categories, such as lithological units. There are no standard methods to define the suitability of the accuracy because many factors can disturb the mathematical procedures, such as the number of classes, shape and size of individual areas, the way in which test points are selected. These factors depend on the objective to which the final result of the GIS is addressed.

*Logical consistency* concerns how well the logical relations among data elements are maintained. Again there is no standard

measure of logical consistency, but it can be established arbitrarily. For example, when data sets with slight discrepancies in position are overlayed, this creates "slivers" in the region between the two boundaries. This inconsistency can be corrected using the facilities of the GIS software.

The *spatial resolution* is defined by the smallest discernible or the smallest unit represented in a data set. In this study, different spatial resolutions (SR) were defined according to the information source. Although the TM data provide a SR of 30 m, the images were modified to 50 m which reduces storage space with only minimal loss of information. The chosen SR of geophysical data was 500 m, and was defined as the half distance between flight lines. The geochemical contour maps have a SR of 250 m and represent the mean half distance between sample points.

The **macrolevel** components consist of the data quality pertinent to the data set as a whole. They include completeness, time, and lineage.

The *completeness* can be subdivided into coverage, classification and verification. The completeness of coverage is the proportion of data available for the area of interest. Table 5.6 shows the completeness of coverage of the study area.

]

| | |
|---|---|
| Geological data | 85% |
| Geochemical data | 45% |
| Thematic Mapper | 100% |
| Radar | 100% |
| Magnetic data | 80% |
| Radiometric data | 80% |

**Table 5.6**: *The completeness of coverage of the study area*

The completeness of classification is an assessment of how well the chosen classification is able to represent the data. This evaluation is qualitative and depends on the specific aims of the investigation. In this particular area, almost all the different types of geological information area were available, therefore the completeness of classification was considered good. The completeness of verification refers to the amount of distribution of field measurements or other independent source of information that were used to develop the data. There is no standard method to report completeness of verification in GIS. In this study the completeness of verification is indicated within the data set as an attribute of the geographic features.

*Time* is related to the date of the source material. Although this factor may be critical for many types of geographic information, such as vegetation cover, it can be neglected in the present analysis. In this study, all the data are recent, and most refer to unchanging physical or chemical characteristics of the sample collected. Table 5.7 shows the dates of the source material.

| | |
|---|---|
| Geological maps | 1978, 1980, 1987 |
| Geochemical data | 1979, 1980 |
| Airborne magnetic data | 1978 |
| Airborne radiometric data | 1978 |
| Landsat Thematic Mapper | 1988 |
| Radar | 1981 |

**Table 5.7**: *Date of the source material for the study area*

The *lineage* of a data set is its history i. e. the source data and the processing steps. This information is reported in each relevant chapter of this work.

The **usage components** are specific to the resources of the organization and include accessibility and direct and indirect costs. *Accessibility* refers to the ease of obtaining and using data. With reference to this work, almost all the data were provided by the "Companhia Baiana de Pesquisa Mineral, Brazil" (Bahian Company of Mineral Exploration), and the data were manipulated using the facilities of the Open University. *Direct cost* refers to the price paid for the data and indirect cost includes all the time and materials used to make use of the data. These aspects are beyond my control have been subject to considerable experimentation, and therefore have not been evaluated in this work. They would need to be assessed in applying my techniques in a commercial context.

## 5.7 The decision model

A model is a set of inter-related characteristics which represent facts or phenomena in the real world. GIS users must choose one or several to achieve satisfactory results. In this work, I will apply GIS technology to target areas for gold mineralisation in the Archaean terrains of the Contendas-Mirante region. I must emphasise that in defining gold mineralisation models, it is very important to establish precisely the GIS functions to be used.

Syngenetic and epigenetic gold deposits can be distinguished according to depositional and genetic models. The former represents a synthesis of empirical data drawn from many Archaean gold deposits with a minimum of genetic interpretation, and the latter in an exercise to provide the means to interpret the isotopic and compositional characteristics of the auriferous fluids and some related hydrothermal minerals. In this work I concentrate on depositional models, because the majority of the data relates to mesoscopic scale. The depositional model can be divided according to the structural setting and lithological associations.

### 5.7.1 The structural model

It has long been known that many Archaean gold deposits occur in deformed rocks (*Newhouse*, 1940). Individual deposits commonly occupy specific structural features such as fold hinges, shear zones or fracture networks, and most deposits exhibit a variety of these structural types. Mine scale structures, rather than being random features are a reflection

of regional structural patterns which relate to the deformational history of the terrain in which they are located.

At the largest scale, gold deposits are clearly associated with shear zones as in the Superior Province of Canada (*Andrews et al*, 1986; *Burrows* and *Spooner*, 1986; *Fyon* and *Lane*, 1985), Australia (*Clark et al*, 1986; *Groves* and *Phillips*, 1987; *Groves et al*, 1985), India (*Hamilton* and *Hodgson*, 1986), Africa (*Foster* and *Wilson*, 1984) and Brazil (*Silva*, 1987; *Nonato*, 1986).

Shear zones are zones of anomalously high ductile strain with a variable sense of displacement. They transect or form the boundaries between granite-greenstone and metasediments, and deform all Archaean lithologies and hence are not restricted to certain units. Nevertheless, these zones form discrete linear, mappable units of deformed rock up to several kilometres in width and up to hundreds of kilometres in length. In the majority of cases in Bahia State it is impossible to correlate lithologies and structures across such zones, and movement across them is uncertain.

Zones of ductile deformation also form in response to the ascent and emplacement of both major batholiths and smaller plutons. *Stott* and *Smith* (1988) pointed out that gold-bearing structures can be developed in deformation zones that had been created or reactivated by emplacement of plutons.

The deformation zones constitute mappable units in which lithological units are characteristically transposed into parallelism. Figure 5.11 shows the behaviour of the

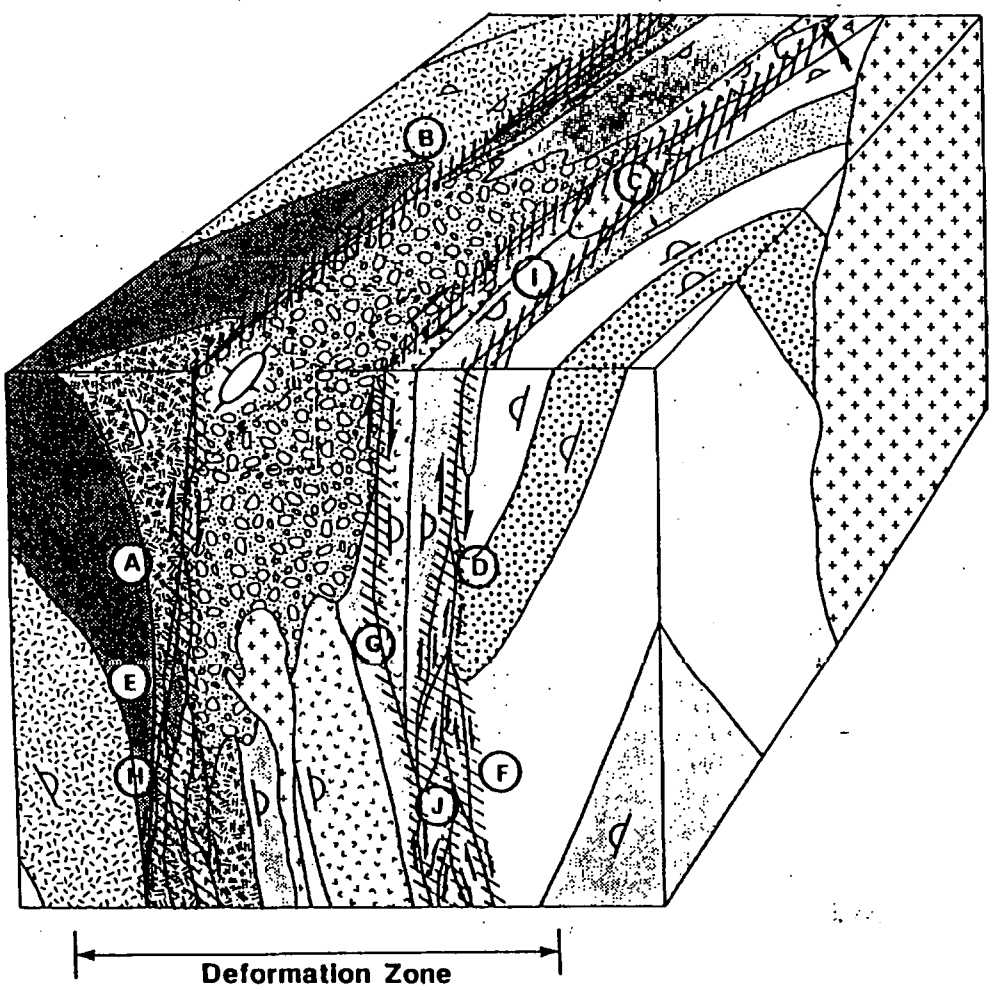


Metasediments 1

Intrusive rocks

Metasediments 2

Calc-alkaline felsic metavolcanics

Calc-alkaline basalts

Fe-tholeiitic basalts

Mg-tholeiitic basalts

Gabbro

Komatiitic basalts

Komatiites

The lithologies may be:
A - ROTATED
B - FOLDED
C - DISLOCATED
D - TRUNCATED
E - THINNED
F - THICKENED
G - REPEATED
H - TRANSPOSED
I - At outcrop scale, and in some instances at mine scale, deformation zones are parallel to bedding and are only evident as anomalous reversals in facing direction (J)

Figure 5.11 : *A shematic block diagram of a greenstone belt, indicating large scale features of deformation zones (from Colvine et al, 1988)*

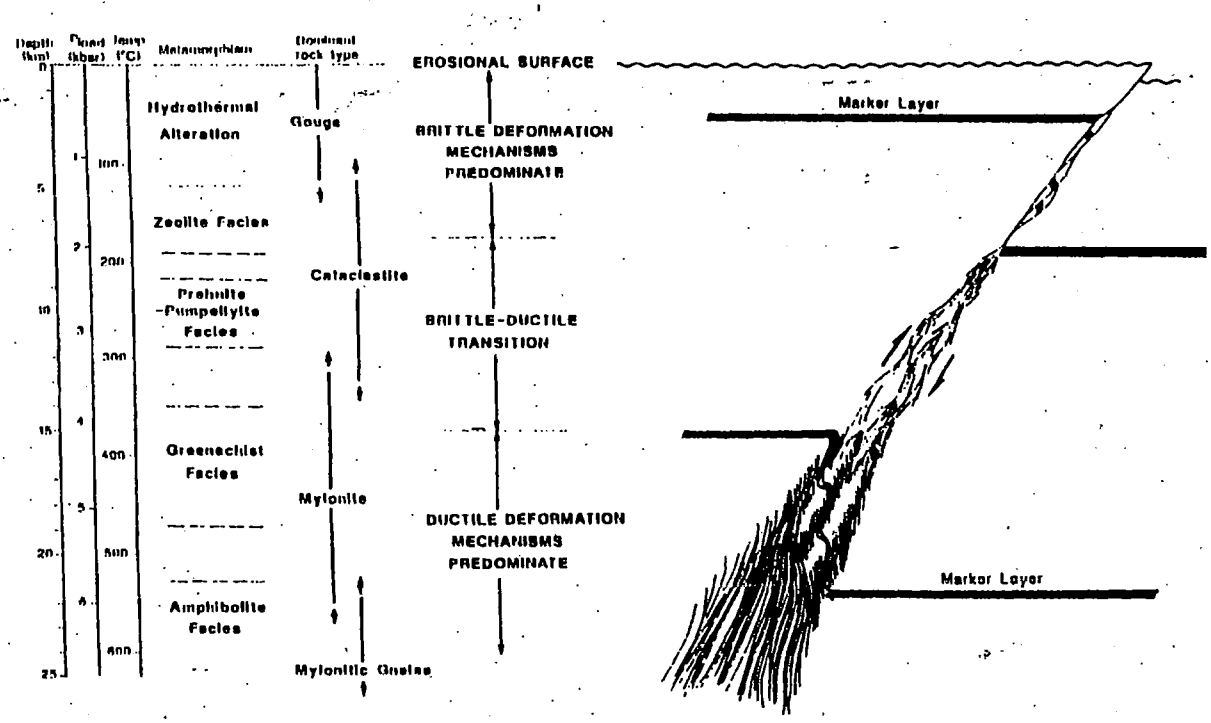


Figure 5.12 : *Deformation regimes as a function of depth (from Simpson, 1986)*

lithologies within or along the margins of deformation zones in a typical greenstone belt sequence.

According to *Corfu* and *Andrews* (1987), timing and depth variations are important in the development of deformation zones and related gold deposits. Regional scale fault zones and shear belts are culminating stages in the progressive history of crustal shortening, and gold deposits hosted within these late stage deformation zones are an integral part of the final stage in Archaean crustal evolution. *Simpson* (1986) presented the correlation between depth and variation of deformation zones (Figure 5.12).

At shallow depths dominated by brittle processes (upper crust, sub- to lower-greenschist facies), deformation zones are narrow, discrete faults that commonly contain relicts of underformed rocks separated by zones of gouge and breccia. At intermediate depths (middle and upper crustal levels, greenschist to lower amphibolite facies) shearing becomes increasingly ductile. As a result the deformation zone anastomoses and widens, and brittle structures become less common. At greater depths, the occurrence of relicts diminishes, deformation zones become continuous, and brittle deformation occurs only under condition of rapid changes in pore fluid pressure or strain rate. At these great depths, deformation zones may become shallow-dipping taking advantage of horizontal anisotropies (*Coward*, 1984). Figure 5.13 illustrates the relationships between depth and deformation regimes.

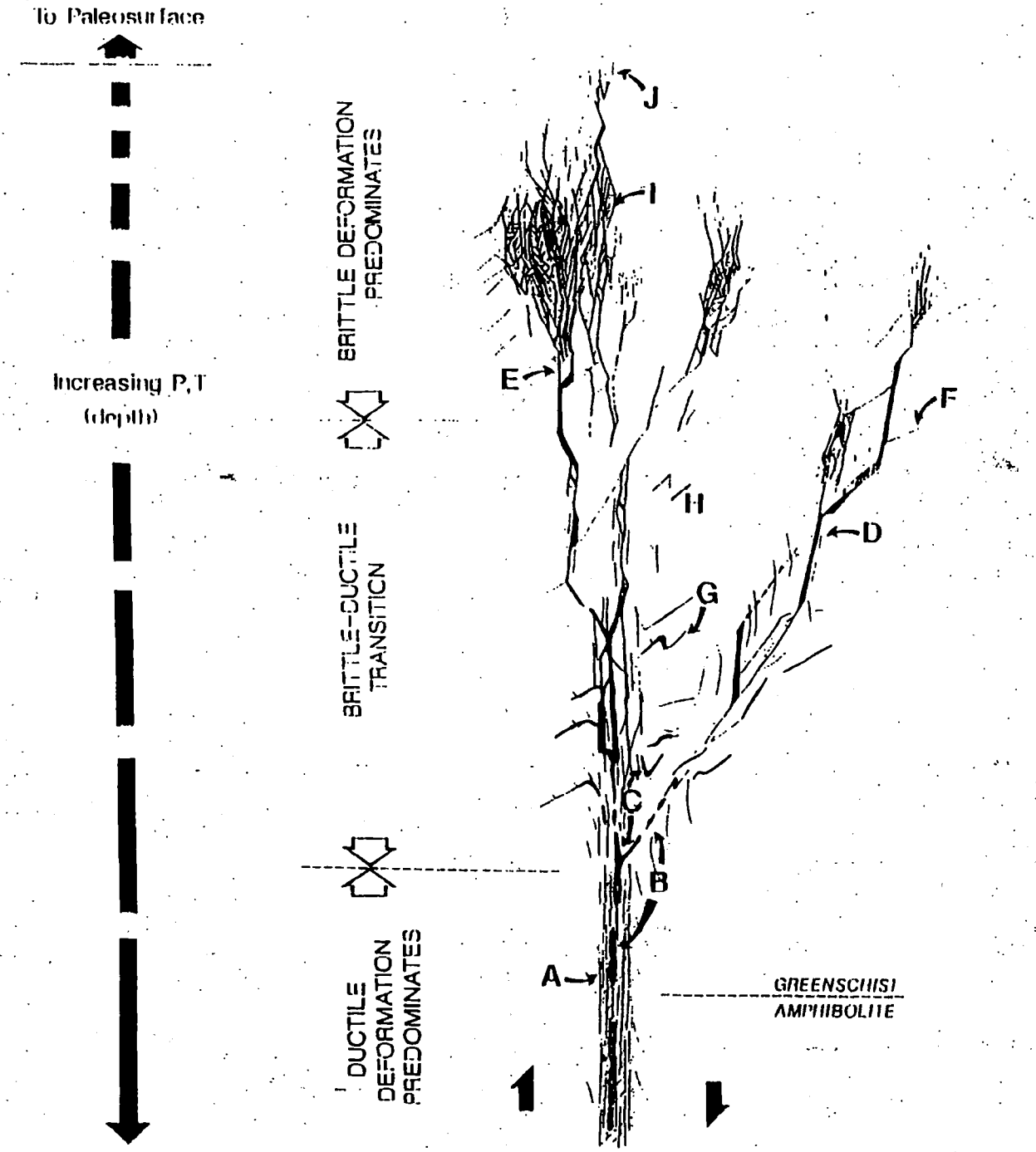


Figure 5.13 : *Schematic representation of an ideal gold ore zone. The figure illustrates (a) replacement veins, (b) boudinaged veins, (c) saddle reef veins (d) Riedel shear veins, (e) "break ore" veins, (f) undeformed and (g) deformed tension veins, (i) breccia veins, (j) pervasive silicifications. Vein systems are interpreted to widen and become increasingly complex with elevation (from Colvine et al, 1988)*

Gold mineralisation is usually hosted in small scale structures within the larger deformation zones (*Colvine et al*, 1988). These structures are highly permeable zones, and therefore preferred sites for mineralisation. In general, gold is associated with large volumes of fluid that have altered the host rocks. This fluid, through its influence on the ductile-brittle behaviour of the rocks, will also affect the form and distribution of gold-bearing structures.

*Colvine et al* (1984), suggested that some gold occurrences are located in portions of deformation zones which have undergone increased extension during wrench faulting. In some instances enhanced permeability in dilational areas is a preferred location for mineralisation, relative to the compressional portions of a transcurrent shear system (*Sibson*, 1987).

Areas of enhanced permeability along whole deformation zones may contain a number of significant deposits which together form a gold field. They are usually composed of one or more ore zones, whose shape, orientations and distribution can be related to small scale structures within deformation zones. Ore zones are lenticular, tabular or irregularly shaped bodies composed of veins, breccia and/or stockwork systems. They are generally hosted by structures which transect stratigraphy.

According to *Colvine et al* (1988), the ore zones of the gold deposits can be found within:

(a) zones of anomalously high strain within a deformation zone,
(b) pre-existing structural anisotropies,
(c) a preferred lithology, where a strong competency contrast

exists between adjacent rock types, and

(d) fold limbs and fold noses.

In zones of anomalously high strain, both brittle and ductile deformation style are recorded, depending on the depth in the crust at which they formed. In pre-existing structural anisotropies, the ore zone can occur where sympathetic bedding-controlled splays to a shear zone intersect that shear, or due to intersection of two shear zones (*Boyle*, 1979). Where a strong competency contrast exists, structurally more competent lithologies can be preferentially mineralized. The competency difference may be a result of lithological differences, or may result from alteration processes (*Roberts*, 1987). In fold limbs and fold noses, permeable zones can be created as a result of contrasting thicknesses and competencies. *Colvine et al* (1988), pointed out that "saddle reef" gold deposits in fold noses have long been known.

Gold-bearing veins include replacement extension, breccia and fracture types. In most cases veins transect lithological contacts and are not restricted to a specific rock type. The characteristics of each of these types of gold-bearing vein structure were pointed out by *Hodgson* (1988) and are shown in Figure 5.13.

The ore zones and vein systems that make up gold deposits display vertical and lateral changes in mineralisation style. These variations reflect a change in deformation style from brittle to ductile. Usually gold deposits are both smaller than the deformation zones in which they occur and of limited

vertical extent. Systematic changes in the style of deformation are generally not evident within any one deposit.

*Colvine et al* (1988), suggested an idealized variation in gold mineralisation that will occur with changes in deformation (Figure 5.13), based on the following evidence:

(a) most deposits hosted in greenschist facies rock contain ore in shear or tension veins or the deposits contain mainly extension, breccia and fracture-filling veins,
(b) deposits hosted in higher grade terrains have texture and vein types indicative of brittle-ductile deformation,
(c) some deposits display a mineralisation style indicative of a transition between different pressure-temperature regimes, and
(d) the dominant deformation style in high-grade terrains is ductile. Deformation in these terrains does not appear to have produced dilatancies.

### 5.7.2 The lithological model

Although all greenstone lithologies have been found to host gold, certain lithologies favour gold deposits most frequently. According to *Groves et al* (1985), gold deposits can be divided into those hosted in volcanic-intrusive rocks and those in banded iron-formation (BIF). *Colvine et al* (1988), suggested that pelitic sedimentary rocks can also host gold mineralisation.

*Siems* (1984), divided gold deposits into: (a) deposits associated with continental volcanism, and (b) submarine-exhalative deposits. Deposits associated with continental volcanism include:

(a) deposition in a volcanic or non volcanic environment near-surface portion, of a system that flowed out at the surface (hot-springs model);
(b) deposition at and along the interface of a hot, hydrothermal cell beneath a cooler, shallower cell, resulting in lateral zoning (stacked-cell convection model); and
(c) deposition in sequential, vertical zones due to vertical convection, resulting in vertical zoning (closed-cell convection model).

Submarine-exhalative gold deposits include:
(a) stratiform and vein deposits associated with submarine, volcanogenic exhalative processes; ore transporting fluids may be originally seawater, evolved seawater magmatic or metamorphic water in origin;
(b) vein and replacement deposits hosted by, or related to, epizonal felsic intrusives; magmatic waters are likely to be involved in ore transportation;
(c) vein and replacement deposits emplaced by metamorphic processes; ore transporting fluids may be evolved connate waters or metamorphic in origin; and
(d) vein and replacement deposits possibly related to both epizonal intrusions and metamorphism; magmatic, metamorphic or evolved connate waters might be present.

The most important volcanic/intrusive rocks that host gold mineralisation are tholeiitic basalts and dolerites. It is remarkable that apart from the oxide facies of BIF, these tholeiitic mafic rocks are the most Fe-rich in the greenstone belt sequence (*Groves et al*, 1986). These rocks may have

suffered diverse metamorphic transformations, varying from low grade to amphibolite facies. When amphibolite facies is present, two different types of gold deposits can be recognized:

(a) those which are clearly metamorphosed equivalents of deposits formed at lower grades, and

(b) deposits with several characteristics that set them apart from more typical greenstone belts.

Gold is generally associated with shear zones typified by K-metasomatism and intense carbonation haloes, in which regionally extensive albite-actinolite assemblages in mafic rocks are replaced by chlorite-calcite assemblages. Sometimes gold deposits occur restricted to a particular part of the tholeiitic basalt sequence producing a gross stratabound appearance.

Only a few gold Archaean deposits are entirely hosted within clastic sedimentary rocks (*Macdonald*, 1983). Pelitic sedimentary rocks commonly respond to shear in a ductile fashion, and hydrothermal fluids may be preferentially focussed through adjacent, more competent rocks such as basalts or BIF, which also are geochemically more favourable for sulphidation and mineralisation. Well developed vein systems are observed to terminate abruptly against argillaceous units, illustrating the effects of lithologic competency contrasts during deformation and fluid migration (*Pattison et al*, 1986)

Gold related to BIF can be distinguished into two types:

(a) stratiform-like mineralisation constituting a mixed

carbonate-sulphide facies type of BIF, and

(b) discordant vein-type mineralisation. Gold occurs as particles and also as microscopic to submicroscopic inclusions in arsenopyrite, pyrrhotite and other sulphides.

Gold deposits hosted in BIF can be found in many Archaean terrains. In Zimbabwe, there are several gold deposits associated with As-bearing BIF (*Saager et al*, 1987). In Brazil, the most important gold mines confined in BIF occur in almost all chemical facies, however, the ore is particularly rich in sulphide facies. Some of the Archaean gold-bearing sulphide lodes of the Kolar Goldfield, in India, are hosted in the sulphide facies of the BIF.(*Singh*, 1980). A great variety of Archaean BIF is present in the Canadian Shield, where the oxide facies is wide spread, carbonate facies is present locally and sulphide facies is very common (*Colvine et al*, 1988) Gold is relatively uniformly distributed in thin but laterally extensive beds of cherty sulphide-rich iron-formation. BIF is widely distributed in the Archaean Yilgarn Block, Western Australia. In the majority of the cases, gold occupies structurally complex zones within the BIF (*Groves et al*, 1985).

A comparison of Archaean gold deposits is presented in Table 5.8. It provides the means to establish both a selection of required data to be addressed to the GIS environment and a GIS strategy, and to define the GIS functions to be used.

The preprocessing and interpretation of the available data set will be discussed in Chapter 6 (remotely sensed data), 7 (geophysical data) and 8 (geochemical data).

The selected data were:

a) lithological units;

b) major and minor regional structures

c) mineralisation type; and

d) local intrusions.

### 5.7.3 The GIS approach

The GIS strategy was:

a) to define lithological units in the CMB which contain mafic volcanics and chemical sediments, especially BIF. This will be achieved by using the existing geological information and the interpretation of magnetic data;

b) by using magnetic and remotely sensed data to carry out a structural interpretation to mark fold axes, shear zones, faults and fractures;

c) the mineralisation type will lead us to define the element association that can be found in close relationship with gold;

d) the radiometric data will be used to map local granitoid intrusions.

The chosen GIS functions were:

a) Boolean operations to select specific areas, lines or point data;

b) proximity analysis to increase the area of influence of a particular feature;

c) neighbourhood operations to enhance subtle features and to overlay relevant information;

d) region operations to extract statistical parameters and to perform mathematical operations.

| LOCATION | MAJOR LITHOLOGY | ORE HOST LITHOLOGY | MAJOR REGIONAL STRUCTURE | LOCAL STRUCTURE | MINERALIZATION TYPE | LOCAL INTRUSIONS |
|---|---|---|---|---|---|---|
| Water Tank and Morning Star (AUS) GROVES et al ,1984 | Ultramafic to mafic flows and tuffs with interbedded BIF | BIF and minor altered and schistose basalt | Asymetric folding | Cross-faulting | Fine sulphide impregnation and dissemination in veins | Albite porphyry dykes |
| Mt. Charlotte (AUS) GROVES et al, 1984 | Tholeiitic mafic flows and a thick mafic sill overlain by black shales | Dolerite sill and underlaying mafic flows | Tight isoclinal fold. Several major strike faults modify fold structures | Tight isocline offset by stratigraphy discordant faults | Disseminated fine sulphides | Sodic porphyries |
| Hunt Mine (AUS) PHILLIPS and GROVES, 1984 | Tholeiitic mafic and ultramafic flows and massive Fe-Ni-Cu | Carbonatised mafic schists | NNW Trending faults | Fault zone subparallel to the major trending | Disseminated parallel to foliation | Felsic porphyry dykes |
| Passagem de Mariana (BRA) BOYLE, 1979 | Schists, phyllites, coarse clastic sediment | BIF | Anticlinorium | Drag folds and discordant shear and fractures zones | Massive sulphides | Granites |

| | | | | | | |
|---|---|---|---|---|---|---|
| Red Lake (CAN) ANDREWS, 1983 | Ultramafic and mafic flows and differentiated sills intercalated with epiclastic sediments | BIF and basalts | Intense zones of shear and mylonitisation | Highly altered sheared and folded zones | Vein systems parallel to oblique to foliation | Granitoids |
| Consolidated Mosher Mines (CAN) HODGSON and MACGEEHAN, 1982 | Greywackes, siltstones with BIF intercalated | BIF, feldspar porphyry and minor wacke | Distral strike slip reverse fault | Isoclinal S-drag folds, minor shearing sub-parallel to sediment contacts | Disseminated in sulphidic siliceous sheared tuff | Granitoids |
| Golden Giant (CAN) MACDONALD, 1983 | Epiclastic and volcaniclastic sediments with minor mafic flows | Sheared and mylonitised felsic tuffs | Regional synclinal folding | Concordante sheared zone on limb of steeply dipping homocline | Disseminated with pyrite | Quartz-feldspar porphyry dykes |
| Yellowknife (CAN) BOYLE, 1979 | Pillowed to massive basaltic flows | Variably calcsilicate sericitic schists | Subparallel reverse faults | Intersecting brecciated to schistose shear zones | Complex quartz lenses en echelon and sub-parallel to foliation | Granitoids |

| | | | | | | |
|---|---|---|---|---|---|---|
| Lupin (CAN) KERSWILL, 1983 | Argillite and greywacke with BIF intercalated | BIF | Offset syncline | Steeply plunging isoclinal drag folds near axes of major fold | Disseminated in bands parallel to foliation | None |
| San Antonio (CAN) HODGSON and MACGEEHAN, 1982 | Tuffaceous, feldspathic and lithic sediments with minor basalts | Diabase (gabbro) sill | Superimposed anticline/syncline | Fractures and shear zones sub-parallel to intrusive-sediment contact | Sheeted to stockworked quartz veinlets | Diabase, minor feldspar porphyry |
| Dupont Mine (CAN) SMITH et al. 1984 | Ultramafic to mafic basaltic with ultra-mafic sills covered by felsic to intermediate pyroclastic | Schistose mafic and ultramafic flows | Limb of tight steeply dipping anticline | Steep dipping reverse faulting | Concordant layers | Granodiorites |

| | | | | | | |
|---|---|---|---|---|---|---|
| Kolar Goldfield (IND) SINGH, 1980 | Mafic pillowed flows and sills, with coarse clastic sediments | Strongly sheared and foliated amphibolitised rocks | Limb of major synclinal | Superimposed dextral and sinistral drag folds and thrust faults | En echelon sheared sheared quartz veins, stringers and lenses | Granitoids |
| Prestes (GHA) KESSE, 1984 | Basaltic lavas and tuffs overlying by clastic sediments | Clastic sediments | Shear zones | Fractures related to emplacement of intrusions | En echelon quart-veins | Granites |
| Sheba (SOU) VILJOEN, 1984 | Ultramafic and mafic schists, clastic sediments, horfelses | Laminated stratiform chert zones | Refolded series of synclines | Tight isoclinal | Interlayered sulphide-rich bands | Granitoids |
| Homestake (USA) BOYLE, 1979 | Predominantly clastic sediments | BIF | Regional doming and faults | Isoclinal folds and faults | Pencil-like replacement | Porphyries |

| | | | | | | |
|---|---|---|---|---|---|---|
| Kilo (ZIM) LAVREAU, 1984 | Foliated and heavily schistose amphibolites overlying by phyllites to schistose rocks | BIF and graphitic schists | Large scale thrust faults | Young rift faulting and fracturing | Massive quartz pods | Granitic to tonalitic batholiths |
| Vubachickwe (ZIM) SAAGER et al, 1987 | Mafic and felsic flows and tuffs, intercalated with lesser ultramafic flows | BIF | Refolded synform | Homocline | Interlayers and lenticular planar masses | Dolerite sills and quartz-feldspar porphyroids |

**Table 5.8**: *Worldwide comparison of characteristics of some Archaean gold deposits. AUS=Australia, BRA=Brazil, CAN=Canada, GHA=Ghana, IND=India, SOU=South Africa, USA=United States, ZAI=Zaire and ZIM=Zimbabwe (modified from Siems, 1984)*

# CHAPTER 6: THEMATIC MAPPER AND RADAR DATA

## 6.1 Introduction

The most important objective of remote sensing is to extract environmental and natural resources data related to the Earth. The methods for collecting remotely sensed data, their transmission to ground receiving stations, initial processing and distribution are discussed in great details in various papers and books of which the text-books of *Sabins* (1978), *Lillesand* and *Kiefer* (1979), *Siegal* and *Gillespie* (1980) and *Drury* (1987) are outstanding. This discussion will not be covered in any more detail here.

The 8.5 million $km^2$ of Brazil is completely covered by Landsat 5, TM data, Landsat 1-3 (Multispectral Scanner and Return Beam Vidicon - RBV), and side looking airborne radar (SLAR) imagery. The former programme is coordinated by the Brazilian Space Research Institute (INPE) and the latter was coordinated by Radambrasil Project of the Ministry of Mines and Energy. In 1981, 500,000 $km^2$ were imaged by the Shuttle Imaging radar (SIR-A).

Intense use of remote sensing imagery has resulted in Brazil being entirely mapped at 1:1,000,000 scale, and more detailed geological mapping programmes are being conducted either for the most developed portions of the country or areas with specific geological interest.

This study uses only RADAM-radar and Landsat 5 Thematic Mapper (TM). RADAM-radar data are photomosaics, these photographic images were digitized using a drum scanner at Joyce-Loebl. TM images were acquired as digital records on computer compatible tape (CCT) corrected for the geometric distortion of Earth rotation.

In the study area, climate, soil, vegetation and rock weathering play an important role in geological remote sensing. Rock exposure is generally less than 15% of the total area, drainage systems are usually shadowed by vegetation.

This chapter presents the pre-processing and processing analysis undertaken on the imagery data and the results obtained with respect to structural analysis and lithological discrimination.

## 6.2 Geometric correction of TM and radar

Since Landsat imagery uses Space Oblique Mercator (SOM) or Hotine Oblique Mercator (HOM) coordinates, and the geological, geochemical and geophysical data have UTM coordinates, geometric correction of TM and radar imagery had to be done. To reduce data volume and make conversion from pixel coordinates to UTM coordinates simpler, a resampled pixel size of 50 m was selected.

To apply geometric correction to TM, control points were identified in both the image and 1:50,000 topographical maps

of the area. These points represented road intersection and/or streams junctions. The distribution of these points includes points near the corners and at the centre of the image to achieve a good precision in the transformation. Ten points were selected and UTM coordinates for each point were extracted from the topographical map by using a high precision ALTEK digitising tablet. Table 6.1 shows the location of the points and errors obtained in the fit at each control point.

| POINT | PIXEL | LINE | EASTING MAP | EASTING IMAGE | NORTHING MAP | NORTHING IMAGE |
|---|---|---|---|---|---|---|
| 1 | 2050 | 422 | 313100 | 313039 | 8470600 | 8470674 |
| 2 | 1233 | 1541 | 281200 | 281491 | 8440800 | 8440765 |
| 3 | 1230 | 2935 | 272300 | 272561 | 8399400 | 8399302 |
| 4 | 1990 | 1369 | 305100 | 305238 | 8442700 | 8442747 |
| 5 | 844 | 972 | 273600 | 273456 | 8459300 | 8459209 |
| 6 | 2875 | 2205 | 326600 | 326424 | 8414200 | 8414209 |
| 7 | 1934 | 2510 | 296500 | 296327 | 8409000 | 8409032 |
| 8 | 186 | 1655 | 249600 | 249431 | 8441700 | 8441709 |
| 9 | 658 | 1830 | 262600 | 262449 | 8434400 | 8434547 |
| 10 | 1433 | 752 | 292300 | 292480 | 8463600 | 8463411 |

Standard error of pixel estimate = 165.10
Standard error of the line estimate = 78.51

**Table 6.1**: *Position and errors in the fit of control points. (SOM to UTM)*

Resampling is necessary whenever a geometrical operation such as warping, rotation or enlargement is performed on digital images. This is because the DNs have to be estimated at locations where no measurements have been made. Three resampling algorithms are commonly used: nearest neighbour, bilinear interpolation and cubic convolution.

The nearest neighbourhood algorithm takes the value of the closest input pixel to the corresponding one in the

transformed output array is accepted as equal to the new one. Bilinear interpolation is just the two dimensional equivalent of linear interpolation. The DN in the output image is found by interpolating among the four pixels surrounding resampling site in the input image.

Cubic convolution calculates the average DN value for the 16 input pixels grouped around any new pixel after warping. This procedure produces a less blocky image with fewer edge abnormalities than the faster nearest neighbour method (*Drury*, 1987). In this study cubic convolution resampling was used.

A radar mosaic is an uncontrolled lay down of image strips that registers only approximately with UTM. So registration to the resampled TM images is essential. Common tie points such as river juncyions, were selected on both radar and TM images (Table 6.2) and the radar was registered to the geocoded TM image using the resulting polynomial transform and nearest neighbour resampling. The very different responses between the two imaging systems makes selection of tie points very difficult.

| POINT | PIXEL RADAR | LINE RADAR | PIXEL TM | NEW PIXEL RADAR | LINE TM | NEW LINE RADAR |
|---|---|---|---|---|---|---|
| 1 | 4359 | 332 | 1031 | 1030 | 1025 | 1024 |
| 2 | 5164 | 365 | 1414 | 1414 | 1036 | 1035 |
| 3 | 3974 | 1372 | 831 | 830 | 1556 | 1555 |
| 4 | 5449 | 1694 | 1533 | 1533 | 1679 | 1679 |
| 5 | 5362 | 1042 | 1531 | 1531 | 1379 | 1378 |
| 6 | 4023 | 1992 | 861 | 861 | 1871 | 1872 |

Standard error of pixel estimate = 0.30
Standard error of line estimate = 0.60

**Table 6.2**: *Position and errors in the fit of control points (radar to TM).*

## 6.3 Preprocessing Landsat TM data

In this study pre-processing techniques applied to the imagery include correction of atmospheric effects and contrast stretching. TM imagery data used in this study have not a cloud-free status but for our purposes it is acceptable. TM band 6 (10.4μm - 11.7μm) was not used in this work mostly because a historical data set were not available. TM data were provided with no special processing, apart those normally applied at the ground receiving station at Cuiaba, Brazil.

The atmosphere affects TM images by absorbing, scattering, and reflecting light. The atmosphere contains $O_2$, N, significant amounts of water vapour, ozone ($O_3$) and $CO_2$. All of these interact with electromagnetic radiation by vibrational and rotational transitions, the net effect being absorption of energy in a particular wavelength. Where electromagnetic radiation interacts with particles smaller than its wavelength, such as molecules of $O_2$ and N, it results in diffusion of radiation by matter (commonly called scattering), affecting short wavelengths (blue and ultraviolet radiation). When atmospheric particles are similar in size to the wavelength of the incoming radiation, such as giant molecules of water or fine dust, this affects wavelengths longer than that of blue light (*Drury*, 1987).

Removal of these atmospheric effects leads to more representative reflectance values and better quality images. This removal is accomplished in several ways, by using:

a) sophisticated techniques that rely on direct meteorological measurements fed into models for calculating the expected atmospheric spectroradiances under specific weather condition;

b) shadows derived either from cloud or mountains usually have low DN in band 4, and the lowest DN may be near or at zero. Shadow-related values above zero in other bands are assumed to be introduced solely from atmospheric radiance, and these are then subtracted from all other brightness values in the scene; c) graphical method which it is a common atmospheric correction based on the histograms of multispectral images containing deep water bodies or topographic shadows. Band 4 usually has some pixels with a zero, or nearly zero DN in water bodies or shadows. It is assumed that the displacement of the low end of the other histograms is due to scattering component. The displacement of each band is subtracted from all pixels in the image.

A dark pixel subtraction was chosen for atmospheric correction. The offset of TM bands 1, 2, 3, 4 and 5 due to atmospheric scattering was calculated as a function of TM7. Table 6.3 shows the offset in DN values for each TM band. The correction was done by subtracting the respective offset from each pixel in the scene. Although this method is only an approximation of a true atmospheric correction (*Schowengert*, 1983), it was considered to be effective for the purposes of this study

| TM BAND | OFFSET(DN) |
|---|---|
| 1 | 50 |
| 2 | 22 |
| 3 | 15 |

| TM BAND | OFFSET(DN) |
|---|---|
| 4 | 8 |
| 5 | 2 |
| 7 | 0 |

**Table 6.3:** *DN values subtracted from each TM band of the study area, for correcting atmospheric effects*

TM images possess radiometric resolution of 8 bits. This means that there are 256 possible grey levels ranging from 0 (black) to 255 (saturation). In the majority of images the full dynamic range is not completely used; consequently they have poor contrast. Contrast of one image is the measure of the spread or range of intensity levels which occur within it. In order to understanding the contrast of one image two features must be considered, the intensity distribution and histogram. Intensity distribution is the distribution of the grey level of the image, and the histogram shows the shape of this distribution.

Contrast stretching is the transformation of the images to achieve a better range of tones between black and white. This process involves the transformation of the DN of all pixels of an image according to some rule. The computer achieves the replacement of the input DN by output DN using a transfer function or look-up table (LUT) and can be expressed as a graph of input DN against output DN.

Contrast stretching can be done using diverse algorithms such as linear, logarithm, exponential, histogram equalization and Gaussian normalization and other more sophisticated methods. Linear stretching may be of two types: gain/bias modification and mean/standard deviation adjustment (*Nirblack*, 1986). The first type sets the DN values in a range to a minimum and maximum, with a control over the overall brightness given by an additive or subtractive constant. In the second type the mean and standard deviation (sd) are specified by the user, and the image is linearly transformed accordingly by setting 3 sds either side of the mean (128) to 0 + 255. Linear stretching produces a histogram which is similar in shape to

that of the original, but has a different mean value and spread. Logarithmic stretching enhances dark areas preferentially. Exponential enhancing produces a better distribution of DN in brighter areas. Histogram equalization spread out the peaks in the histogram, but leaves the flatter parts alone as they are already of the required shape. The Gaussian normalization produces a mathematically specified histogram having a normal distribution.

A linear contrast stretching of the TM images of the study area was performed, as all other tried methods had little advantage. Table 6.4 presents the DN transformation in the rescaled data.

| TM BAND | ORIG. DN | RESCALED | ORIG. DN | RESCALED |
|---|---|---|---|---|
| 1 | 50 | 0 | 95 | 255 |
| 2 | 15 | 0 | 60 | 255 |
| 3 | 15 | 0 | 78 | 255 |
| 4 | 15 | 0 | 80 | 255 |
| 5 | 15 | 0 | 210 | 255 |
| 7 | 5 | 0 | 250 | 255 |

**Table 6.4:** *Rescaled TM data to the full 0 to 255 grey level range by linear contrast stretching*

## 6.4 Preprocessing radar data

Radar senses primarily roughness or geometric characteristics of the surface, which are generally important for geologic mapping. Radar, however, also senses the dielectric properties of the surface, which are highly dependent on soil moisture. However, it is very difficult to separate dielectric properties from roughness and topographic effects. A large

number of terrain features can interact in radar imagery in creating a very complex response.

Soil type differences should not be detectable in radar data, if only the dielectric constants of the dry soils are considered. Man-made objects on the surface are the subject of many geography or land use mapping efforts, but in the interpretation for geological investigation the same objects add confusion. These objects appear in radar imagery as bright areas which when numerous can cause acute problems. Response from slopes can be enhanced or degraded according to the moisture in the slopes facing the radar (*Blanchard*, 1979).

Radar data does not suffer effects of the atmosphere, thus it is not necessary to apply atmospheric correction. However, the digitized radar images suffered from oversaturation introducing during scanning. This meant that many pixels were set at 255. Although this cannot be overcome, a careful contrast stretching can reduce this bias. The inherent high contrast of radar means that most edges are well displayed. The DN transformation in the rescaled data is presented as follows: 20 original DN rescaled to 0 and 200 original DN rescaled to 255.

In the study area, radar imagery was used for structural interpretation and ancillary data combined with geophysical data (radiometric imagery) for improving lithological discrimination.

## 6.5 Processing TM data

For geological applications image processing methods aim at improving the spectral contrast allowing lithological discrimination and enhancing textural features for structural

interpretation. Using RGB colour displays means that a maximum of only three bands can be combined at the same time.

Several digital image processing techniques, aimed at lithological discrimination and structural analysis were applied to the TM data. These included generation of three-band false colour composites, principal component analysis, decorrelation stretching, band ratioing, and edge enhancement detection of single bands.

### 6.5.1 False colour composite

Pseudo colour images or false colour composites (FCC) are the most effective way of displaying raster data, because visual perception in grey tone is limited (about 20 or 30 grey levels) but, the eyes can easily distinguish hundreds of thousands of different colours. This is particularly important for geological interpretations. Even when rocks or soils are ocluded by vegetation, its health condition is balanced by the minerals present in the rock or soil, and geological interpretation is often still possible.

I shall consider here two types of colour images, one generated by using false colour composite (FCC) and the other derived from density slicing techniques.

FCCs are based on Young's additive primary colours model. The principle is that given three suitably chosen primary colours (red, green and blue), it is possible to produce the full spectrum of colour by mixing the primaries in appropriate proportions. This theory works because the eyes perceive colours simplistically by performing the reverse of this process: an incoming natural colour stimulates three types of colour-sensitive cells in the eyes to varying degrees, and the

brain perceives the colour in terms of the three stimulus values.

The standard FCC using MSS images is obtained by assigning band 4 to blue, band 5 to green and band 7 to red. The origin of this traditional recipe can be traced to the second World War when the false colour infrared film (Ektachrome 2236) was developed to detect camouflage against a vegetation background. For TM data, using bands 2, 3, and 4 as blue, green and red simulates the MSS system. The standard FCC has severe limitations, especially when the data contain more than three channels. Another disadvantage is that the shorter wavelength bands suffer much more from atmospheric scattering, and often have low contrast. FCC can be used for multiband combinations such as ratios and groups of multiplicatively combined data such as radar versus radiometrics (Chapter 7).

Density slicing is one simplification of the data. Analysing the histogram of the input images it is possible to classify different ranges of DN in the overall histogram into categories or group of categories. These ranges can be highlighted by assigning a colour to each pixel whose DN falls within the range as the appropriate colour. This technique is often used to simplify a scene to assess gross variations or to express continuous variation in a single type of surface. By using different LUTs for RGB, a single 0 to 255 range of data, normally expressed as a grey scale image, can be rendered in a range of 256 colours (*Drury* and *Walker*, 1986). This is particularly useful in analysis of geophysical data such as those for magnetic, radiometric and gravity properties.

The interpretation of a FCC is relatively easy because the colours produced relate to reflectance from the surface, following Young's additive theory of colours. The limitation of FCC is that only three bands can be displayed at a time. *Drury* and *Hunt* (1989) pointed out that a particular band combination is rarely adequate to display the full variance of lithologies in the scene and additional band combinations may be required for a full interpretation.

Interband spectral correlation produces redundancy, and this correlation is the major reason for the incomplete use of colour space in FCCs (*Rothery*, 1987).

There are 120 possible combinations using the six reflected TM bands. Definition of the best RGB combination quantitatively involves tedious statistical analysis (*Sheffield*, 1985) that does not necessarily produce images that are the best for qualitative interpretation (*Crosta* and *Moore*, 1989).

The selection of bands used in this study was based on an interactive approach on visual inspection of the TM bands, an understanding of the geology of the area, and the probable spectral constraints. The chosen target lithologies were: BIF, mafic-ultramafic rocks and granites. Spectral characteristics of vegetation and rocks were provided by *Hunt* and *Ashley* (1979), *Hunt* *et al* (1973,1974).

Between 0.35 and 1.3μm electronic transitions in iron-bearing minerals cause characteristic absorption features near 0.43, 0.65, 0.85 and 0.93μm. In the range from 1.3 to 2.5μm the characteristic minima are caused by vibrational transitions in a number of $OH^-$ minerals, (such as clays) sulphates and water-bearing minerals. TM band 5 covers a general reflectance high

for most minerals, while TM band 7 covers a range of narrow features centred on the clay, mica, chlorite and serpentine absorption around 2.2μm *Hunt et al* (1973,1974).

BIFs are best characterised by hematite features and those related to goethite, jarosite and limonite formed by oxidation of sulphide BIF facies.

Unaltered granites should not display any significant spectral features. However, the presence of altered feldspars can induce spectral features related to $Fe^{3+}$ oxides and hydroxylated minerals.

Both basic and ultrabasic rocks offer the potential of prominent spectral features because of the presence of abundant ferromagnesian minerals. Gabbros and norites show very strong ferrous iron bands near 0.9 and 1.85μm. Ultrabasic rocks show well-defined bands near 0.95μm. However, alteration results in variable iron staining in basaltic rocks and the formation of a range of $OH^-$ minerals, dominated by chlorites. The release of abundant, dark $Fe_3O_4$ (magnetite) during serpentinization tends to quench spectra of altered ultramafic rocks obscuring the otherwise distinctive serpentine absorption around 2.2μm *Hunt et al* (1973,1974).

TM band 4 was a obligatory choice for iron oxide and vegetation features. Granitic soils occupy an intermediate reflectance position in TM4 between maximum of vegetation and the minimum of iron oxide minerals. TM7 was selected for hydroxyl mineral features. The choice of the third band was made by experimentation, TM1 proving the most useful. The results revealed that combination of TM4, TM7 and TM1, as RGB was the most suitable.

Figure 6.1 presents TM4, TM7 and TM1 as RGB after linear contrast stretching for a subset of the study area. Geological formations present in the area include granulitic sequence, migmatites and gneisses, volcanic-sedimentary rocks and young surficial deposits (see Figure 3.1). In the FCC image (Figure 6.1) the granulitic sequence is distinguished by its bright green colour in the eastern part of the image. The volcanic-sedimentary sequence is characterized by colour variations on the image. Quartzites of the Rio Gaviao Subunit show as red, the lake in the northeastern part of the study area, appears as vivid bluish, probably due to the water being very sediment rich. Meta-arenites of the Rio Gaviao Subunit and the Lower Unit are represented in the image as pale green interbanded with cyan. The hues and textural information from the linearly stretched colour composite image, did not define with accuracy any rock units except locating a few isolated outcrops. This is due to the dense agricultural vegetation cover, and the lack of exposure.

### 6.5.2 Principal component analysis and decorrelation stretching techniques

Principal component analysis (PCA) is probably one of the most potent methods available for analysis of multicorrelated data. Although PCA is an arithmetical operation, due to its importance and particularities, it will be discussed separately. The efficient separation of data in PCA is a great aid in improving the fidelity of digital classification. This can be improved still further by a deliberate attempt to arrange the new axes to maximise separation between the field of known classes (*Drury*, 1987).

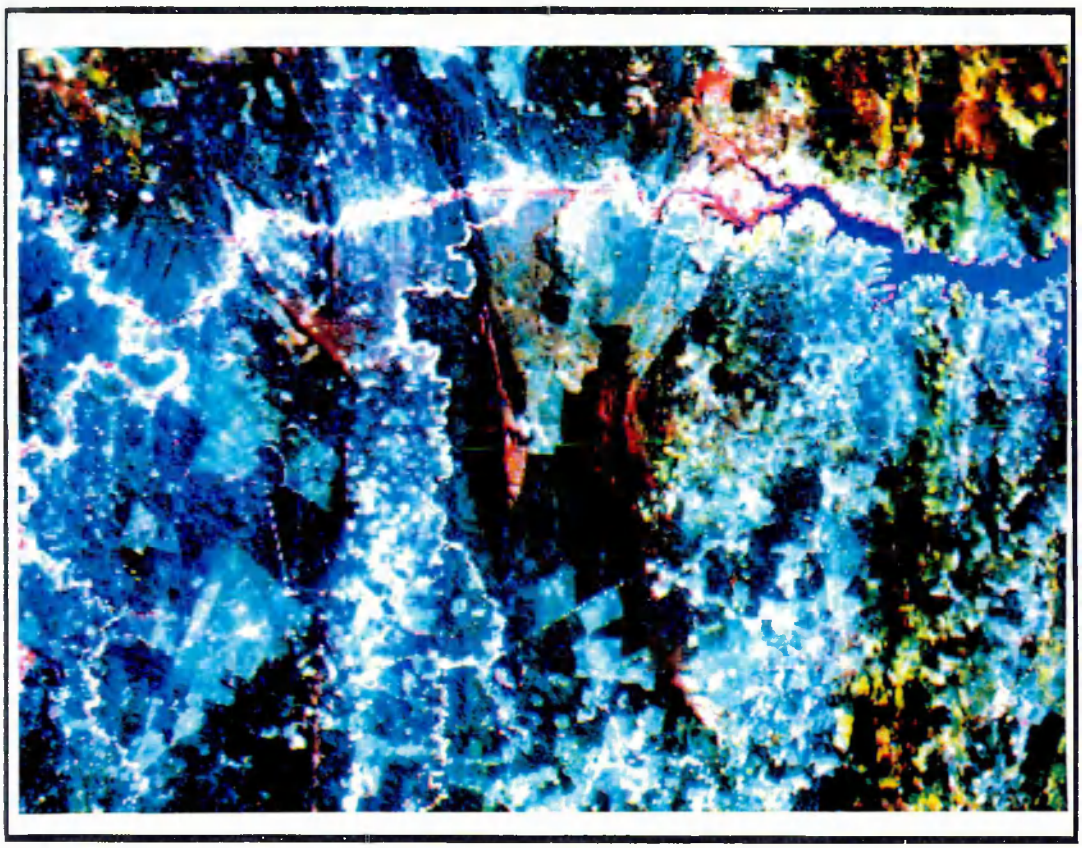

Figure 6.1: *FCC of TM4, TM7 and TM1, as RGB, respectively*

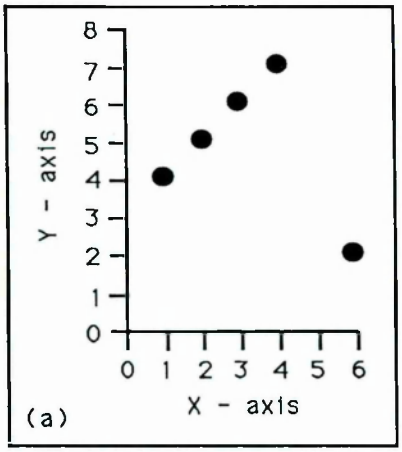


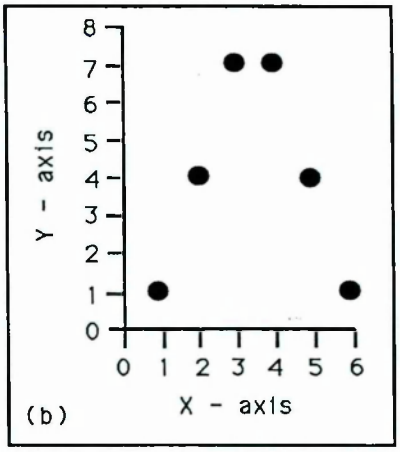


| X | Y | $\bar{X}$ | $\bar{Y}$ | $(X-\bar{X})$ | $(Y-\bar{Y})$ | $(X-\bar{X})(Y-\bar{Y})$ | |
|---|---|---|---|---|---|---|---|
| 1 | 4 | 3.5 | 5.3 | -2.5 | -1.3 | 3.25 | |
| 2 | 5 | | | -1.5 | -0.3 | 0.45 | (a) |
| 3 | 6 | | | -0.5 | 0.7 | -0.35 | |
| 4 | 7 | | | 0.5 | 1.7 | 0.85 | |
| 5 | 8 | | | 1.5 | 2.7 | 4.05 | |
| 6 | 2 | | | 2.5 | -3.3 | -8.25 | |
| Σ 21 | 32 | 3.5 | 5.3 | | | 0 | |

| $(X-\bar{X})^2$ | $(Y-\bar{Y})^2$ | $(X-\bar{X})^2 (Y-\bar{Y})^2$ | $[(X-\bar{X})^2 (\bar{Y}-\bar{Y})^2]^{1/2}$ |
|---|---|---|---|
| 6.25 | 1.69 | 10.56 | 3.25 |
| 2.25 | 0.09 | 0.20 | 0.45 |
| 0.25 | -0.49 | 0.12 | 0.35 |
| 0.25 | 2.89 | 0.72 | 0.85 |
| 2.25 | 7.29 | 16.40 | 4.05 |
| Σ 6.25 | 10.89 | 68.06 | 8.25 |
| | | | 17.20 |

with $X_6$ , $Y_6$ : $r=0$

without $X_6, Y_6$: $r=+1$

$$r = \frac{\sum (X-\bar{X})(Y-\bar{Y})}{\sum [(X-\bar{X})^2 (Y-\bar{Y})^2]^{1/2}}$$

| X | Y | $\bar{X}$ | $\bar{Y}$ | $(X-\bar{X})$ | $(Y-\bar{Y})$ | $(X-\bar{X})(Y-\bar{Y})$ | |
|---|---|---|---|---|---|---|---|
| 1 | 1 | 3.5 | 4 | -2.5 | -3 | 7.5 | (b) |
| 2 | 4 | | | -1.5 | 0 | 0 | |
| 3 | 7 | | | -0.5 | 3 | -1.5 | |
| 4 | 7 | | | -0.5 | 3 | 1.5 | |
| 5 | 4 | | | 1.5 | 0 | 0 | |
| 6 | 1 | | | 2.5 | -3 | -7.5 | |
| Σ 21 | 24 | | | | | 0 | |

| $(X-\bar{Y})^2$ | $(Y-\bar{Y})^2$ | $(X-\bar{X})^2 (Y-\bar{Y})^2$ | $[X-\bar{X})^2 (Y-\bar{T})^2]^{1/2}$ |
|---|---|---|---|
| 6.25 | 9 | 56.25 | 7.5 |
| 2.25 | 0 | 0 | 0 |
| 0.25 | 9 | 2.25 | 1.5 |
| 0.25 | 9 | 2.25 | 1.5 |
| 2.25 | 0 | 0 | 0 |
| 6.25 | 9 | 56.25 | 7.5 |
| Σ | | | 18 |

$r = 0$

**Figure 6.2:** *Two examples where the correlation index is 0 although the curves show some correlation*

or perform a principal component analysis, *Canas* and *Barnett* (1985) summed up the following mathematical operations:

a) calculate the variance-covariance matrix for the image data;

b) compute the eigenvalues and eigenvectors of the variance-covariance matrix. The eigenvectors define the principal component (PC) directions and the eigenvalues measure the variances of the feature space distribution along the new PC axes;

c) implement the PCA by forming a weighted sum of the raw images using the eigenvectors components as the weighting factors (these are the "direction cosines" of the PC axis).

To apply this technique, an area was selected having the minimum possible contribution of vegetation and water reflectance from which the covariance matrix was derived. Strictly speaking, this is not PCA but canonical analysis. Table 6.5 shows the PCA statistical parameters obtained in this test area.

| | EIGENVECTORS | | | | | | | | | | | |
|---|---|---|---|---|---|---|---|---|---|---|---|---|
| | TM1 | TM2 | TM3 | TM4 | TM5 | TM7 | %TM1 | %TM2 | %TM3 | %TM4 | %TM5 | %TM7 |
| PC1 | .43 | .39 | .45 | .34 | .40 | .44 | 19 | 18 | 20 | 16 | 17 | 19 |
| PC2 | .54 | .50 | .07 | -.32 | -.35 | -.47 | 24 | 23 | 3 | -15 | -15 | -20 |
| PC3 | .35 | -.08 | -.55 | -.46 | .59 | .11 | 16 | -4 | -25 | -22 | 25 | 5 |
| PC4 | .10 | .10 | -.44 | .72 | .19 | -.48 | 4 | 4 | -20 | 34 | 8 | -21 |
| PC5 | -.58 | .48 | .19 | -.22 | .49 | -.33 | -26 | 22 | 9 | -10 | 21 | -14 |
| PC6 | .24 | -.59 | .51 | -.04 | .31 | -.49 | 11 | -28 | 23 | -2 | 13 | -21 |

**Table 6.5**: *Statistical parameters for PCA on TM bands*

The PCA on TM data produced the percentage of total variance contributed by each eigenvalue as follows: 77%, 13%, 5%, 2%,

1.8% and 1% in PC1, PC2, PC3, PC4, PC5 and PC6, respectively. 95% of variance is represented by the sum of PC1, PC2 and PC3, and albedo and most of the spectral information are concentrated in them. By looking into the percentages presented in Table 6.5, PC1 incorporates positive mixtures of all TM bands with well balanced contribution from all bands. PC2 contains dominant contribution from TM1, TM2 and TM7. PC3 has a prevailing contribution of TM3, TM4 and TM5, where TM5 is high, TM4 and TM3 is low or vice-versa. PC4 incorporates a great contribution of TM3, TM4 and TM7, where TM4 is high TM3 and TM7 is low and vice-versa. PC5 and PC6 together representing very low percentage (less than 1%) of the total variance contributed for each eigenvalues, will not be considered here.

In general, applications of PCA to lithological mapping imply two methods: a)combining PC1 with PC2, PC3 or PC4 (*Trefois*, 1988), (b)using only three "spectral" PCs with little noise such as PC2, PC3 and PC4 (*Kaufman*, 1989). Neither of these methods avoids the major problem in the use of PCA: the colours generated by a FCC have no simple relationships to spectral features in the original bands. This is due to the fact that each component is a complex weighted additive combination of all bands.

An attempt to overcome these problems was suggested by *Crosta* (1990) using the spectral contrast images produced by PCA of band-pairs and producing a FCC using the second PCs which are much easier to interpret visually than standard PC colour composites, because only two images are involved in defining the amount of each primary colour.

A technique called decorrelation stretching developed by *Soha* and *Schwartz* (1978) allows colour information in a three band colour composite to be accentuated after PCA. Decorrelation stretching is based on a PCA of the three bands. Instead of combining the three new components obtained after PCA, each PC is firstly contrast enhanced, and then all three are inversely transformed back to the original coordinate system for display.

The main advantage of this technique is that the colours in the image remain intuitively obvious and can readily be interpreted in terms of likely differences in spectral response of surface materials (*Rothery* and *Hunt*, 1990). Applications of this technique to geological remote sensing have produced good results (*Rothery*, 1987; *Drury* and *Hunt*, 1988).

Decorrelation stretched images were produced using the following procedure.

a) The eigenvector matrix A, which relates the original bands TM1, TM2, TM3, TM4, TM5 and TM7 to their principal components PC1, PC2, PC3, PC4, PC5 and PC6 is given by the following coefficients:

| | Bnd1(B1) | Bnd2(B2) | Bnd3(3) | Bnd4(B4) | Bnd5(B5) | Bnd7(B7) |
|---|---|---|---|---|---|---|
| PC1 | 0.43 | 0.39 | 0.45 | 0.34 | 0.40 | 0.44 |
| PC2 | 0.54 | 0.50 | 0.07 | -0.32 | -0.35 | -0.47 |
| A = PC3 | 0.35 | -0.08 | -0.55 | -0.46 | 0.59 | 0.11 |
| PC4 | 0.10 | 0.10 | -0.44 | 0.72 | 0.19 | -0.48 |
| PC5 | -0.58 | 0.48 | 0.19 | -0.22 | 0.49 | -0.33 |
| PC6 | 0.24 | -0.59 | 0.51 | -0.04 | 0.31 | -0.49 |

b)Using these coefficients, the relationship between the original TM bands and the principal components (PC) derived from these channels can be expressed thus:

PC1=0.43*TM+0.39*TM2+0.45*TM3+0.34*TM4+0.40*TM5+0.44*TM7

PC2=0.54*TM1+0.50*TM2+0.07*TM3-0.32*TM4-0.35*TM5-0.47*TM7

PC3=0.35*TM1-0.08*TM2-0.55*TM3-0.46*TM4+0.59*TM5+0.11*TM7

PC4=0.10*TM1+0.10*TM2-0.44*TM3+0.72*TM4+0.19*TM5-0.48*TM7

PC5=-0.58*TM1+0.48TM2+0.19*TM3-0.22TM4+0.49*TM5-0.33*TM7

PC6=0.24*TM1-0.59*TM2+0.51*TM3-0.04*TM4+0.31*TM5-0.49*TM7

c)After contrast stretching the PCs, it is necessary to apply the inverse transformation. This is achieved simply by inverting the eigenvector matrix A to $A^{-1}$, as shown below:

$A^{-1}$ =

| | PC1 | PC2 | PC3 | PC4 | PC5 | PC6 |
|---|---|---|---|---|---|---|
| B1 | 0.43 | 0.54 | 0.35 | 0.10 | -0.58 | 0.24 |
| B2 | 0.39 | 0.50 | -0.08 | 0.10 | 0.48 | -0.59 |
| B3 | 0.45 | 0.07 | -0.55 | -0.44 | 0.19 | 0.51 |
| B4 | 0.34 | -0.32 | -0.46 | 0.72 | -0.22 | -0.04 |
| B5 | 0.40 | -0.35 | 0.59 | 0.19 | 0.49 | 0.31 |
| B6 | 0.44 | -0.47 | 0.11 | -0.48 | -0.33 | -0.49 |

d)The final step is to multiply the $A^{-1}$ matrix by the principal components and arithmetically to combine them, as shown below:

DS1= 0.43*PC1+0.54*PC2+0.35*PC3+0.10*PC4-0.58*PC5+0.24*PC6

DS2= 0.39*PC1+0.50*PC2-0.08*PC3+0.10*PC4+0.48*PC5-0.59*PC6

DS3= 0.45*PC1+0.07*PC2-0.55*PC3-0.44*PC4+0.19*PC5+0.51*PC6

DS4= 0.34*PC1-0.32*PC2-0.46*PC3+0.72*PC4-0.22*PC5-0.04*PC6

DS5= 0.40*PC1-0.35*PC2+0.59*PC3+0.19*PC4+0.49*PC5+0.31*PC6

DS7= 0.44*PC1-0.47*PC2+0.11*PC3-0.48*PC4-0.33*PC5-0.49*PC6

A false colour composite using DS4, DS7 and DS1, as RGB, was created (Figure 6.3). The colours in this image have the same meaning as in the FCC of TM4, TM7 and TM1. However saturation and intensity have been greatly enhanced, and this result shows a better range of colours. More lithological units can be recognized in this image. In the western part, phyllites of the Rio Gaviao Subunit are dark blue and can be separated from meta-arenites (in purple) of the Areiao Subunit. The mafic-ultramafic Rio Jacare sill reveals discrete cyan hues. Vegetation is distinguished by its bright red colour. To the eastern side, the granulites present bright green colour. Although this image shows a more range of colours very little could be added to the existing geological maps in terms of lithological discrimination due to the constraints described in the section 6.5.1, in particular the swamping effect of vegetation rendered as red colour.

### 6.5.3 Band ratioing

Arithmetical operations are straight mathematical operations of addition, subtraction, multiplication, division or ratioing, exponentiation, taking logarithms and evaluating trigonometrical functions. They are very useful, quick to apply and easy to understand. One or more raster data sets can be used to perform these operations. Contrast stretching for instance is achieved using only one image according to pre-defined mathematical functions such as straight line, logarithmic or exponential look-up tables. All arithmetical operations have to be rescaled. In some cases the result

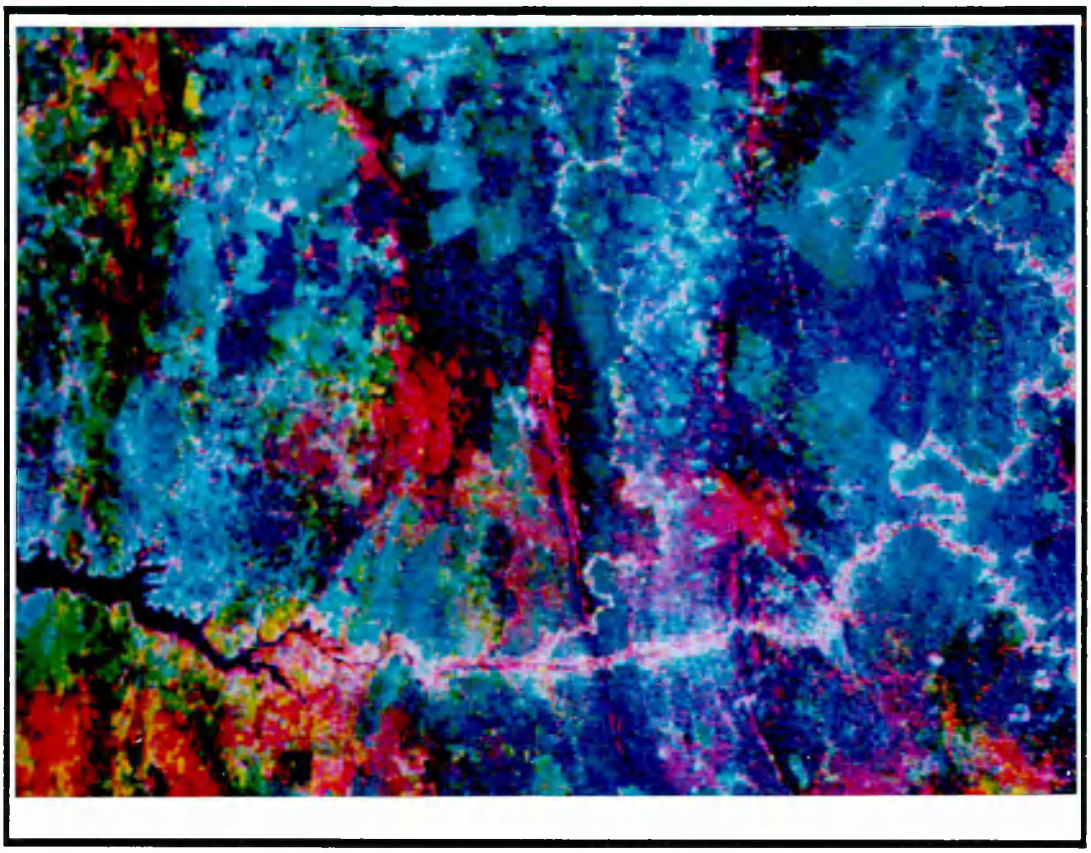

Figure 6.3: *FCC of DS4, DS7 and DS1, as RGB, respectively*

overflows the 0 to 255 range (addition and multiplication), or produces very small numbers (ratioing) or negative numbers (difference).

Division or ratioing is done simply by dividing the DN or spatial attributes of a pixel in one image by that in another image. Theoretically, in the case of DN this should produce a range of new values for the pixel from zero to infinity. Because of the restricted range in each band of the data and the strong correlation between bands, in practice ratios seldom fall outside the range 0.25-4.0. This narrow spread itself poses a problem. The ratio values must be rescaled to positive integers in the range 0 to 255 (*Drury*, 1987). Ratioing is usually applied because it can suppress information which is common in both images while simultaneously enhancing differences. Ratio values reflect the slope or gradient of lines, they are related to by a tangent function. Any pixel whose spectral intensities plot on one of these lines will be presented by the same intensity value in the final image, no matter what is its distance from the origin of the feature space along the line. This is the reason why ratio suppresses common information such as topographic shading and albedo. One of the most important limitations of ratios is that if two distinct cover types have similar spectral signatures but different albedo, then their corresponding clusters in feature space will lie along the same line of constant slope. The ratio value will be the same for different materials.

Ratioing has been used extensively in image processing analysis, mostly in areas with very little vegetation cover and has some advantages over FCC. Spectral information may be

ambiguous due to the broad bandwidths of the TM imagery, which results in averaging out of absorptions that may occur within each band. Single ratio images, each of which having enhanced the responses of the surface in a particular spectral region, may be compiled into a colour composite that contains information from up to six bands rather than just three.

There are two ways to perform ratioing. The first is a simple arithmetical operation which involves a division of one pixel from one image to the coregistred pixel in another image. The second is called a "pseudoratio" and it is applied to a very well correlated data. "Pseudoratio" technique was developed by *Hunt* (1988) and involves a principal component transformation of the two bands selected for the ratio. The highly correlated topographical and albedo information goes to the first principal component (PC) and the uncorrelated data, which approximates to the arithmetical ratio, goes to the second PC. In this study both methods were applied to the TM imagery. However, due to the similarity of the results, only the single arithmetical operation is presented here.

The substantial presence of vegetation in the study area is well defined by the usual vegetation index or ratio TM4/TM3. The strong characteristic chlorophyl absorption of green vegetation near 0.65μm (TM3) and the high infrared reflectance of living plants at 0.83 (TM4) gives this ratio a high value for vegetation (*Drury*, 1987). Alternative ratios for vegetation enhancement are TM4/TM1 and TM5/TM1, but iron oxides also show high values (*Crosta*, 1990).

Several TM ratios have been proposed for mapping iron staining, such as TM3/TM1, TM5/TM1, TM3/TM2, TM4/TM2, TM5/TM4, TM7/TM1 and TM7/TM4 (*Crosta*, 1990).

In the study area, a well known BIF occurrence was selected for test. TM bands 1, 7, 5, 4 and 3 were selected and the following ratios were applied: TM7/TM5, TM5/TM4 and TM3/TM1. However, the distinction of the BIF itself, is not very well marked mainly because the BIF represents thin slices hosted in metavolcanic rocks.

### 6.5.4 Edge enhancement

The appearance of lineaments on imagery is controlled by many factors. These include changes in spectral reflectance across lithological boundaries, shadowing effects caused by illumination of the irregular surface from a source and topographic patterns due to varying resistance to erosion.

An imaging system samples a continuous function at discrete intervals, the high-frequency information cannot be recorded at the same precision as the lower frequency data, thus the process results in some suppression of the high-frequency data including edges (*Chavez* and *Bauer*, 1982).

Lineament interpretation from the original images often yields partial results, mostly because some of these lineaments do not appear clearly. In order to highlight lineaments or detect high-spatial frequency data, several enhancement were undertaken.

Our eyes are extremely sensitive to edges, or sharp changes in brightness due either to tonal contrast changes or variations in solar irradiance due to topography. In a geological

context, edges and lines are possibly indicators of lithological boundaries and faults, respectively.

To enhance edges in an image, therefore improving its interpretability, a spatial filtering (SP) technique was developed. This technique is based on the creation of a shift-multiply-sum operation, as illustrated in Figures 6.4.and 6.5.

Filter masks (FM) always have odd numbers of columns and rows and one centred pixel. Output images are obtained by overlaying FM and moving it over every pixel on the image The DN of each pixel overlain by the FM is multiplied by the corresponding weighting factor, and the product are summed.

High pass (edge enhancement) filters normally enhance features which are less than half the dimensions of the convolution matrix used (*Chavez*, 1987). Edge enhancement can be performed in a variety of ways, but they are fundamentally area operations. The central concept is that you cannot detect the presence of an edge from the intensity value of any single pixel. An edge is an intensity derived from the differences between pixels.

The edge enhancement technique includes basically two methods which are mathematically closely related: spatial domain (convolution transformation) and frequency domain (Fourier transformation). Frequency domain filtering is the more powerful, but it is also the more expensive of computer time and involves highly complex mathematics. Most images-processing computers employ convolution filters (*Drury*, 1987).

I shall consider here two examples of edge enhancement, Sobel or directional filters and Laplacian operators (Figures 6.6 and 6.7).

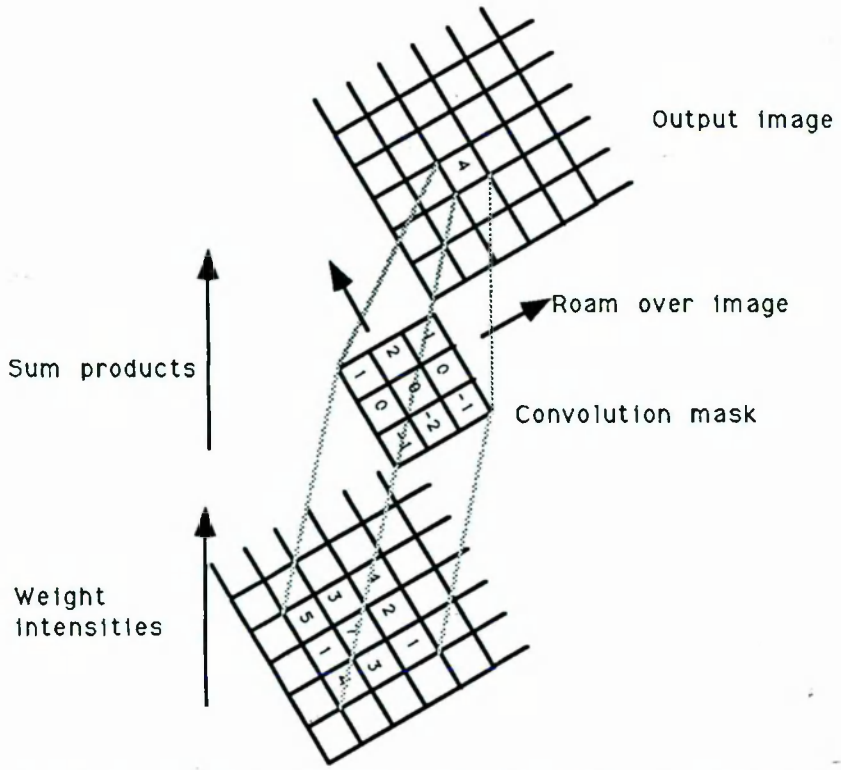


Figure 6.4: *9 original pixels contributing to one output pixel*

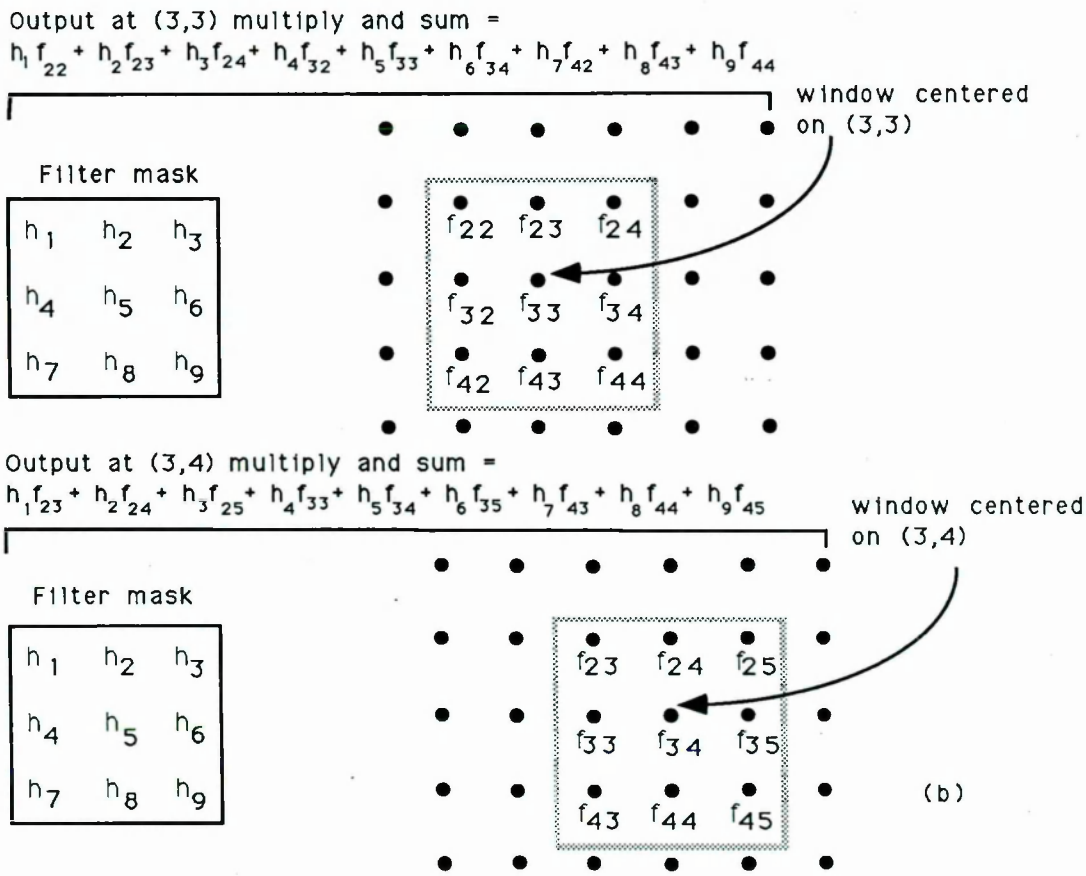


Figure 6.5: *The shift-multiply-sum operation*

The Sobel operator (Figure 6.7) is a gradient operator which, when applied to a continuous function, produces a vector at each point whose direction gives the direction of maximum change of the function at that point, and whose magnitude gives the magnitude of this maximum change (*Nirblack*, 1986).

The Laplacian filter (Figure 6.7) which in one dimension reduces to a second derivative, is also computed by convolving a mask with the image. The second differential will also identify the maximum gradients because it will pass trough zero at the peak or through of the first differential.

The image selected to enhance was the first PC, (Figure 6.8) because it is largely free of system noise and provides an excellent source for structural interpretation because it contains the bulk of data variance (*Drury*, 1984).

For producing edge enhanced images, directional filters where the weightings are asymmetric about an axis through the box, were applied. To perform a complete directional analysis, all eight principal compass directions should be considered. For our purposes, only four directions (northwest, north, northeast and east) are considered here. Effectively they enhance all possible orientations of edge.

Different kernel sizes were tested, the optimum kernel size to enhance linear features related to small-scale planar fabrics being 9x9. Figures 6.9 and 6.10 show the results obtained from a northwestern 5x5 directional filter and a 9x9 northwestern directional filter applied on PC1, respectively. The 9x9 kernel size (Figure 6.10) shows lineaments which should correspond to geological features (faults and fractures), whereas the 5x5 kernel size (Figure 6.9) can enhance other

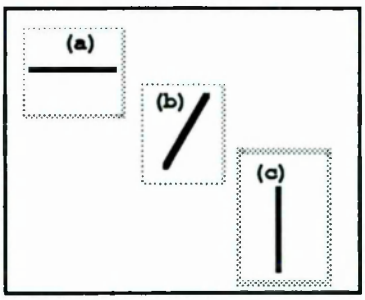


**Figure 6.6**: *Structural features*

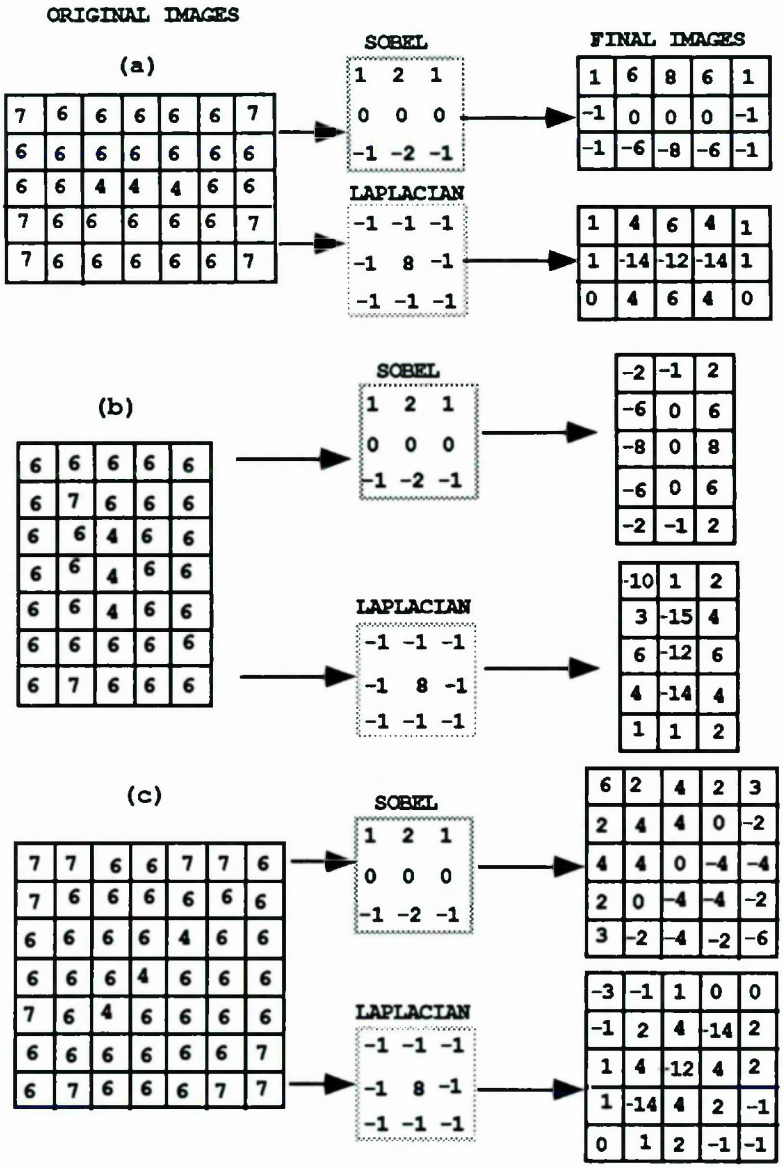


**Figure 6.7**:*Edge detection masks*

linear features such as roads, due to the spatial resolution of the image, therefore artificial artifacts can be created.

Figure 6.10 shows all edges lying NE-SW with their bright side facing NW enhanced. In the case of Figure 6.11, the edges were enhanced by a 9x9 north directional filter, and all edges lying E-W with their bright side facing northern appear enhanced. Figures 6.12 and 13 show the same area enhanced by a 9x9 northeast and east directional filter, respectively. In these cases, edges lying NW-SE and N-S were enhanced.

Figure 6.14 presents a comparison between the structural interpretation carried out on these enhanced images and the mapped lineaments from the available geological maps. Lineaments in blue represent those derived from the interpretation of enhanced TM imagery, and in red those derived from the existing geological maps. In this case, the edge enhancing techniques added around 20% to the number of known lineaments.

This interpretation will be compared with the results achieved from the structural analysis undertaken on enhanced radar data, in section 6.7.

## 6.6 Processing radar data

Radar data, having side viewing geometry and long wavelength, have proved to be extremely useful for Earth observation. Fractures traces are often well expressed in radar imagery, as has long been noted (*Sabins et al*, 1979). The facing and reverse slopes of even slight declivities are cast into relative highlight and shade by the oblique illumination of mapping radar. The linearity of these features catches the eye of the interpreter. It follows that radar imagery should lend

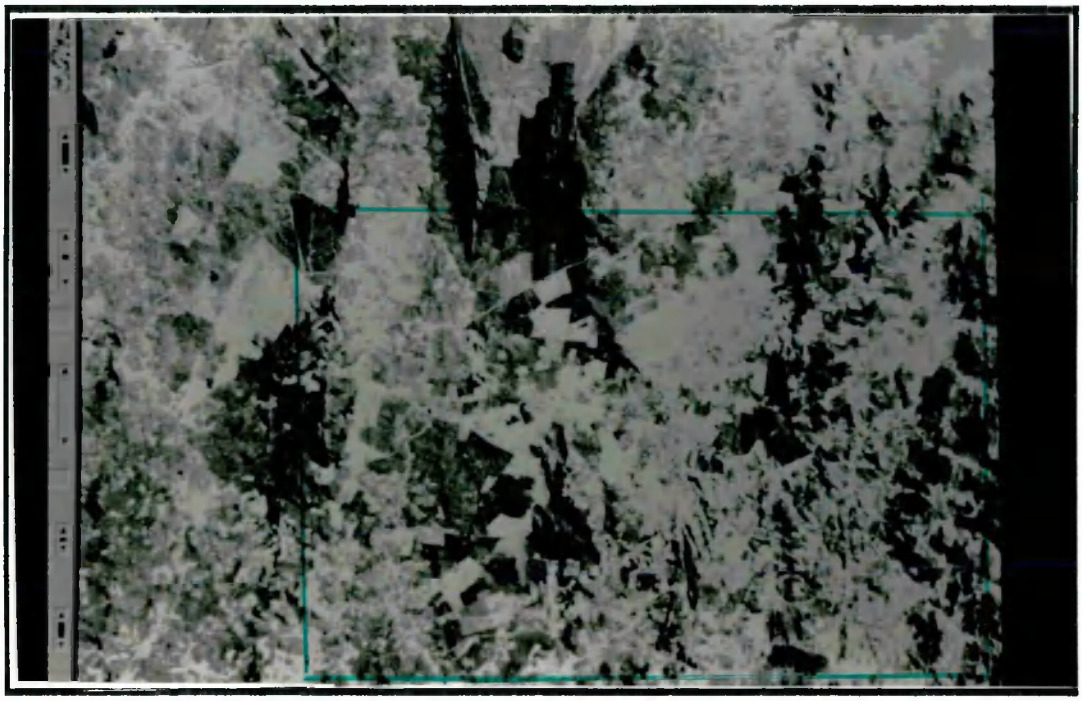

Figure 6.8: *First PC of TM bands for part of the study area*

Figure 6.9: *Pseudo illuminated image of PC1 implemented by a 5x5 northwest first derivative filter (The green square represents the area to be enhanced by 9x9 directional filters)*

Figure 6.10: *Pseudo illuminated image of PC1 implemented by a 9x9 northwest first derivative filter*

Figure 6.11: *Pseudo illuminated image of PC1 implemented by a 9x9 north first derivative filter*

Figure 6.12: *Pseudo illuminated image of PC1 implemented by a 9x9 northeast first derivative filter*

Figure 6.13: *Pseudo illuminated image of PC1 implemented by a 9x9 east first derivative filter*

itself to fracture traces studies and it is the case that numbers of these studies have been carried out for oil, mineral and water exploration and engineering geological purposes.(*Vincellete* and *Soeparjadi*, 1976; *Vincent* et al, 1979 *Sabins* et al, 1979).

Edge enhancement techniques aiding structural analysis were applied to radar data (Figure 6.15). Figures 6.16, 6.17 and 6.18 present the results of edge enhancement using a 9x9 kernel size in northern, northeastern and eastern directions, respectively. However, this technique ignores a lot of variation in the radar image which lies between linear features and is distributed in approximately homogeneous patches (*Drury*, 1987).

Lineaments suspected of being fractures (faults or joints) were interpreted from the enhanced radar imagery, and the resulting map was compared with those interpreted from Landsat TM data and existing geological maps. Only those lineaments identified from the radar in the southern part of the study area,but not found in Landsat TM data or previous geological maps, are plotted as Figure 6.19. It is important to note that these additional lineaments derived from radar data were located not just in cloud-covered areas in the Landsat TM data, but also in many cloud-free areas as well. As a guide for future remote sensing experiments, it should be noted that the radar data added around 15% to the number of lineaments either from Landsat TM data or previous geological maps.

## 6.7 Discussion of the results

Although various image processing techniques were applied to Landsat TM imagery, in terms of lithological discrimination,

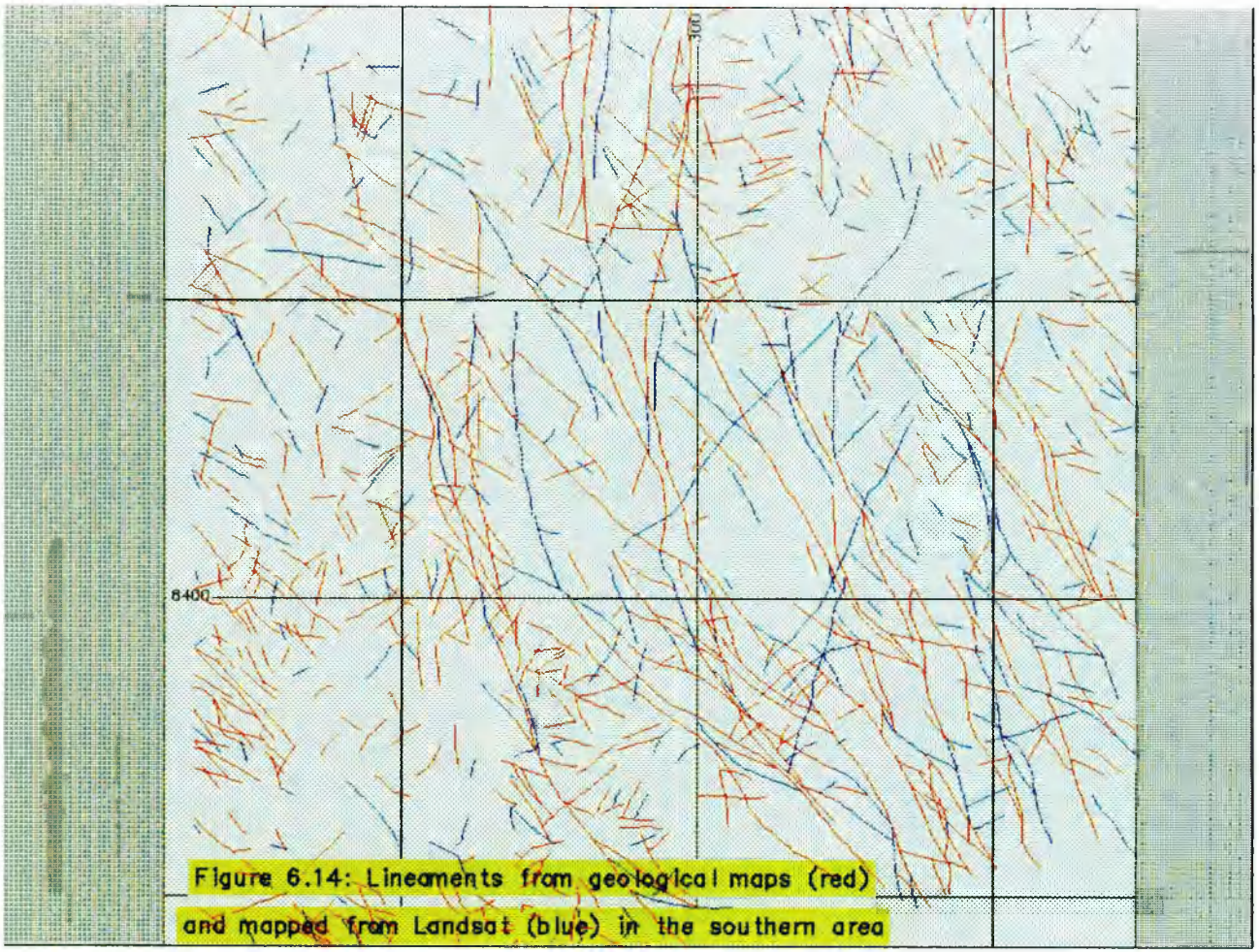


Figure 6.14: Lineaments from geological maps (red) and mapped from Landsat (blue) in the southern area

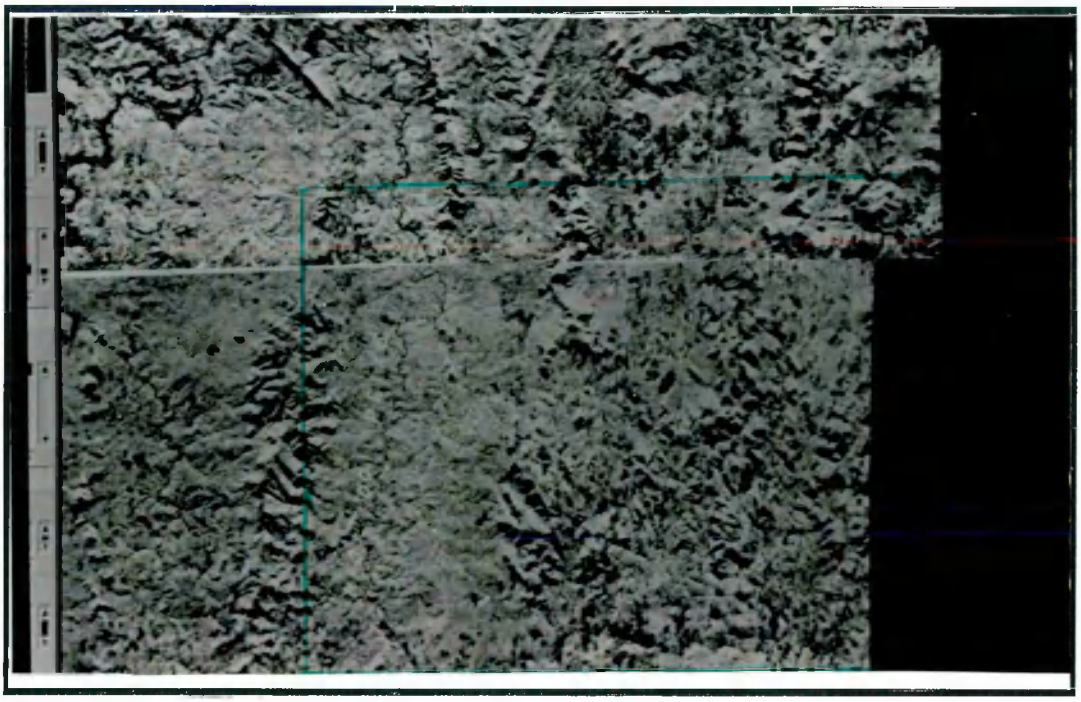

Figure 6.15: *Radar image of the study area. The green square corresponds to the TM images enhanced by a 9x9 first derivative filters*

Figure 6.16: *Pseudo illuminated image of radar implemented by a 9x9 northwest first derivative filter*

Figure 6.17: *Pseudo illuminated image of radar implemented by a 9x9 northeast first derivative filter*

Figure 6.18: *Pseudo illuminated image of radar implemented by a 9x9 north first derivative filter*

very little could be added to the existing geological maps. The main factors which have contributed to this are:

a) boundaries between major stratigraphic units in the greenstones are often gradational in the field,
b) the poor resolution of TM imagery,
c) the domination of vegetation cover, and the lack of outcrops.

On the other hand, remotely sensed data have proved to be important sources of information on structural basis, particularly fracture patterns. Structural analysis is important because faults are often the critical factor in localizing many hydrothermal ore deposits by guiding or trapping the fluids as they circulate. Confidence in detection of linear features in Landsat TM and radar images will necessarily remain low until some reasonable number of them are checked and verified in the field. The interpreted lineaments were checked by overlaying them on the mapped lineaments.

The results show that most lineaments mapped from the TM and radar data in fact correspond with previously mapped fractures. However, the interpretation of the TM and radar has improved the previous structural framework of the study area by adding some important lineaments and many smaller, less certain ones.

An integrated interpretation of radar and TM data is presented in Figure 6.20 which shows the main faults (in green) and the fracturing systems (in red) for southern part of the study area. The dominant trend of faults is roughly north-south, corresponds to high-angle reverse faults and possibly has been

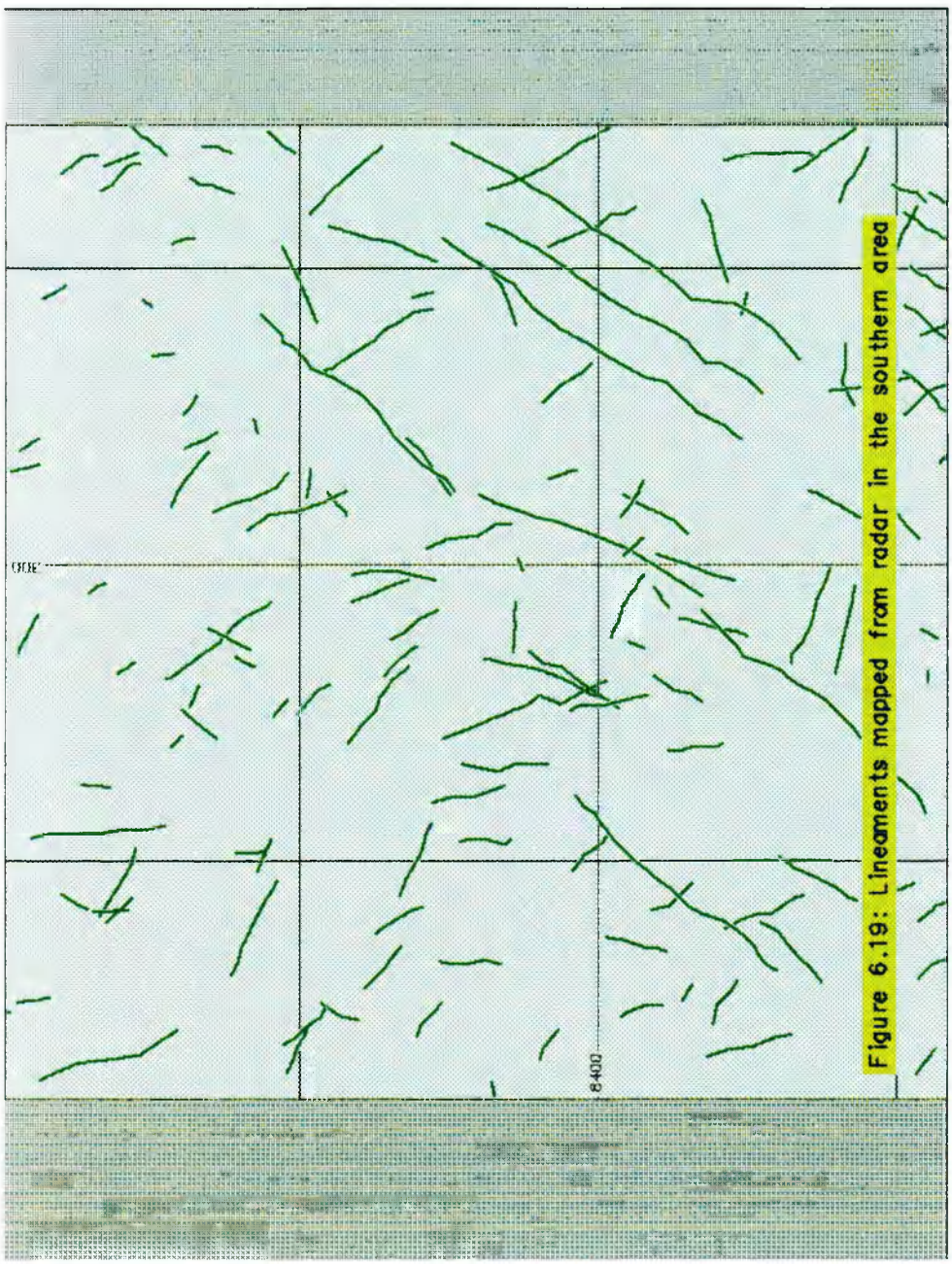


Figure 6.19: Lineaments mapped from radar in the southern area

developed during the later stages of the main deformation of the Contendas-Mirante belt.

Two other trends which dislocate the longitudinal faults can also be recognized: a northwest-southeast system widely distributed in the study area, very well marked by the presence of expressive quartz veins and having highest density in the southern area, and secondary lineament set trending northeast-southwest which in some places are orthogonal to the north-south foliation.

This interpretation will be integrated with other data sets in Chapter 9.

Figure 5.20: Lineaments mapped from Landsat and geological maps (red) and radar (green) in the southern area

# CHAPTER 7: MAGNETIC AND RADIOMETRIC DATA

## 7.1 Introduction

The magnetic field of the Earth is thought to be derived from a self-exciting dynamo in the fluid nickel-core (*Richards* and *Walraven*, 1975). Part of the variation in the field measured at or above the surface derives from minerals with a high magnetic susceptibility. It can be divided into ancient remanent magnetism and field induced by the present field.

Known magnetic substances lose their permanent magnetism when heated above the Curie temperature. For instance, for iron, nickel, magnetite and basalts these temperatures are 770°C, 360°C, 580°C and 550°C, respectively. In a normal geothermal gradient, these temperatures will be reached within the crust at depths of about 20 km.

Aeromagnetic surveys measure variations of the order of 1/4 of the Earth's main field. The System Internationale (SI) unit of magnetic intensity or field strength is called the tesla (T). The relationship between T and cgs units is 1 nanotesla (nT)

is equal to $10^{-5}$ oersted or 1γ. Since magnetic anomalies are entirely caused by the amount of magnetic minerals contained in the rocks, it is necessary to discuss very briefly these minerals, and in particular their magnetic susceptibilities. The ease which these minerals may be magnetised is measured by a quantity called magnetic susceptibility.

All minerals can be broadly classified into two groups according to their magnetic properties. Diamagnetic minerals are those which have negative susceptibility and paramagnetic minerals those which have positive magnetic susceptibility.

Table 7.1 presents the magnetic the average magnetic susceptibilities of various minerals and rocks.

| MINERALS | SUSCEP.*10nT |
|---|---|
| graphite | -8 |
| quartz | -1 |
| cassiterite | 32 |
| chalcopyrite | 90 |
| limonite | 220 |
| pyrrhotite | $1.25*10^5$ |
| ilmenite | $1.5*10^5$ |
| magnetite | $5*10^5$ |

| ROCKS | SUSCEP.*10nT |
|---|---|
| dolomite | 0 - 75 |
| sandstones | 1 -1660 |
| gneiss | 10 - 2000 |
| serpentinite | 250 - 1400 |
| granite | 0 - 4000 |
| gabbro | 80 - 7200 |
| basalts | 20 - 14500 |
| peridotite | 7600 - 15600 |

**Table 7.1**: *Magnetic susceptibilities of various minerals and rocks (from Telford et al, 1982)*

As we can see, the susceptibility of magnetite is several times larger than that of any other mineral, and 3 to 4 orders of magnitude greater than that of most common rocks.

Consequently, rock susceptibilities are strongly controlled by their magnetite content.

The magnetization is made up the two different components:

(a) permanent or remanent magnetization, and

(b) induced magnetization.

The former is not always present, but may be completely independent of the Earth's present field as it formed at different latitudes during continental drift and when the Earth's field may have had normal or reversed polarity. The latter is produced by the Earth's field and is proportional in magnitude to the strength of the Earth's field, the local magnetic susceptibility being the constant of proportionality.

Commercially available magnetometers which measure the total magnetic field may be divided into three groups: the fluxgate, proton precession and optically pumped alkali vapour magnetometer. The principles of these three types are well described in the literature: *Wyckoff* (1948), *Waters* and *Phillips* (1956) and *Royer* (1967).

Advances in sensor design have permitted shorter sampling intervals and improved measurement accuracy, with the result that overall resolution has been greatly improved (*Paterson*, 1983). In the study area, a proton magnetometer was used and covered 11110 line-kilometres.

Airborne gamma-ray spectrometry (AGRS) measures the intensity of gamma radiation in a photon-energy spectrum expressed in terms of electron volts (eV) i.e. an energy dispersive system is employed. In brief, the principle of this radiation is based on the instability of the atomic configuration of some chemical elements. Although at least twenty naturally

occurring elements are now known to have radioactive isotopes, only gamma-ray emissions from $^{235}U$, $^{238}U$, $^{232}Th$ and $^{40}K$ are easily detectable and of importance in exploration.

Gamma radiation is electromagnetic radiation with wavelengths from $10^{-5}$ to $10^{-10}$ μm representing an excess of energy produced primarily by the radioactive decay of the isotopes $^{40}K$, $^{232}Th$ and $^{238}U$ series.

$^{40}$Potassium forms 0.011% of natural potassium and emits gamma rays at 1.461 MeV, whose intensity indicates directly the potassium content.

$^{232}$Thorium forms a radioactive series of daughter isotopes not having a distinct gamma-ray peak. One daughter isotope $^{208}Tl$ may be detected from gamma-rays with energies of 2.62 MeV.

Uranium also decays through a series of daughter products. One of them, $^{214}Bi$, is often used to identify $^{238}U$, and gamma-rays with 1.76 MeV characterise this isotope (*Richards* and *Walhaven*, 1985). The U and Th values thus measured are termed equivalent uranium (eU) and equivalent thorium (eTh), that is, estimates of U and Th concentration based on gamma-ray emission from $^{214}Bi$ and $^{208}Tl$ respectively, assuming radioactive equilibrium.

Only high energy gamma-rays can be detected in the air from aircraft, much radiation being absorbed by only a few metres of air. Even then, the levels are much reduced and the flying height has to be as low as possible. Gamma radiation is affected by standing water, vegetation, snow and waterlogged overburden which absorb it totally. The main radioactive minerals and their respective occurrences are shown in Table 7.2.

| RADIOACTIVE MINERALS | MAIN OCCURRENCE |
|---|---|
| K<br>a)orthoclase, microcline and muscovite;<br>b)alunite;<br>c)sylvite and carnalite; | a)main constituents in acid rocks and pegmatites;<br>b)alteration in acid volcanics;<br>c)saline deposits in sediments; |
| eTh<br>a)monazite;<br>b)thorianite, thorite and uranothorite; | a)granites, pegmatites and gneisses; b)granites, pegmatites and placers; |
| eU<br>a)uraninite and gummite;<br>b)carnotite; | a)granites, pegmatites and with vein deposits of Ag, Pb and Cu;<br>b)sandstones |

**Table 7.2**: *Radioactive minerals and their main occurrences (from Telford et al, 1982)*

For measuring natural radiation three instruments are available: the Geiger counter, scintillation meter and pulse-height analyser or gamma-ray spectometer. The Geiger counter responds primarily to beta-radiation, consequently it can only be used in ground transversing.

The scintillation meter is based on the counting of scintillations produced by radiation bombardment of a particular crystal. The best scintillation detector is made by growing natural crystals of sodium iodide treated with thallium. Although a considerable amount of scintillometric airborne surveys have been undertaken, the results are not particularly useful since only total count are measured with no discrimination of source isotopes. The gamma-ray spectrometer is in fact an extension of the scintillometer, which can separate the characteristic gamma-rays of K, Th and

U by energy-dispersive pulse-height analysis. This instrument has made AGRS more attractive for mineral exploration over the last twenty years.

Scintillometric methods were first used in the late thirties for stratigraphic correlation in oil well logging (*Kokesh*, 1951). For uranium prospecting this method became quite popular in the forties and fifties, but declined with the decrease in demand for uranium. However AGRS was revived in the late sixties not only for uranium prospecting but for many others purposes by the development of energy dispersive spectrometry (*Telford et al*, 1982; *Bateham et al*, 1983).

This chapter discusses the importance of these surveys for gold exploration and presents the final products which will be integrated with other data sets in Chapter 9.

## 7.2 Aeromagnetics and gold exploration

The magnetic method has traditionally been applied to petroleum exploration to determine the depth and major structure of crystalline basement rocks underlying sedimentary basins. This technique is also intensely applied in mineral exploration (*Paterson* and *Reeves*, 1985).

Although the magnetic method does not indicate directly any ore bodies other than those with magnetite or ilmenite, it has proved to be an extremely important ancillary technique for discovering mineral deposits. Through its detection of contrasts in magnetic susceptibitities at depth, aeromagnetics has long found a general use in geological mapping, especially in poorly exposed terrains. Particularly efficient at delineating igneous dykes and faults, the complex variations in magnetic fields induced over magnetic bodies with different

shapes, altitude and latitude demands both complex mathematical analysis and *a priori* knowledge of local geology before quantitative modelling can be applied. Here the approach is to use magnetic data in a simple way to aid geological mapping. The more important research aims for mineral exploration are:

a)to delineate volcano-sedimentary belts covered by sediments or hosted in strongly metamorphosed terrains (*Reeves*, 1985);
b)to identify and outline post-tectonic intrusives, both mafic and ultramafic (*Kimbel* et al, 1984) or acid rocks (*Drury* and *Walker*, 1988);
c)to recognise and interpret faults, shear zones and fractures (*Drury* and *Walker*, 1987);
d)to map palaeosurfaces and unconformities as an aid to exploration for detrital minerals and/or unconformity-related uranium (*Roux*, 1970);
e)to detect deposits of magnetic iron;
f)to select environments favourable for groundwater exploitation including fracture systems in crystalline rocks and bedrock aquifers under alluvial cover, as well as to support studies for geologic disposal of nuclear and other wastes (*Ermanovics* et al, 1984).

Focussing on aeromagnetics and gold exploration, several case studies have been described in the literature. Many gold deposits of Archaean age are closely associated with BIF or mafic and ultramafic volcanic rocks which usually have high magnetic susceptibility.

*Roux* (1970) presented one of the most impressive results. The palaeoplacer deposit of Rand Goldfield, in South Africa, a

magnetite-bearing shale could be detected beneath the thick unconformable cover, and was used to predict the position of the overlying gold-bearing conglomerate.

The relationships between the gold deposits at Val d'Or, in Canada, and magnetic anomalies is described by *Hood et al* (1982). At Ashanti Mine, in Ghana, magnetic surveys show that gold occurs where the magnetic character of the greenstone belt changes due to the presence of rocks with high magnetite content, and where it is cut by other structures (*Cudjoe*, 1970).

In Western Australia, of the ten largest gold deposits only one (Great Fingal) is not clearly associated in some way with a magnetic body shown by the aeromagnetic maps (*Woodwall*, 1979).

In terms of gold related to lineaments, two examples are outstanding:

(a)the occurrence of the Kalgoorlie mines (Western Australia) on the Kalgoolie-Shark Bay feature traced from magnetic maps (*O'Driscoll*, 1981), and

(b)at Geita Mine, in Tanzania, gold occurs where a NNE striking fault cuts a BIF. Both the fault and BIF were mapped from magnetic maps (*Batteham et al*, 1983).

## 7.3 Gamma-ray spectrometry and gold exploration

In terms of surface geological mapping, the importance of AGRS lies in the different geochemical properties of U, Th and K and the varying proportions of these elements produced by different dispersion processes. To characterize an important lithological unit, it is essential to analyse the particular response in the three channels. Because of the ease by which

gamma radiation is affected by water, vegetation, exposure pattern and surface conditions, the amplitude of the response is irrelevant.

Basic factors are geochemistry and mineralogy of U, Th and K. Uranium in $U^{6+}$ form is highly soluble and precipitates under reducing condition as $U^{4+}$ complexes. Potassium is stable in rock forming minerals, such as feldspar, but enters solution weathering, and it may be absorbed on clay minerals after diagenesis. Thorium is frequently concentrated in heavy resistant minerals, such as allanite, monazite, zircon, etc.

Mature sandstones contain low K and U but may have high Th in heavy minerals, arkosic sandstones often give K anomalies because of the presence of potassic feldspar, heavy mineral placers often give Th anomalies because they commonly contain some monazite. Granites are usually characterized by high-amplitude (K-U-Th anomalies) and mafic granulites often have low emissions (*Beherendt*, 1971).

AGRS is extremely important for prospecting uranium, thorium, titanium and zirconium-bearing heavy minerals. Carbonatites, such as at Oka (Canada) could be recognised because they have a very low U/Th ratio. Kimberlites can also be detected due to their distinctive signature (*Telford et al*, 1982).

*Slaney* (1985) using radiometric data in SW Nova Scotia (Canada) separated granitoid rocks into distinct phases in an attempt to determine how plutons crystallized and to indicate areas of potential tin mineralisation. As result, granodiorites are best seen on the eTh and eTh/K ratio maps and the Davis Lake pluton contains: a)in southwest margin, highest values in all three radioelements; b)high eTh at the

margin against granodiorite; c)in east Kemptiville, there is an average of U and low eTh; and d)in northwest margin, there is a modest increase in eTh and K levels.

With respect to gold mineralisation, much valuable information can be extracted from radiometric data. Important anomalies can sometimes be associated with particular geological feature such as faults and acid dykes (*Adams*, 1968).

A close spatial association with granitoids is often cited in descriptions of Archaean gold deposits. In the Abitibi belt it was noted that post-tectonic, intrabelt plutons constitute more than 25% of host rocks for gold mineralisation, although they form less than 4% of the surface exposure of the belt (*Colvine et al*, 1988). Clearly identification of plutons in poorly exposed terrains, and discrimination of granitoids of different petrogenetic type is a possibility using AGRS.

Apparently no single compositional type of granite is associated with gold deposits. Many of the intrusions are granodiorites or trondhjemites (Red Lake and Porcupine in Canada), but compositions range to K-rich, Si-poor syenites to K-rich, Si-rich granites. The compositional variation suggests that the magmas have been generated from different source rocks, probably at different levels in the Archaean crust (*Colvine et al*, 1984).

Understanding the true role of these intrusive suites in the gold deposits still awaits the acquisition and interpretation of adequate petrological and petrochemical data bases. However, despite these difficulties, the close spatial associations of gold deposits with a temporally distinct

intrusion remain an important characteristics of Archaean gold deposits (see Chapter 5, Table 5.8).

In summary, regional aeroradiometric surveys should be capable of discriminating different geological units, and thus adding to mapping potential in poorly known areas. Due to diverse mineralogical composition, granites, gneisses and migmatites, various components of volcanosedimentary belts and granulite sequences should theoretically be discriminable.

## 7.4 Preprocessing geophysical data

The preprocessing techniques applied to geophysical data include the conversion of the original scattered data into grid data with a regular interval, then converting into images using different methods.

The data set from the northern area was recorded on tape in ASCII format files, and that from the southern area was available as contour maps (magnetic) and flight line profiles (radiometric).

For the northern area the conversion into raster format was done by gridding the scattered data using interpolation methods. With respect to the southern area the contour maps and profiles were manually digitized, then converted to scattered data, and then gridded using interpolation methods. The next step was to convert these vector files into raster images. The resultant images are the most suitable for interpretation because raster data may be statistically analysed, enhanced for visual analysis and combined arithmetically with other images.

Because of the different forms of the raw data the results of interpolation differ. Those produced manually from contour and

profiles are obviously degraded compared with those from the digital line data, simply because contouring omits values between contour intervals, and profiles are compressed in amplitude.

### 7.4.1 Raster data derived from interpolation methods

Interpolation is a mathematical technique that is used to estimate values between existing data, without distorting their meaning or substance inside the area covered by existing observations. Many of the raster maps of the study area were generated from scattered data by interpolation. Due to the importance of this technique I shall briefly review the interpolation methods and their purposes. It is possible for any spatial array to define the best values for blank sites. Important reviews of interpolation techniques are those of *Webster* (1984) and *Lam* (1983).

The most common interpolation techniques are: Thiessen polygons (TP), trend surface analysis (TSA), minimum tension surface (MTS), weighted moving averages (WMA), Fourier series, splines and kriging.

The TP is also known as Voronoi polygons or Dirichlet cells. The TP is based on the fact that observations located close together tend to be more alike than observations spaced further apart. The TP divides an area up in a way that is totally dependent on the array of the points: equal regular squares for regular square grids or irregular network for data irregularly spaced (Figure 7.1.a). *Ripley* (1981) has provided a mathematical discussion of the principles involved in TP operation.

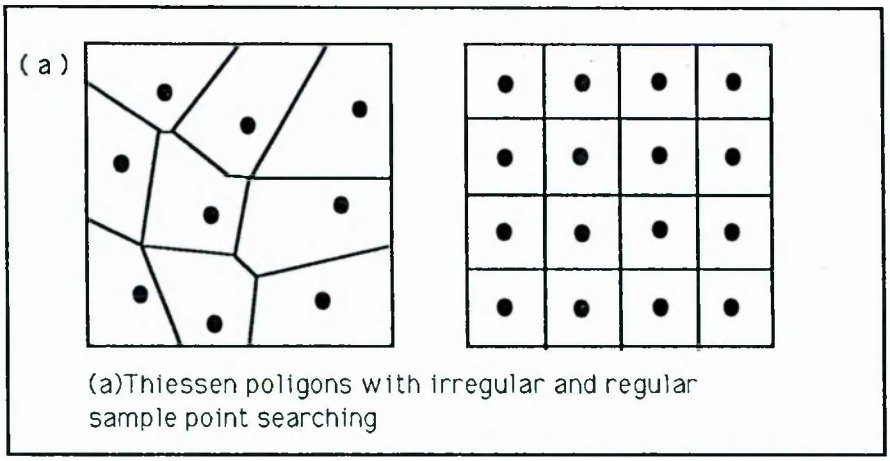


(a)Thiessen poligons with irregular and regular sample point searching

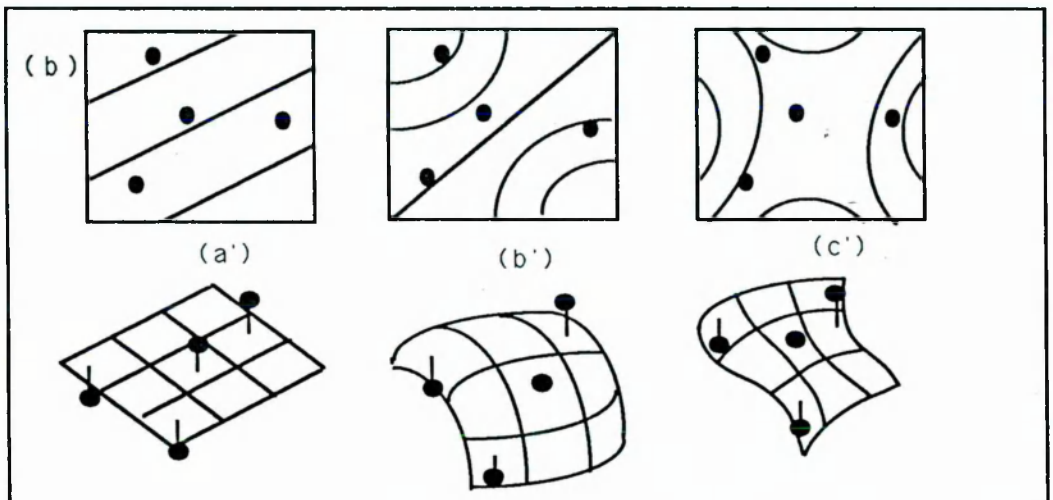


Trend surface in two and three spatial dimensions: (a)linear, (b)quadratic, (c)cubic

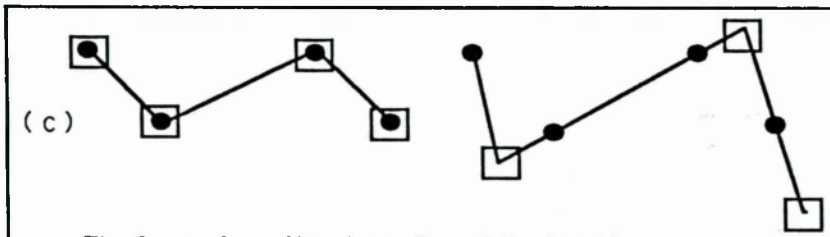


The form of a spline depending of the location of the break points ( □ )

Figure 7.1: *Methods of spatial interpolation (a)Thiessen polygon (b)trend surface, (c)spline*

The TSA and MTS are based on modelling the gradual variations by polynomial regression. The main difference between them is that the TSA has a polynomial with higher order. Both TSA and MTS are based in fitting a polynomial line or surface by least squares through the data points. By increasing the number of terms it is possible to fit any complicated curve exactly (*Burrough et al*, 1977). The TSA and MTS can be applied in one or two dimensions and the output depends on the number of parameters involved. A horizontal plane is zero order (Figure 7.1.b.a'), an inclined plane is first order, a quadratic surface is second-order (Figure 7.1.b.b') and a cubic-order has 10 or more parameters (Figure 7.1.b.c'). The geochemical and geophysical images of the study area were generated using MTS. The results achieved were outstanding and will be discussed in Chapters 8 and 9.

The Fourier series (FS) can be used to describe one or two dimensional variation by modelling the observed variation by a linear combination of sine and cosine waves (*Burrough*, 1986). Zone dimensional FS have been used to analyse time series (*Chatfield*, 1980), and there have been many applications in studies of climatic changes. Two dimension FS have proved useful in sedimentary geology, because some primary structures such as ripple marks represent periodic features.

Splines are mathematical equivalents of flexible rulers that achieve the best locally fitting smooth curves by eye. (*Burrough*, 1986). As they are piecewise functions, they are fitted to a small number of data points exactly, while at the same time confirming that the joins between one part of the curve and another are continuous. The points which separate lines are called break points and the values at these points

are called knots (*Pavlidis*, 1982). The form of a spline is strongly dependent on the selected break points as can be seen in Figure 7.1.c. Because of certain mathematical difficulties in calculating simple splines over a wide range or separate sub-intervals, most practical applications use a special kind of spline called B-splines. B-splines are themselves the sum of other splines that by definition have the value of zero outside the interval of interest (*Pavlidis*, 1982).

The WMA technique is based on computing an average value from a local neighbourhood or window. The WMA can be applied in one or two dimensions. In two dimensions, narrow windows emphasise short-range variations and broad windows will reduce short-range variations in favour of longer range effects (*Burrough*, 1986). The contribution that a given sample point makes to an average interpolated value at a blank site, is a function of the distance between that observation and the site. *Ripley* (1981) emphasised that the values estimated by moving averages are susceptible to clustering in the data points, and also to whether or not the observations are affected by a planar trend. Figures 3.5.a and (b) (see Chapter 3) show the effect of varying the value of the radius (R) which is the user-defined unit around each grid node to search for data points affecting it. It is very clear that small R may cause undefined areas. There is a direct relationship between R and undefined areas, when R increases the undefined areas decrease, but some artifacts may appear (Figure 3.5.b, in Chapter 3).

Kriging is a method developed by *Matheron* (1971) and *Krige* (1970). This interpolation method is optimal in the sense that the interpolation weights are chosen so as to optimise the

interpolation function, thus a best linear unbiased estimate of the value of a variable is obtained at a given point. According to *Burrough* (1986), the regionalised variable theory assumes that the spatial variation of any variable can be expressed as the sum of the three major components: (a)a structural component associated with a constant mean value or a constant trend; (b)a random spatially correlated component; (c)a random noise or residual error term;

The irregular spatial variations are called regionalised variables and are too unpredictable to be modelled by a smooth mathematical function, but can be described better by a stochastic surface. The term stochastic is applied to data randomly distributed; that follow some random probability distribution or pattern, so that their behaviour may be analysed statistically but not predicted precisely. The interpolation makes a start exploring and then modelling the stochastic aspects of the regionalised variable. The resulting information is used to estimate the weights for interpolation. The soil map of the study area (see Chapter 3, Figure 3.6) was generated using this technique.

There are advantages and disadvantages among the various interpolation methods. Furthermore, the method should be carefully designed as a function of the raw data and the purposes to which they are applied. Table 7.3 presents a summary of advantages and disadvantages of the described interpolation methods.

| INTERPOLATION METHOD | ADVANTAGES | DISADVANTAGES |
|---|---|---|
| THIESSEN POLYGONS | 1.Are the best for qualitative (nominal) data because other methods are inapplicable. | 1.The size and shape of the areas depend on sample lay-out.<br>2.One data point per cell.<br>3.No error estimates possible. |
| TREND SURFACE ANALYSIS AND MINIMUM TENSION SURFACE | 1.Are superficially easy to understand, at least with respect the way the surfaces are calculated.<br>2.Light to moderate computer loading.<br>3.Are the best for demonstrating broad features and remove them prior to other methods. | 1.Edge effects outliers 2.Complex polynomials. do not necessarily have meaning.<br>3.Errors are rarely spatially independent. |
| FOURIER SERIES | 1.Is the best for periodic features.<br>2.Moderate computer loading. | 1.The data set must show a periodic feature. 2.It is used most for structural analysis than mapping. |
| SPLINES | 1.Produces very smooth surfaces.<br>2.The interpolation is a quick process.<br>3.Retain small scale features.<br>4.It is possible to modify one part of the curve without having to recompute the whole. | 1.There are problems when very high order splines are used to smooth sinuous boundaries.<br>2.No direct estimates of the errors associated. |

| | | |
|---|---|---|
| MOVING AVERAGES | 1.Quick contour plots of moderately smooth data.<br>2.Moderate computer loading. | 1.Results depends on configuration of data. point and size of the window.<br>2.Simple version assume isotropy.<br>3.No errors estimates unless calculated. |
| KRIGING | 1.Best for situations where the most detailed estimates and their errors are required.<br>2.Average local values can be represented by a continuous surface. | 1.Practical and theorical problems of non-stationarity in data.<br>2.Large computing costs for mapping. |

**Table 7.3**: *A comparison of methods of interpolation (from Burrough, 1986)*

The geophysical data of the study area were gridded using the minimum tension surface (MTS) method. Figures 7.2.a, (b), (c) and (d) show the magnetic, uranium, potassium and thorium images, respectively, of the northern part of the study area. Figures 7.3.a, (b), (c) and (d) present the magnetic, uranium, potassium and thorium images, respectively, of the southern part of the study area.

The most obvious difference resulting from the different sampling is the presence of line artifacts in the manually digitized radiometric data from the southern area (Figures 7.3.b, c, and d). The manually digitized magnetics (Figure 7.3.a) look as good as those from the digital records.

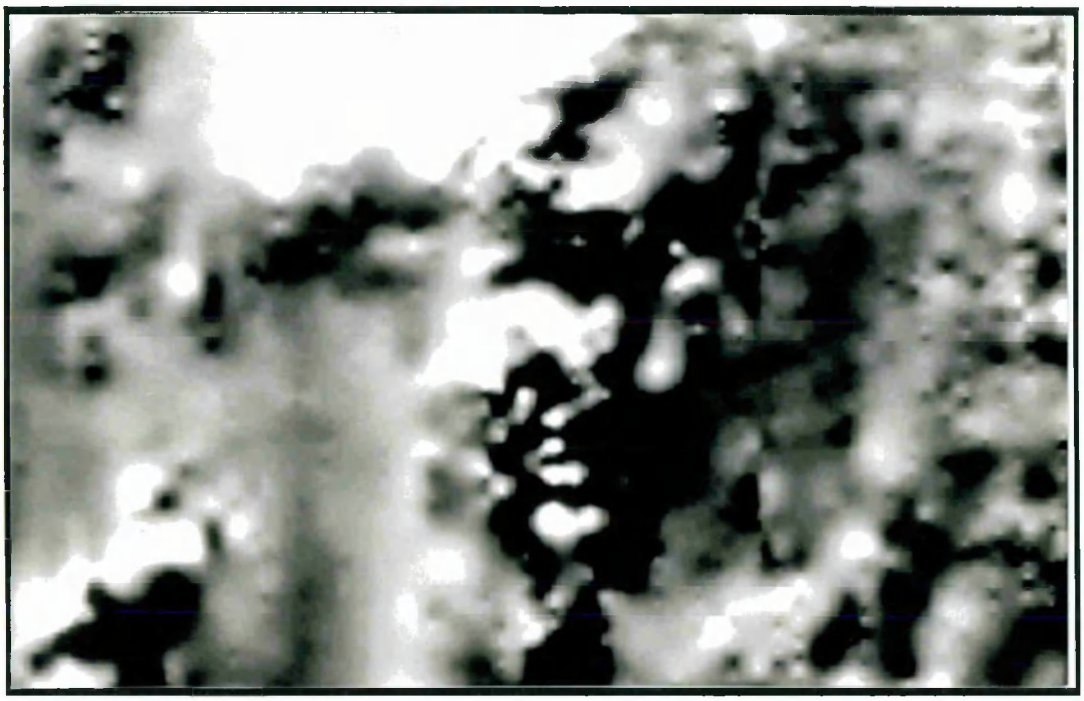

Figure 7.2.a: *Magnetic image of part of the northern part of the study area*

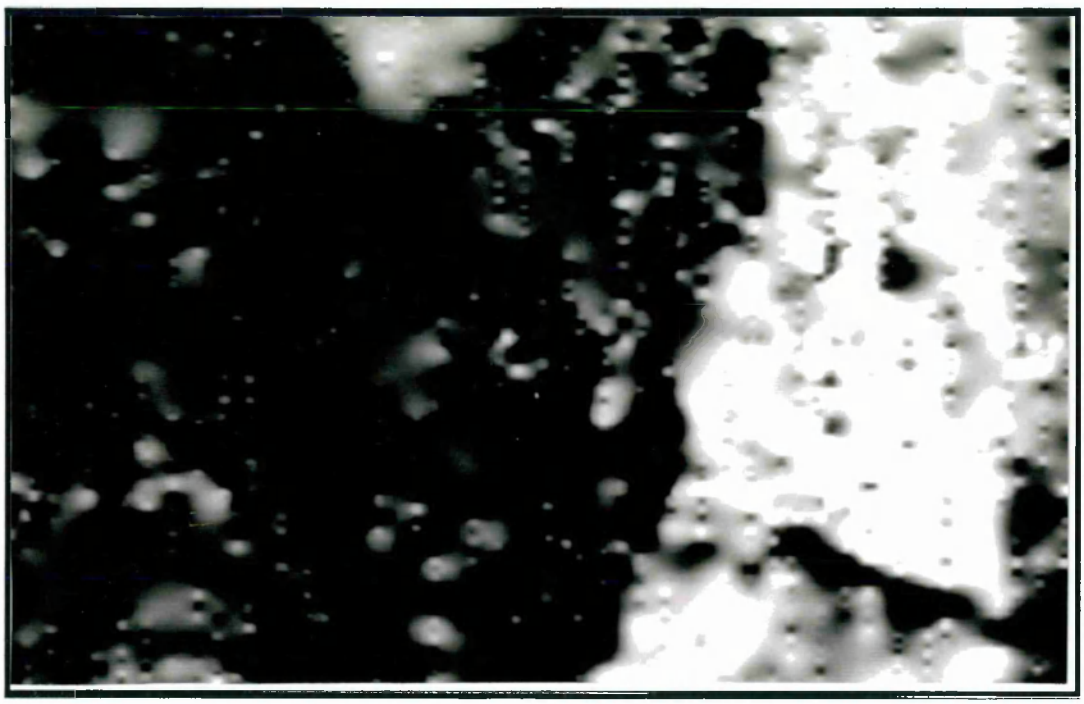

Figure 7.2.b.: *Radiometric (eU) image of part of the northern part of the study area*

0 15 km

~~7.16.A~~
7.17A

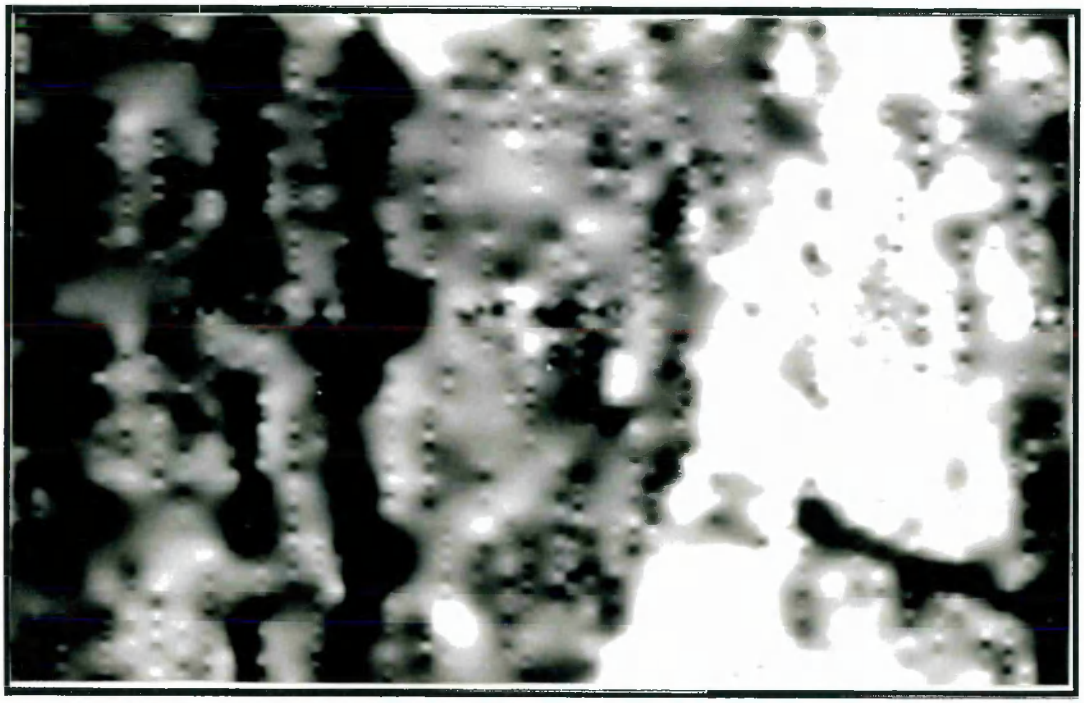

Figure 7.2.c: *Radiometric (K) image of part of the northern part of the study area*

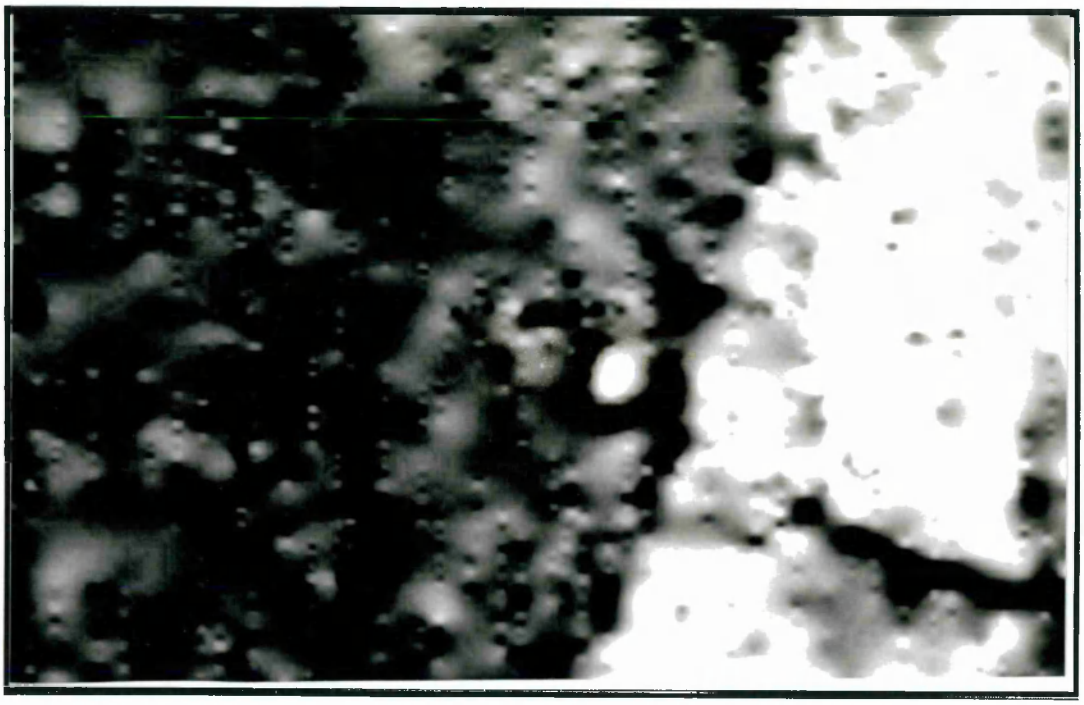

Figure 7.2.d.: *Radiometric (eTh) mage of part of the northern part of the study area*

0 15 km

Duplicate page

| | | |
|---|---|---|
| MOVING AVERAGES | 1.Quick contour plots of moderately smooth data.<br>2.Moderate computer loading. | 1.Results depends on configuration of data. point and size of the window.<br>2.Simple version assume isotropy.<br>3.No errors estimates unless calculated. |
| KRIGING | 1.Best for situations where the most detailed estimates and their errors are required.<br>2.Average local values can be represented by a continuous surface. | 1.Practical and theorical problems of non-stationarity in data.<br>2.Large computing costs for mapping. |

**Table 7.3**: *A comparison of methods of interpolation (from Burrough, 1986)*

The geophysical data of the study area were gridded using the minimum tension surface (MTS) method. Figures 7.2.a, (b), (c) and (d) show the magnetic, uranium, potassium and thorium images, respectively, of the northern part of the study area. Figures 7.3.a, (b), (c) and (d) present the magnetic, uranium, potassium and thorium images, respectively, of the southern part of the study area.

The most obvious difference resulting from the different sampling is the presence of line artifacts in the manually digitized radiometric from the southern area (Figures 7.2.a, b, and c). The manually digitized magnetics (Figure 7.2.a) look as good as those from the digital records.

Figure 7.3.a: *Magnetic image of part of the southern part of the study area*

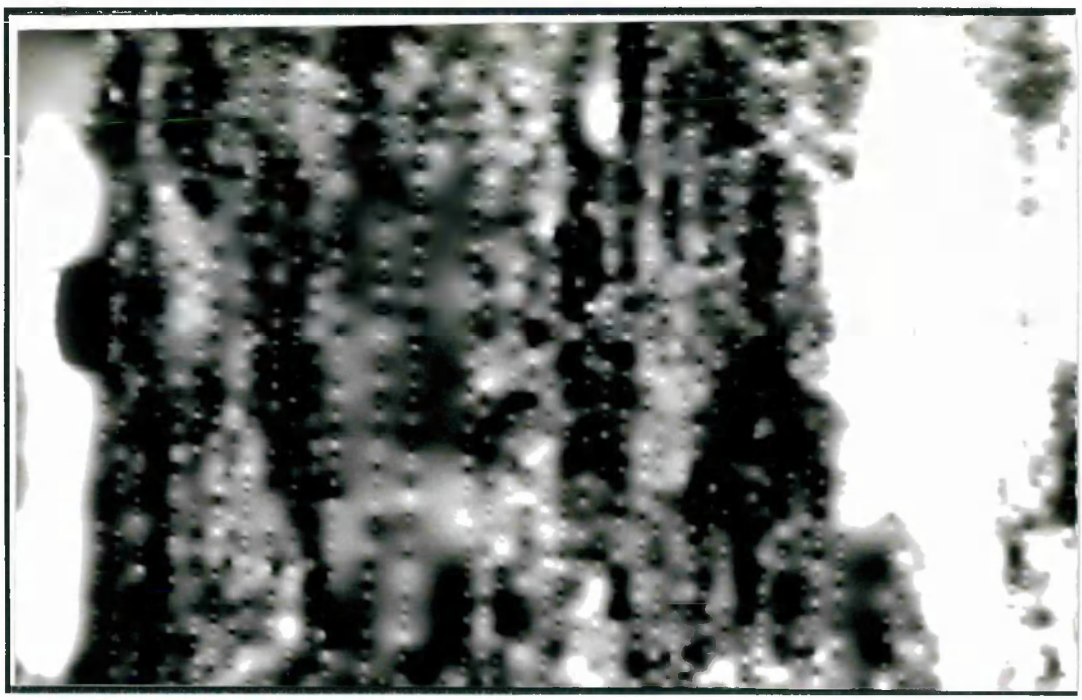

Figure 7.3.b.: *Radiometric (eU) image of part of the southern part of the study area*

0 15 km

~~7.17.A~~
7.17.C

Figure 7.3.c: *Radiometric (K) image of part of the southern part of the study area*

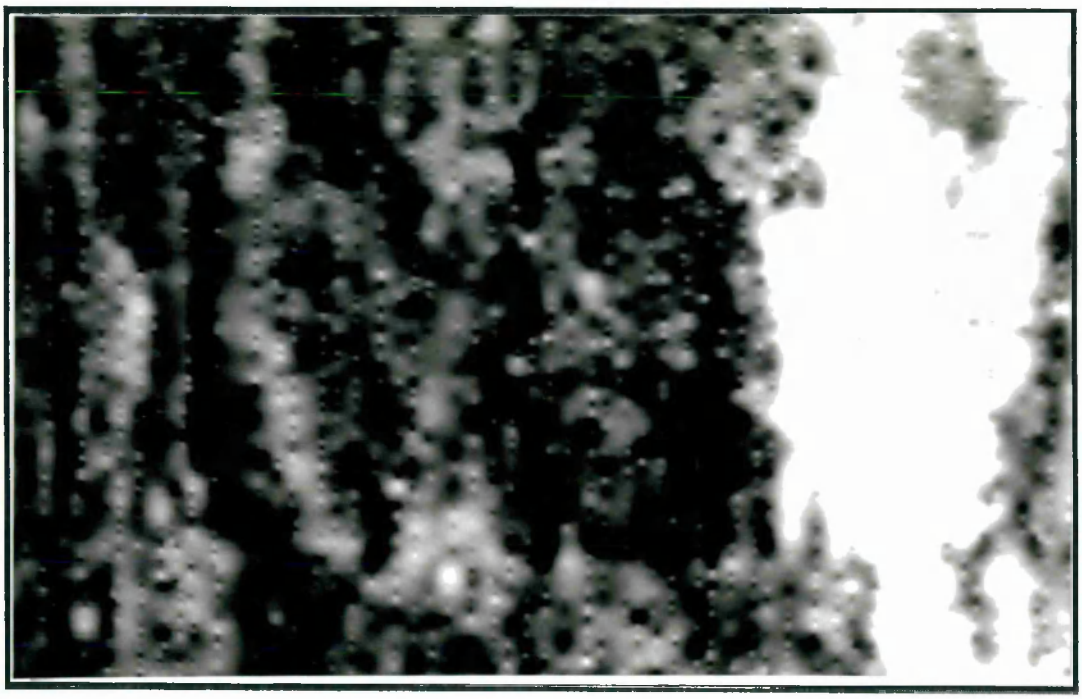

Figure 7.3.d.: *Radiometric (eTh) image of part of the southern part of the study area*

0 15 km

7.17.B
7.17.D

## 7.5 Processing geophysical data

The image processing techniques used in this work comprise: filtering, contrast stretching, colour enhancement (see also Chapter 6), data reduction and neighbourhood operation.

By using filtering, artifacts such as regular small points and imperfections where areas were gridded using a small amount of data points were removed. This noise has been almost eliminated by using a median filter, with a kernel size of 7x7, whose dimensions approximated twice those of the offending defects (*Drury* and *Walker*, 1987). Conceptually simple, the median filter is somewhat awkward to implement because of the pixel value sorting required. By using a median filter, a pixel value is replaced by the median of its immediate neighbours. The median of a set of numbers is the value such that 50% are above and 50% are below. Figure 7.3.e presents the radiometric (eU) image of the northern area after filtering and Figure 7.3.f shows the radiometric (eU) image of the southern area after convolution. These figures when compared with the raw images (Figures 7.2.b and 7.3.b) show that almost all the artifacts have been removed. However, the effects of N-S flight lines still remain and would require operations in the frequency domain to remove successfully.

Contrast stretching was applied to the images transforming the compressed DN range to the full 0 to 255 range. The frequency distribution of the radiometric data was strongly skewed with some 70% to 80% of the data close to the mode and a long tail extending towards the high values. To take advantage of the whole grey scale a logarithmic stretch was used. The magnetic data were enhanced using linear stretching because of the

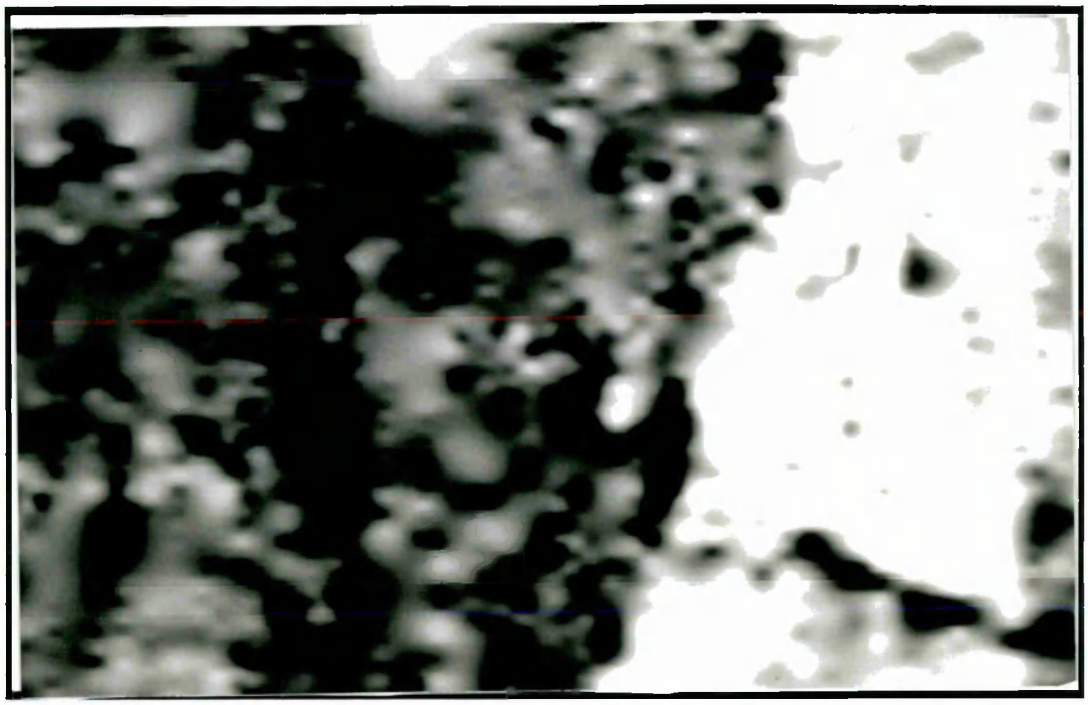

Figure 7.3.e: *Radiometric (eU) image of part of the northern part of the study area after convolution (median filter)*

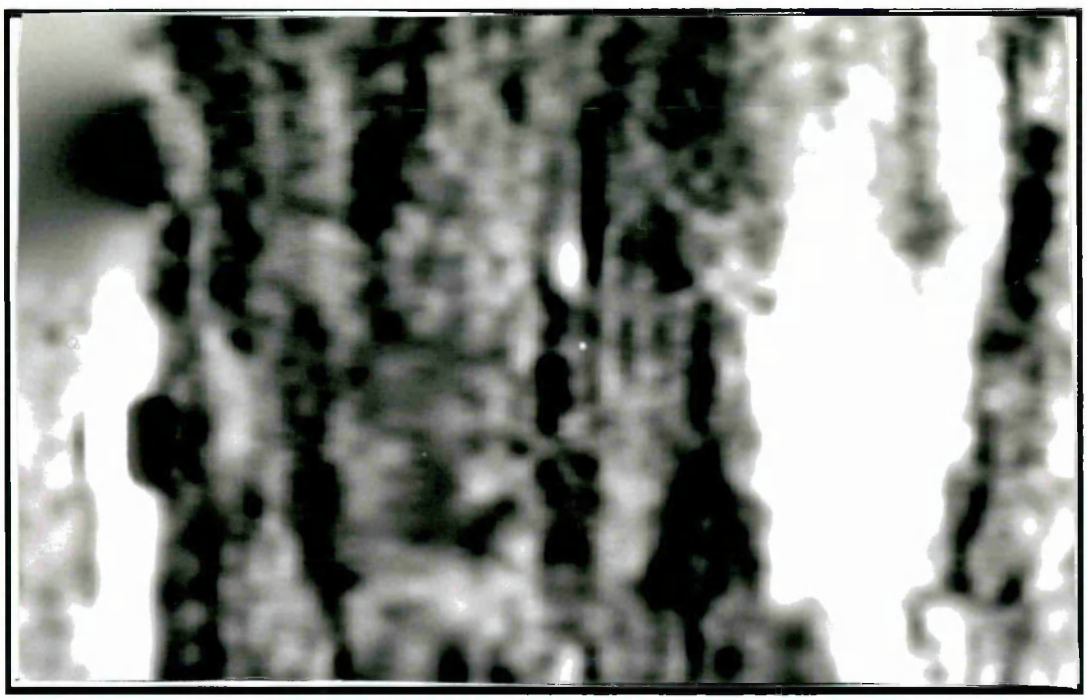

Figure 7.3.f.: *Radiometric (eU) mage of part of the southern part of the study area after convolution (median filter)*

0 15 km

normal frequency distribution. Table 7.4 shows the DN transformation in the rescaled data.

For data integration, the preprocessed files were resampled to the 50 m pixel size adopted for the TM and radar data base. However, for visual interpretation they were maintained at 250 m pixel size.

| Geophysical data | Original DN | Rescaled | Original DN | Rescaled |
|---|---|---|---|---|
| Magnetic | 160 | 0 | 225 | 255 |
| Uranium | 25 | 0 | 248 | 255 |
| Potassium | 60 | 0 | 245 | 255 |
| Thorium | 15 | 0 | 240 | 255 |

**Table 7.4**: *Rescaled geophysical data to the full 0 to 255 range*

### 7.5.1 Enhancing magnetic features

Human vision can distinguish in excess of 1 million colours compared with 30 to 40 grey levels. However, visually discerning fine spatial detail is better using grey level images with suitable contrast and edge enhancement (*Drury* and *Walker*, 1987).

An attempt to enhance magnetic high spatial features was undertaken by using a directional first derivative filter. The importance of directional filters is that the eye needs cues to depth such as shading (present in TM and radar because of illumination).

Force-field data contain no such cues and appear bland and flattish. Therefore directional filtering which mimics shading and enhances features with different directions is needed (*Drury* and *Walker*, 1987).

Figures 7.3.g, (h), 7.4.a and (b) show the four directions of filtering for magnetics of the part of southern area. The four directions of the filters are presented below.

| | | | | |
|---|---|---|---|---|
| -2 | -1 | -1 | -1 | 0 |
| -1 | -2 | -2 | 0 | 1 |
| -1 | -2 | 0 | 2 | 1 |
| -1 | 0 | 2 | 2 | 1 |
| 0 | 1 | 1 | 1 | 2 |

Northwest

| | | | | |
|---|---|---|---|---|
| 0 | -1 | -1 | -1 | -2 |
| 1 | 0 | -2 | -2 | -1 |
| 1 | 2 | 0 | -2 | -1 |
| 1 | 2 | 2 | 0 | -1 |
| 2 | 1 | 1 | 1 | 0 |

Northeast

| | | | | |
|---|---|---|---|---|
| 1 | 1 | 0 | -1 | -1 |
| 1 | 2 | 0 | -2 | -1 |
| 2 | 2 | 0 | -2 | -2 |
| 1 | 2 | 0 | -2 | -1 |
| 1 | 1 | 0 | -1 | -1 |

East

| | | | | |
|---|---|---|---|---|
| 1 | 1 | 2 | 1 | 1 |
| 1 | 2 | 2 | 2 | 1 |
| 0 | 0 | 0 | 0 | 0 |
| -1 | -2 | -2 | -2 | -1 |
| -1 | -1 | -2 | -1 | -1 |

South

Data reduction was undertaken using the Lepeltier technique (*Lepeltier*, 1969), this is more appropriate for the geochemical data in Chapter 8, where it is discussed in more detail. The frequency distribution of the grey level of the magnetic images of the northern area roughly suggests a lognormal distribution in such a way that the Lepeltier concepts for establishing background and threshold can be applied.

Table 7.5 presents the statistical parameters defined for the northern and southern area.

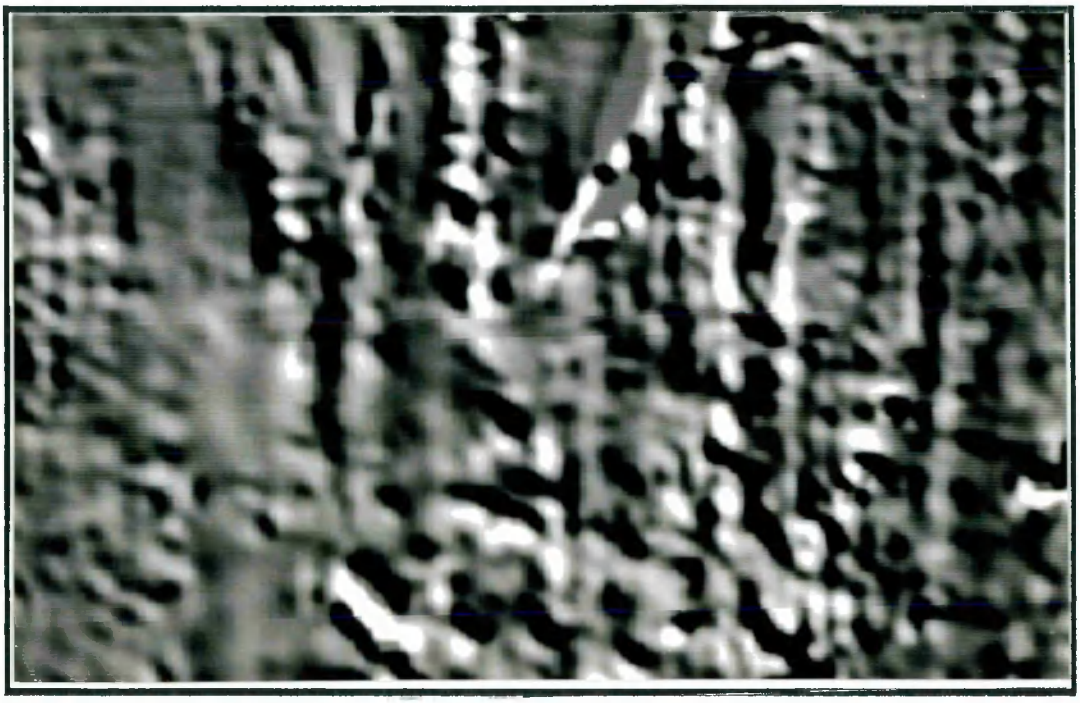

Figure 7.3.g: *Pseudo-illuminated magnetic image implemented by a northwest first derivative filter of the northern part of the sdtudy area*

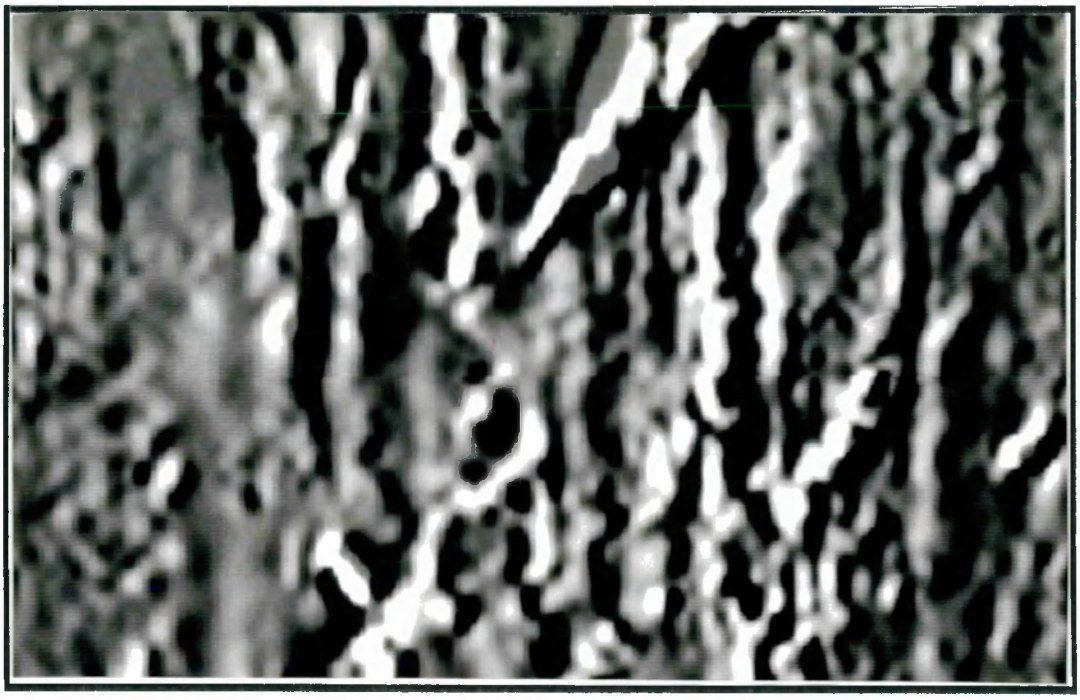

Figure 7.3.h: *Pseudo-illuminated magnetic image implemented by a northeast first derivative filter of the northern part of the study area*

0 15 km

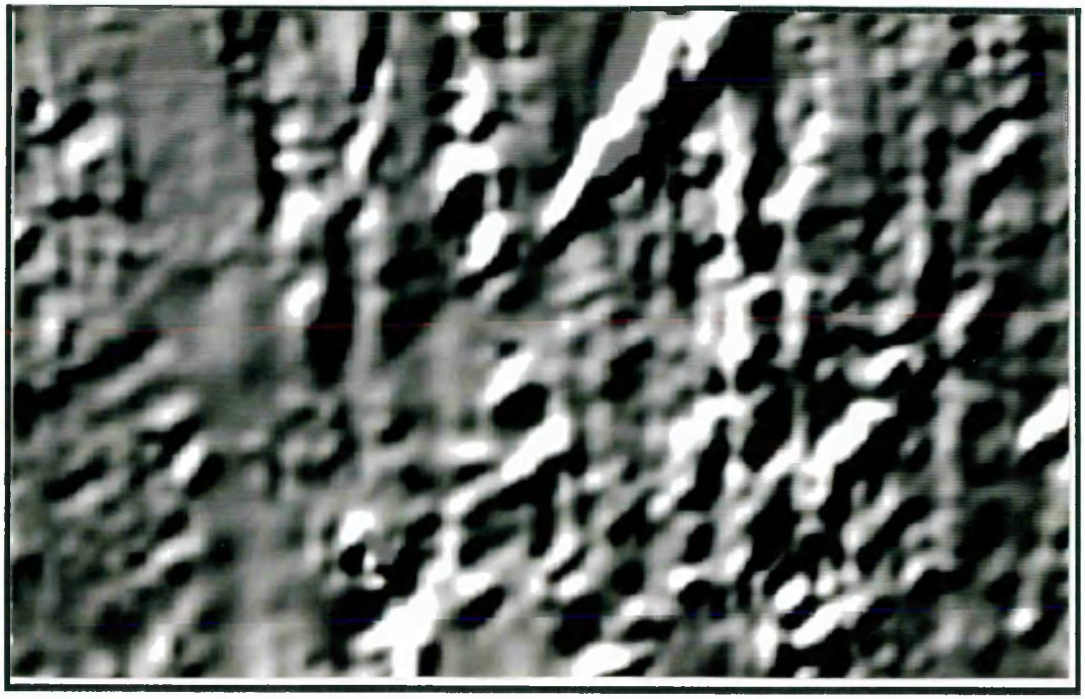

Figure 7.4.a: *Pseudo-illuminated magnetic image implemented by a eastward first derivative filter of the northern part of the study area*

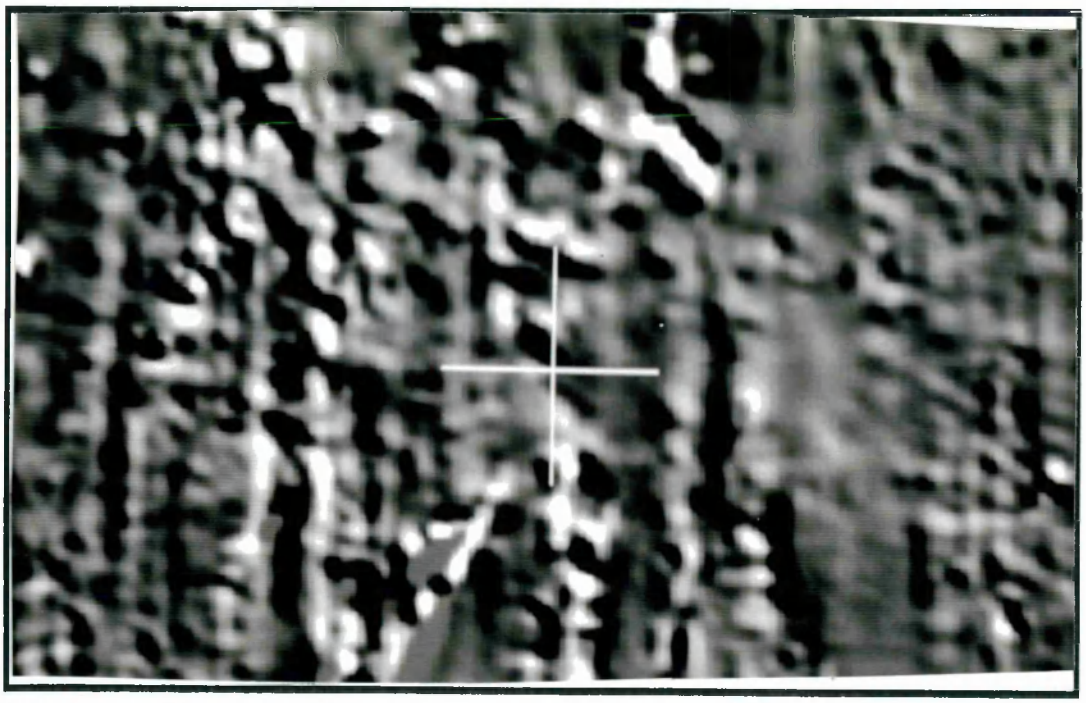

Figure 7.4.b: *Pseudo-illuminated magnetic image implemented by a southward first derivative filter of the northern part of the studty area*

0 15 km

| Elements | Northern area | Southern area |
|---|---|---|
| Pixel size | 250 | 250 |
| Min. Northing | 8451250 | 8382000 |
| Max. Northing | 8506750 | 8451000 |
| Min. Easting | 283500 | 236000 |
| Max. Easting | 337750 | 337000 |
| Min. Z | 23814 nT | 24100 nT |
| Max. Z | 25219 nT | 25100 nT |
| background | 24800 nT | 24600 nT |
| st. deviation | 55 | 207 |

**Table 7.5:** *Characteristics of the magnetic image of the northern and southern part of the study area*

Based on background (b) and standard deviation (sd), four magnetic zones were defined:

a) zone A: areas with a high magnetic field. Values generally higher than 24910 nT (>b +2s);

b) zone B: areas with a moderate magnetic field. Values ranging from 24856 nT to 24910 nT (b+s to b+2s);

c) zone C: areas with a low magnetic field. Values ranging from 24801 nT to 24909 nT (b to b+s);

d) zone D: areas with a very low magnetic field. Values less than 24800 nT (0 to b).

Figures 7.4.c and 7.4.e present the data reduction of the magnetic images of the northern and southern area, respectively. Zones D, C, B and A appear as yellow, blue, green and red, respectively.

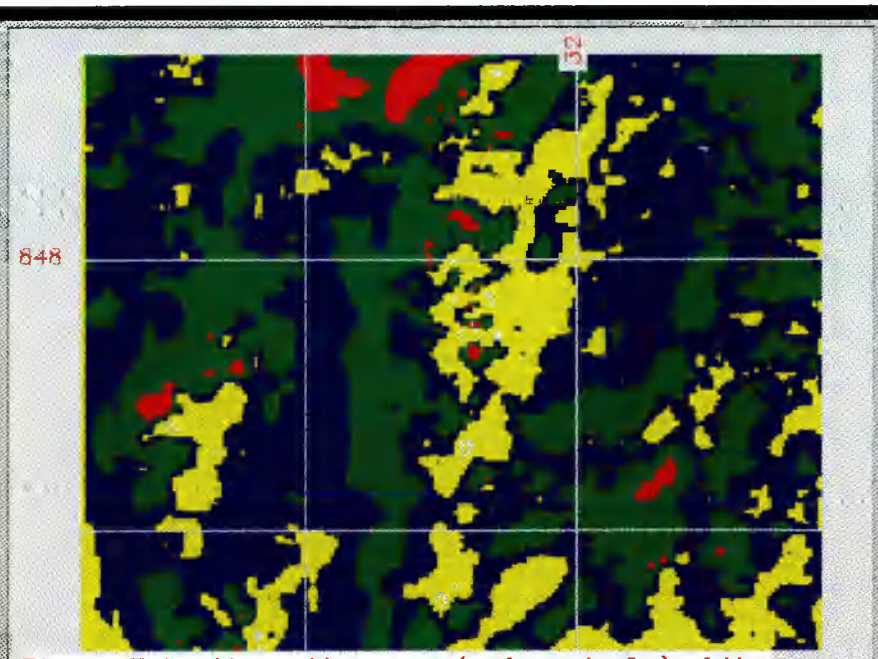


Figure 7.4.c: Magnetic zones (value > b+2s) of the northern area

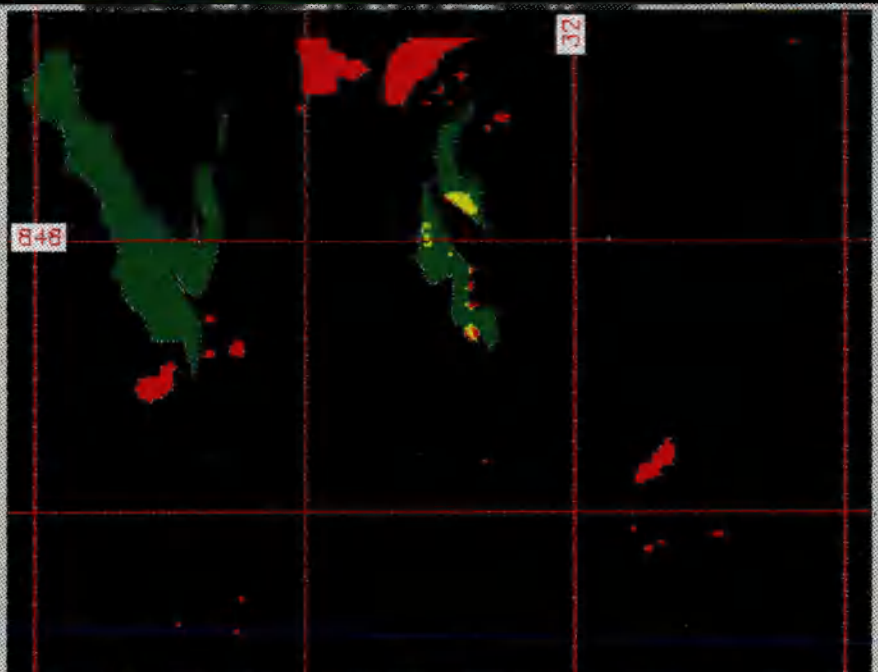


Figure 7.4.d: Magnetic anomalies (in red) over the Lower Unit (in green) of the northern area

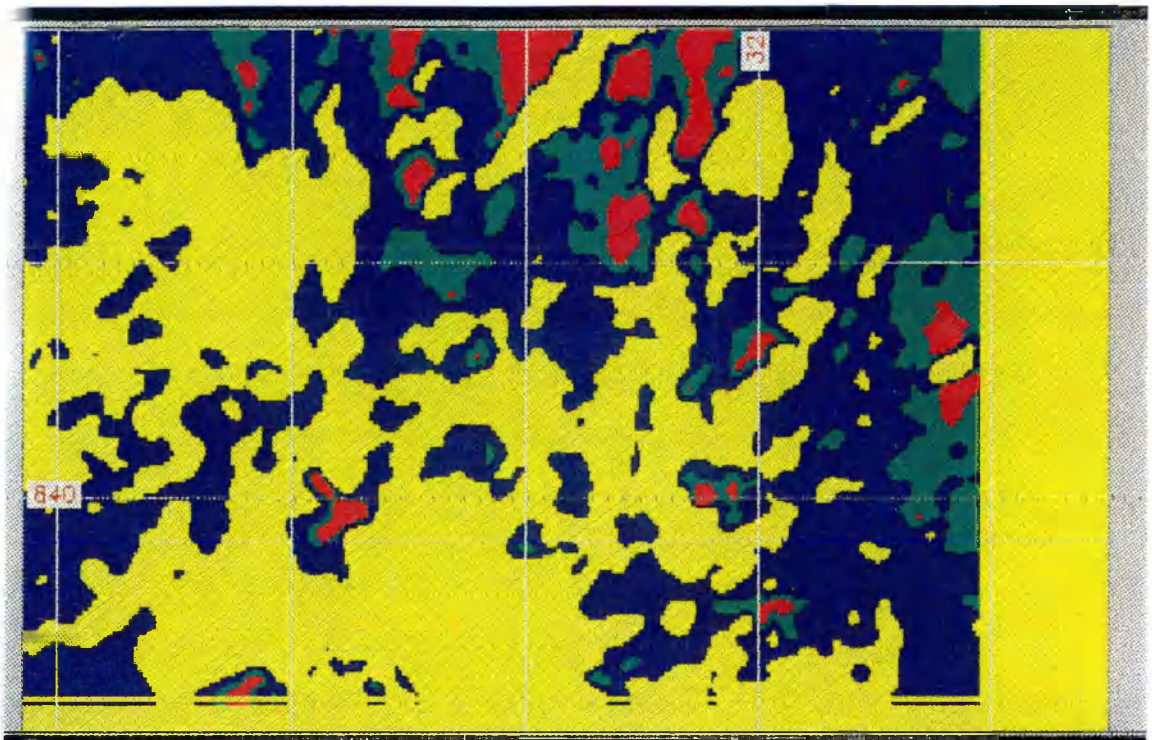


Figure 7.4.e: Magnetic zones (values >b+2s) of the southern area

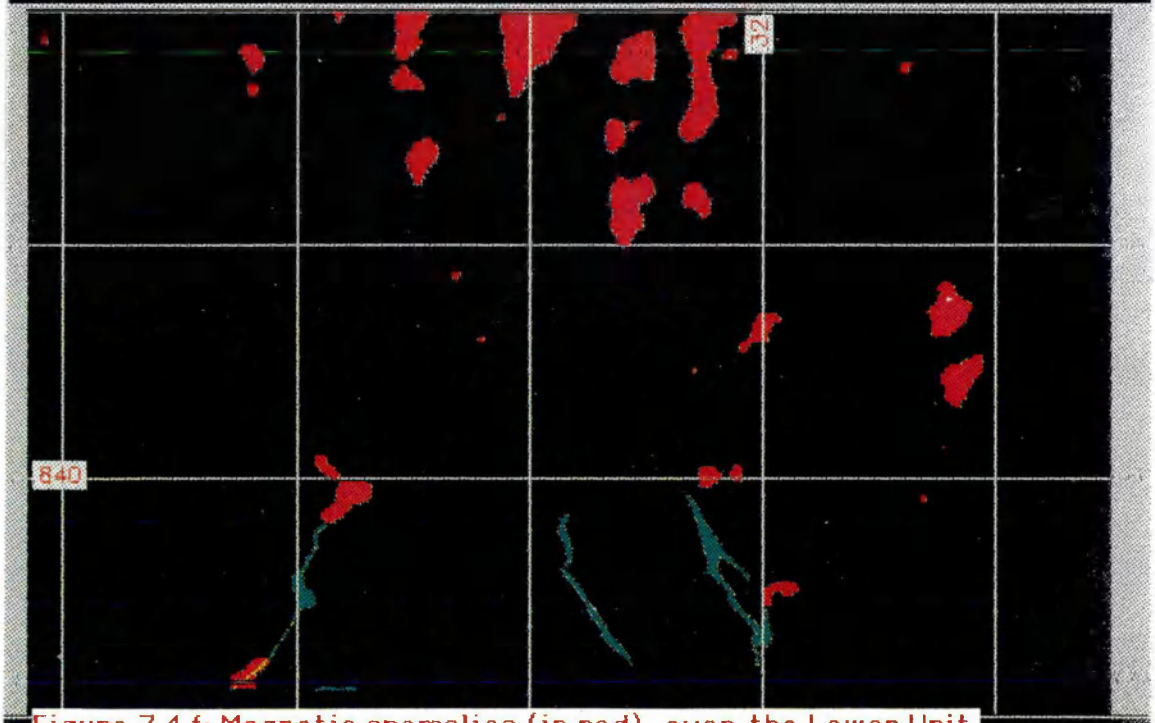


Figure 7.4.f: Magnetic anomalies (in red) over the Lower Unit (in green) of the southern area

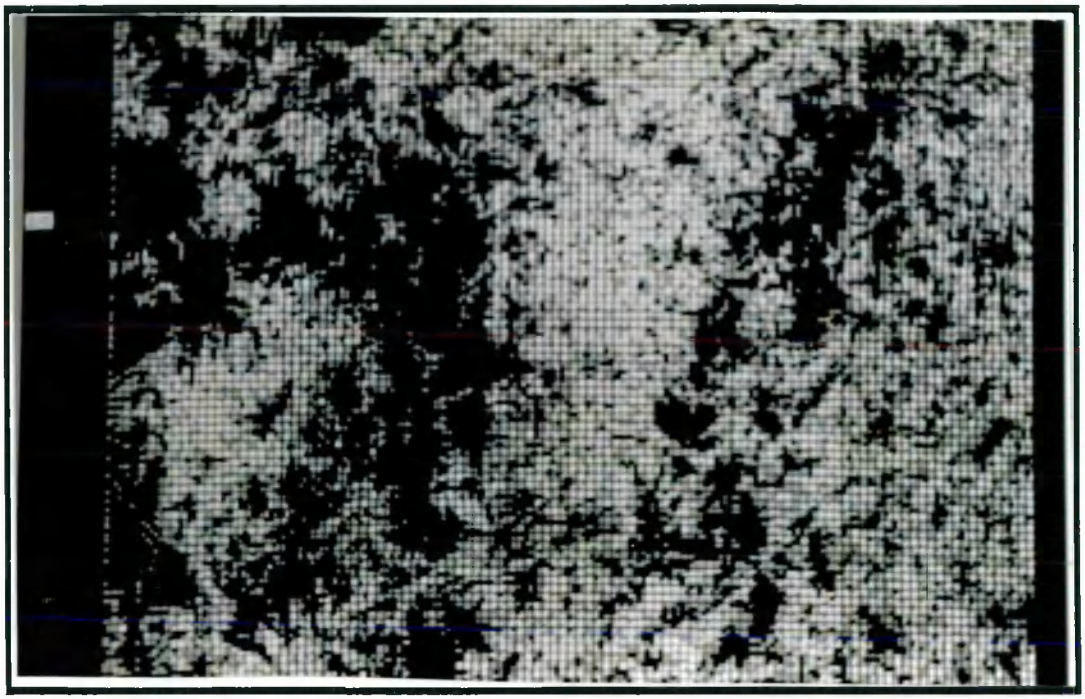

Figure 7.5.a: *Enhanced magnetic image using kernel "A" (northern area)*

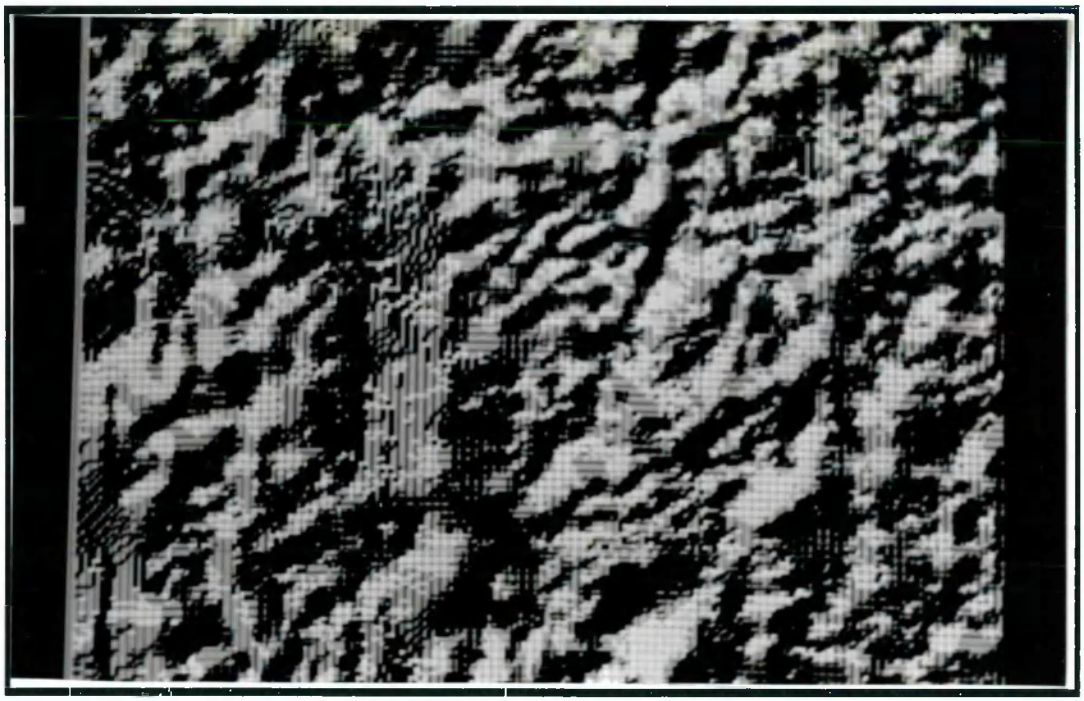

Figure 7.5.b: *Enhanced magnetic image using kernel "B" (northern area)*

0 15 km

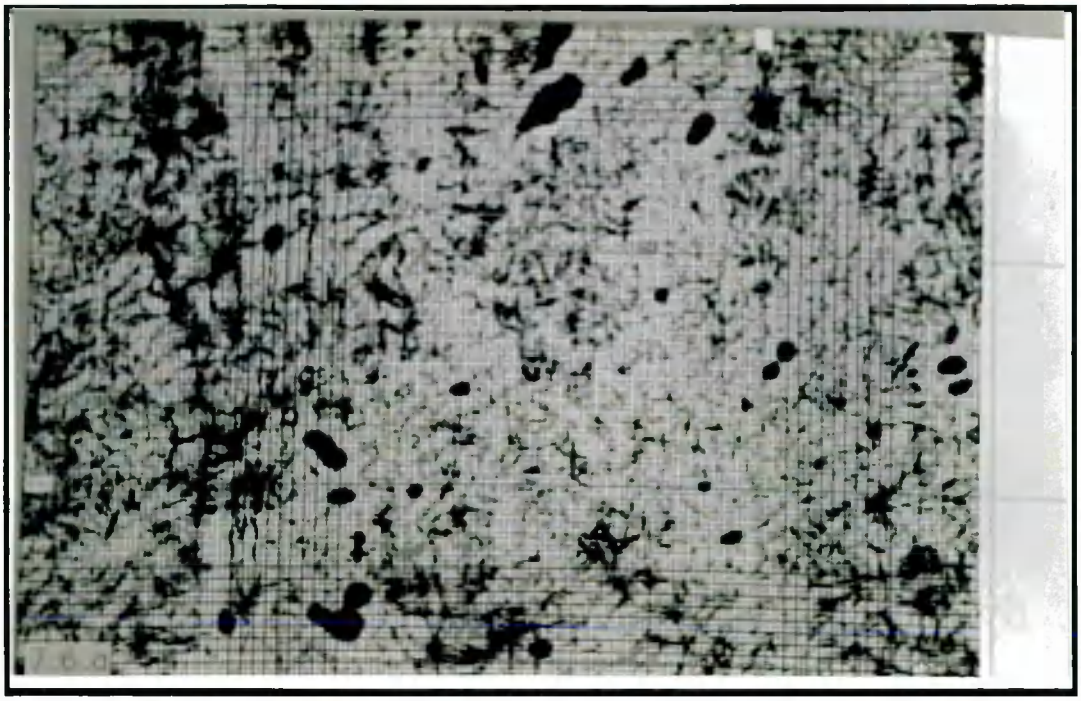

Figure 7.5.c: *Enhanced magnetic image using kernel "A" (southern area)*

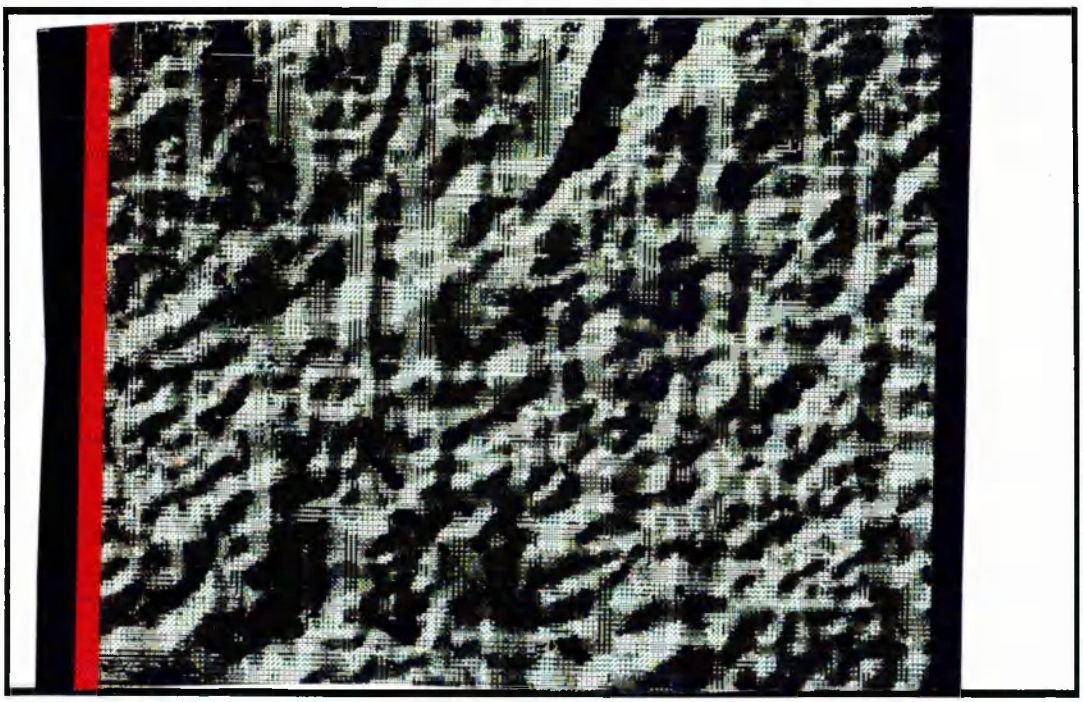

Figure 7.5.d: *Enhanced magnetic image using kernel "B" (southern area)*

0 15 km

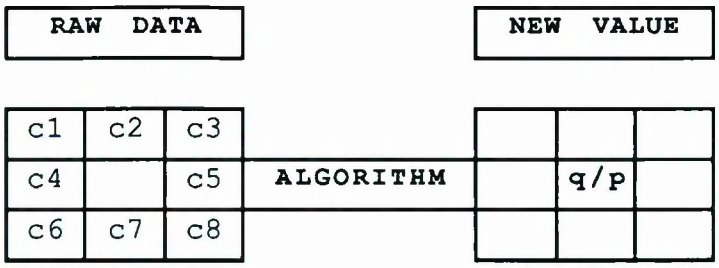


$$\mathbf{p} = (c1 + 2c4 + c6) - (c3 + 2c5 + c8)$$

$$\mathbf{q} = (c6 + 2c7 + c8) - (c1 + 2c2 + c3)$$

Aspect is given one of 24 values based on directions of 090°, 075°, 060°, 045°, and so on. Each direction is given 15 degrees of the 360 degree circle with intervals centred on the E, NE, N, NW, W, SW, S and SE directions. Aspect value is then determined by the interval in which the ratio of **q** to **p** falls. Figures 7.5.b and (d) present the enhanced magnetic images of the part of northern and southern area, respectively.

### 7.5.2 Enhancing radiometric data

The main use of radiometrics is in discriminating surface lithologies, and so it complements aeromagnetic, which is deeply penetrating. To enhance radiometric features the following methodologies were adopted:

a) false colour composite;

b) ratioing;

c) masking, and

d) combining radiometrics with imagery.

The main characteristics of the radiometric images of the northern and southern part of the study area are presented in Table 7.6.

| | NORTHERN AREA | SOUTHERN AREA |
|---|---|---|
| Rows | 223 | 285 |
| Columns | 218 | 325 |
| Min. Northing | 8451250 | 8380000 |
| Max. Northing | 8506750 | 8451000 |
| Min. Easting | 283500 | 257000 |
| Max. Easting | 337750 | 338000 |
| Min. eTh | 13 $s^{-1}$ | 8 $s^{-1}$ |
| Max. eTh | 323 $s^{-1}$ | 321 $s^{-1}$ |
| Min. K | 134 $s^{-1}$ | 3 $s^{-1}$ |
| Max. K | 499 $s^{-1}$ | 442 $s^{-1}$ |
| Min. eU | 24 $s^{-1}$ | 15 $s^{-1}$ |
| Max. eU | 155 $s^{-1}$ | 143 $s^{-1}$ |

**Table 7.6**: *Characteristics of the radiometric images of the study area (250m grid spacing)*

A false colour composite (FCC) of eU, eTh and K was produced to take advantage of the most effective way for displaying raster data, because the visual perception of human vision in grey tone is limited. The most suitable combination was eU, eTh and K as RGB, respectively. Figures 7.6.a and (b) show the FCCs of the part of the northern and southern area, respectively.

In an attempt to suppress information which is common in both images, and at the same time enhance differences, ratioed images were computed, and a colour ratio composite (CRC) was generated (Figure 7.7)

Masking is a technique which provides the user with the capability of defining specific areas of interest within a

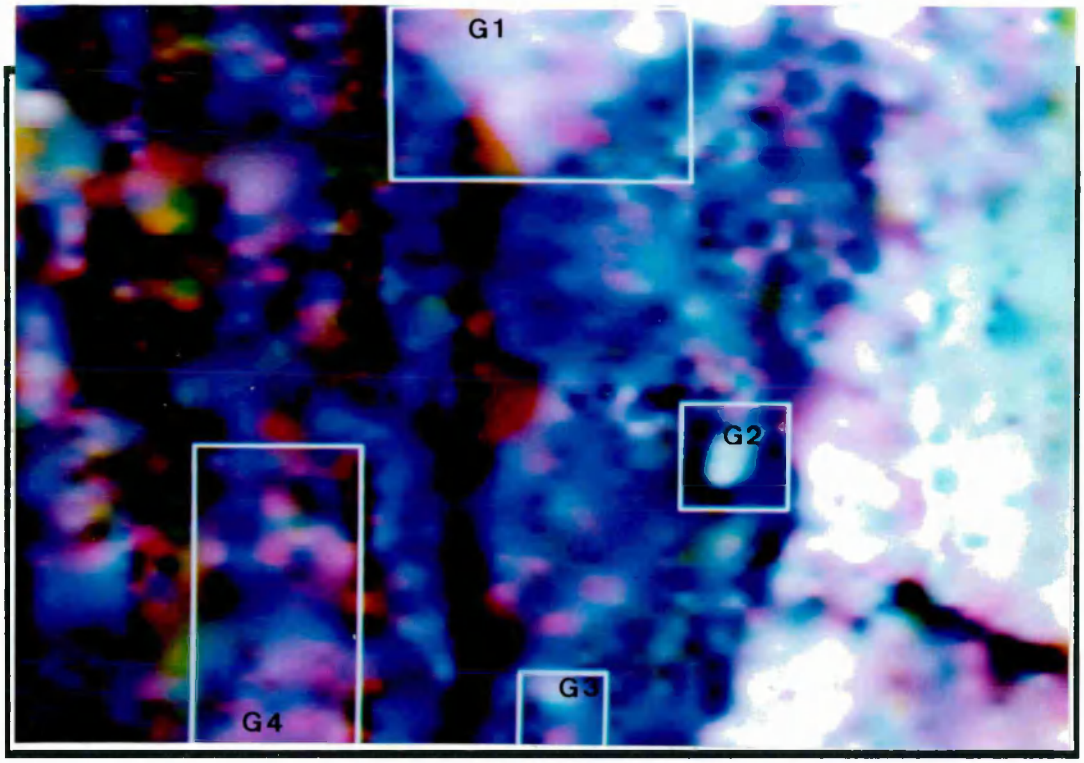


Figure 7.6.a: *A FCC of eU, eTh and K as RGB, of part of the northern area*

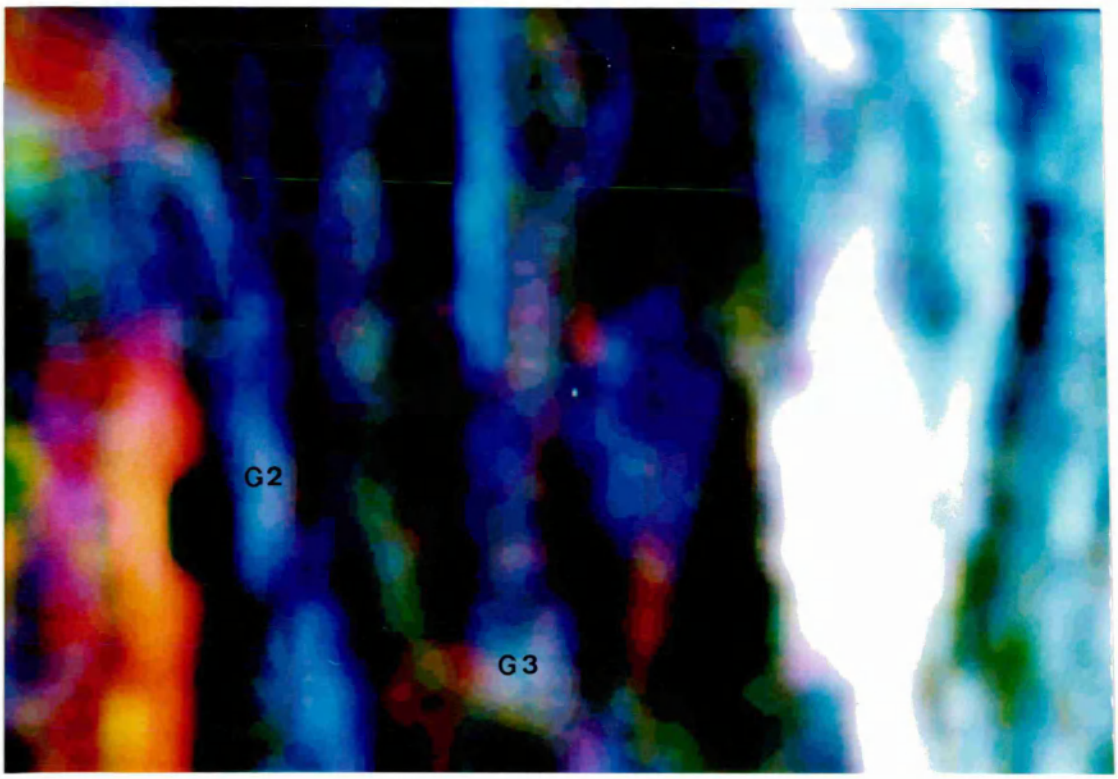


*Figure 7.6.b: A FCC of eU, eTh and K as RGB of part of the southern area*

0 15 km

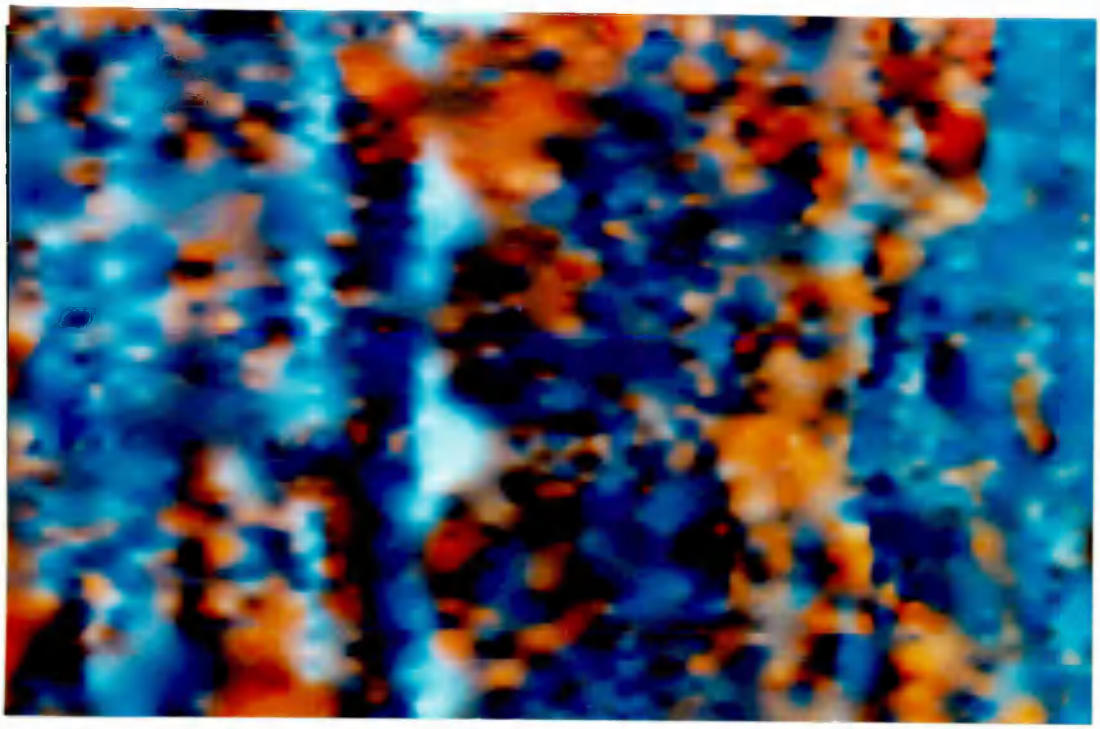

Figure 7.7: *A CRC of radiometric image of the northern area. eU/eTh, eU/K and eTh/K as RGB, respectively*

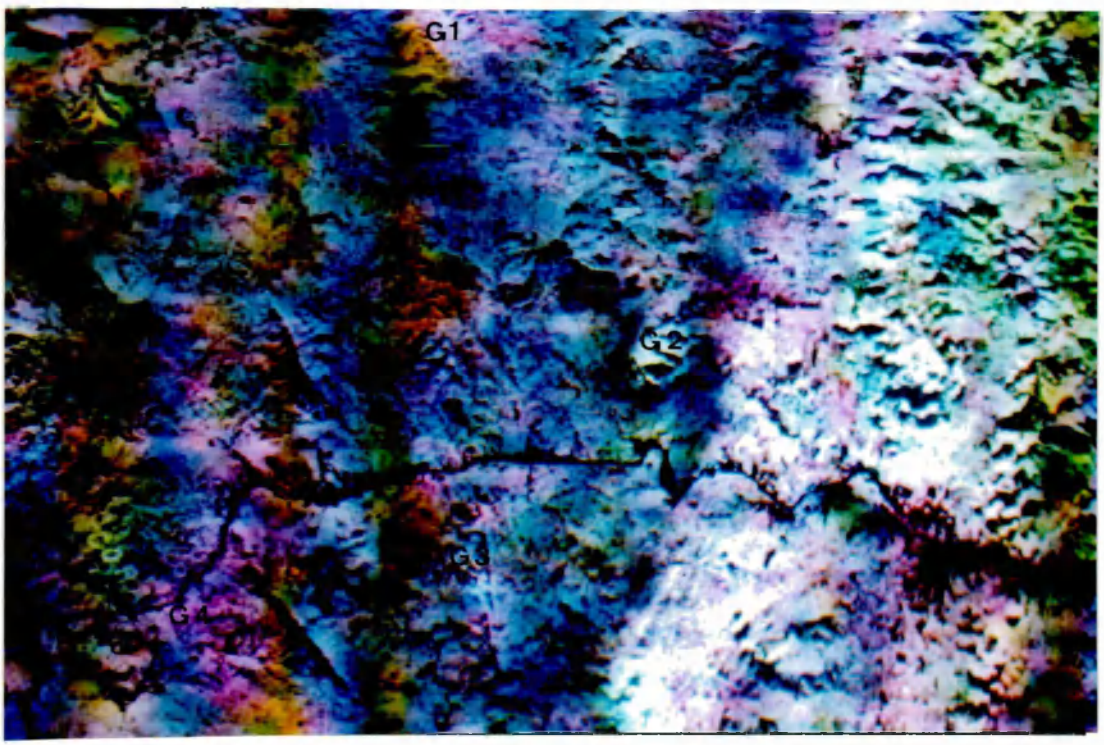


Figure 7.8: *A combination of radar*eU, radar*eTh and radar*K as RGB, respectively of part of northern area*

0 15 km

particular image. These can be specified using regular geometric shapes, circles or strings of corner coordinates. The effectiveness of an analysis is often dependent upon the ability to clearly define the exact data to be studied and to limit the data to this definition. It is important both to be able to define exact areas of interest for specific analysis and to be able to quickly define general areas for an overview.

In this study, I concentrate the interpretation on the radiometric survey undertaken over the Contendas-Mirante belt; thus a mask was applied in both northern and southern areas to create in relief this volcanic-sedimentary sequence. Thus, the granulite sequence to the east and the migmatites to the west were suppressed. A mask was also applied to suppress areas where artifacts are present.

A combination of radiometrics and radar was carried out aiming at allowing a comparison between terrain and geophysical patterns, that is seeking evidence for deep extensions of fractures that control some elements of the terrain. Poor resolution of radiometrics and noise mean that it is difficult to see boundaries. This can be overcome to some extent by incorporating data with finer spatial resolution containing edges related to topography and fractures. Figure 7.8 shows the combination of radar*eU, radar*eTh and radar*K in RGB, respectively.

## 7.6 Interpretation of the results

Magnetic images were interpreted taking into consideration both zones of similar magnetic susceptibility and discontinuities in the images i.e. attempting to identify

lithologies and faults or lineaments. This interpretation will be compared with existing geological maps. The criteria for selecting magnetic units in the magnetic zones was based on the uniformity or non-uniformity of magnetic patterns. The first case would represent data from one source and the other from various sources.

Radiometric images were used for lithological discrimination on the basis of the relative response of the three diagnostic channels. However, for tracing boundaries it is essential to integrate with another data set, such as remotely sensed data, mainly because of the dispersion effects. Detection of lineaments using radiometric images is not precise, but sometimes displacement of zones with similar radiometric levels could indicate faults.

### 7.6.1 Lithological interpretation

In this section I present the results achieved in terms of lithological discrimination using both magnetic and radiometric data.

Pseudocolour rendition of the magnetic data does not allow much lithological discrimination. A magnetic data reduction method (MDRM) is presented here as an attempt to discriminate lithologies. MDRM does not give information about depth, shape or dip of the magnetic bodies, being merely qualitative. However, MDRM enables the identification of areas, in a particular lithological unit, with high magnetic field in which magnetite-rich rocks should be present.

The methodology to apply MDRM was:

a)by using GIS functions to reclassify, the 12 categories of the original geological map were simplified to six, as

follows: the Upper and Lower CMB Units, granites, mafic-ultramafic rocks, migmatites and granulites. (Figures 7.9.a and g);

b)the same GIS function was used to reduce the 255 original categories of the magnetic images to 4 categories as follows: 0 to 127 (0 to b),zone A, 128 to 178 (b to b+2s), zone B, 179 to 210 (b+s to b+2s), zone C, and >210 ( > b+2s), zone D;

c)an overlay operation was carried out using the resultant geological maps and the magnetic images;

d)by using Boolean operation, each lithological unit was analysed separately, in relation to magnetic zones (Figures 7.9.b, c, d, e, f, g, h, i, j, k, m, and n). The lower key by Figure 7.9.b shows the colours used to indicate different types of lithology-anomaly coincidence.

e)statistical parameters were obtained to establish the percentages and areas of occurrence of important features. Table 7.7 shows the areal distribution of the four magnetic zones of the northern and southern area, and Table 7.8 presents the percentages and areal distribution of coincident areas of a particular lithological unit and magnetic zones.

| | **NORTHERN AREA** | | **SOUTHERN AREA** | |
|---|---|---|---|---|
| ZONES | %Tot.area | $km^2$ | %Tot.area | $km^2$ |
| A | 1.89 | 45.24 | 5.57 | 294.75 |
| B | 33.69 | 805.95 | 12.14 | 641.95 |
| C | 48.28 | 1155.17 | 42.37 | 2240.54 |
| D | 16.14 | 386.15 | 39.92 | 2111.07 |

**Table 7.7**: *The areal distribution of the magnetic zones of the northern and southern areas*

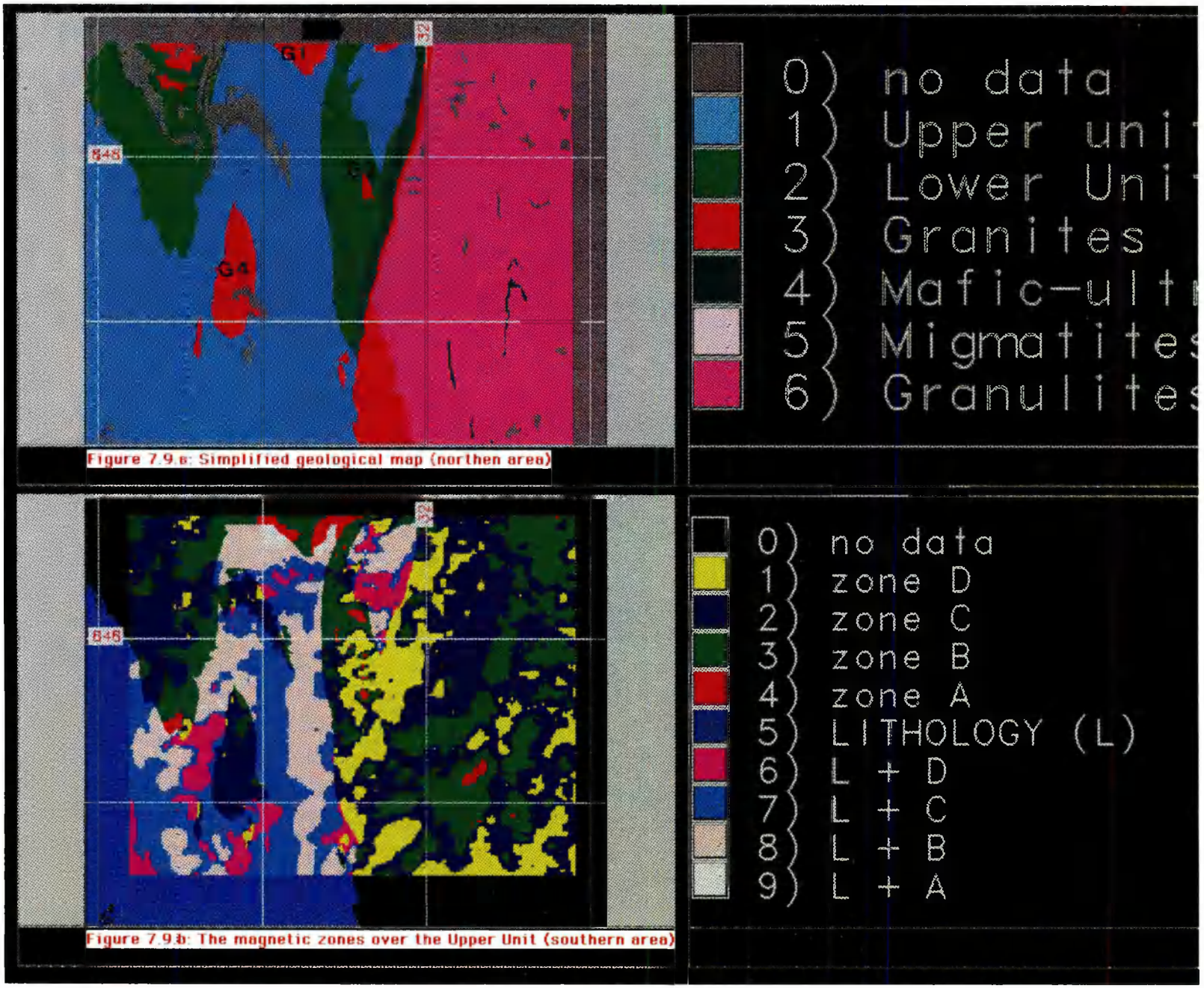


Figure 7.9.a: Simplified geological map (northen area)




Figure 7.9.b: The magnetic zones over the Upper Unit (southern area)

32
848
Figure 7.9.c: The magnetic zones over the Lower Unit (northern area)
32
848
Figure 7.9.d: The magnetic zones over granites (northern area)
32
848
Figure 7.9.e: The magnetic zones over mafic-ultramafic rocks (northern area)
32
848
Figure 7.9.f: The magnetic zones over granulites (northern area)

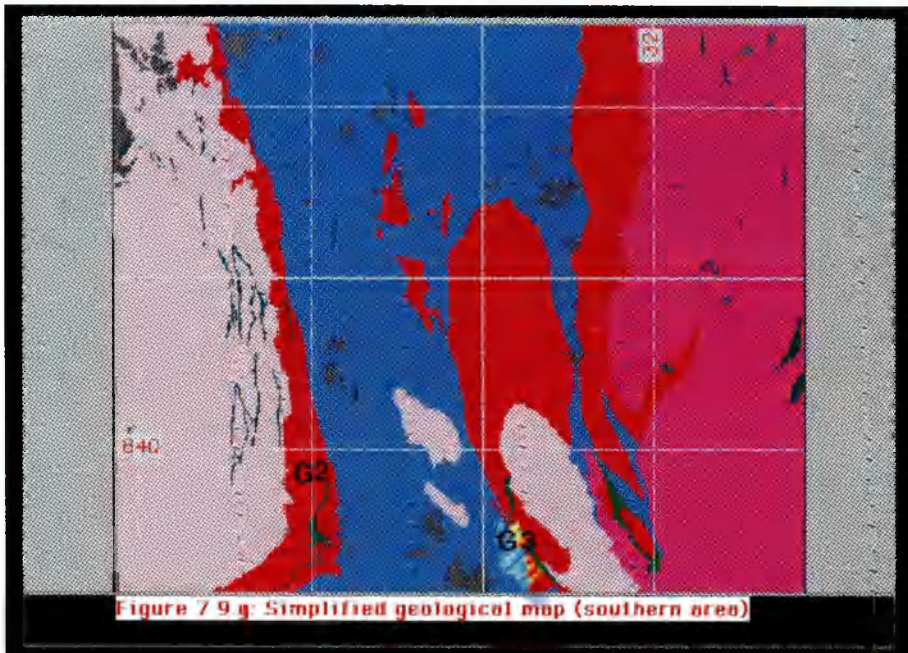


Figure 7.9.g: Simplified geological map (southern area)

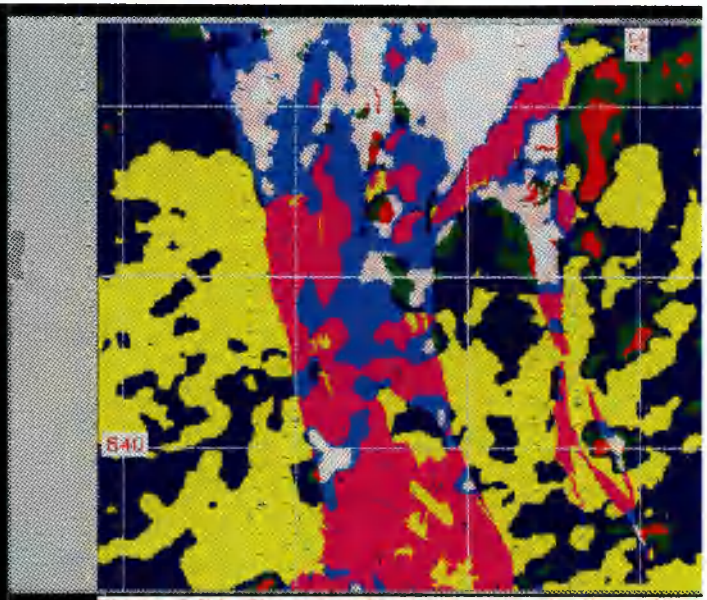


Figure 7.9.h: The magnetic zones over the Upper Unit (southern area)

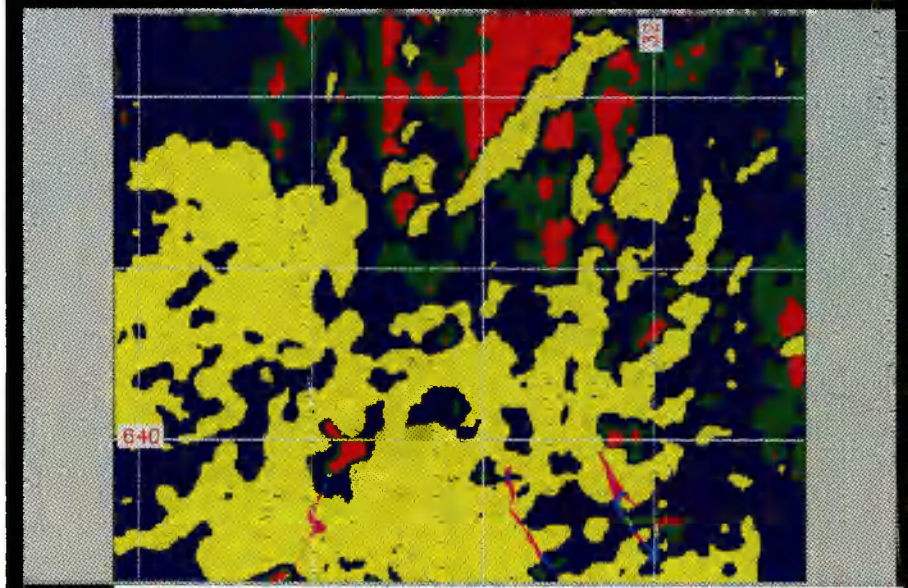


Figure 7.9.i: The magnetic zones over the Lower Unit (Southern area)

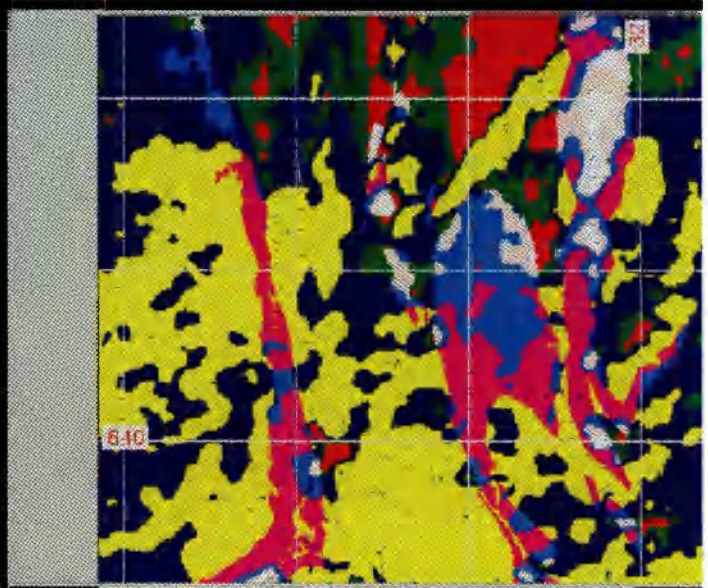


Figure 7.9.j: The magnetic zones over granites (southern area)

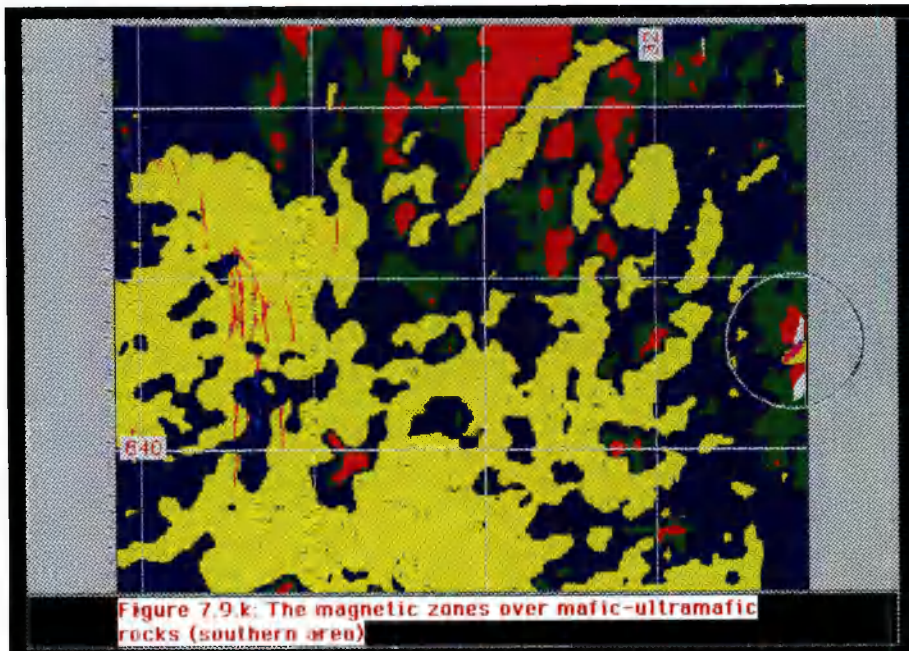


Figure 7.9.k: The magnetic zones over mafic-ultramafic rocks (southern area)

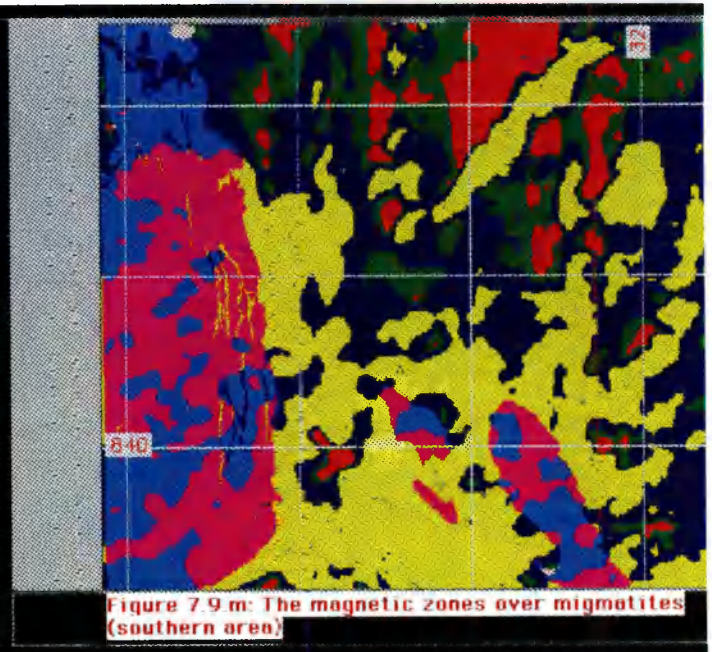


Figure 7.9.m: The magnetic zones over migmatites (southern area)

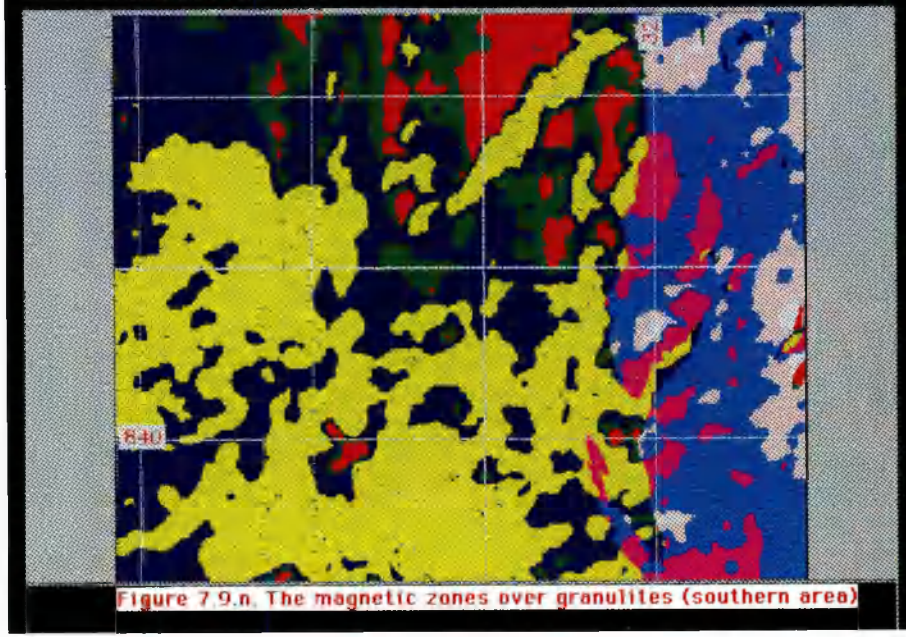


Figure 7.9.n: The magnetic zones over granulites (southern area)

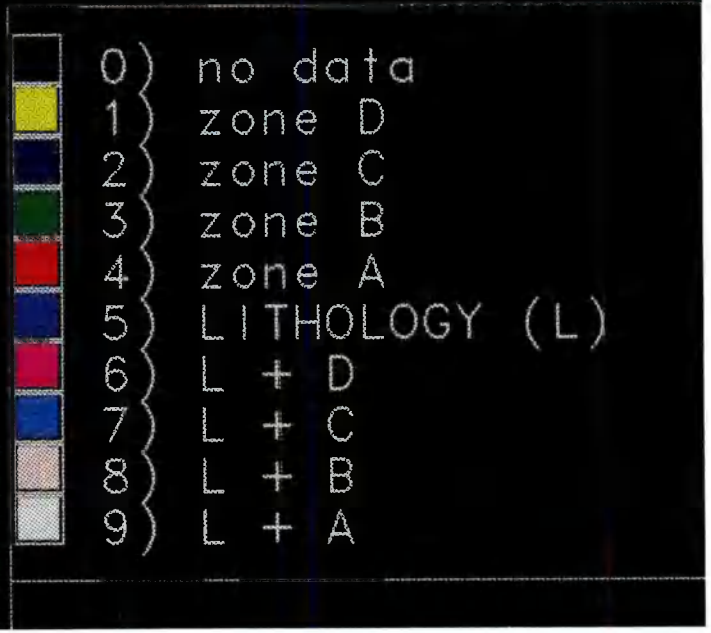

| | NORTHERN AREA | | | | | | | | SOUTHERN AREA | | | | | | | |
|---|---|---|---|---|---|---|---|---|---|---|---|---|---|---|---|---|
| | ZONE D | | ZONE C | | ZONE B | | ZONE A | | ZONE D | | ZONE C | | ZONE B | | ZONE A | |
| | % | $km^2$ | % | $km^2$ | % | $km^2$ | % | $km^2$ | % | $km^2$ | % | $km^2$ | % | $km^2$ | % | $km^2$ |
| UU | 3.6 | 117 | 11 | 360 | 9.1 | 301 | .5 | 15 | 12 | 660 | 9 | 487 | 5 | 265 | 3.8 | 200 |
| LU | 1.7 | 57 | 4.3 | 141 | 3.6 | 118 | .3 | 9.5 | .3 | 14 | .2 | 8.9 | - | - | - | - |
| GR | .9 | 31 | 2.7 | 90 | .8 | 28 | .3 | 8.8 | 8.4 | 445 | 6.3 | 334 | 2.3 | 121 | 1.1 | 59 |
| MU | .9 | 30 | .7 | 22 | .4 | 12 | - | - | .4 | 20 | .2 | 13 | - | - | .1 | 4.9 |
| MIG | - | - | - | - | - | - | - | - | 13 | 695 | 10 | 541 | .4 | 5.7 | - | - |
| GRAN | 4.1 | 136 | 14 | 452 | 8.5 | 281 | .15 | 5 | 4.5 | 239 | 16 | 799 | 4.4 | 235 | .5 | 25 |

**Table 7.8**: *The areal distribution and percentage of coincident areas of geological units (UU=Upper Unit, LU=Lower Unit, GR=granites, MU=mafic-ultramafic rocks, MIG=migmatites and GRAN=granulites) and magnetic zones of the northern and southern area*

To demonstrate the use of the MDRM, three examples are presented here.

a)a gold target in development is located in the northern area. This occurrence is closely related to BIF hosted in the Lower Unit of the CMB (see Chapter 3, section 3.6). Figure 7.9.c shows circled, the coincident area of a high magnetic zone (zone A) and the Lower Unit at the same place as the gold occurrence. Other areas with this coincidence are shown in red stipple.

b)the Rio Jacare sill hosts an important Ti-V-PGE deposit related to magnetite-rich pyroxenite (see Chapter 3, section 3.6). Figure 7.9.e presents circled, the coincident area of a moderate magnetic field (zone B) over part of the Rio Jacare sill at the same place of the location of the Ti-V-PGE mine. Other areas of coincidence are indicated by red stipple.

c)Figure 7.9.k shows circled, in the southern area, the coincident plots of a high magnetic field (zone A) and ultramafic rocks.

Chapter 9 will discuss the coincident areas of the Lower Unit and mafic-ultramafic rocks with high magnetic field (see Figures 7.4.d and f) in the context of other data sets.

To seek lithological discrimination using radiometric data, ratioed images and FCCs were used. The methodological approach used to apply the combination of eU, eTh and K for lithological discrimination was:

a)to identify anomalous responses of the radiometrics by visual analysis of FCCs, combined radiometrics with radar (Figure 7.8) and ratioed images.

b)to compare the results with the existing geological maps, and

c)by using Boolean operations to extract anomalous areas (to be addressed in the final GIS environment).

Although ratioed images have been used successfully elsewhere for lithological discrimination (*Harris*, 1989), in this case they did not enhance the difference between granites and other lithologies. Despite the promise of the method, the low signal to noise ratio resulted in very poor quality images that are not interpretable (see Figure 7.7)

FCCs of eU, eTh and K as RGB of the northern area (Figure 7.6.a) and southern area (Figure 7.6.b), and radar*eU, radar*eTh and radar*K, as RGB of the northern area (Figure 7.8), proved to be very useful for some lithological discrimination. Areas in white represent regions with high

radiometric responses in all channels. At the southeastern corner, the black linear feature is related to a lake.

Proportionate mixes of the primary colours result in magenta, cyan and yellow colours that can be interpreted on a relative basis as mixtures of the three spectrometer channels. A comparison with the geological maps (Figures 7.9.a and 7.9.g) shows a good correlation and in fact has improved the geological knowledge of the area. Large areas with high eU, eTh and K are correlated to granulitic sequences in the eastern part of the study area. This combination has also been very useful for mapping granitic bodies and possibly areas of hydrothermal alteration.

The possibility of separating different granites is important as pointed out by *Slaney* (1988) where tin mineralisation is related to a particular granitic phase in Nova Scotia (Canada) with a specific radiometric response.

According to the radiometric responses, granites of the study area appear to be divisible into four different types, though no attempt can be made to truly define them in terms of exact proportion of U + K + Th due to the poor quality of the data and uncertainties in the gamma-ray absorption. G1 appears mostly white with pale red and blue patches, G2 presents white and blue patches, G3 shows magenta, white and cyan patches, and G4 appears magenta and blue patches (Figure 7.6.a).

Table 7.9 shows the main characteristics of these granites.

| GRANITE | eU($^{-s}$) | eTh($^{-s}$) | K ($^{-s}$) | %Tot.area | km$^2$ |
|---|---|---|---|---|---|
| G1 | 106-130 | 101-202 | 273-363 | 1.34 | 44.3 |
| G2 | 99-121 | 151-273 | 239-306 | 0.86 | 28.3 |
| G3 | 81-104 | 116-156 | 269-442 | 1.39 | 45.7 |
| G4 | 91-105 | 101-125 | 253-276 | 2.8 | 94.9 |

**Table 7.9**: *The main characteristics of the four different granites of the study area*

In the southern part of the study area (Figure 7.6.b) the granulitic sequence located in the eastern part presents the same patterns of the northern area. To the west, areas with yellow and orange colours which represent high eU, eTh and low K, and high eU, eTh and moderate K, respectively, correspond to gneiss-migmatitic lithologies of the Gaviao Block. Only G2 and G3 were recognized in the southern area (Figure 7.6.b) which represent 2.8% (148.4 km$^2$) and 0,6% (32.0 km$^2$) of the total area, respectively.

### 7.6.2 Structural interpretation

In this section I present the results achieved by using edge enhancement techniques (Figures 7.3.g, h, i, j and 7.5 a, b, c, d) on magnetic images. The detection of magnetic lineaments using this techniques is clearly useful for enhancing features which probably represent structural lineaments extending to deep levels.

Since the aeromagnetic method is picking up signatures from depth, the presence of strong linear features may suggest deep seated structures, which may have had greater controls over hydrothermal circulation than many of surface mapped faults.

The structural interpretation carried out on enhanced magnetic images shows that two preferred magnetic northeastern and northwestern trends can be recognized (Figures 7.10 and 7.11) of which there was very little or no hint on the original images (see Figures 7.2.a and 7.3.a).

It is expected that magnetic lineaments might be coincident with mapped faults. A comparison between the magnetic trends and mapped and interpreted lineaments from the TM and radar images can be seen from Figures 7.10 and 7.11, and Figures 6.14 and 6.19 in the previous Chapter. In general terms, the interpretation has shown that there is a correspondence between the NW mapped and interpreted lineaments and NW magnetic lineaments. The improvement in the structural framework of the study area can be noticed by the presence of conspicuous NE magnetic lineaments of which very few were marked on the previous maps.

## 7.7 Discussion of the results

Although direct discoveries of ore deposits are not frequent using geophysical methods, when integrated with other data sets, they have substantially promoted the study of geological features and stimulated new ideas relevant to the exploration for precious and base metals.

The digital image processing of airborne geophysical data of the study area has shed interesting new light on geological mapping and in consequence mineral exploration, by revealing structural and lithological features which were difficult to discern from conventional contour maps and/or stacked profiles.

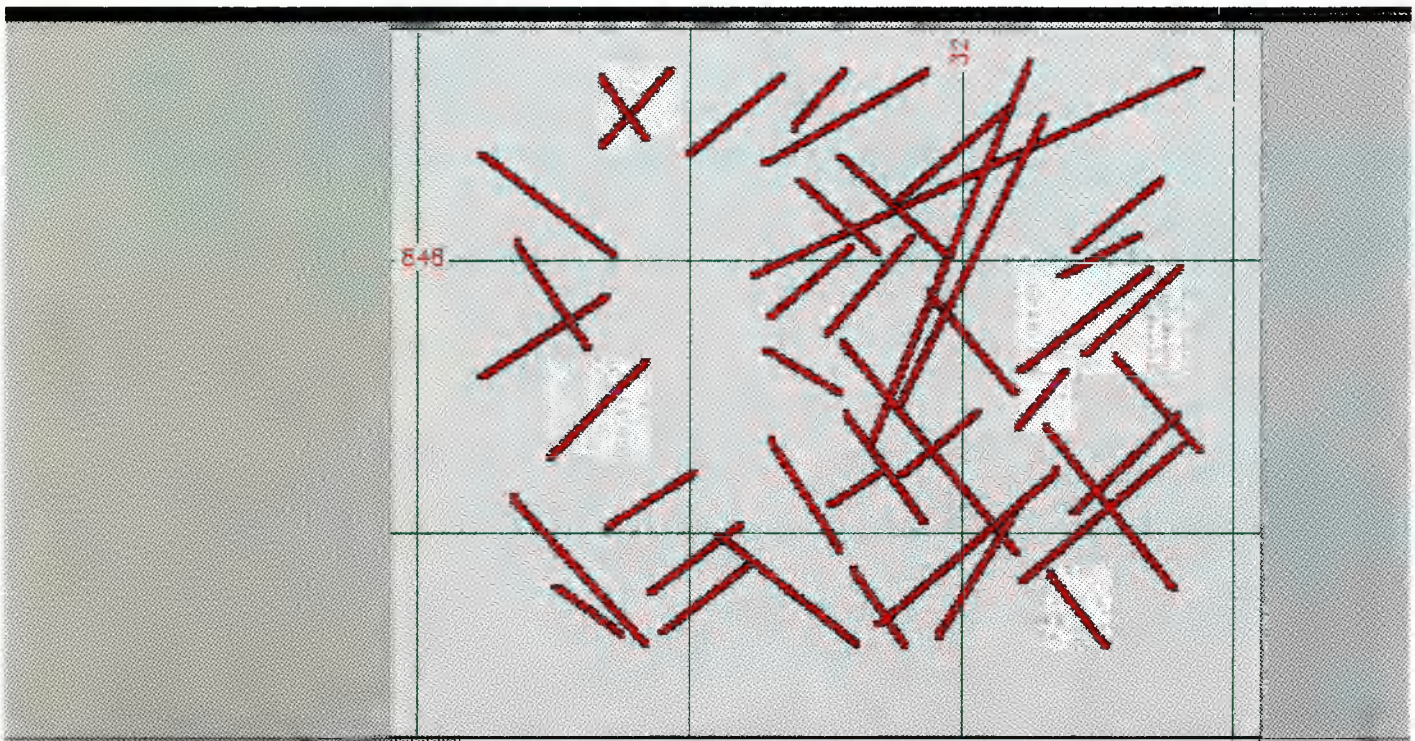


Figure 7.10: Structural analysis of the magnetic image (northern area)

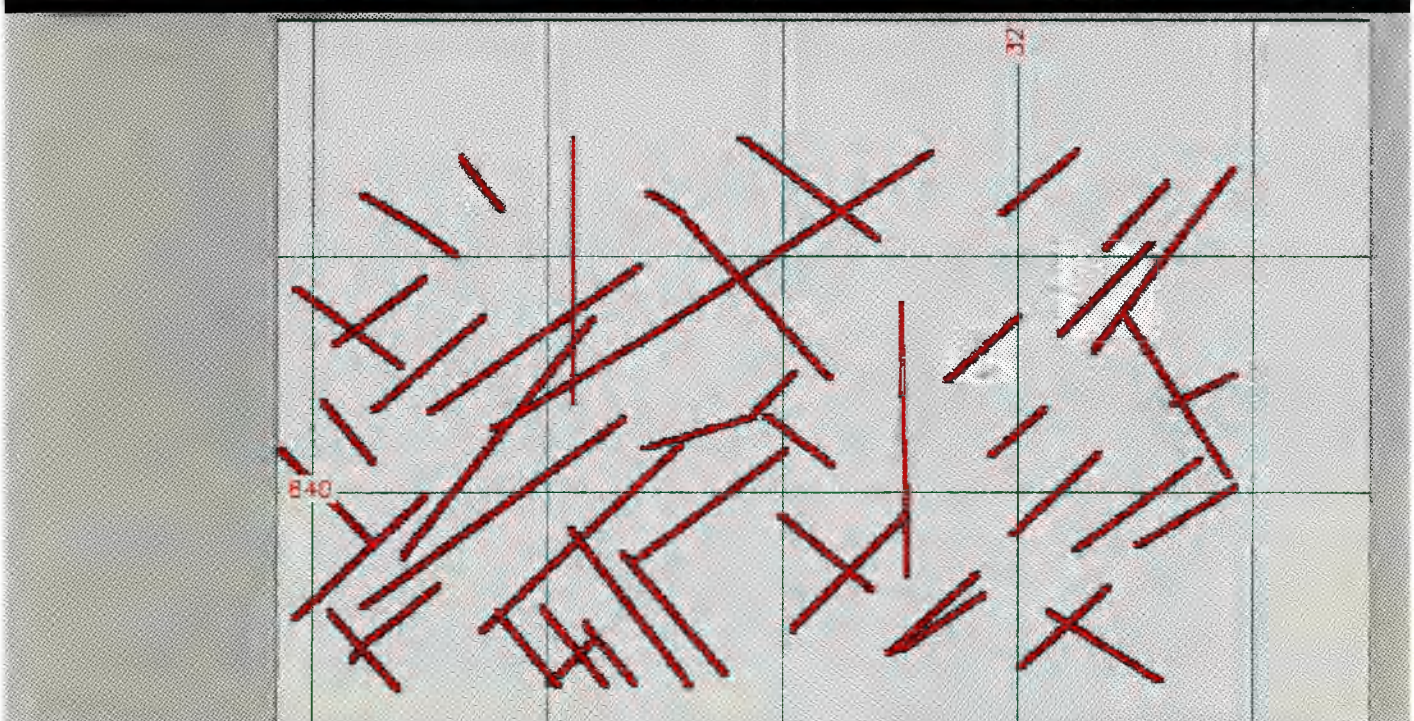


Figure 7.11: Structural analysis of the magnetic image (southern area)

The magnetic data reduction method (MDRM) is shown to be a valuable tool for defining areas with the presence of magnetite-rich rocks. Areas in the vicinity of well known occurrences with the same characteristics were recognized, increasing the expectation of new occurrences. Especially the anomalous areas in the Rio Jacare sill where along 40 km only five areas have been selected, one of them representing the TI-V-PGE mine (Maracas Mine) with the same magnetic response. The scattered selected areas have close relationships with the described pipe-like model for the Maracas Mine (see Chapter 3, section 3.6). The detection of magnetic lineaments using edge enhancing techniques, has proved to be useful for enhancing features which represent structural lineaments, some of which may have greater controls over hydrothermal circulation.

The first observation from the radiometric images is that although the results are as expected for many lithologies (except for granulites) there is a hint that the mapping failed to identify the extent of some lithologies correctly. That is because the radiometrics are blurring boundaries due to all sort of effects: poor resolution, high noise, soil movement, weathering, variable vegetation cover and soil moisture, etc.

The unusually high eU, eTh and K content found over granulites may be related to a different soil depth, variable weathering processes, vegetation cover and soil moisture. The fact that some granites show different radiometric responses, indicates that the radiometrics may be revealing subtle differences in granite geochemistry there are important in mineral exploration, especially for gold. Moreover, there may be more granites than have been mapped. Although there is no

correspondence between granite type G3 and the available geological maps of the northern area, the radiometric data strongly suggest the existence of such a granitoid, perhaps hidden by thick soil or overlooked in the reconnaissance geological mapping.

# CHAPTER 8: THE GEOCHEMICAL DATA

## 8.1 Introduction

Concentration of a single element is exceptional in nature. It is more common to find a group of related elements with anomalously high concentrations in a particular mineral deposit and the dispersion haloes associated with it. Such a suite of elements is frequently characterized by similar electronegativities and ionic radii and hence position in the periodic table.

In stream sediment reconnaissance, the dispersion of elements is controlled by Eh-pH conditions, colloidal phenomena, biological and hydrolytic reactions and diffusion, as well as stream flow. Furthermore, some physical characteristics play an important role, such as the different resistances of minerals to alteration and weathering processes (*Levinson*, 1980).

All these interrelated processes do not necessarily predict which elements will be found concentrated together. Empirical

geochemical data built up over many years provide the means to group diagnostic element associations. (*Boyle*, 1974).

Another important feature of geochemical surveys is the capability of indirectly determining the existence of specific elements. This is achieved by using certain elements as indicators called "tracers" or pathfinders to predict the presence of other elements which are frequently too low in concentration to be detected. For instance, in certain terrains the presence of As, Sb and Bi (*Levinson*, 1987) may indicate the existence of gold and Ni may imply Platinum Group Elements (PGE) in its vicinity (*Boyle*, 1979).

Dispersion processes reduce the concentration of elements in element associations because of the physicochemical environment with increasing distance from their source.

This chapter describes the methodology used for extracting useful information from geochemical data, analyses the most common alteration and elemental associations found in Archaean gold deposits, and presents the final product to be incorporated in the GIS together with information from the other data sets (Chapter 9).

## 8.2 Description of the data set

In drainage reconnaissance surveys the sampling technique is of primary importance. Too many types of rivers and too many lithological units are generally sampled in any one data set. Sampling drainages of different orders can cause severe interference in the concentration of the element because of the different controls of dispersion processes and dilution effects. Interpreting a data set over an area with diverse lithological units can be misleading. Element concentrations

are a function of lithological units: what is an anomalous value in the context of one lithology may be part of the background for another, eg. 72 ppm is background for mafic igneous rocks, but anomalous for a granite (*Rose et al.* 1979).

The best way to limit the sample heterogeneity due to varying pH, organic content and grain size, is to split the survey into drainages of different orders and separate lithological units when possible, and to statistically interpret each of them separately. However, even if this is possible the same degree of precision cannot be achieved in drainage surveys as in soil or biogeochemical surveys where closely comparable samples are possible. However, such better controlled surveys are difficult to conduct over large areas, where soil type and vegetation vary markedly.

The stream-sediment samples of the study area were collected only from small channels draining catchment areas typically in the range of 2 to 5 $km^2$. Due to the geological complexity of the study area, drainage samples obtained from areas with the same lithology were not feasible. Instead, the samples were classified into generalised geochemical domains that were separately interpreted. Statistical parameters for each domain were established to compare the results and to define regional backgrounds and thresholds.

Table 8.1 presents the geochemical domains (A-D) related to specific lithologies.

| Geochemical domains | Lithologies |
|---|---|
| A | Quat. and Tert. sediments |
| B | Contendas-Mirante belt |
| C | Migmatites and gneisses |
| D | Granulites |

**Table 8.1**: *Geochemical domains and related lithologies of the study area*

According to *Lepeltier* (1969) the frequency distribution of elements that are important to geochemical exploration in stream sediments follows a lognormal law. These concentrations must be statistically analysed and several parameters calculated.

The first to be defined is the background (b). The background corresponds to the mode (the value which occurs with the greatest frequency) and median values (the value midway in the frequency distribution), and is the geometric mean (the sum of all observations divided by the number of observations) of the results. The geometric mean is a more significant value than the arithmetic mean. It is also a more stable statistic, less subject to change with the addition of new data and less affected by high values.

The second important parameter to define is the standard deviation (s) of the data. The third parameter is the threshold, which is a function of these two statistics. The threshold, or upper limit, is conventionally taken as the value above which the data are considered to be anomalous. The threshold (t) can be defined by using two different methods: (a)by the equation: $t = b+2s$, where t is the threshold, b is the background and s is the standard deviation, or (b)graphically, as the distribution of the elements have a

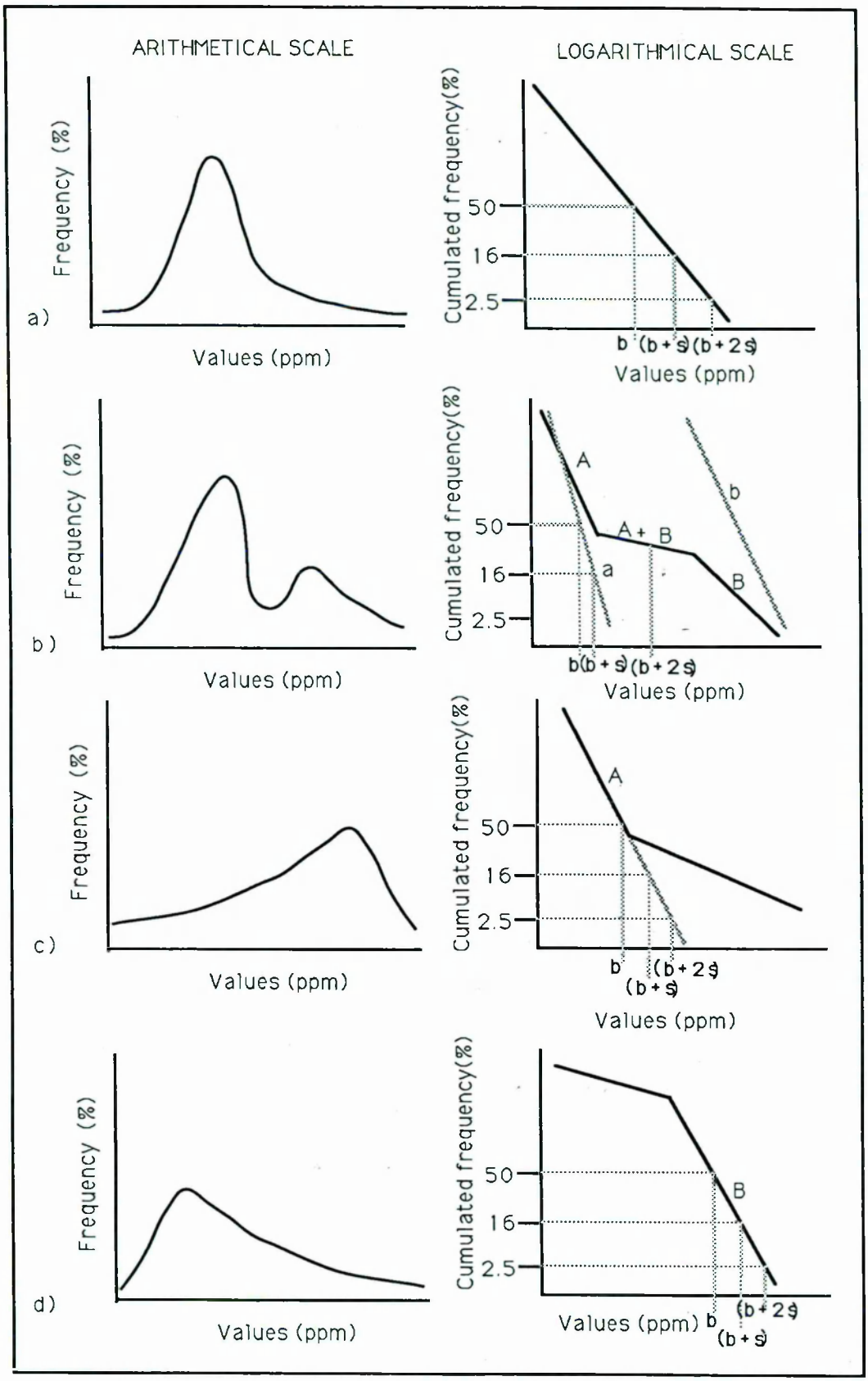


Figure 8.1. : *Frequency distributions. a)homogeneous populations. (b), (c) and (d) heterogeneous populations*

lognormal pattern, 95% of the individual values fall between b+s and b-2s, that is to say that only 2.5% of the population exceeds the upper limit b+2s, this upper limit is conventionally taken as the threshold level. Geochemical data sets can be classified into homogeneous and heterogeneous populations. A homogeneous population (Figure 8.1.a) is represented as straight line on a logarithmical scale, and b and t can easily be defined as shown. Heterogeneous populations include:

a)a mixture of two populations. The arithmetical graph gives two peak histograms and the logarithmical graph shows two breaks (Figure 8.1.b) On this diagram branch "A" corresponds to the background population, branch "A+B" to a mixture of background and anomalous populations, and branch "B" to the anomalous population. By splitting the data at a value taken around the middle of the branch "A+B", it is possible to separate the total data set into two elementary ones appearing as "a" and "b" (Figure 8.1.b). The general background and b+s are taken with branch "a", and the threshold as the abscissa of the middle of branch "A+B";

b)an excess of high values. The arithmetical graph gives a frequency curve skewed to the right (Figure 8.1.c). To define the geochemical parameters the branch "A" should be extended as a straight line and the background and threshold are taken with the extended branch (Figure 8.1.c);

c)an excess of low values. The arithmetical graph gives a frequency curve skewed to the left (Figure 8.1.d). Provided that the proportion of the low values is less than 20%, they do not interfere in the definition of b and t, which are taken

on the branch "B" (Figure 8.1.d). If the low population is bigger than 20% it is not recommended to take the geochemical parameters graphically.

The fourth parameter is the data set hierarchical levels. The minimum and maximum values which correspond to the whole interval can be divided into four priorities based on statistical parameters. Priorities of fourth, third, second and first order in this work are referred to categories corresponding to 0 to b, b to b+s, b+s to b+2s and >b+2s, respectively. Unfortunately, this was the form in which the data were available, the raw ppm values being inaccessible.

The fifth parameter is the correlation between data sets. This was achieved by using the Pearson product moment correlation coefficient.

Although almost the whole study area is covered by geochemical stream sediment surveys (SSS), only the southern part representing 3320 $km^2$ or 30% of the whole area, concern us here. This limitation is derived from the good quality of the SSS undertaken in this area, in terms of sample density, analysed elements and also the geological and geophysical data coverage.

By using this data base, 2024 sample locations were defined. The 14 selected elements (As, Ba, Co, Cr, Cu, Fe, Mg, Mo, Ni, Nb, Pb, Sr, Ti and V) were defined because they act in some way as gold pathfinders (*Boyle*, 1978). Data for Au itself and the pathfinders Bi and Sb are not available. In the study area, the statistical parameters calculated are shown in table 8.2.

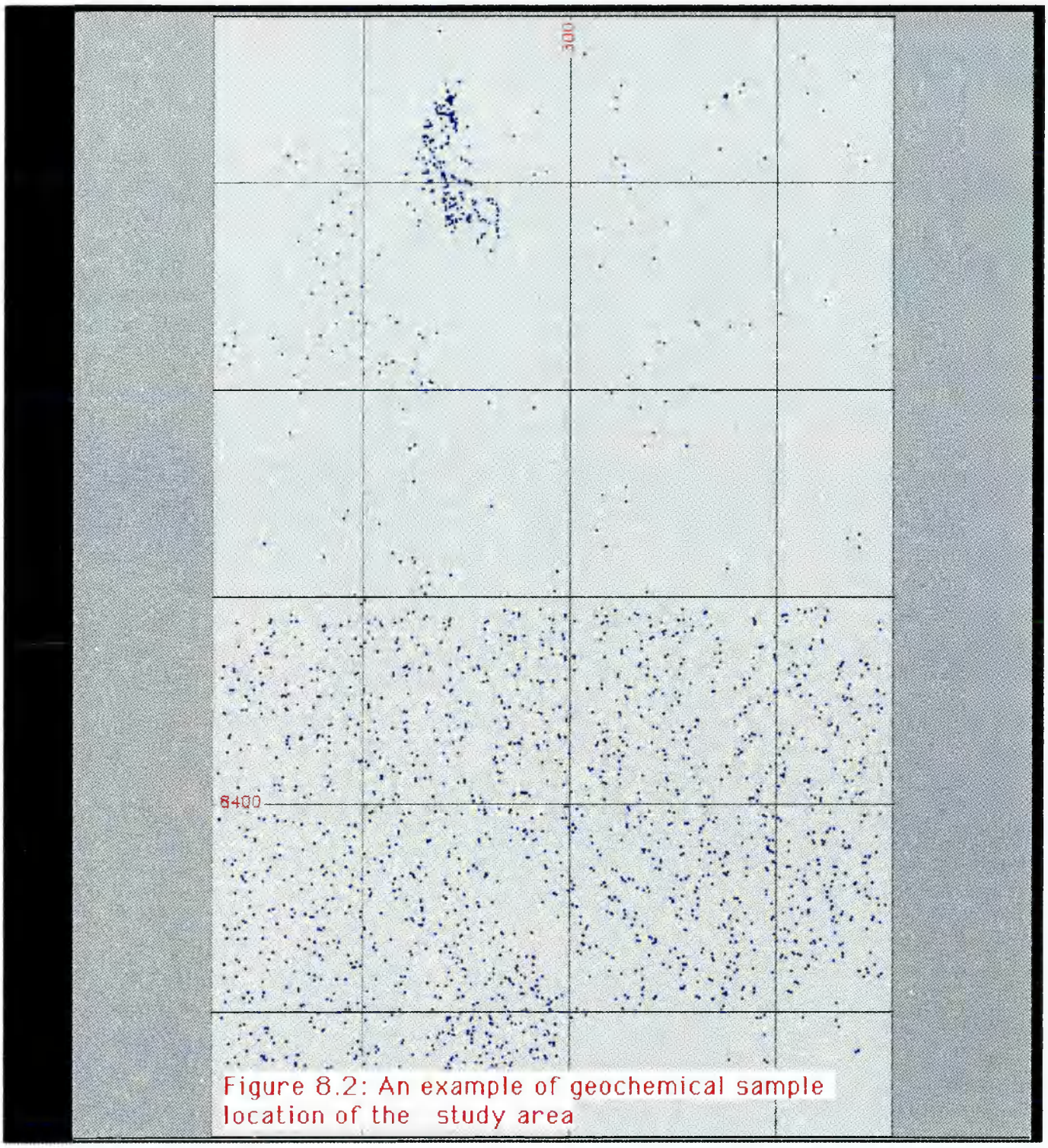


Figure 8.2: An example of geochemical sample location of the study area

| | Geochemical domains (from Table 8.1) | | | | | | | | | | | |
|---|---|---|---|---|---|---|---|---|---|---|---|---|
| | (B) Contendas-Mirante belt | | | | (C) Migmatites, gneisses | | | | (D) Granulites | | | |
| Ele-ment | b ppm | s ppm | b+s ppm | b+2s ppm | b ppm | s ppm | b+s ppm | b+2p ppm | b ppm | s ppm | b+s ppm | b+2s ppm |
| As | 1 | 1.5 | 2.5 | 4 | 0.7 | 0.80 | 1.50 | 2.30 | 0.9 | 1.05 | 1.95 | 3 |
| Ba | 286 | 255 | 541 | 796 | 294 | 243 | 537 | 780 | 489 | 397 | 886 | 1283 |
| Co | 14 | 13 | 27 | 40 | 12 | 11 | 23 | 34 | 12 | 12 | 24 | 36 |
| Cu | 19 | 19 | 38 | 57 | 11 | 10 | 21 | 31 | 17 | 20 | 37 | 57 |
| Cr | 103 | 177 | 280 | 457 | 63 | 120 | 183 | 303 | 63 | 156 | 219 | 375 |
| Fe** | 2.5 | 2.0 | 4.5 | 6.5 | 1.8 | 1.70 | 3.5 | 5.2 | 2.2 | 1.8 | 4.0 | 5.8 |
| Mg** | 0.29 | 0.39 | 0.68 | 1.07 | 0.28 | 0.5 | 0.78 | 1.28 | 0.13 | 0.23 | 0.36 | 0.59 |
| Mo | 8 | 6 | 14 | 20 | 7 | 14 | 11 | 15 | 7 | 3 | 10 | 13 |
| Ni | 29 | 34 | 63 | 97 | 22 | 31 | 53 | 84 | 21 | 26 | 47 | 73 |
| Nb | 20 | 18 | 38 | 56 | 21 | 23 | 44 | 67 | 33 | 49 | 82 | 131 |
| Pb | 21 | 13 | 34 | 47 | 21 | 14 | 35 | 49 | 38 | 29 | 67 | 96 |
| Sr | 198 | 112 | 310 | 422 | 21 | 12 | 33 | 45 | 165 | 61 | 226 | 287 |
| Ti* | 0.43 | 0.8 | 1.23 | 2.03 | 0.36 | 1.03 | 1.38 | 2.42 | 0.57 | 1.09 | 1.66 | 2.75 |
| V | 72 | 94 | 166 | 260 | 211 | 263 | 474 | 737 | 44 | 54 | 98 | 152 |

** % **Table 8.2**: *Geochemical parameters of the study area*

Figure 8 3.a, (b) and (c) present the correlation coefficient matrix. In the Contendas-Mirante domain the best correlations are: V-Fe-Ti-Co-Cr-Ni, Co-Cr-Ni, Fe-Cr-Co, Fe-Cu and Fe-Ti. In the migmatite-gneiss domain the best correlations are: V-Fe-

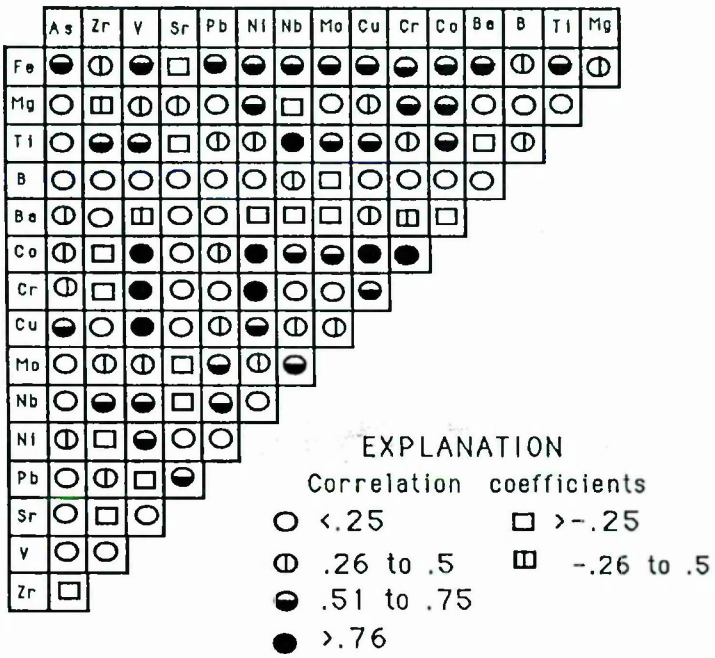


Figure 8.3.c: *Correlation matrix in the Granulite domain.*

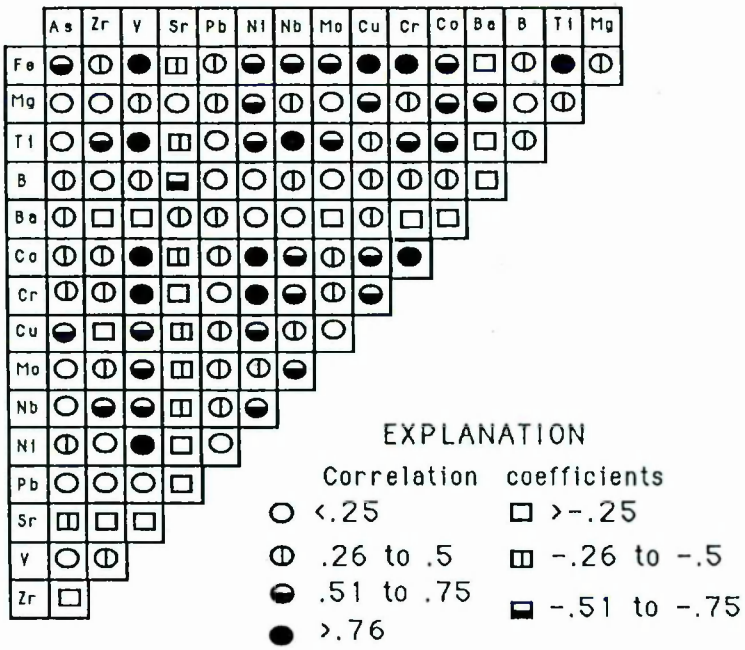


Figure 8.3.a: *Correlation matrix in the Contendas-Mirante domain*

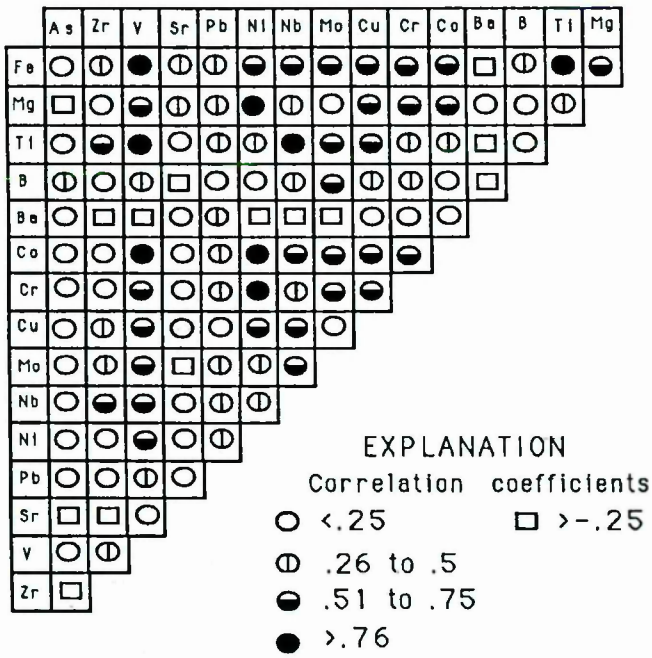


Figure 8.3.b: *Correlation matrix in the Migmatite-gneisses domain*

Ti-Co, Ni-Mg-Co-Cr and Fe-Ti. In the granulite domain the best correlations are:V-Co-Cr-Cu, Ni-Co-Cr, Ti-Nb, Cu-Co and Cr-Co.

Traditionally, interpretation of stream-sediment surveys (SSS) ends in a vector map. Anomalous sites are assigned different graphic symbols with different shapes and sizes. In this study I present the interpretation of the SSS using a raster model because, as I will demonstrate in due course, when compared to the vector model, this model is far more effective and can easily be integrated with other data sets. Ideally image files must be produced using raw data. In this work the data collected from several reports were already compressed. Thus, the image files were generated only using four categories extrapolated to 0-255 grey level range.

The anomalous sites represent point locations which must be integrated with other data sets having geographical and geological information. Based on the foregoing statistical analysis each site can be represented by a range of values corresponding to priorities 1 to 4. Ideally, a sample represents the upstream catchment but when this catachment is small, comparable with sample density, reduces to an array of rectangular cells between which interpolation is possible. The cell size was defined according to the sampling density and interval between samples. In this work the dimension of the cell size is 250 m by 250 m based on an average sample interval of 500 m and sampling density of 1.6 samples per $km^2$.

The gridding and interpolation procedure is essentially the same as for geophysical data, described in Chapter 7.

The first step to convert the data into raster format is to grid the irregular data points by using a minimum tension

surface (MTS) interpolation method. This results in files of 325 rows and 165 columns for the selected area.

The second step is to convert the grid files into images, involving extrapolation of the established priorities (1 to 4) to a 0 to 255 grey scale. Although the resulting images have a semicontinuous range due to interpolation, in reality only four levels are present. So data must be density sliced to retain this reality in terms of four grey levels or four colour slices. The third step is to coregister the image files with UTM map coordinates and other raster data.

To assist interpretation, the image files can be enhanced by using different techniques (FCC, density slicing and PCA) so future overlay operations can be easily achieved.

## 8.3 Display techniques

The display techniques adopted in this study comprise both two- and three-dimensional views. In two-dimensional view the image files can be displayed in grey or colour-sliced scales. Figure 8.4 shows an image file as a grey scale, the white and black colours represent the highest and lowest priorities, respectively. To favour interpretation, several density slices were done based on a histogram of the images. This enhancement allows one to look at each of the required priorities in turn (Figure 8.5).

Three dimensional views present the image files more effectively for highlighting anomalous areas (Figure 8.6), but the integration with other data sets is very difficult.

Correlation between two or three image files can be done by simple overlay operations but as the number of image files increase, interpretation becomes more difficult, because of

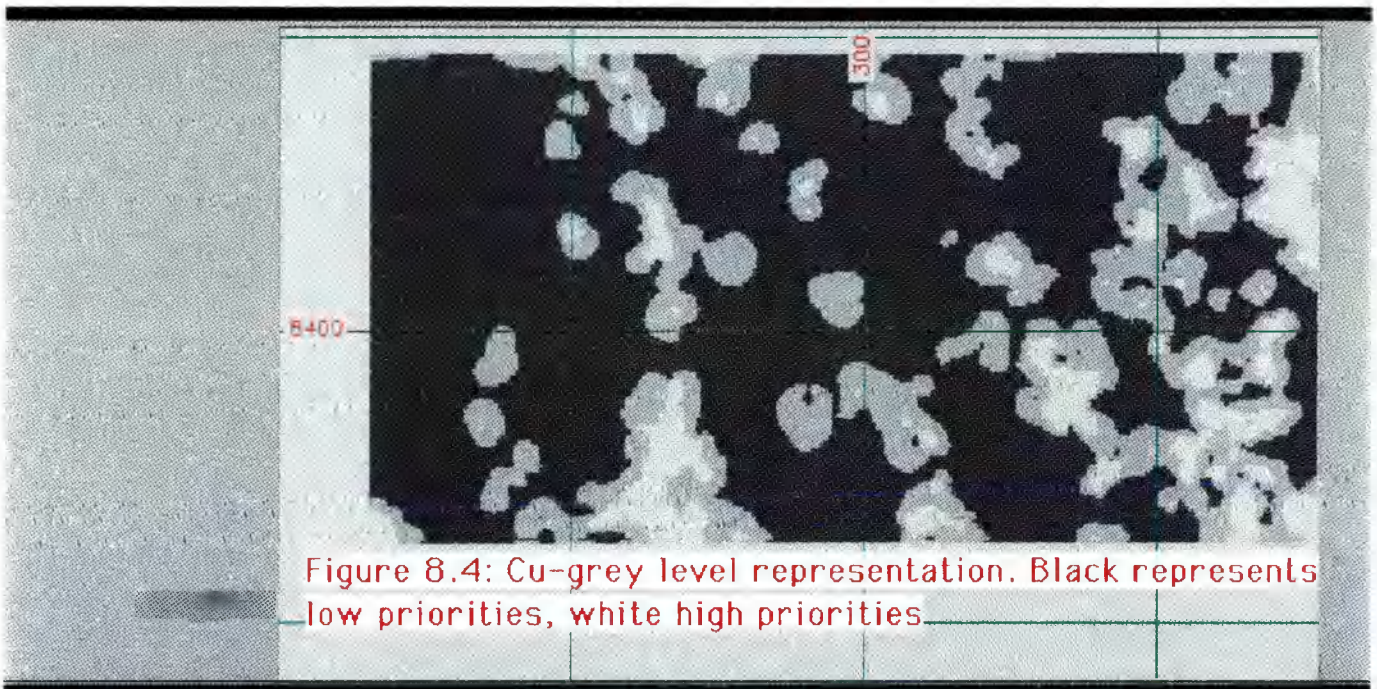


Figure 8.4: Cu-grey level representation. Black represents low priorities, white high priorities

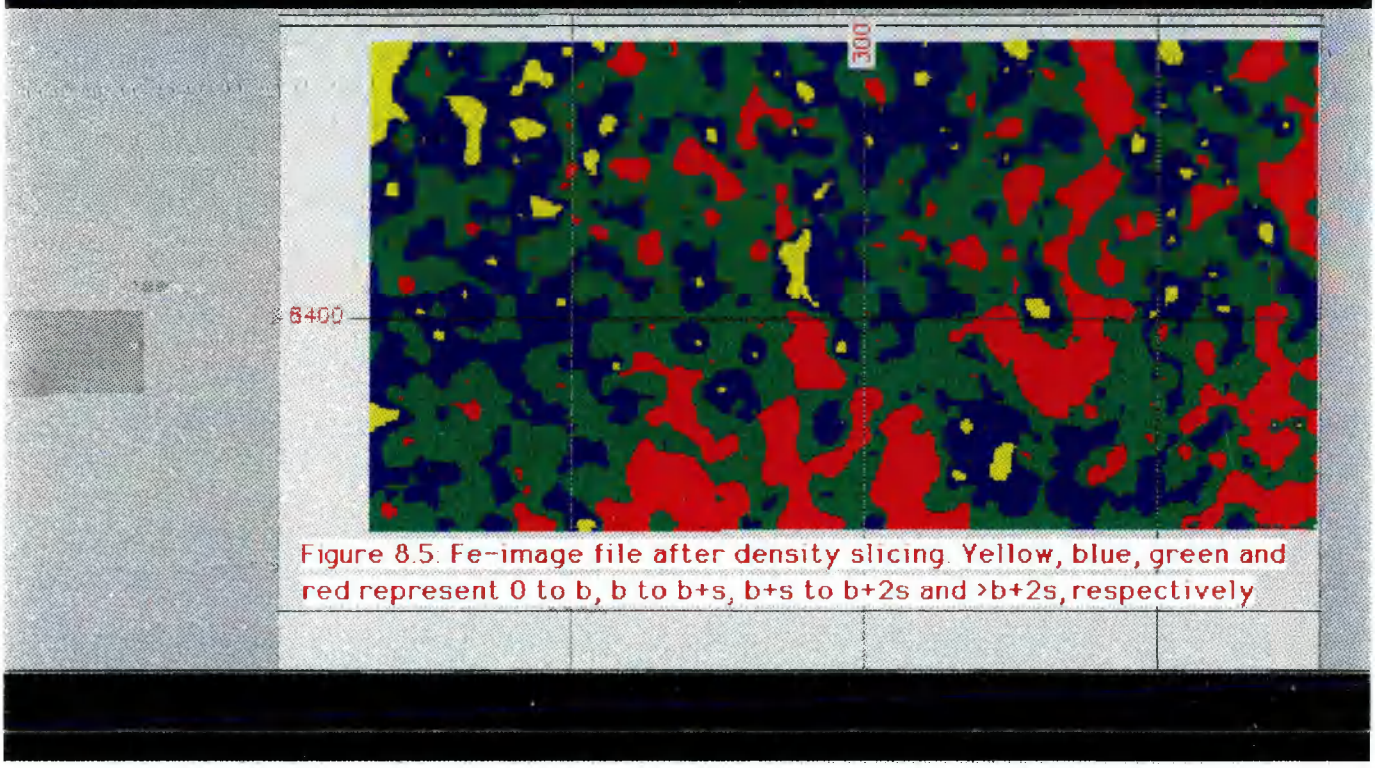


Figure 8.5. Fe-image file after density slicing. Yellow, blue, green and red represent 0 to b, b to b+s, b+s to b+2s and >b+2s, respectively

the colour similarities of the composite image. Figure 8.7 shows an overlay of values greater than b+2s of Cu (in red), As (in yellow) and Fe (in blue) where Cu+As, Cu+Fe. As+Fe and As+Fe+Cu appear as orange, magenta, green and white, respectively.

Three image files can also be displayed in red, green and blue as a FCC (Figure 8.8). The relationship between respective images can be interpreted according to the rules of colour addition presented in Table 8.3. All possible triplet data set combinations have been examined. However, only one combination which helped the comparison between FCC and PCA are included in this study.

Well correlated data sets ($r \geq 0.50$) were integrated by using PCA. The grey scale images were enhanced using density slicing.

| Primary colour | Colour addition |
|---|---|
| Red | Red + Green = Yellow |
| Green | Red + Blue = Magenta |
| Blue | Green + Blue = Cyan |
| | Red + Green + Blue = White |

**Table 8.3**: *Colour addition chart*

## 8.4 Hydrothermal alteration or primary dispersion and elemental associations in some gold deposits

It is beyond the scope of this work to discuss the geochemistry of gold. Many authors, such as *Boyle* (1974, 1979), *Keays* (1984), *Henley* et al (1984), *Siems* (1984),

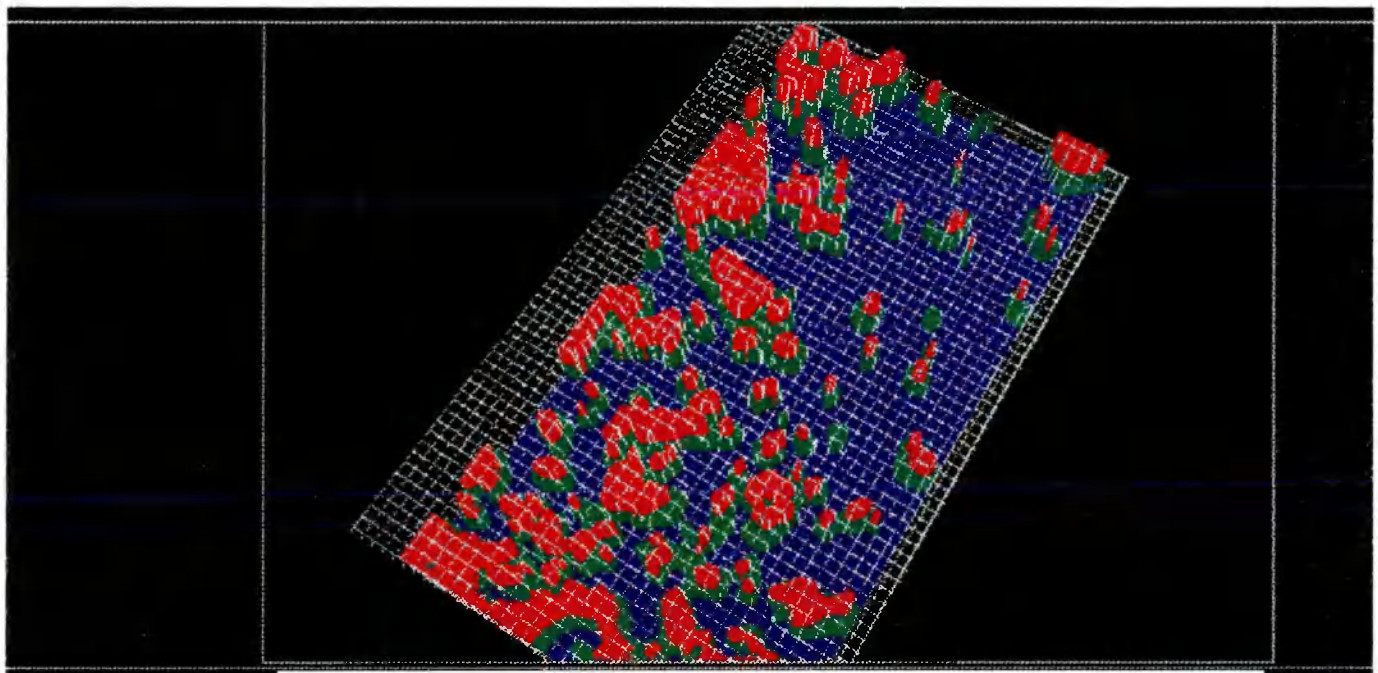

Figure 8.6: The three dimensional view of As distribution

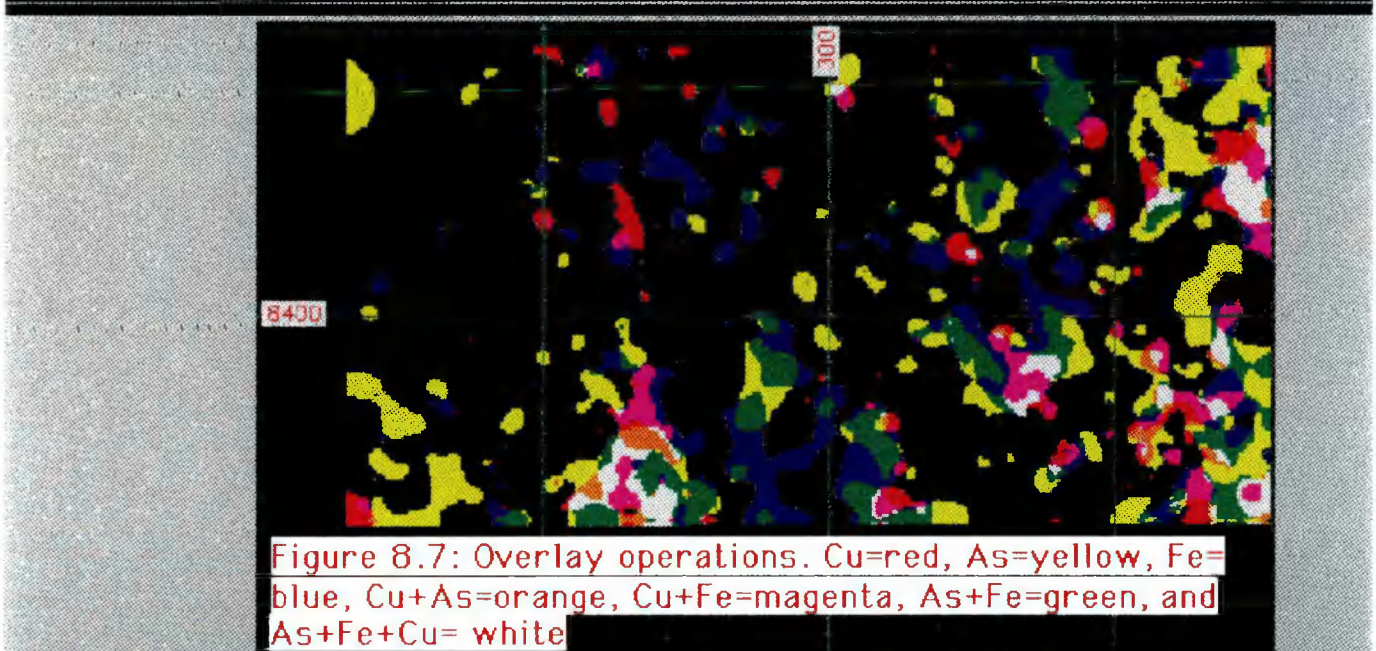


Figure 8.7: Overlay operations. Cu=red, As=yellow, Fe=blue, Cu+As=orange, Cu+Fe=magenta, As+Fe=green, and As+Fe+Cu= white

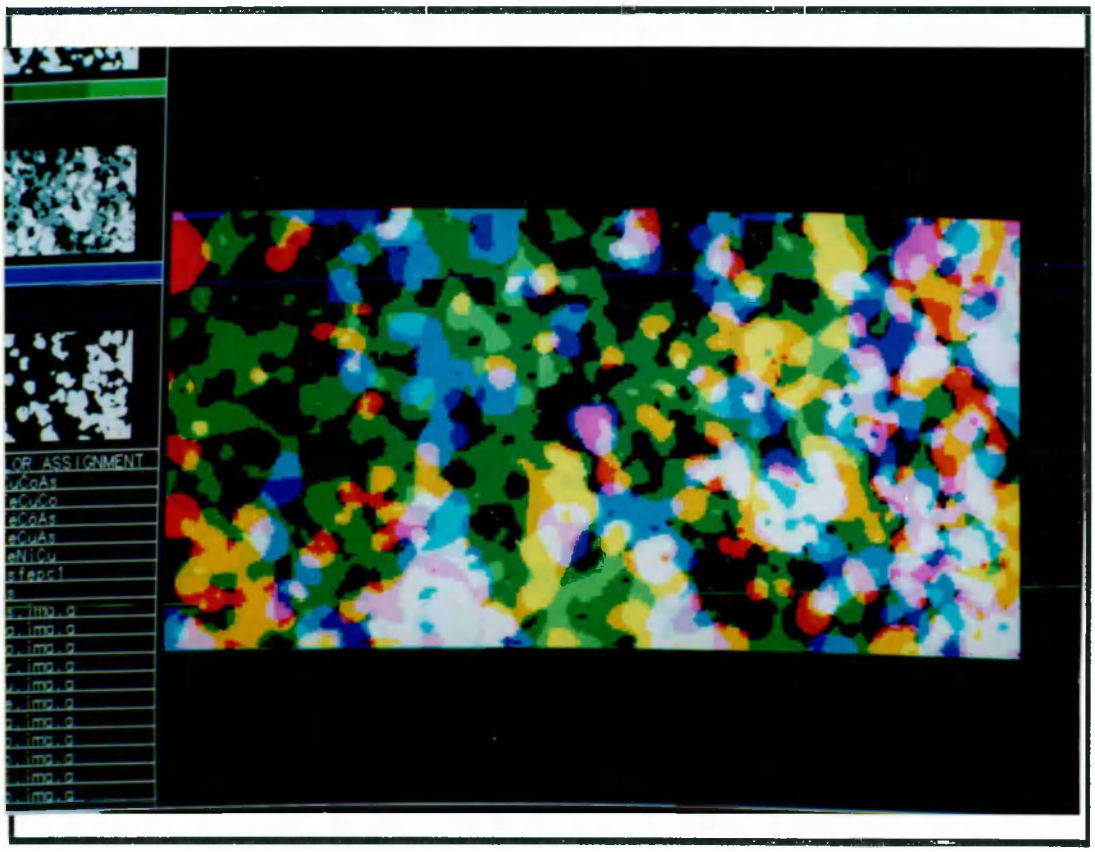


Figure 8.8: *False colour composite (FCC) of As, Cu and Fe as RGB, respectively*

*Kerrich* (1984), *Foster* et al (1986), *Colvine* et al (1989) among others, have exhaustively covered this subject.

I concentrate here on defining the hydrothermal alteration and main elemental associations related to gold deposits which can be found in some Archaean deposits. These associations will be correlated with similar suites in the study area.

Hydrothermal alteration is extremely important in mineral exploration. Many ore bodies are enveloped by halos of wall rock alteration, which if appropriately interpreted, can define exploration targets. The environment of ore deposition is also clarified, at least in part, from the assemblages of alteration minerals and the elemental associations.

*Barnes* (1979, reviewed the state-of-the-art situation on many sources of data which can be used to indicate physicochemical environment. These sources include: P-T studies based on fluid inclusions in ore and gangue minerals, and isotopic analysis of fluids and minerals; chemical compositions of fluids in inclusions in active geothermal areas; and phase equilibria based on experimental studies.

*Siems* (1984) pointed out that many factors can affect the formation of hydrothermal minerals and these can vary from one place to another. The main factors include: temperature, pressure, rock type, permeability, duration of the hydrothermal activity, volume changes, composition, stages of activity, hydrothermal fluid-wall equilibrium and types of metasomatism.

*Colvine* et al (1984) have suggested that alteration associated with Archaean gold deposits can be described in terms of

inherent characteristics and fundamental variables (Table 8.4).

| INHERENT CHARACTERISTICS | FUNDAMENTAL VARIABLES |
|---|---|
| 1.On a regional scale, the patterns of alteration often appear roughly conformable with regional volcanic stratigraphy and are spatially related to major structures | 1.Lithology: the relationship between precursor mineral assemblages, alteration style and products |
| 2. The intensity of scale of alteration vary proportionally with bulk rock composition | 2. PT conditions: the relationship between metamorphic grade of the host rocks, the hydrothermal regime and the alteration assemblages stabilised |
| 3. The elemental association includes enrichment in As, W, Mo, Sb, Te, Se, Bi, Cr and B | 3. Alteration - Permeability: the relationship between alteration and structurally induced permeability |
| 4. Deduced temporal relationships suggest that gold mineralisation was preceded by widespread, intense Fe-carbonatization and closely accompanied in time and space by subsequent localized silicification, alkali metasomatism and sulphidation | |
| 5. *Kerrich* and *Hodder* (1982) suggested that the alteration is mineralogically and geochemically distinct from that associated with synvolcanic, massive base metal sulphide deposits | |
| 6. Regional deformation events both preceded and accompanied the establishment of gold-related alteration (*Cherry*, 1983) | |

| |
|---|
| 7. While most known deposits are hosted in rocks of middle to upper greenschist grade, important deposits also occur in amphibolite and granulite domains |
| 8. The relationship between gold-associated alteration and regional metamorphism assemblages indicate that alteration was either synchronous with and/or slightly post-dated the regional metamorphic peak |

**Table 8.4**: *Characteristic features of alteration in Archaean gold deposits (modified from Colvine et al, 1984)*

In terms of geochemical stream sediment surveying, the alteration zoning or the arrangement of zones and patterns are particularly important. This is a result of the combination of many different controlling factors. Figure 8.9 presents a hypothetical map that illustrates the zonal patterns which are due to the following:

(a)progressive ages of fractures that guide infiltration flow,

(b)progressive changes in pressure and temperature (PT) conditions at a particular site of observation,

(c)differences in chemical and mineral composition between different wall rocks,

(d)changes in chemical composition of hydrothermal fluids at source,

(e)pore fluids diffusing through wall rocks and chemically evolving with different distances from fractures,

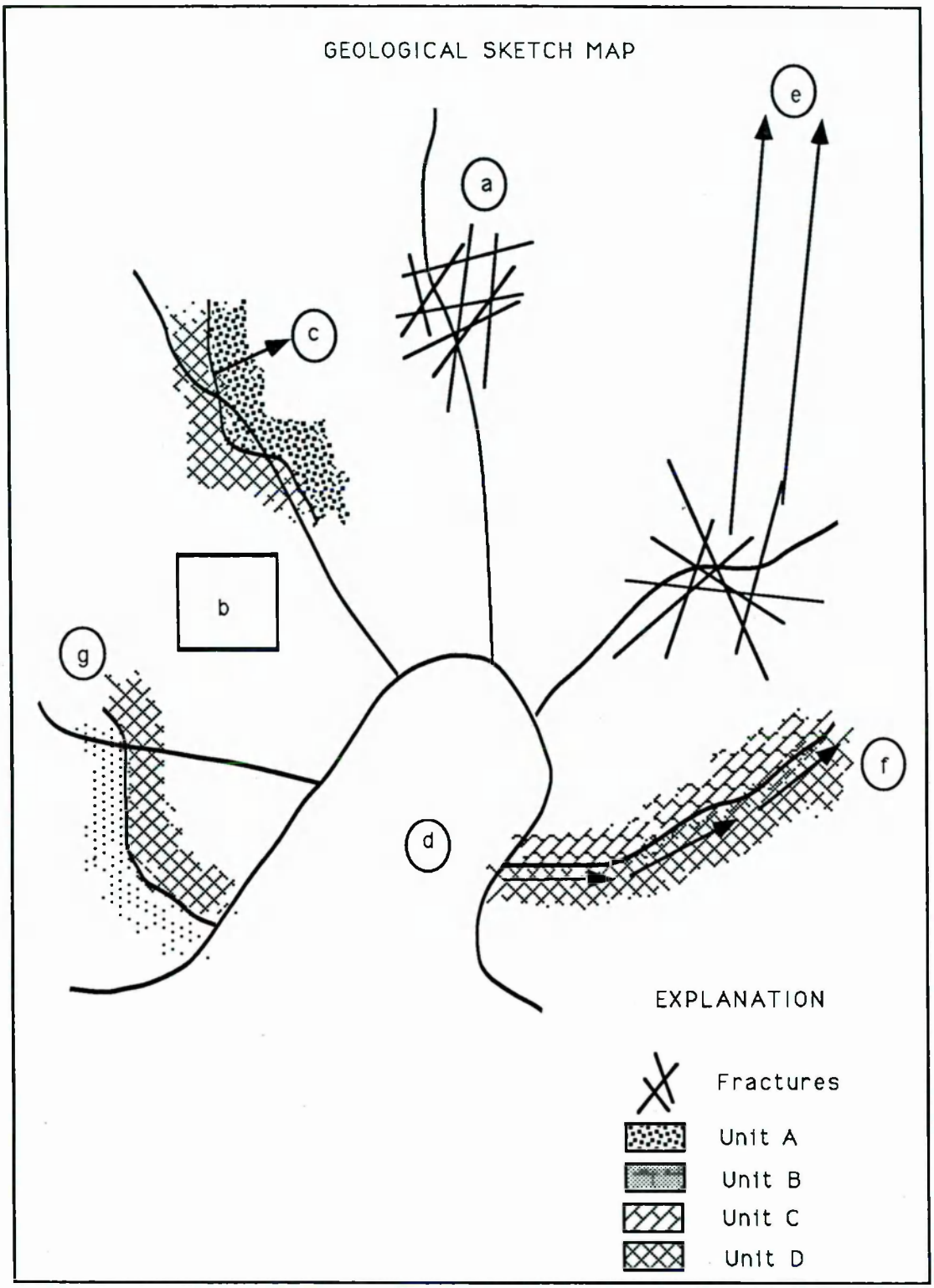


Figure 8.9: *Alteration zoning and patterns of possible areas for gold concentration. Explanation in the text*

(f)progressive changes in composition of hydrothermal fluids between their source and the observation site brought about by PT changes, precipitation and reaction with wall rock or previously precipitated vein minerals, and

(g)effect of chemical insulation provided by previously altered wall rock (*Siems*, 1984).

Total widths of sequences of zones can differ from a few centimetres to many hundreds of metres. The order of patterns within the sequences may or may not change. Also, the relative widths of individual patterns may or may not change. Some patterns may be missing in places and reversals in the zoning sequence are possible due to changing chemical parameters (*Rose* and *Burt*, 1979).

In this study I consider the following alteration zones: Silicate alteration, alteration in greenschist, amphibolite and granulite domains, and alteration in gold-bearing massive sulphides.

### 8.4.1 Silicate alteration

Silicate alteration is a hydrothermal alteration of rocks with high content in Ca, Mg and (or) $CO_2$, producing silicates. The altered rocks resulting from this process are termed tactites or skarns. This alteration is frequent in carbonate rocks, but any rocks with a high Mg or Ca content can also be altered by this process.

*Siems* (1984) suggested the following classification of skarns according to:

(a)the rock is replaced: skarns can replace the carbonate rocks or the intrusive source rock,

(b) relationship to an intrusion: three possibilities occur, skarn around the intrusion, intrusion around the skarn or skarn with no intrusion present,

(c) the lithology of altered country rocks: skarns can be derived from Ca-rich or Mg-rich protoliths and are called calcic skarn or magnesian skarn, respectively,

(d) the character of the elements of economic interest: copper skarn, iron skarn, tungsten skarn, etc.

(e) the character of the principal mineral: garnet skarn, magnetite skarn, etc.

Gold may be a by-product of some copper skarns, examples of which can be found in the Philippines and in Wales. *Einaudi* (1981) pointed out that calcic magnetite skarn deposits are virtually the only skarn type found in oceanic island-arc terrain. The main characteristics of these deposits include: their association with epizonal dioritic rock emplaced in cogenetic basalt-andesites, an Fe-rich calc-silicate gangue consisting of epidote-ferrosalite with retrograde chlorite-actinolite, which reflects intermediate oxidation states, extensive epidote-pyroxene or albite-scapolite alteration of plutonic and volcanic rocks, a low sulphide content, and a minor metal suite of Cu, Fe, Co and Au.

Magnetite skarn deposits are common in continental margin orogenic belts associated with mesozonal to epizonal felsic plutons (*Siems*, 1984). They are found in most base metal sulphide skarn districts where dolomite is present. In this case, the high magnetite content is a function not of the igneous rock association but rather of the dolomitic wall

rocks in which Fe-rich calc-silicates are not stable. Table 8.5 summarises the main characteristics of iron-skarns.

| | |
|---|---|
| Metal associated | Fe, Cu, Co, Au, and As |
| Tectonic setting | Oceanic island arc; rifted continental margins |
| Associated igneous rocks | syenite; mostly diorite, granodiorite and quartz-monzonite |
| Cogenetic volcanics in ore zone | Basalt and andesite |
| Pluton morphology | Large to small stocks, dykes |
| Skarn type | The intrusive rock is replaced |

**Table 8.5**: *Major characteristics of magnetite skarns (modified from Einaudi et al, 1981)*

### 8.4.2 Alteration of gold deposits in greenschist domains

Different lithologies may exhibit diverse behaviour under the hydrothermal processes of greenschist domains. Mafic and ultramafic rocks presented a broad halo of alteration in relation to the extent of mineralisation. The distribution and style of alteration are in most cases related to structural features on both the regional and local scale. In some examples such as Timmins (*Fyon* and *Crocket*, 1981), Golden mile, Kalgoorlie (*Travis* et al, 1971), tens to hundreds of cubic kilometres of rock are involved. In contrast, there are cases where only a few cubic metres have been affected (*Fyon* and *Crocket*, 1981). The alteration is represented by a complete replacement of the rock matrix, contributing to the

creation of new permeability in the form of interconnected pore spaces.

In the case of mafic lithologies, the mineralogical transformations involve substantial input of $CO_2$, K, Si and S and significant loss of Mg, Ca and Na. The of Fe, Mg and Ca necessary for the generation of Fe-carbonates, silicates and sulphide phases are most probably derived from minerals such as actinolite and chlorite (*Fyfe* and *Kerrich*, 1984). On large scale, alteration zones include calcite, giving an impression of regional scale carbonatization. Around the deposits, ferroan carbonates predominate and at the ore zone scale the alteration phases include ferroan carbonates, quartz, mica, sometimes rich in V, Cr and Ba, and sulphides (*Tihor* and *Crocket*, 1976). The elemental associations found in these deposits are As, Cr, V, Ba, Fe and Cu.

In the case of ultramafic rocks, the alteration zones comprise talc, dolomite, quartz, magnesite and fuchsite. Their relative abundance depends on the bulk composition of the original rock. The elemental associations are very similar to those found in gold deposits associated with mafic lithologies.

With respect to intermediate to felsic lithologies, there is little intense replacement as a consequence of their mineralogical composition (mainly quartz and alkali feldspars), and there is a more competent response to deformation. Nevertheless these rocks can suffer extensive alteration but the secondary mineral assemblages are confined to grain boundaries and interstitial empty spaces. These mineral assemblages consist of white mica, calcite, chlorite and epidote, in approximate order of importance (*Gorman* et al,

1981). Alteration directly related to gold deposits is limited to the wall-rock environment. In some cases "brick red halos" can be recognised as a result of hematization and K-feldspar alteration in syenites and granodiorites. The elemental associations related to these deposits are As, Fe, W and B.

Alteration related to chemical sediments is very localized as enveloping halos around crosscutting quartz veins. These halos range from centimetres to several metres (*Phillips* et al, 1984). The main alteration consists of selective replacement of magnetites by sulphides (pyrite, pyrrothite and arsenopyrite). The elemental associations found in these deposits include Fe, As, Zn and Cu.

### 8.4.3 Alteration of gold deposits in amphibolite and granulite domains

In general, rocks within amphibolite facies show evidence of intense to moderate ductile deformation. The elemental associations found in gold deposits of amphibolite facies are the same as greenschist grade. However, the mineral assemblages resulting from the alteration processes are distinct. According to *Colvine* et al (1984) two different types can be recognised: (a)characterized by the occurrence of Fe-carbonates, white mica, biotite, quartz, albite, calcite and chlorite. This alteration indicates hydrothermal retrograding has occurred, superimposed upon and post-dating the regional metamorphism; (b)characterized by the presence of andalusite, staurolite, garnet, cordierite, antophyllite-cummingtonite, and chloritoid. Secondary minerals occur in close association with the ore zones and include biotite, K-feldspar, garnet, and calcite. It is important to point out

that at outcrop scale, altered rocks are little different in their appearance from surrounding rocks.

Gold deposits associated with rocks in granulite facies are rare. The most important deposit is located in Zimbabwe (Renco Mine). The ore bodies occur within a lenticular charnockite body intruded by pegmatites and young and old diabases. The altered assemblage consists of biotite, green and brown feldspar, epidote, chlorite and sericite which indicate a retrograde metamorphism (*Bohmke* and *Varnell*, 1986). The elemental associations related to gold deposits in amphibolite and granulite domains include Bi, Fe, Ni and Cu.

### 8.4.4 Alteration of gold-bearing massive sulphides

The most important gold-bearing massive sulphides of Precambrian age are related to Cu-Zn-Ag deposits. The altered areas can be found considerable distances from the ore deposits. The most common alterations found in the footwall pipes of these deposits are chloritic, sericitic, silicic and carbonatic.

Alteration of footwall rocks occurs in two forms: (a)pipe-like and (b)transgressive and conformable or semi-conformable with the enclosing rock units (*Sangster*, 1972). Migration and concentration of metals on a geochemical scale in alterated zones in the vicinity of massive sulphides deposits has been extensively used in mineral exploration. The most common elemental associations are Fe, Mg, Ti, Zn and Cu. *Descarreaux* (1973) has studied alteration in these deposits and concluded: (a)$Na_2O$ is intensely leached from the calc-alkaline volcanic rocks close to the ore bodies, (b)the MgO content adjacent to

the ore bodies is very high, and (c)a $K_2O$ enrichment in country rocks of Zinc-rich ore bodies.

## 8.5 Secondary dispersion and surficial patterns

Secondary dispersion applies to the redistribution of the primary dispersion by any later process, usually in the surface environment. Fundamentally, the secondary dispersion is governed by the mobility of the elements. On the other hand mobility of the elements is a function of mechanical properties of the mobile phase, chemical stability of the elements and the pH-Eh of the environment (*Rose et al*, 1979). Table 8.6 shows the mobility of the analysed elements of the study area.

| RELATIVE MOBILITY | OXIDIZING (pH 5-8) | OXIDIZING pH < 4 | REDUCING |
|---|---|---|---|
| Highly mobile | Mo | | |
| Moderately immobile | Mg, V, As, Sr | Mg, Sr, Cu, Co, Ni, V, As | Mg, Sr, Ba |
| Slightly mobile | Ba,Pb,Cu,Ni,Co | Ba | Fe |
| Immobile | Fe, Ti, Zr, Cr | Fe, Ti, Zr, As | Fe, Ti, Zr, Cu, Pb, Co, As,V,Cr |

**Table 8.6**: *Mobility of the elements in surficial environment (from Rose et al, 1979)*

Surficial dispersion patterns are a consequence of diverse dynamic processes. During flood periods very large boulders can be moved several miles in a matter of hours. During quieter periods of stable runoff the solid particles can be regularly distributed. Clay minerals and other fine particles move predominantly in suspension. Coarse material moves by

saltation and gliding in the bed of the stream. Resistant minerals, together with partially weathered rock fragments are the dominant constituents of the sediment in fast-flowing streams. Micaceous minerals can occur and are more readily carried in suspension. During the course of transport, the particle size is liable to be progressively reduced by the combination of chemical and physical disintegration. The effective comminution during transport depends on the stability of the mineral species involved. Erosion and transportation predominate over deposition in the upper reaches of a stream. As turbulence decreases, suspended material begins to settle out and movement by saltation diminishes.

Downstream deposition continues on an increasing scale as the load capacity progressively falls. Surficial patterns can be classified into syngenetic and epigenetic.

Syngenetic patterns are those which were introduced or deposited at the same time as the host matrix and include clastic, hydromorphic and biogenic processes. Epigenetic patterns are those which were introduced into the matrix after its formation (*Rose* et al, 1979). Clastic processes involve residual and transported soils as a result of climatic factors and occur when temperature variation is more important than precipitation. In residual soil the pattern reflect the distribution of the elements in the underlying bedrock surface. Stream sediments collected in this environment reflect the source (Figure 8.10.a). In transported soil the relationship between the secondary dispersion is more complicated. The data set must be carefully analysed,

generally representing heterogeneous population (Figure 8.10.b).

Hydromorphic patterns are basically a function of the movement of solutions. The water table (WT) determines fan-shaped regimes with local modification, resulting from preferential flow along bedrock channel-ways or permeable horizon in the overburden (Figure 8.10.c).

Geochemical parameters can be easily defined but additional geological information is needed to determine where possibly the source is. Biogenic patterns reflect the capacity of the vegetation in absorbing metals. The partially decomposed plant is the sampling source. In view the complexity of the biogeochemical cycle the biogenic anomalies are often less well defined.

## 8.6 Interpretation of the results

The selected elements were grouped according to their elemental associations related to a particular types of gold deposit (Table 8.7). False colour composites were produced by using three elements, displayed in red, green and blue. When only three associated elements are involved, the data set can be easily interpreted. However, when four or more elements are involved, the interpretation using FCC is more complex.

For instance, the four possible FCC combinations for Fe, Cu, Co and As are presented in Figures 8.11, 8.12, 8.13 and 8.14. The anomalous areas, in white, represent the region where priority 1 of the considered elements can be found together.

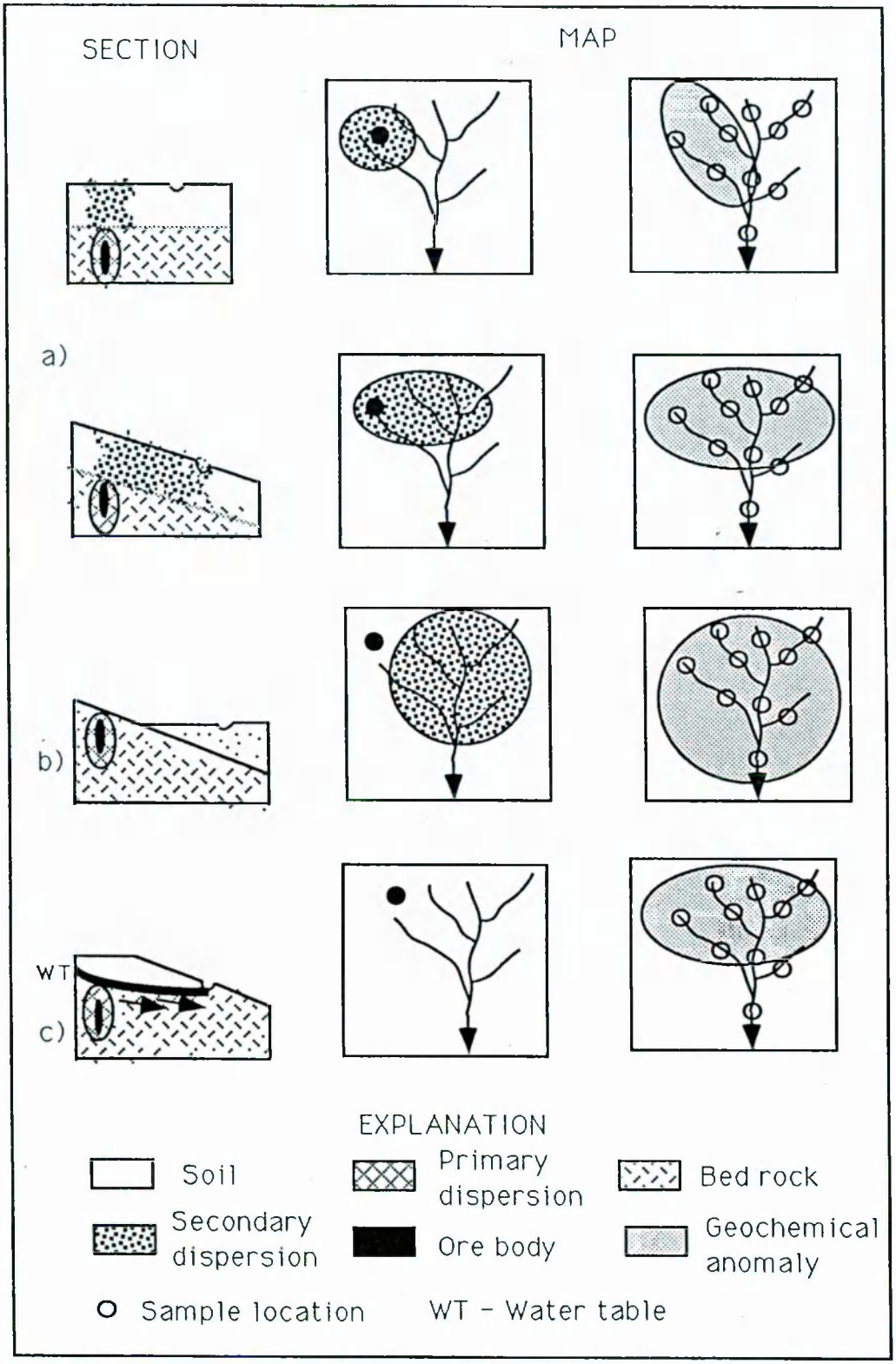


Figure 8.10.: *Secondary Geochemical dispersion and surficial patterns a)residual soil, b)transported soil, c)hydromorphic dispersion*

| ELEMENTAL ASSOCIATIONS | GOLD DEPOSITS |
|---|---|
| Fe, Cu, Co and As | Skarn |
| Fe, Ba, As and Pb | a) associated with volcanic rocks<br>b) structurally controlled |
| Fe, As, Cr, V, Ba, and Cu | a) associated with mafic and ultramafic rocks<br>b) structurally controlled |
| Fe, Ni and Cu | a) associated with mafic granulites<br>b) structurally controlled |
| Fe, Mg, Ti and Cu | a) associated with massive sulphides<br>b) may or may not structurally controlled |
| Fe, Cu, As, Pb | a) associated with massive sulphides<br>b) structurally controlled |

**Table 8.7**: *Elemental associations of the studied area and related gold deposits*

As a result of <NOT> and <OR> Boolean operators the anomalous areas were selected (Figures 8.15, 8.16, 8.17 and 8.18), and Table 8.8.shows the areal distribution of the anomalous areas.

Comparison between the displays resulting from the two methods shows broad coincidence between the white areas in the FCCs with the red patches resulting from Boolean operation.

| ELEMENTAL ASSOCIATIONS | ANOMALOUS AREAS | |
|---|---|---|
| | % TOTAL AREA | $Km^2$ |
| Cu, Co,and As | 4.08 | 150.50 |
| Fe, Cu and Co | 3.14 | 115.69 |
| Fe, Co and As | 3.38 | 124.81 |
| Fe, Cu and As | 2.57 | 94.88 |

**Table 8.8**: *The areal distribution of the anomalous areas from the FCC results by using Fe, Cu, Co and As*

Best results are achieved by using Principal Component Analysis (PCA). It is important to emphasise that when more than three elements are involved PCA is the most effective technique for interpreting well correlated data. There is a problem though in using PCA when the range of variation only covers four steps for each file. It would have been better to apply it to raw data, or to data in byte format. Unfortunately these files were not available.

There are no difficulties in the calculation of statistical parameters such as eigenvalues and eigenvectors. More often difficulties arise in developing a "feel" for the meaning of these quantities.

Tables 8.9.a, (b), (c), (d) and (e) present the coefficient of eigenvectors of geochemical data within the study area and also show the coefficients from the original images corrected with loadings. The use of loading makes the understanding of original element contribution to each PC considerably easier.

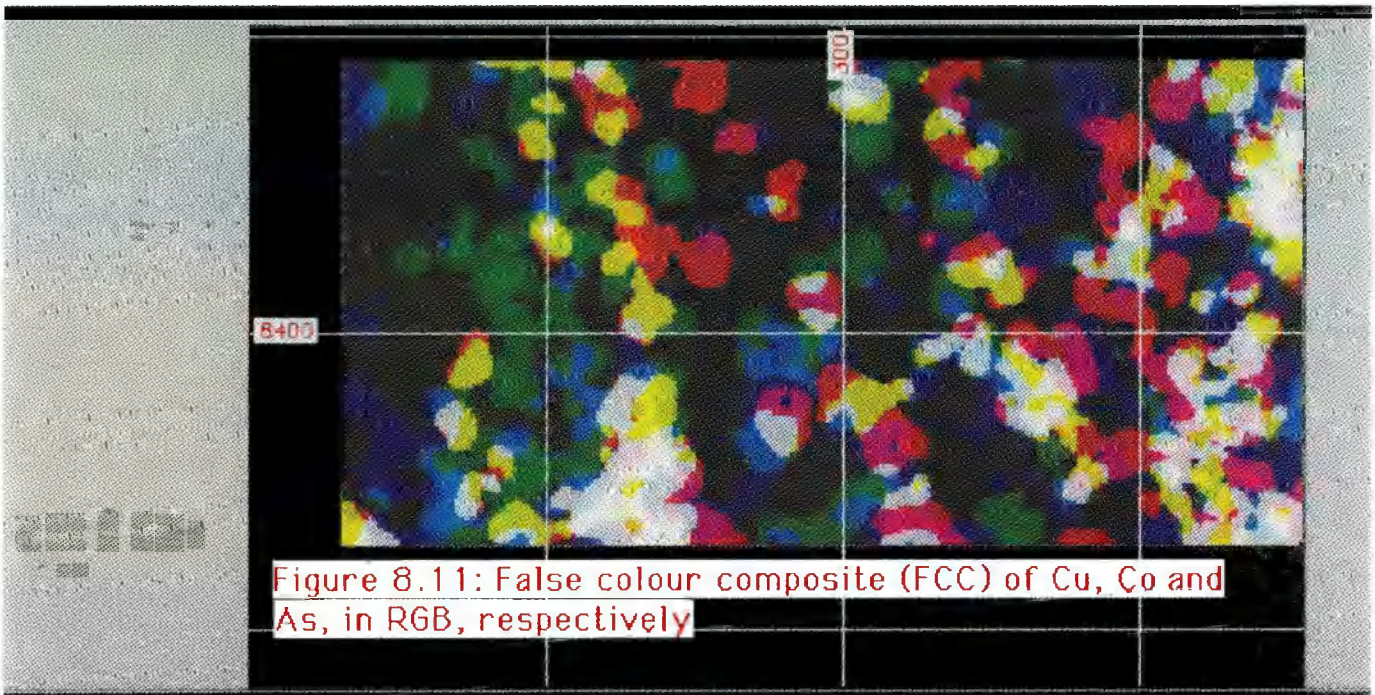


Figure 8.11: False colour composite (FCC) of Cu, Co and As, in RGB, respectively

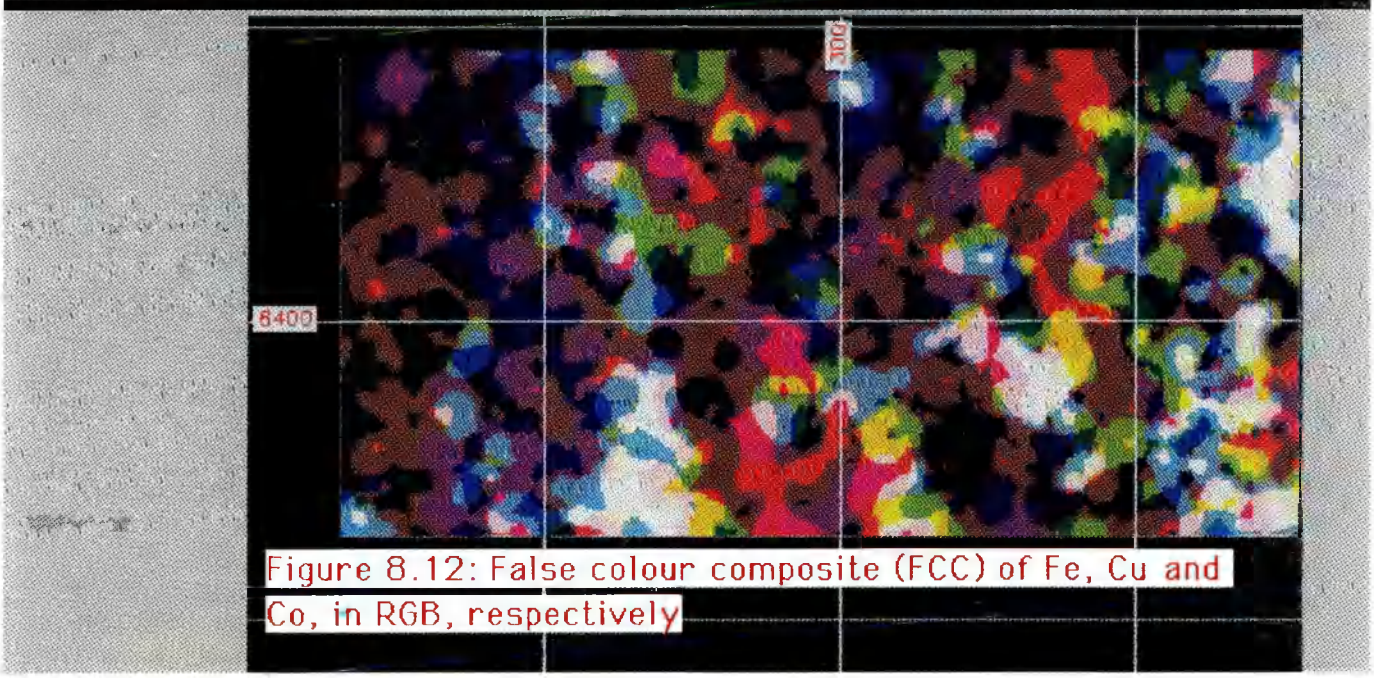


Figure 8.12: False colour composite (FCC) of Fe, Cu and Co, in RGB, respectively

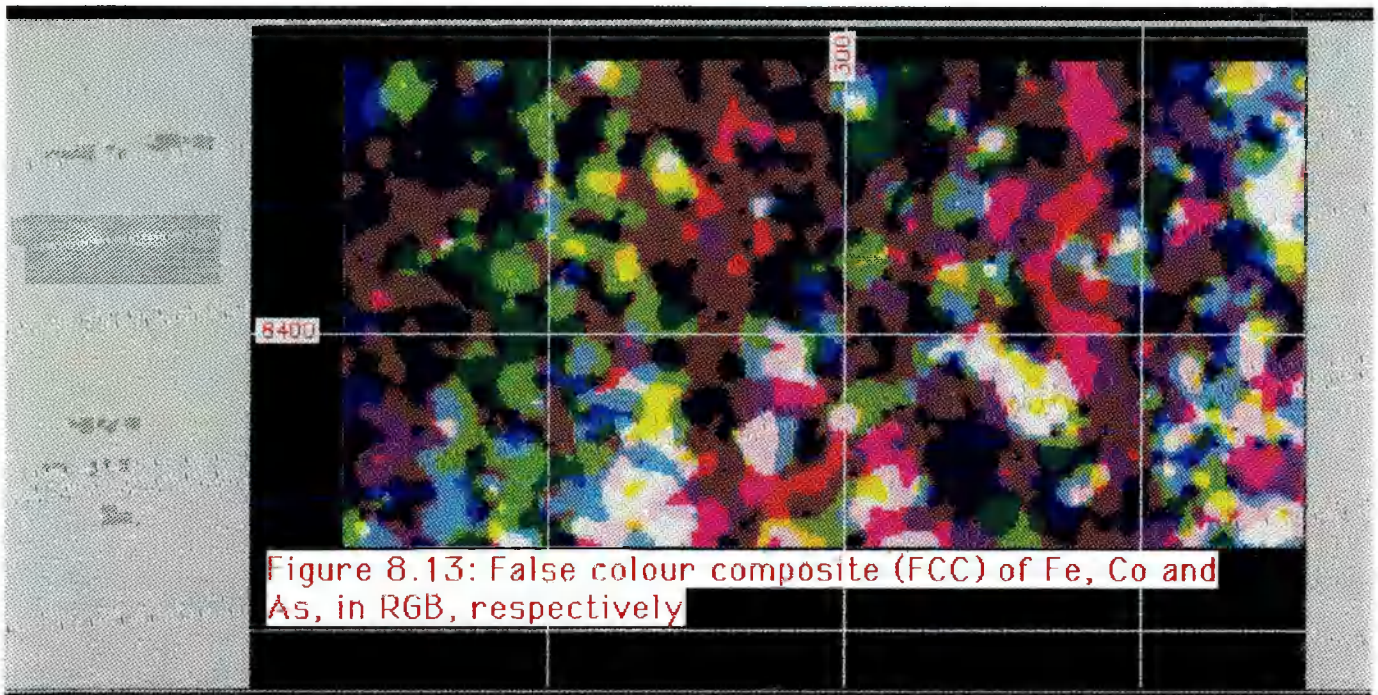


Figure 8.13: False colour composite (FCC) of Fe, Co and As, in RGB, respectively

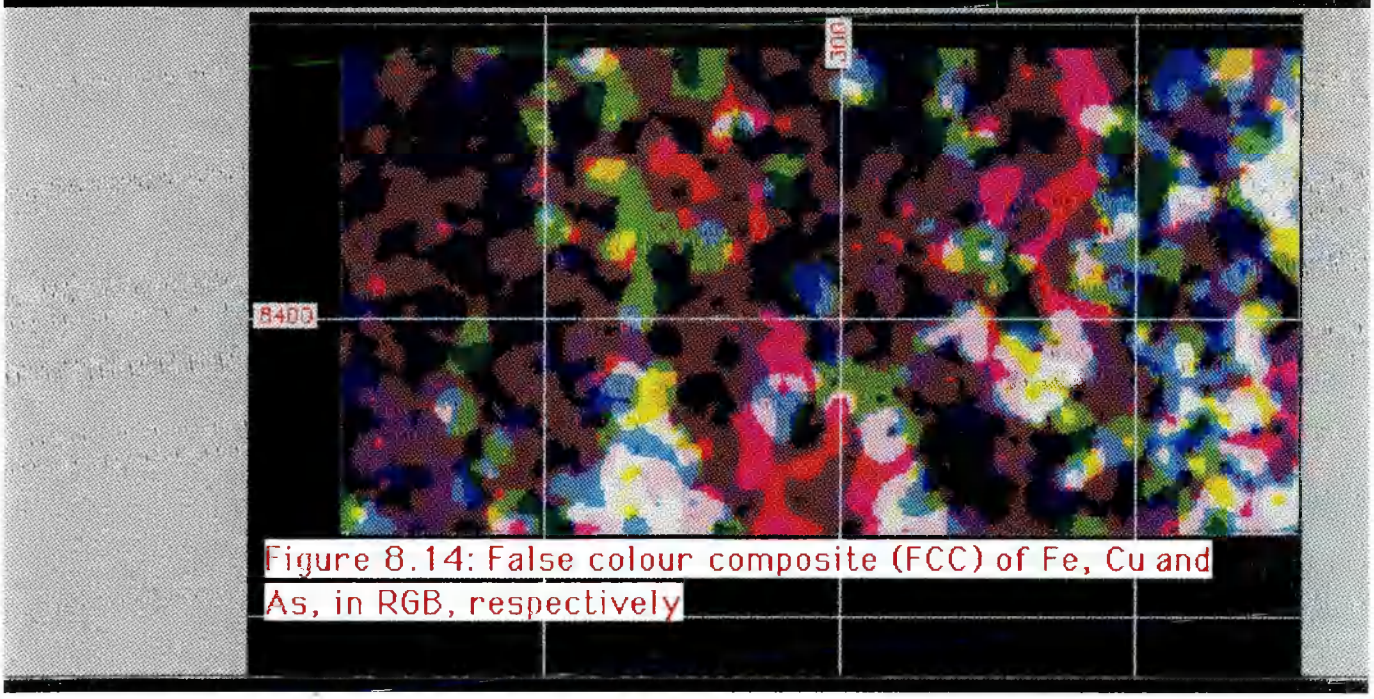


Figure 8.14: False colour composite (FCC) of Fe, Cu and As, in RGB, respectively

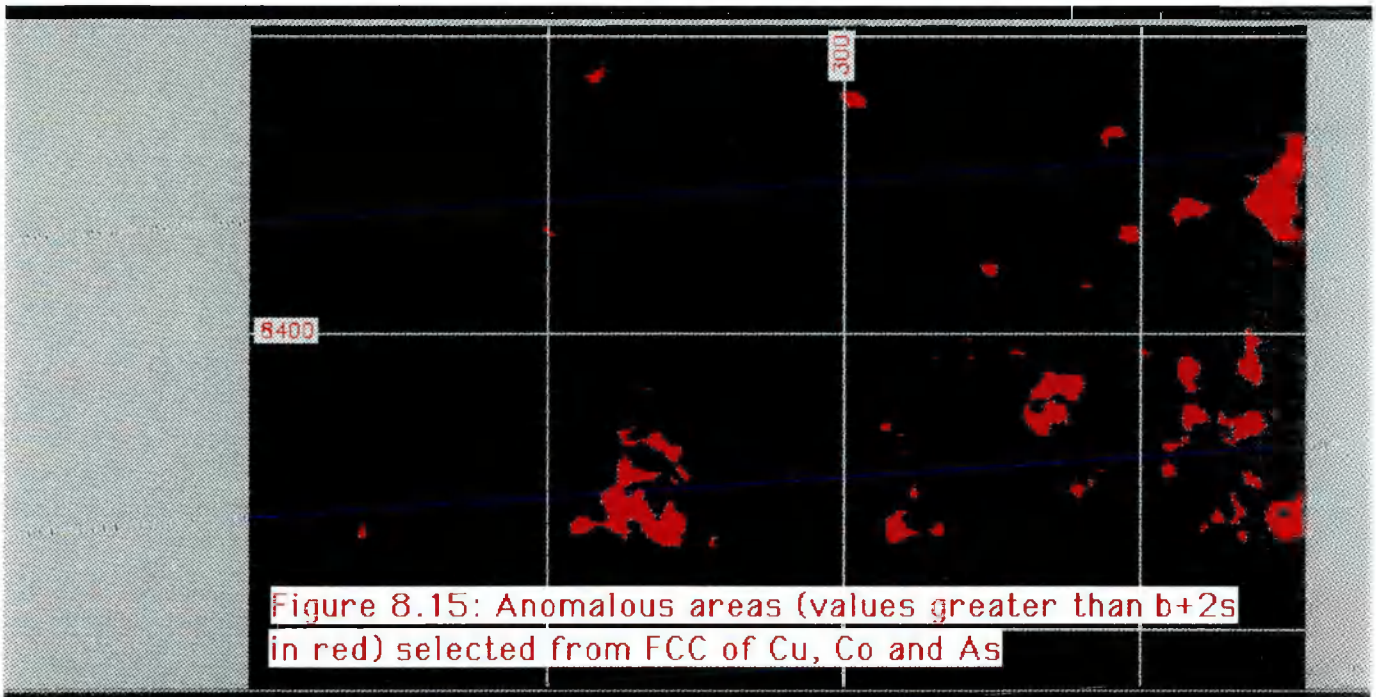


Figure 8.15: Anomalous areas (values greater than b+2s in red) selected from FCC of Cu, Co and As

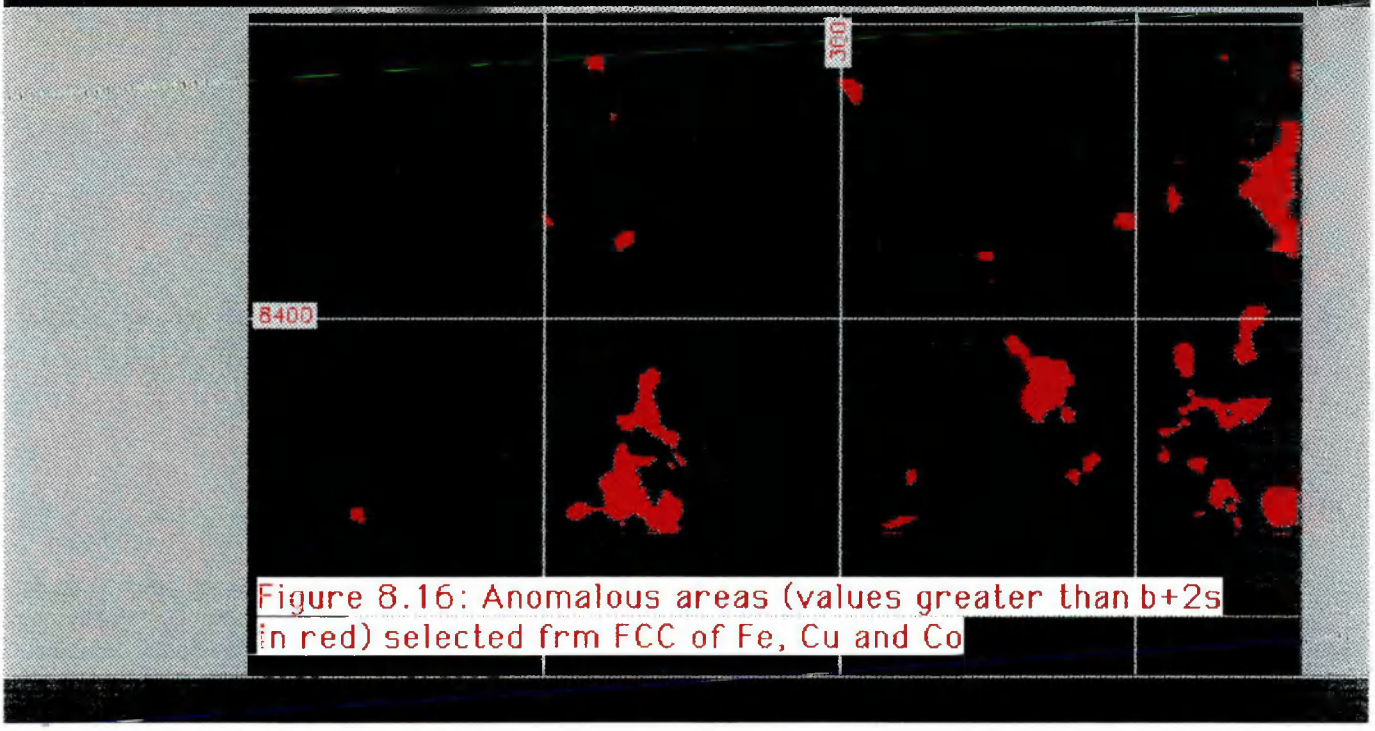


Figure 8.16: Anomalous areas (values greater than b+2s in red) selected frm FCC of Fe, Cu and Co

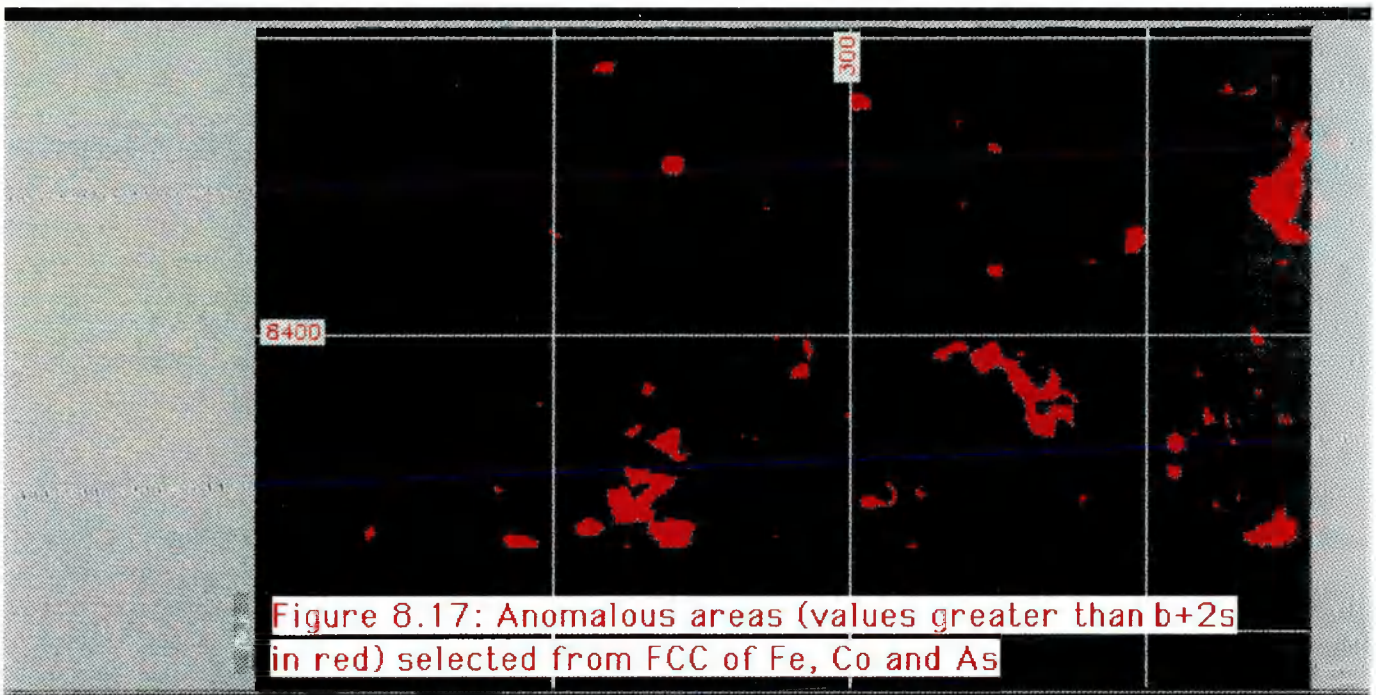


Figure 8.17: Anomalous areas (values greater than b+2s in red) selected from FCC of Fe, Co and As

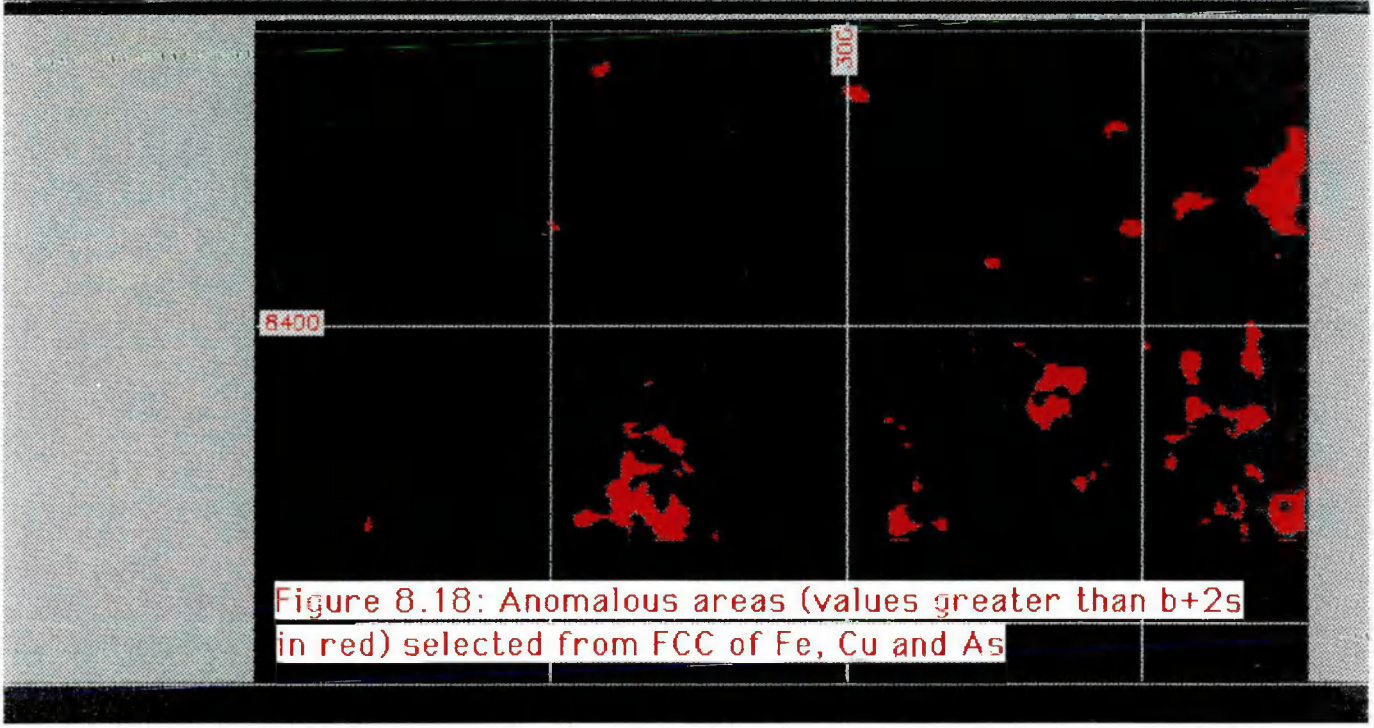


Figure 8.18: Anomalous areas (values greater than b+2s in red) selected from FCC of Fe, Cu and As

| | EIGENVECTORS | | | | | | | |
|---|---|---|---|---|---|---|---|---|
| | Fe | Cu | Co | As | Fe(%) | Cu(%) | Co(%) | As(%) |
| PC1 | .60 | .50 | .48 | .39 | 30.6 | 25.5 | 24.4 | 19.8 |
| PC2 | .22 | -.19 | -.64 | .71 | 12.5 | -10.8 | -36.3 | 40.3 |
| PC3 | -.77 | .27 | .24 | .53 | -42.5 | 14.9 | 13.2 | 29.3 |
| PC4 | -.07 | -.80 | .54 | .26 | 4.2 | -47.9 | 32.3 | 15.6 |

(a)

| | EIGENVECTORS | | | | | | | |
|---|---|---|---|---|---|---|---|---|
| | Fe | Ba | As | Pb | Fe(%) | Ba(%) | As(%) | Pb(%) |
| PC1 | .24 | .73 | .19 | .61 | 13.5 | 41.2 | 10.7 | 34.5. |
| PC2 | .77 | -.39 | .50 | .01 | 46.1 | -23.3 | 29.9 | .06 |
| PC3 | -.46 | .16 | .83 | -.27 | -26.7 | 9.3 | 48.2 | -15.7 |
| PC4 | -.37 | -.54 | .14 | .74 | -20.6 | 30.2 | 7.8 | 41.3 |

(b)

| | EIGENVECTORS | | | | | | | |
|---|---|---|---|---|---|---|---|---|
| | Fe | As | Cu | Pb | Fe(%) | As(%) | Cu(%) | Pb(%) |
| PC1 | .61 | .43 | .44 | .51 | 30.6 | 21.6 | 22.1 | 25.6 |
| PC2 | -.33 | -.27 | -.27 | .86 | -19.1 | -15.6 | -15.6 | 49.7 |
| PC3 | -.61 | .79 | .79 | .02 | -41.8 | 54.1 | 2.7 | 1.4 |
| PC4 | -.39 | -.34 | -.34 | .01 | -24.4 | -21.2 | 53.7 | .6 |

(c)

| | EIGENVECTORS | | | | | | | | | | | |
|---|---|---|---|---|---|---|---|---|---|---|---|---|
| | As | Cr | V | Ba | Fe | Cu | As(%) | Cr(%) | V(%) | Ba(%) | Fe(%) | Cu(%) |
| PC1 | .28 | .54 | .45 | .09 | .51 | .39 | 12.4 | 23.9 | 19.9 | 3.9 | 22.6 | 17.3 |
| PC2 | .09 | -.26 | .05 | .96 | .01 | .03 | 6.4 | -18.6 | 3.6 | 68.6 | 0.7 | 2.1 |
| PC3 | -.50 | -.30 | .79 | -.07 | .04 | .18 | -26.6 | -15.9 | 42.0 | -3.7 | 2.1 | 9.6 |
| PC4 | .63 | -.67 | .11 | -.25 | .30 | .01 | 31.9 | -34.0 | 5.6 | -12.7 | 15.2 | 0.5 |
| PC5 | .38 | .08 | .37 | -.03 | -.81 | .25 | 19.8 | 4.2 | 19.3 | -1.5 | -42.2 | 15.0 |
| PC6 | -.35 | -.31 | -.15 | -.07 | 0 | .87 | -20.0 | -17.7 | 8.6 | -4.0 | 0 | 49.7 |

(d)

| | EIGENVECTORS | | | | | | | |
|---|---|---|---|---|---|---|---|---|
| | Fe | Mg | Ti | Cu | Fe(%) | Mg(%) | Ti(%) | Cu(%) |
| PC1 | .63 | .09 | .64 | .43 | 35.2 | 5.0 | 35.7 | 24.0 |
| PC2 | .48 | .16 | -.76 | .41 | 26.5 | 8.8 | -42.0 | 22.6 |
| PC3 | .61 | -.29 | -.07 | -.73 | 35.9 | -17.0 | -4.1 | -42.9 |
| PC4 | .05 | .94 | .05 | -.34 | 3.6 | 68.1 | 3.6 | -24.6 |

(e)

**Table 8.9:** *Principal component analysis. Loadings expressed as eigenvectors: (a)on Fe, Cu, Co, As; (b)on Fe, Ba, As, Pb; (c)on Fe, As, Cu, Pb; (d)on As, Cr, V, Ba, Fe,Cu; (e)on Fe, Mg, Ti,Cu.*

To demonstrate the use of PCA the following associations (Fe, Cu,Co,As), (Fe,Ba,As,Pb), (Fe,As,Cu,Pb) and (As,Cr,V,Ba,Fe,Cu) were considered (see Table 8.6 for associated deposit types). As a result of the PCA on Fe,Cu,Co and As, the percentages of total variance contributed by each eigenvalue are 48%(PC1), 22%(PC2), 19%(PC3) and 12%(PC4). By looking into the percentages presented in Table 8.8 b, PC1 (Figures 8.19 and 8.20) incorporates a positive mixture of all elements with a balanced proportion. PC2 has a dominant contribution of Co and

As (the negative and positive values of Co and As represent sites where Co is low and As is high, or vice-versa). PC3 has a prevailing contribution of Fe and As, and PC4 has a dominant contribution of Cu and Co. To determine the area where all four elements can be found together at their highest value, we make use of statistics (Table 8.10), and analysis of the histograms (Figures 8.21 to 8.32). The bar histograms show the distribution of the four categories. The pie histograms present the distribution of the four categories in relation to the total area as can be seen in Table 8.11.

| | b | s | b+2s |
|---|---|---|---|
| PC1 | 127 | 40.3 | 207 |
| PC2 | 127 | 42.6 | 211 |
| PC3 | 123 | 44.3 | 211 |
| PC4 | 126 | 41.3 | 211 |

(a)

| | b | s | b+2s |
|---|---|---|---|
| PC1 | 125 | 43.3 | 211 |
| PC2 | 126 | 41.8 | 210 |
| PC3 | 124 | 44.7 | 212 |
| PC4 | 126 | 42.2 | 210 |

(b)

| | b | s | b+2s |
|---|---|---|---|
| PC1 | 124 | 41.2 | 206 |
| PC2 | 125 | 40.3 | 302 |
| PC3 | 126 | 41.6 | 210 |

(c)

| | b | s | b+2s |
|---|---|---|---|
| PC1 | 125 | 40.9 | 207 |
| PC2 | 124 | 43.8 | 212 |
| PC3 | 124 | 41.3 | 206 |
| PC4 | 127 | 42.2 | 211 |
| PC5 | 122 | 44.3 | 210 |
| PC6 | 126 | 39.1 | 203 |

(d)

| | b | s | b+s |
|---|---|---|---|
| PC1 | 128 | 41.1 | 210 |
| PC2 | 127 | 41.3 | 209 |
| PC3 | 129 | 42.6 | 213 |
| PC4 | 124 | 37.8 | 200 |

(e)

| | b | s | b+2s |
|---|---|---|---|
| PC1 | 128 | 41.5 | 210 |
| PC2 | 124 | 43.4 | 210 |
| PC3 | 125 | 43.9 | 213 |
| PC4 | 124 | 40.9 | 206 |

(f)

**Table 8.10**: *Statistical parameters of the PCA (a)on Cu, Fe, Co, As; (b)on Fe, Ba, As, Pb; c)on Fe, Ni, Cu; (d)on As, Cr, V, Ba, Fe, Cu; (e)on Fe, Mg, Ti, Cu; (f)on Fe, As, Cu, Pb*

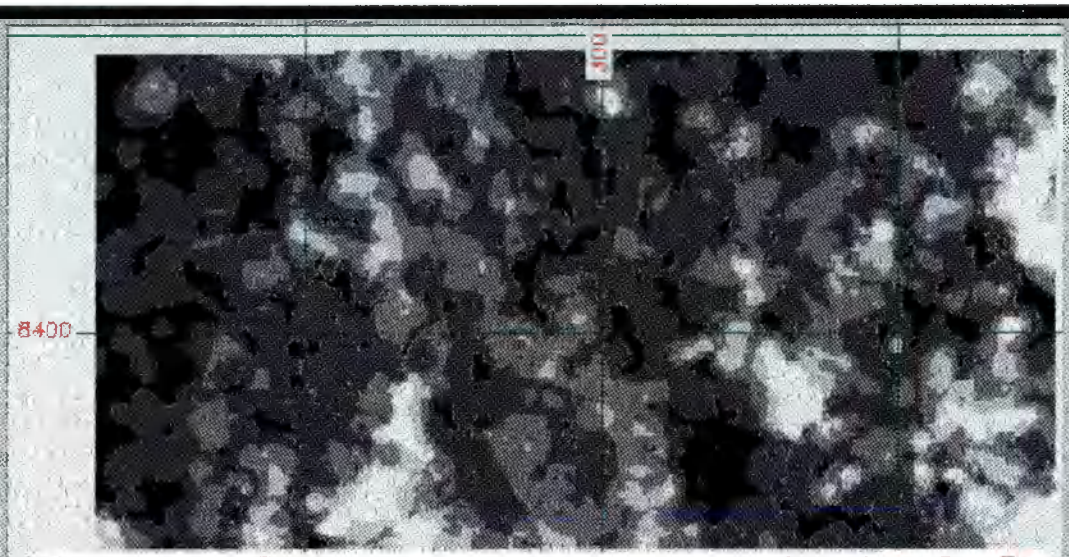


Figure 8.19: Principal Component Analysis (PC1) on Cu, Fe, Co and As, in grey scale.

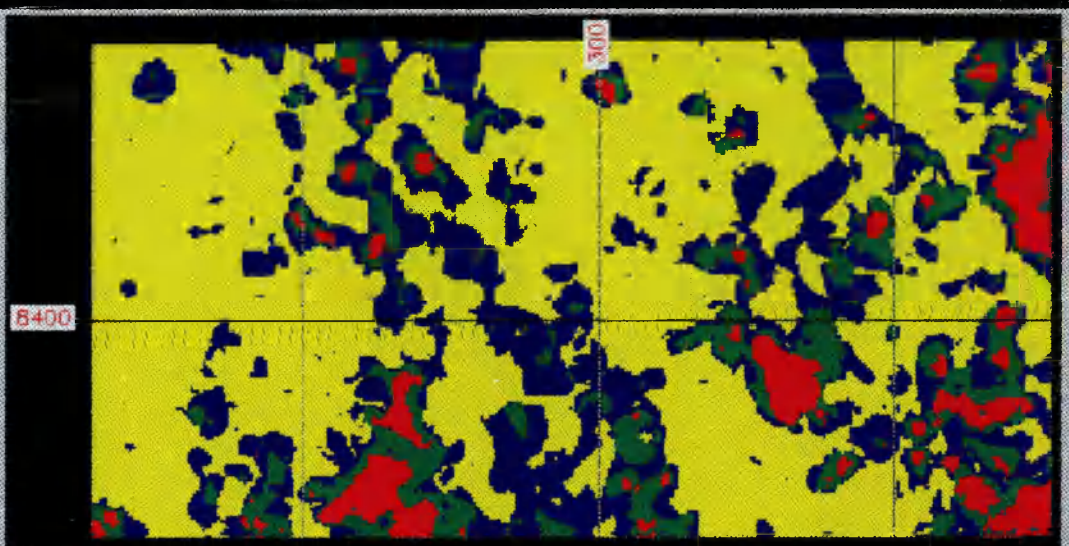


Figure 8.20: Principal Component Analysis (PC1) on Cu,Fe,Co and As. Yellow, blue, green and red represent areas where values are ranging from: 0 to b, b to b+s, b+s to b+2s and >b+2s, respectively

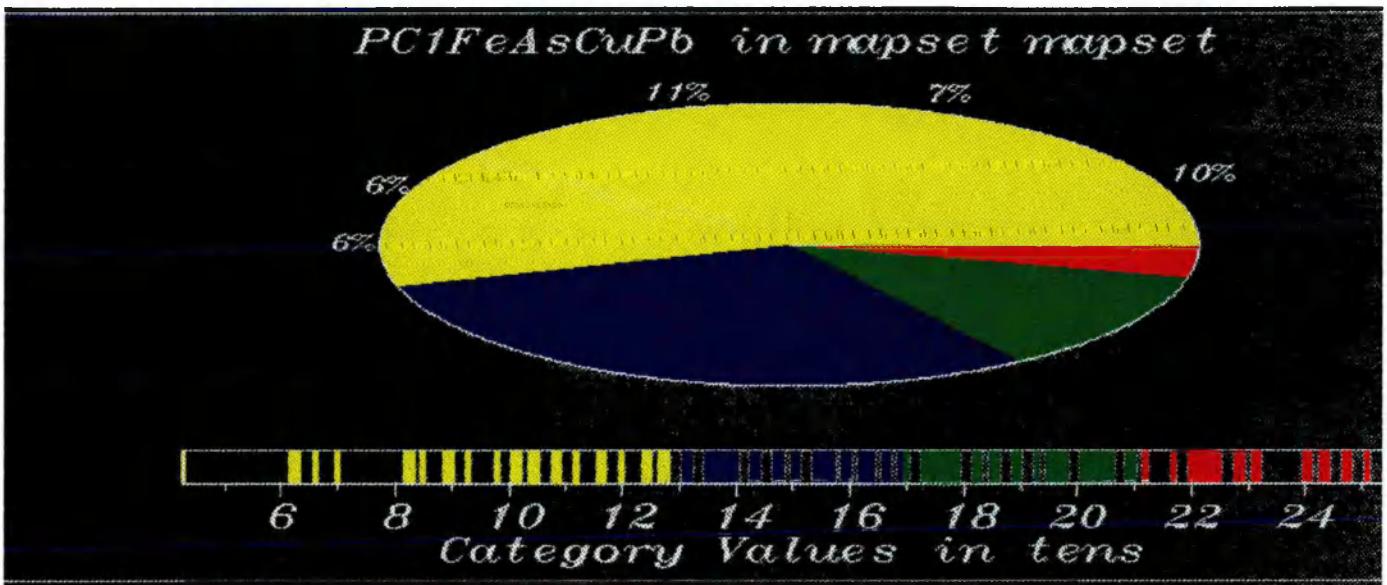


Figure 8.21: Pie histogram of PCA (PC1) on Fe, As, Cu and Pb

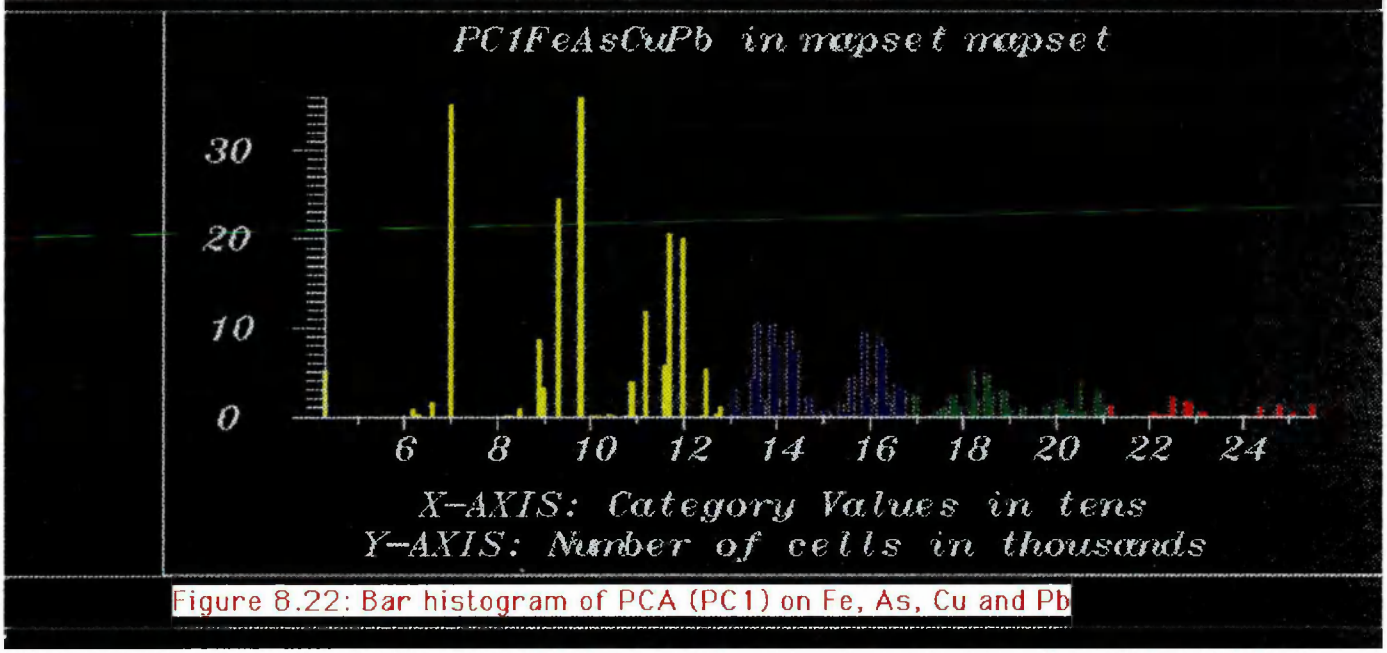


Figure 8.22: Bar histogram of PCA (PC1) on Fe, As, Cu and Pb

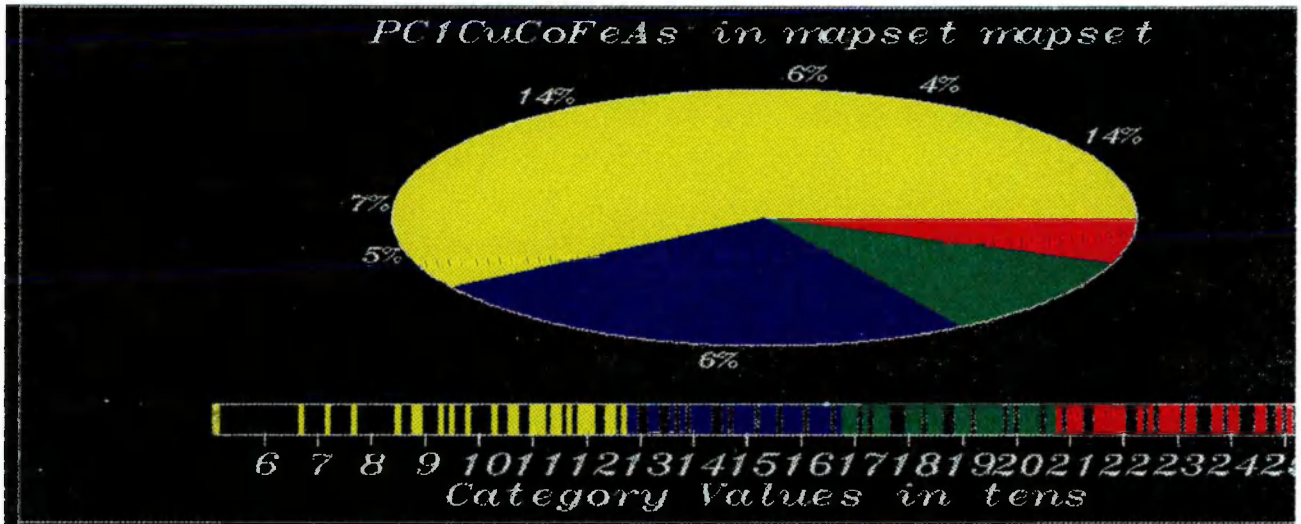


Figure 8.23: Pie histogram of PCA (PC1) on Cu, Co, Fe and As

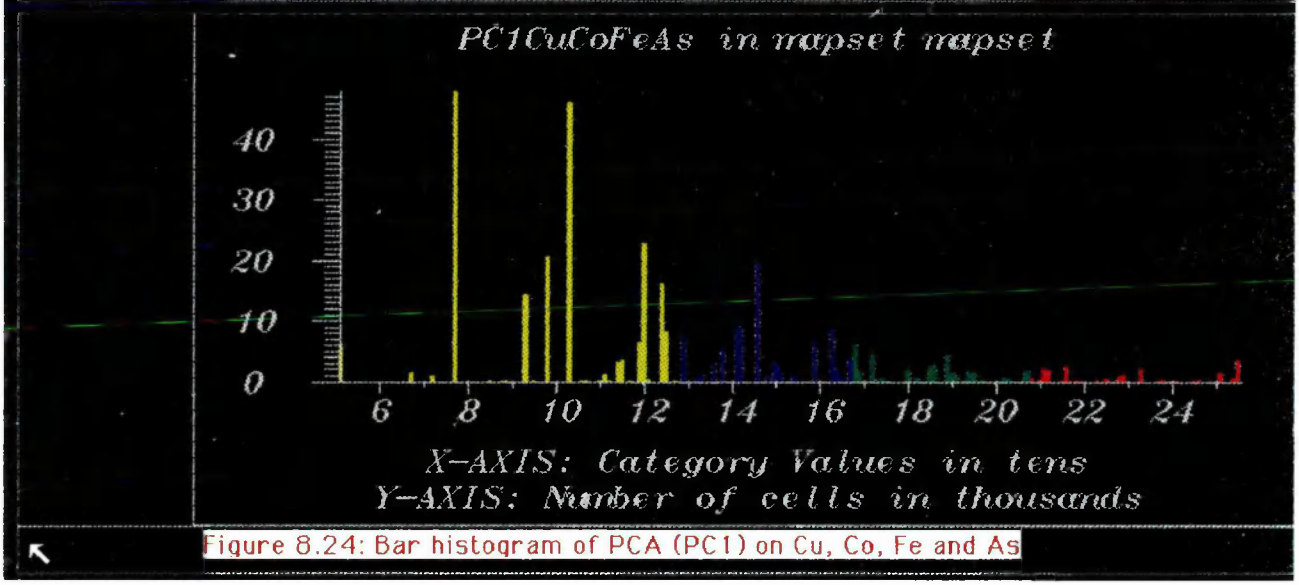


Figure 8.24: Bar histogram of PCA (PC1) on Cu, Co, Fe and As

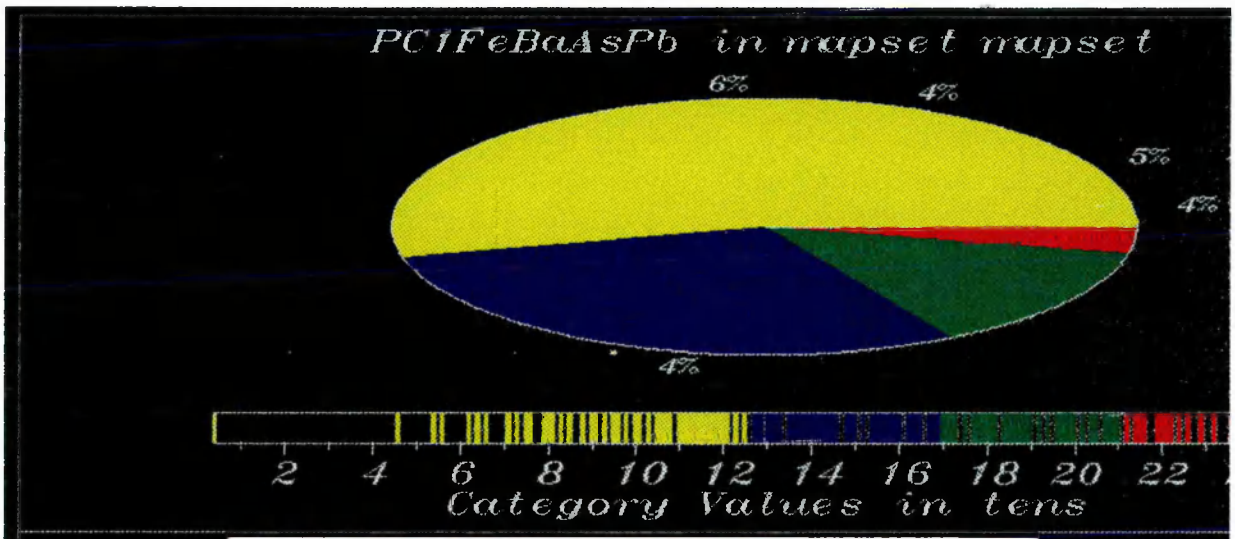


Figure 8.25: Pie histogram of PCA (PC1) on Fe, Ba, As and Pb

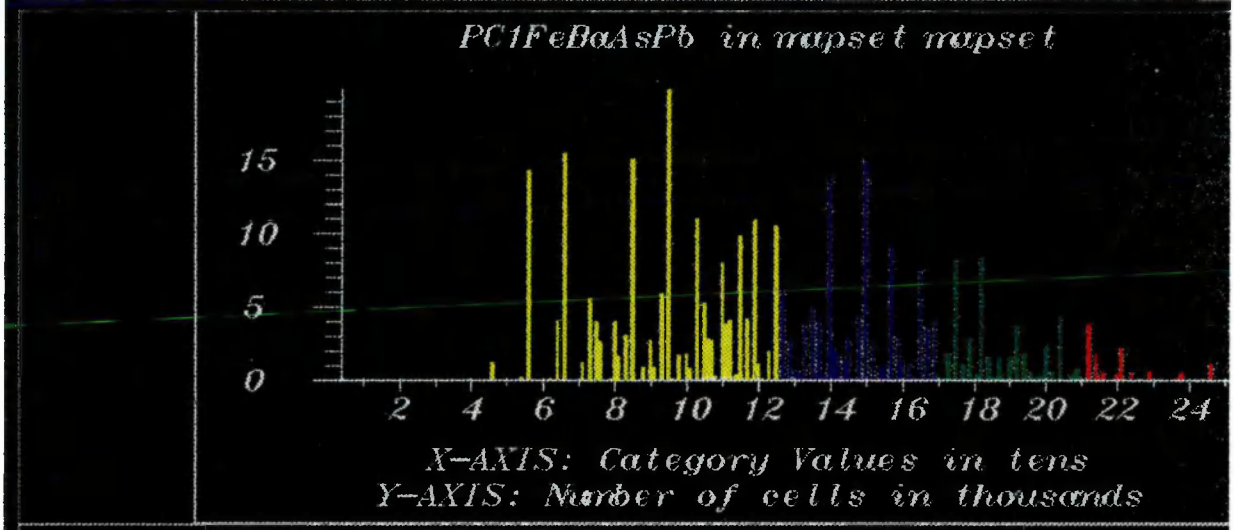


Figure 8.26: Bar histogram of PCA (PC1) on Fe, Ba, As and Pb

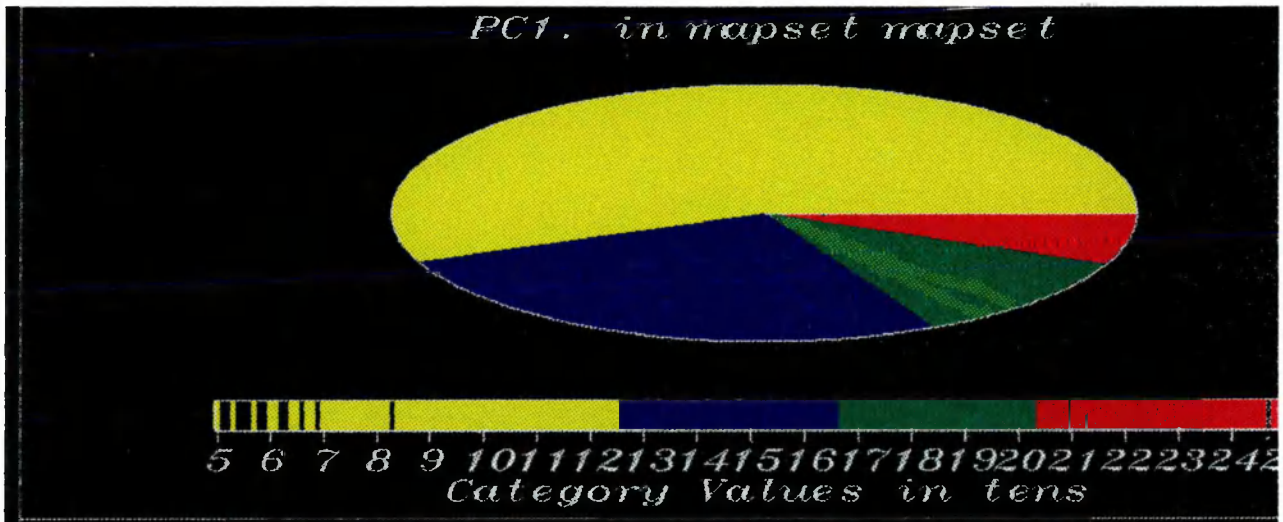


Figure 8.27: Pie histogram of PCA (PC1) on As,Cr,V,Ba,Fe and Cu

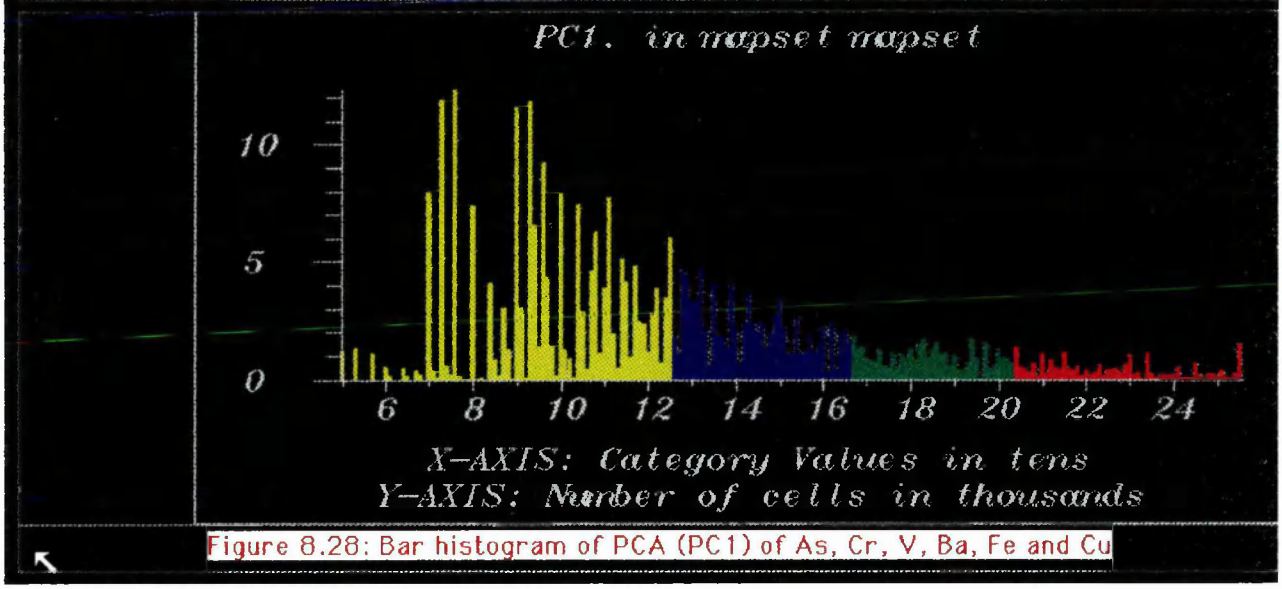


Figure 8.28: Bar histogram of PCA (PC1) of As, Cr, V, Ba, Fe and Cu

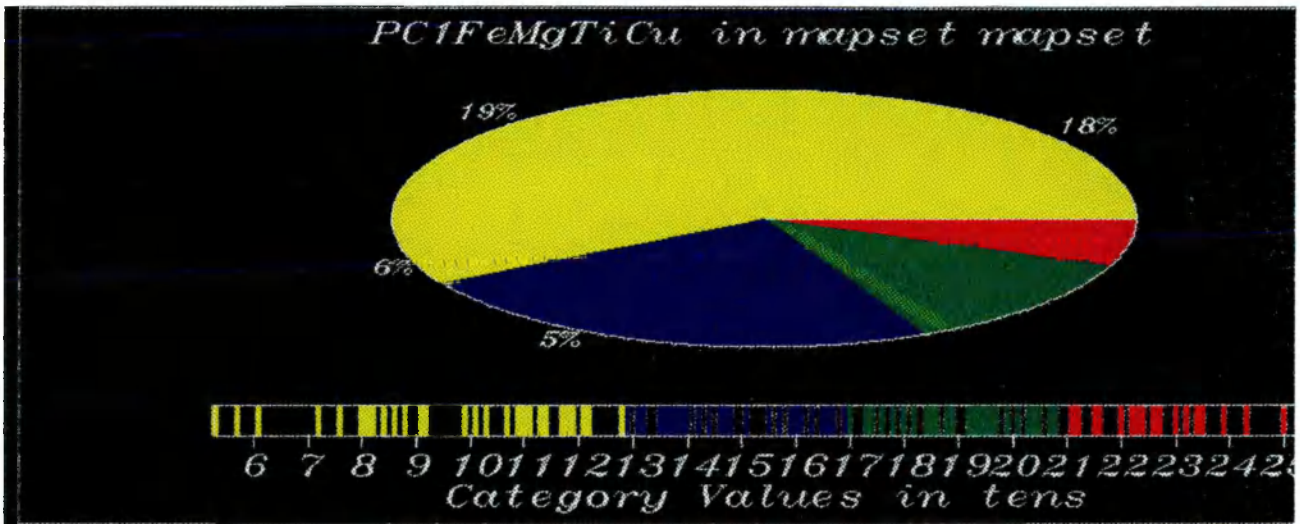


Figure 8.29: Pie histogram of PCA (PC1) on Fe, Mg, Ti and Cu

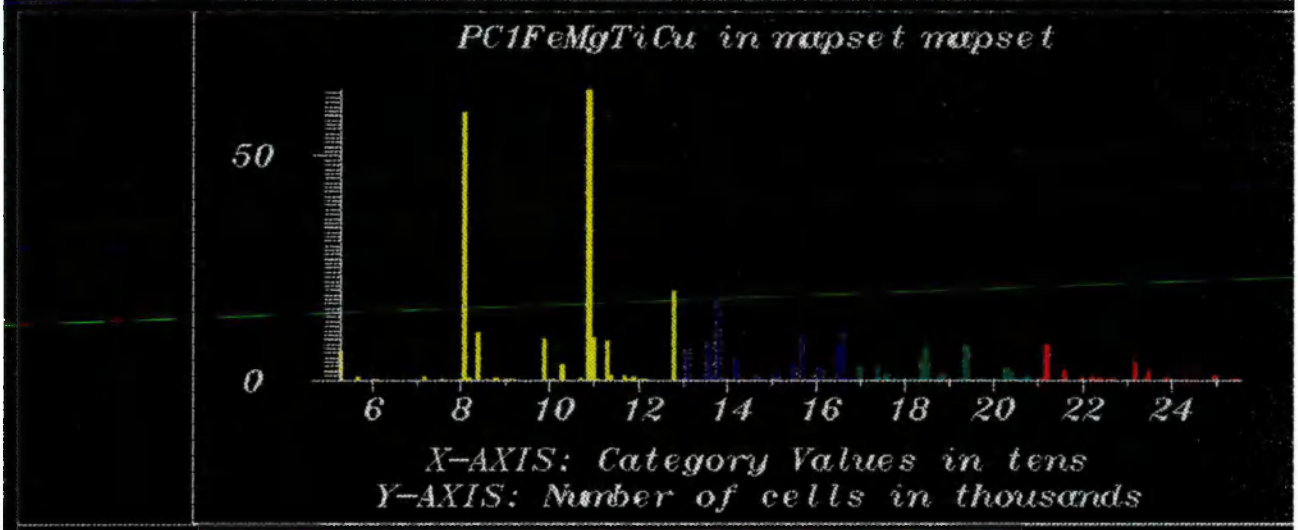


Figure 8.30: Bar histogram of PCA (PC1) on Fe, Mg, Ti and Cu

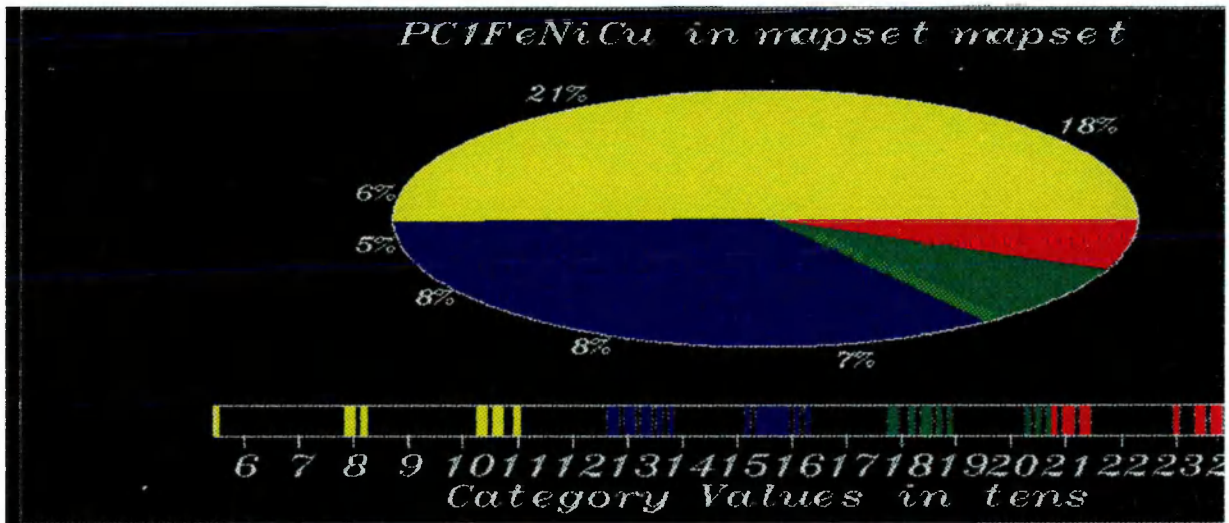


Figure 8.31: Pie histogram of PCA (PC1) on Fe, Ni and Cu

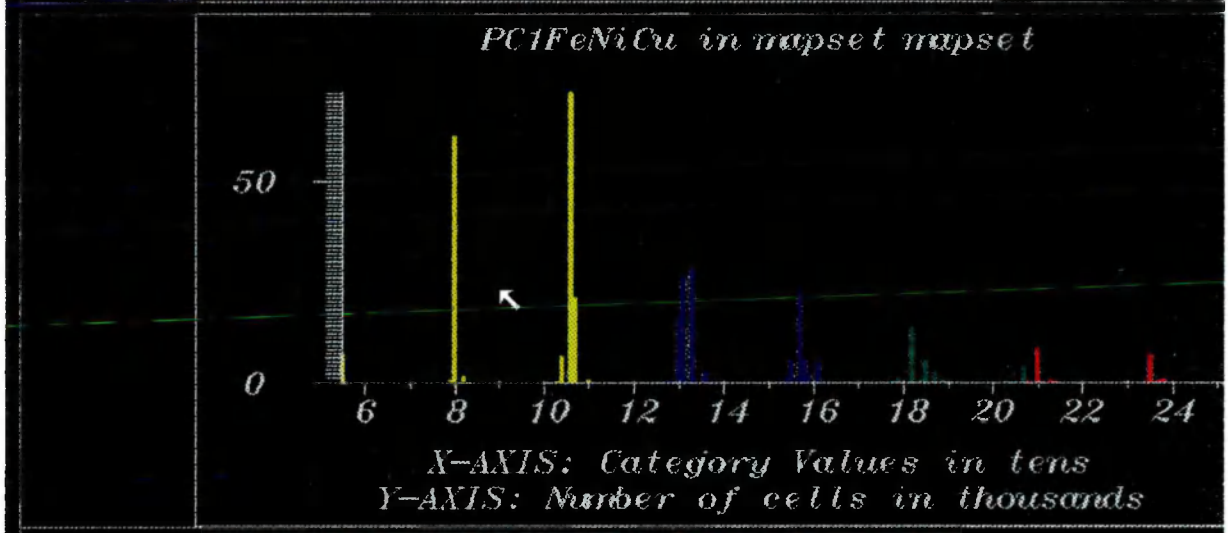


Figure 8.32: Bar histogram of PCA (PC1) on Fe, Ni and Cu

| ELEMENT ASSOCIATION | CATEGORY 4 (0 to b) | | CATEGORY 3 (b to b+s) | | CATEGORY 2 (b+s to b+2s) | | CATEGORY 1 (> b+2s) | |
|---|---|---|---|---|---|---|---|---|
| | % | $km^2$ | % | $km^2$ | % | $km^2$ | % | $km^2$ |
| 1 | 60 | 2040 | 24 | 816 | 11.2 | 381 | 4.75 | 161.50 |
| 2 | 56 | 1904 | 26 | 884 | 14.0 | 476 | 3.98 | 135.32 |
| 3 | 50 | 1700 | 35 | 1190 | 10.6 | 360 | 4.34 | 147.56 |
| 4 | 58 | 1972 | 24 | 816 | 13.9 | 472 | 4.10 | 139.4 |
| 5 | 55 | 1870 | 30 | 1020 | 12.4 | 421 | 2.56 | 87.04 |
| 6 | 53 | 1802 | 28 | 952 | 16.6 | 564 | 2.39 | 81.26 |

**Table 8.11**: *Distribution of the four categories related to the total area. 1:Fe-Cu-Co-As; 2:Fe-As-Cr-V-Ba-Cu; 3:Fe-Ni-Cu; 4:Fe-Mg-Ti-Cu; 5:Fe-Cu-As-Pb; 6:Fe-Ba-As-Pb*

As PC1 has positive mixtures, regions where values are greater than b+2s represent the anomalous areas which represent 4.75% of the total area or 161.50 $km^2$ (Figure 8.33)

The PCA on Fe, Ba, As and Pb presented the following percentages of total variance contributed by each eigenvalue: 45%, 26%, 16% and 13% corresponding to PC1, PC2, PC3 and PC4, respectively. By looking at the percentages presented in Table 8.9.d, PC1 (Figures 8.34 and 8.35) incorporates positive mixtures of all elements with a greater proportion of Ba and Pb. The selected anomalous areas are presented in Figure 8.36, and represent 2.39% of the total area or 81.26 $km^2$. PC2 has a prevailing contribution from Fe, Ba and As, PC3 has a dominant contribution from Fe and As in a similar fashion to that found in the elemental associations Cu,Fe,Co and As, and PC4 has a dominant contribution of Ba and Pb. As a result of the PCA on Fe, As, Cu and Pb, the percentages of total variance

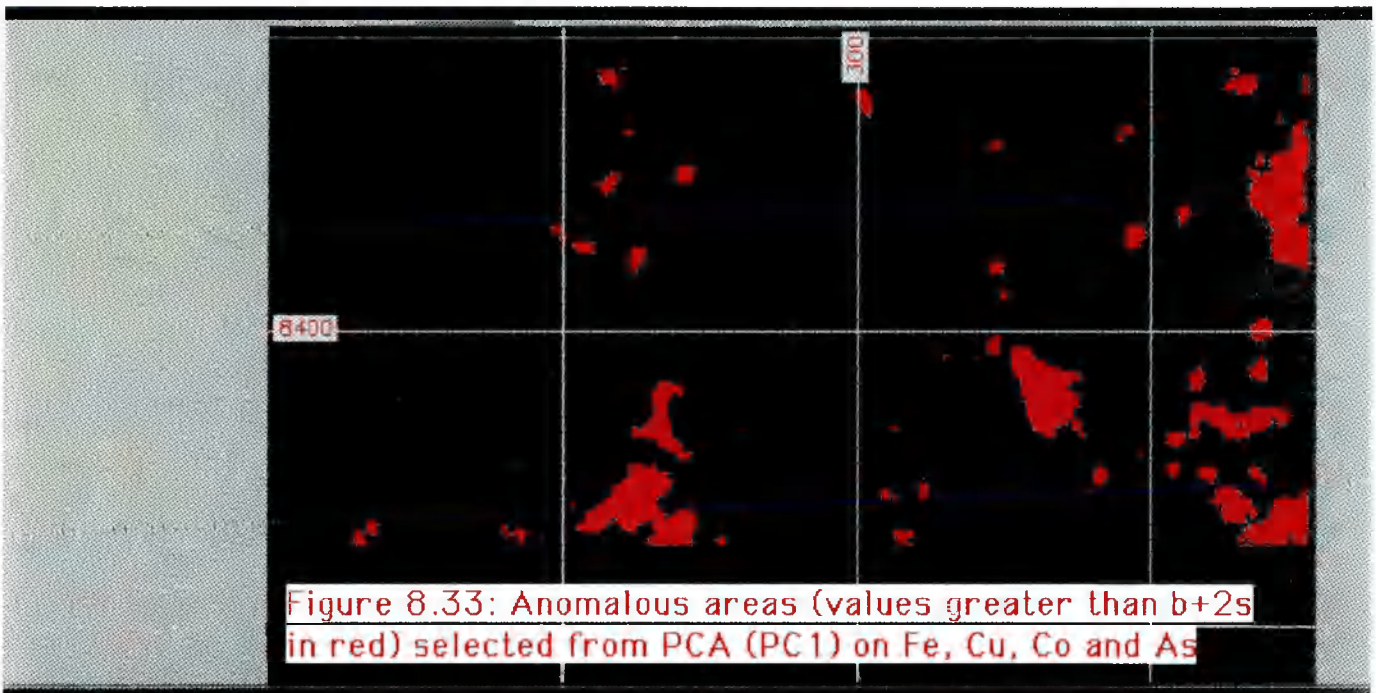


Figure 8.33: Anomalous areas (values greater than b+2s in red) selected from PCA (PC1) on Fe, Cu, Co and As

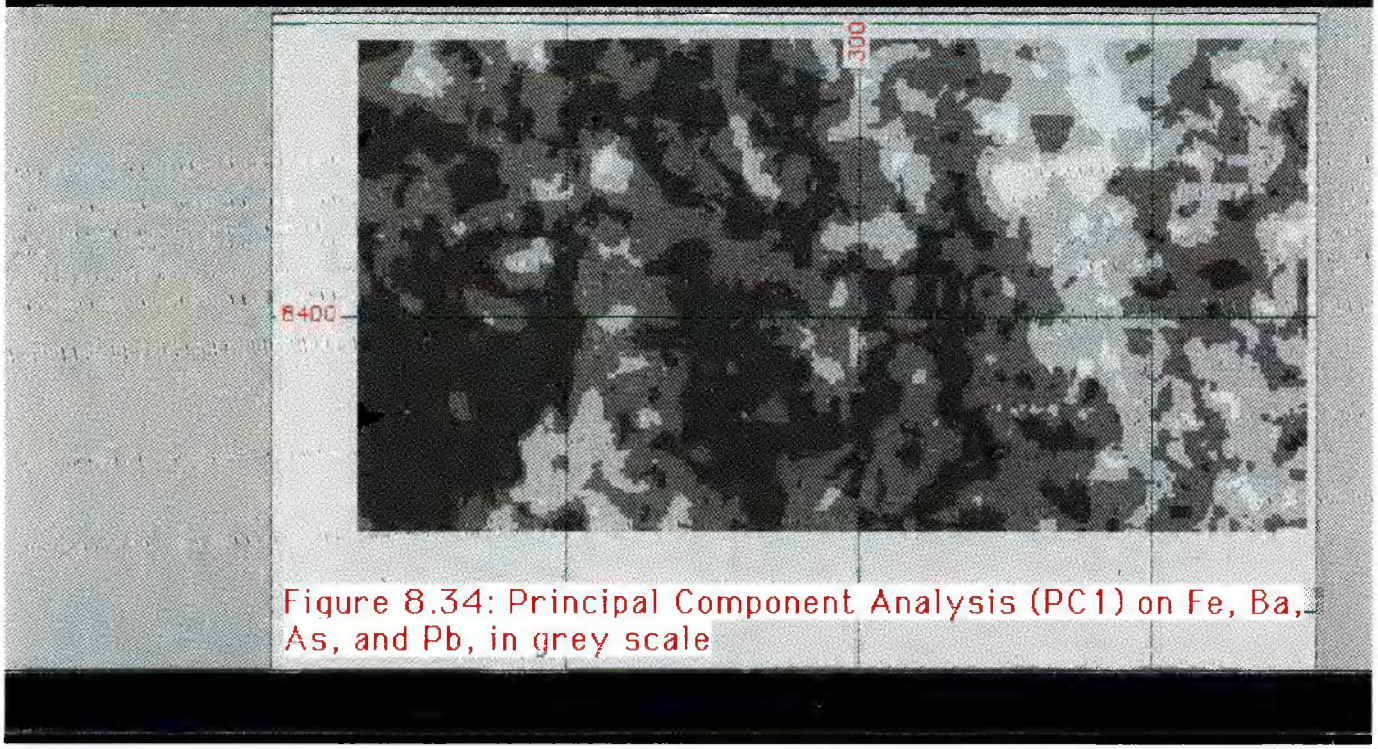


Figure 8.34: Principal Component Analysis (PC1) on Fe, Ba, As, and Pb, in grey scale

contributed by each eigenvalues are: 43%, 25%, 18% and 14% corresponding to PC1, PC2, PC3, and PC4, respectively. By looking at the percentages presented in Table 8.9.f, PC1 (Figures 8.37 and 8.38) incorporates a positive mixture of Fe, As, Cu and Pb with a balanced proportion of each element. Figure 8.39 presents the selected anomalous areas which represent 2.56% of the total area or 87.04 $km^2$. PC2 contains basically information from Pb. PC3 has a greater proportion of As and Fe (sites where As is high, Fe is low, and vice-versa), and PC4 has a dominant contribution from Cu. As a result the PCA on As, Cr, V, Ba, Fe and Cu, the percentages of total variance contributed by each eigenvalue are: 34%, 23%, 14%, 12%, 9, and 8% corresponding to PC1, PC2, PC3, PC4, PC5 and PC6, respectively. By looking into the percentages presented in Table 8.9.h, PC1 (Figures 8.40 and 8.41) incorporates a positive mixture of all elements, although with a smaller proportion of Ba. Figure 8.42 presents the selected anomalous areas which represent 3.98% of the total area or 135.32 $km^2$. PC2 incorporates a very large proportion of Ba, PC3 has a dominant proportion of V, PC4 has a prevailing contribution of As and Cr (where As is high, Cr is low, or vice-versa), PC5 has a dominant proportion of Fe, and PC6 incorporates a greater proportion of Cu. The PCA on Fe, Mg, Ti and Cu presented the percentages of total variance contributed by each eigenvalues as follows: 49%, 22%, 17% and 12% corresponding to PC1, PC2, PC3 and PC4, respectively. By looking into the percentages presented in Table 8.9.j. PC1 (Figures 8.43 and 8.44) although incorporating a positive mixture from Fe, Mg, Ti and Cu, has a prevailing contribution of Fe, Ti and Cu. The selected anomalous areas are presented

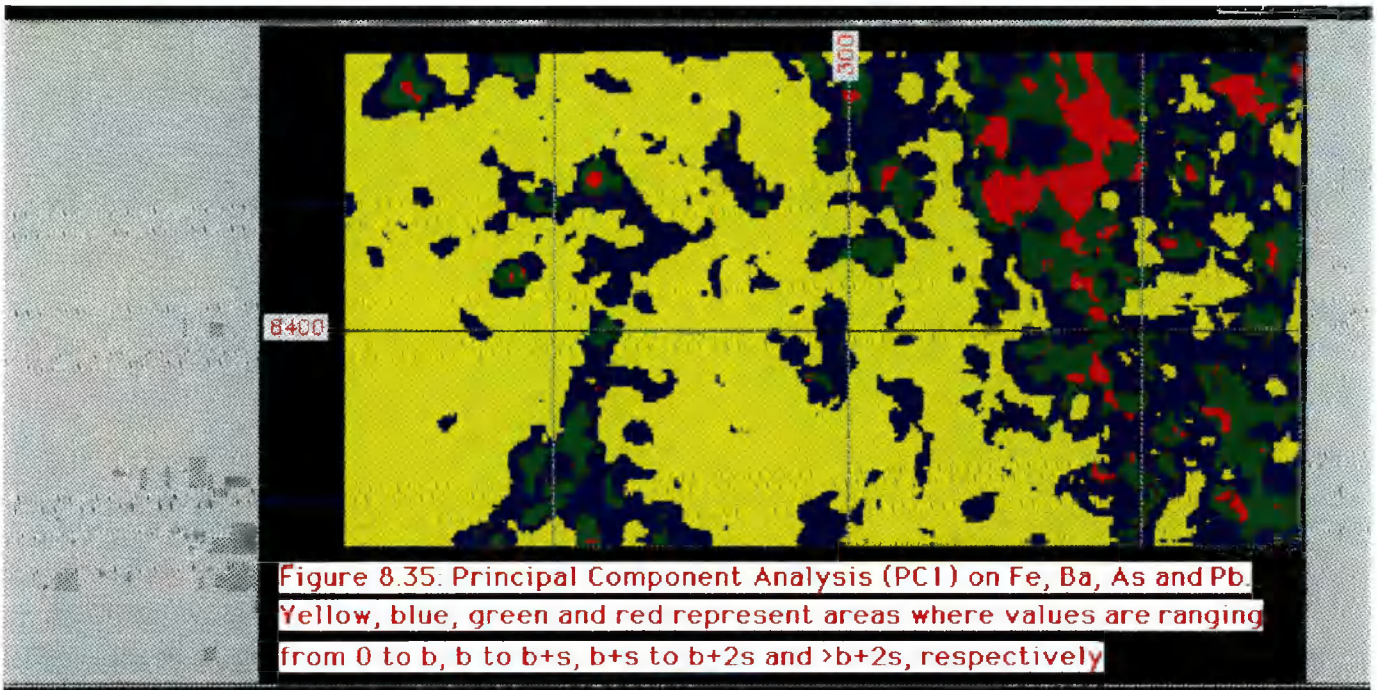


Figure 8.35: Principal Component Analysis (PC1) on Fe, Ba, As and Pb. Yellow, blue, green and red represent areas where values are ranging from 0 to b, b to b+s, b+s to b+2s and >b+2s, respectively

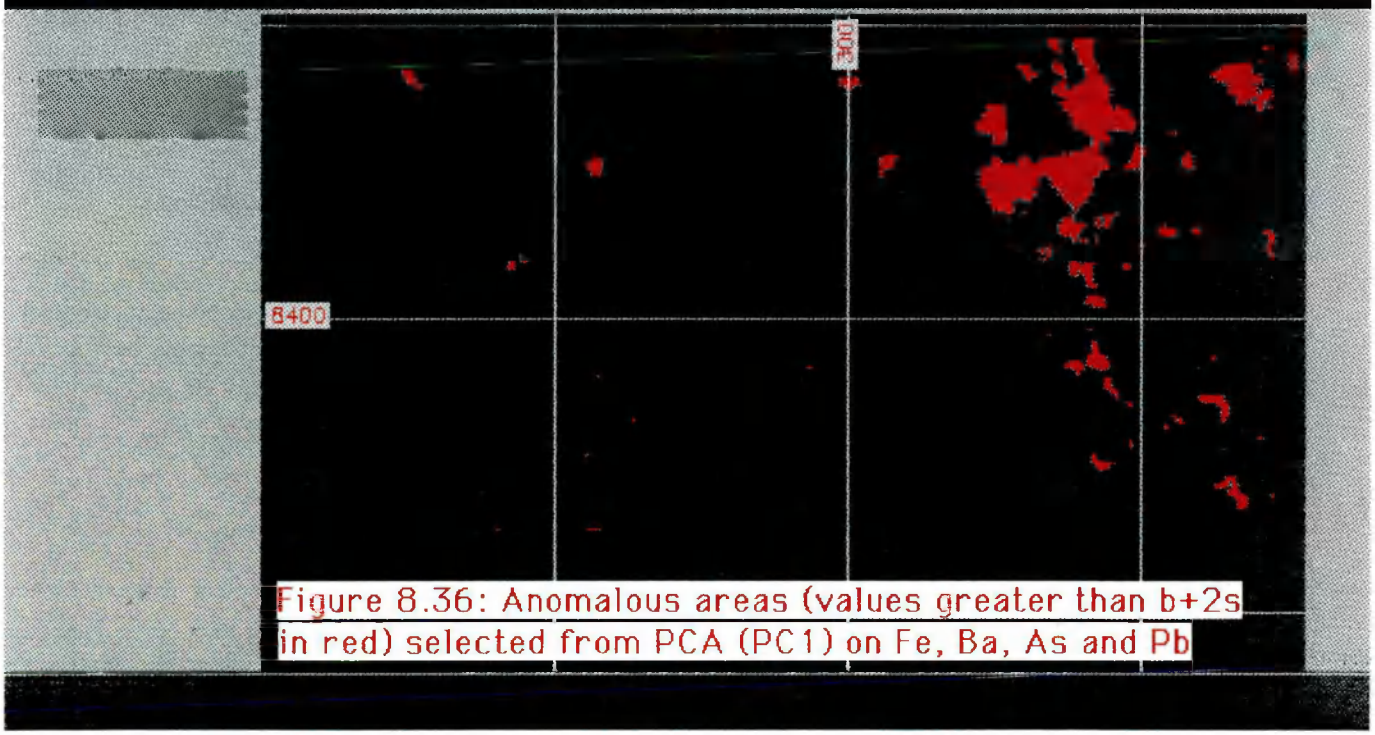


Figure 8.36: Anomalous areas (values greater than b+2s in red) selected from PCA (PC1) on Fe, Ba, As and Pb

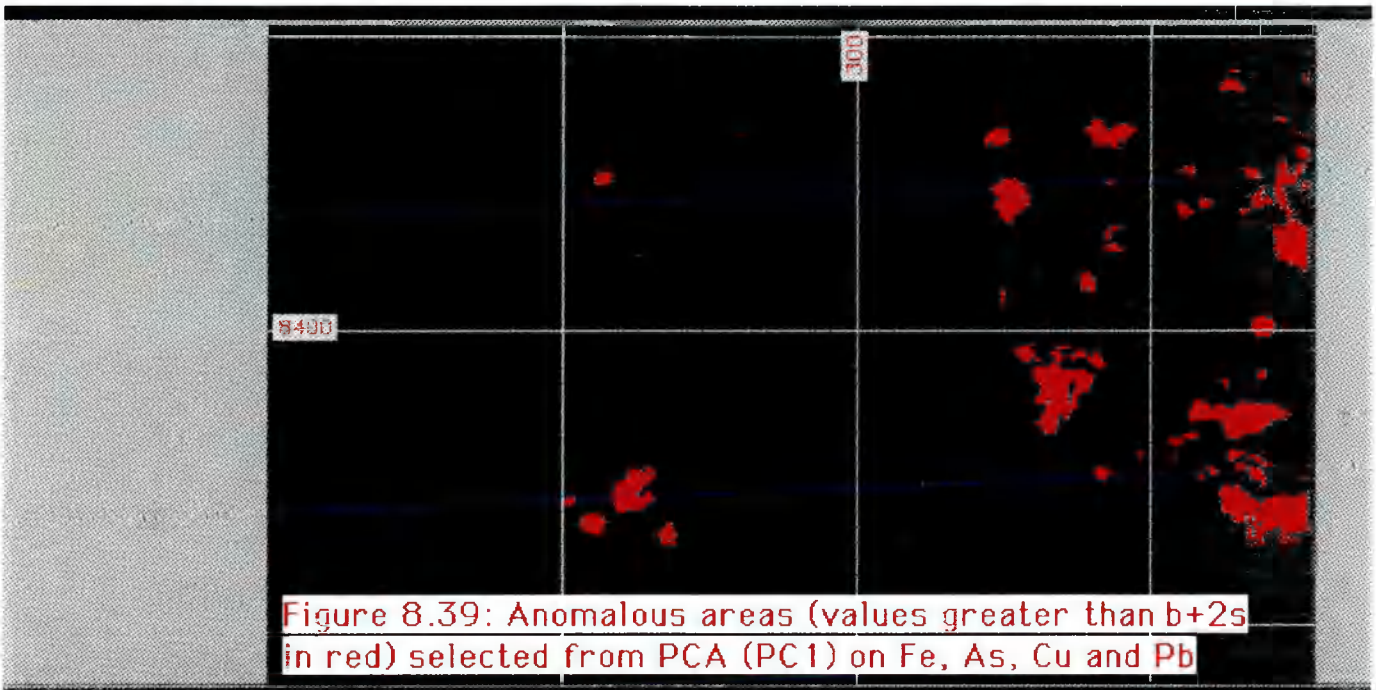


Figure 8.39: Anomalous areas (values greater than b+2s in red) selected from PCA (PC1) on Fe, As, Cu and Pb

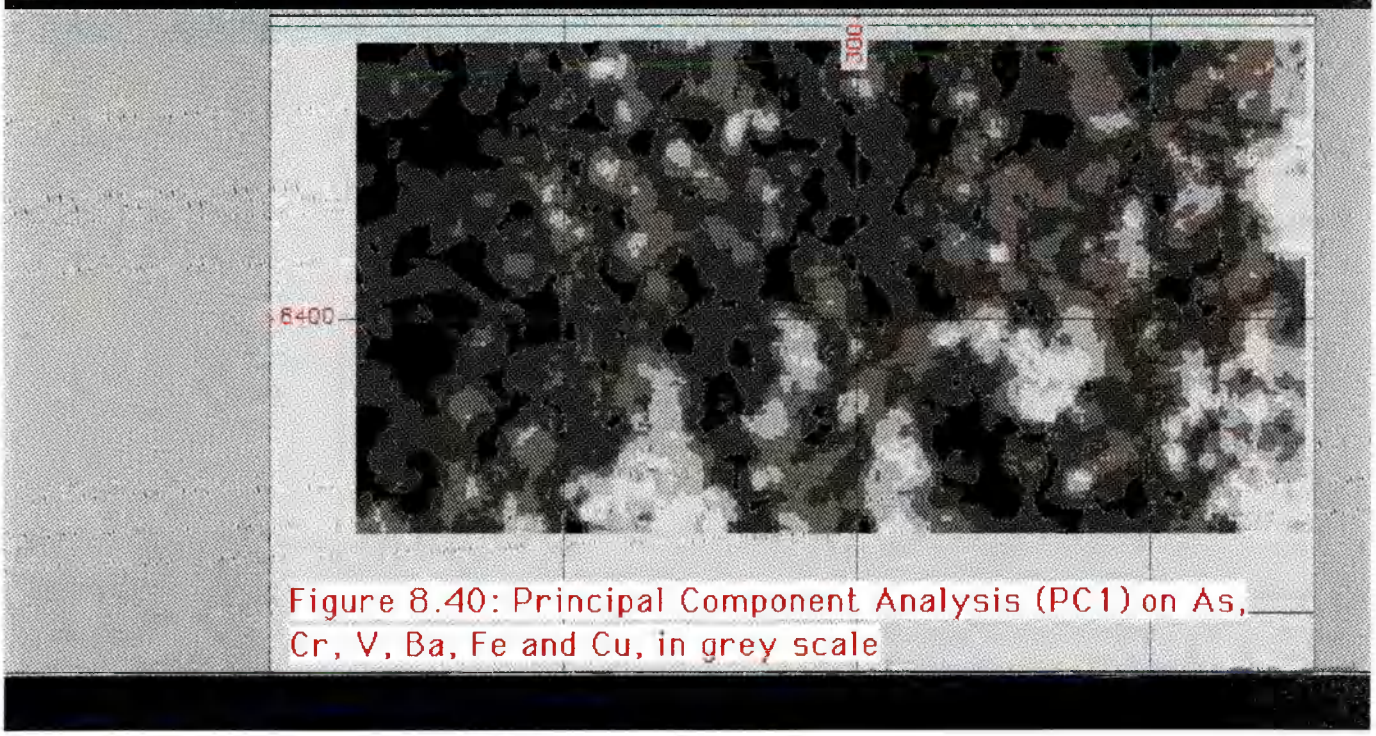


Figure 8.40: Principal Component Analysis (PC1) on As, Cr, V, Ba, Fe and Cu, in grey scale

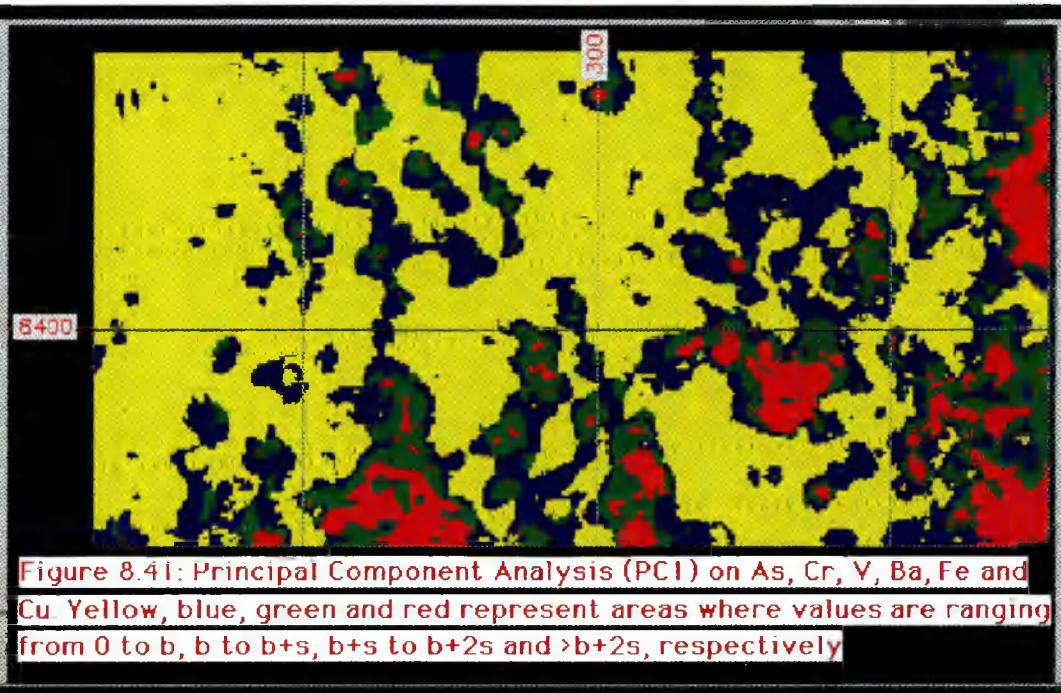


Figure 8.41: Principal Component Analysis (PC1) on As, Cr, V, Ba, Fe and Cu. Yellow, blue, green and red represent areas where values are ranging from 0 to b, b to b+s, b+s to b+2s and >b+2s, respectively

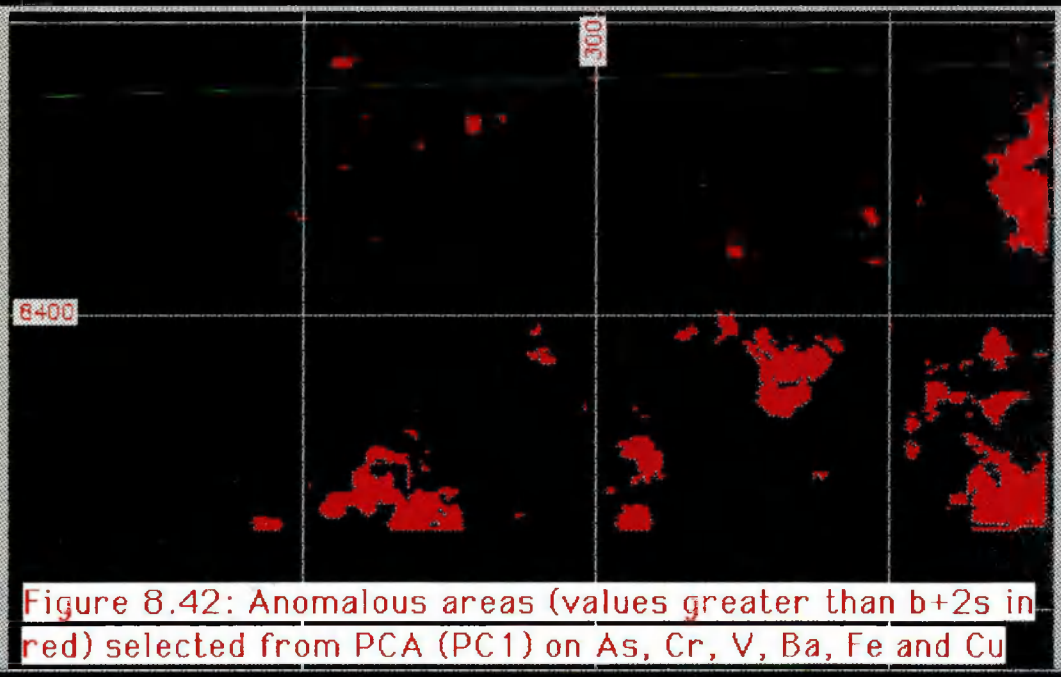


Figure 8.42: Anomalous areas (values greater than b+2s in red) selected from PCA (PC1) on As, Cr, V, Ba, Fe and Cu

in Figure 8.45 and represent 4.10% of the total area or 139.40 $km^2$. PC2 has a greater contribution of Ti, but when Ti is high Fe, Mg and Cu are low, or vice-versa. PC3 incorporates a great proportion from Fe and Cu, and PC4 has a dominant contribution of Mg. As a result of PCA on Fe, Ni and Cu, the percentages of total variance contributed by each eigenvalue are: 58%, 27% and 15% corresponding to PC1, PC2 and PC3, respectively. PC1 (Figures 8.46 and 8.47) incorporates a well balanced positive mixture of Fe (33%), Ni(36%) and Cu(31%). By looking into the statistical parameters, values greater than 207 represent anomalous sites. Figure 8.48 presents the selected anomalous areas which represent 4.34% of the total area or 147.56 $km^2$. PC2 has a dominant mixture of Fe(51%) and Ni(36%). PC3 has a dominant contribution from Cu(53%).

## 8.7 Discussion of the results

The ambiguity of the stream sediment surveys coupled with the complexity of most Archaean terrains in the world have to be integrated with other sources of information. The analysis of geochemical data itself produces a series of potential targets that represent less than 5% of the total study area, without recourse to any other source. With the exception of the Fe-Ba-As-Pb association, all the defined anomalous areas are highlighted in roughly the same location, as can be seen in table 8.12. This association without other information could be reflecting anomalies related to a particular lithology. However various factors such as Fe and Mn content, contamination and rock type change may contribute to the production of non-significant or false anomalies.

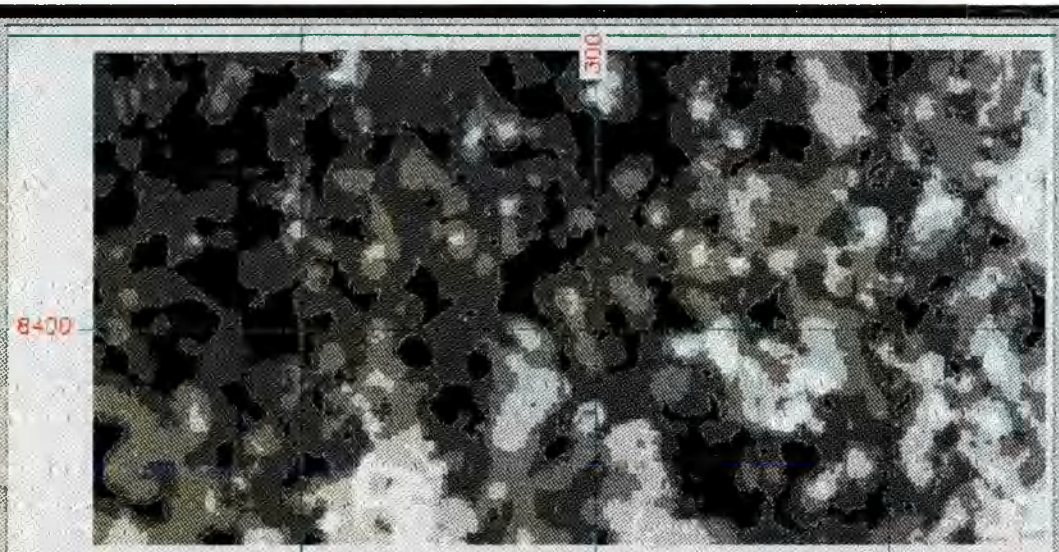


Figure 8.43: Principal Component Analysis (PC1) on Fe, Mg, Ti and Cu, in grey scale

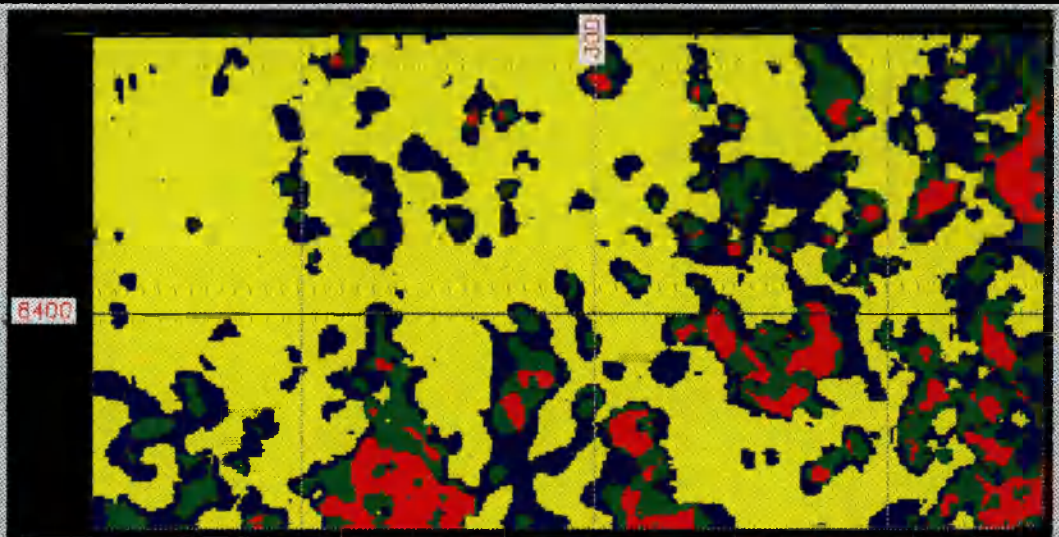


Figure 8.44: Principal Component Analysis (PC1) on Fe, Mg, Ti and Cu. Yellow, blue, green and red represent areas where values are ranging from 0 to b, b to b+s, b+s to b+2s and >b+2s, respectively

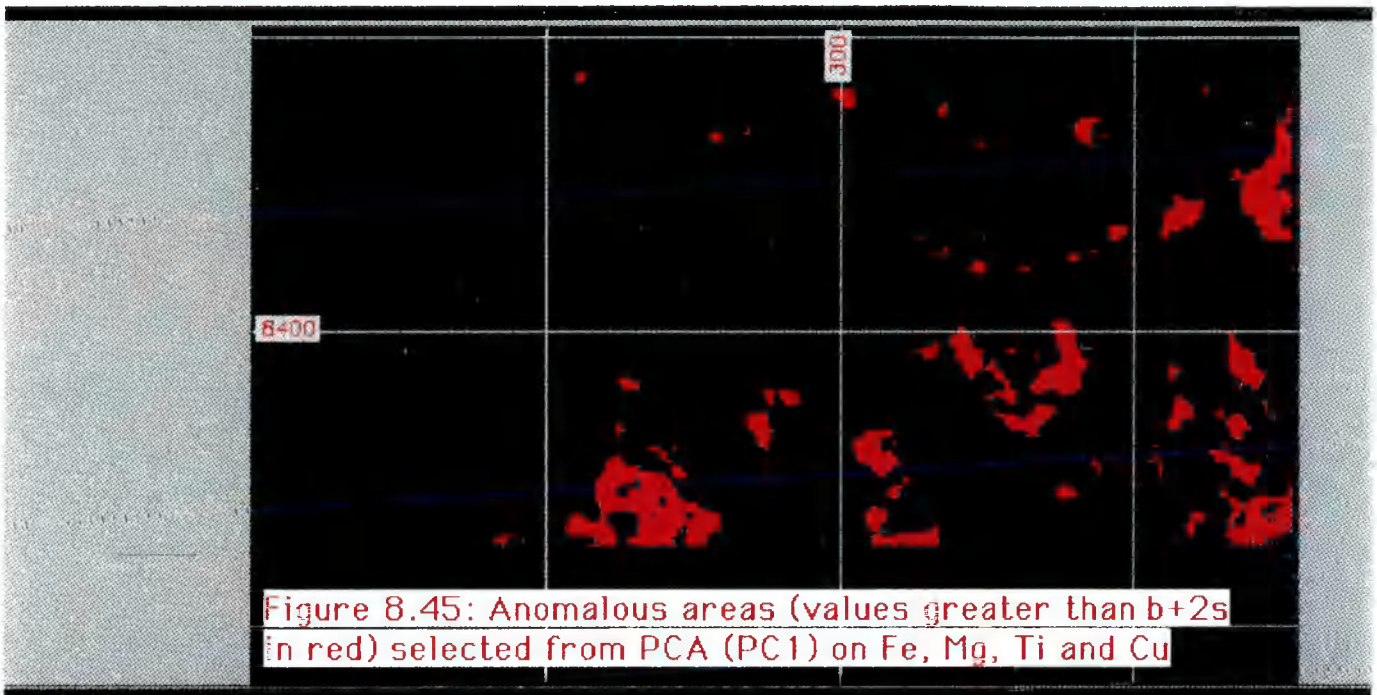


Figure 8.45: Anomalous areas (values greater than b+2s in red) selected from PCA (PC1) on Fe, Mg, Ti and Cu

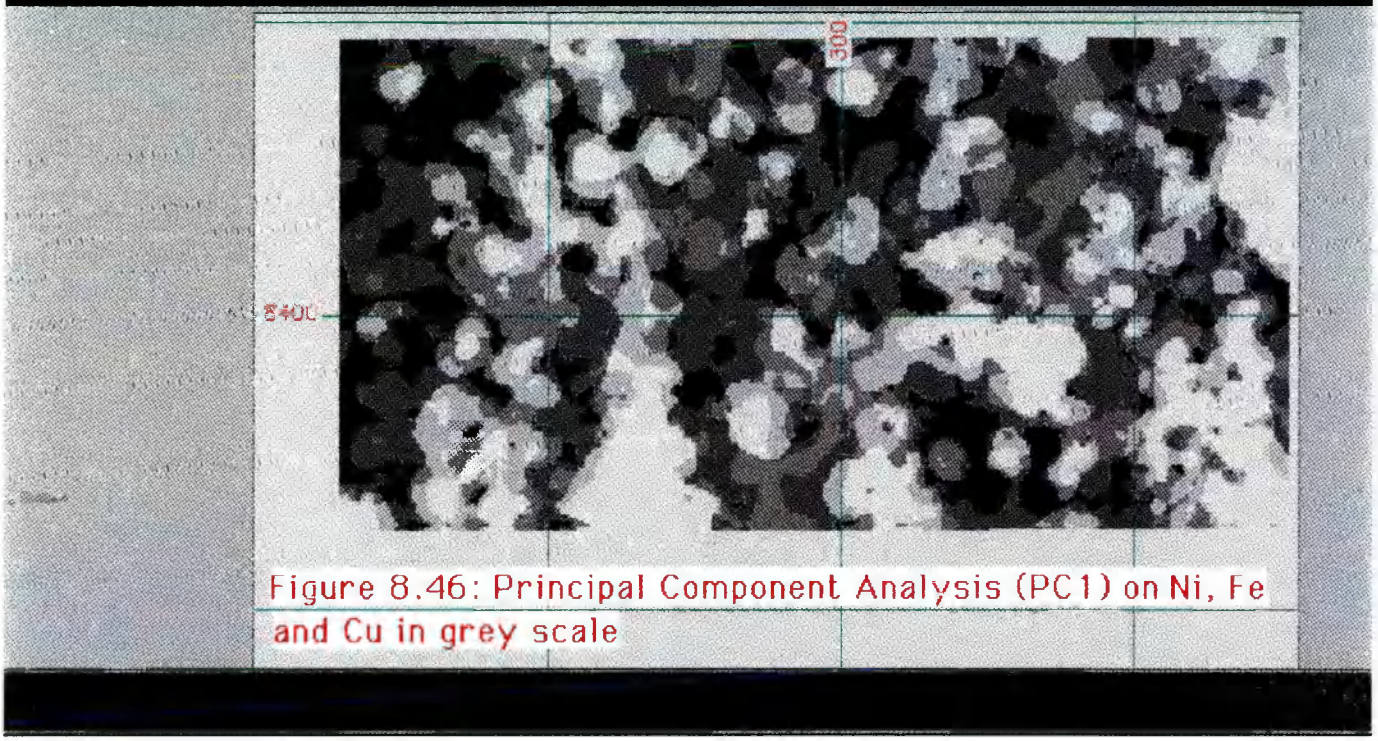


Figure 8.46: Principal Component Analysis (PC1) on Ni, Fe and Cu in grey scale

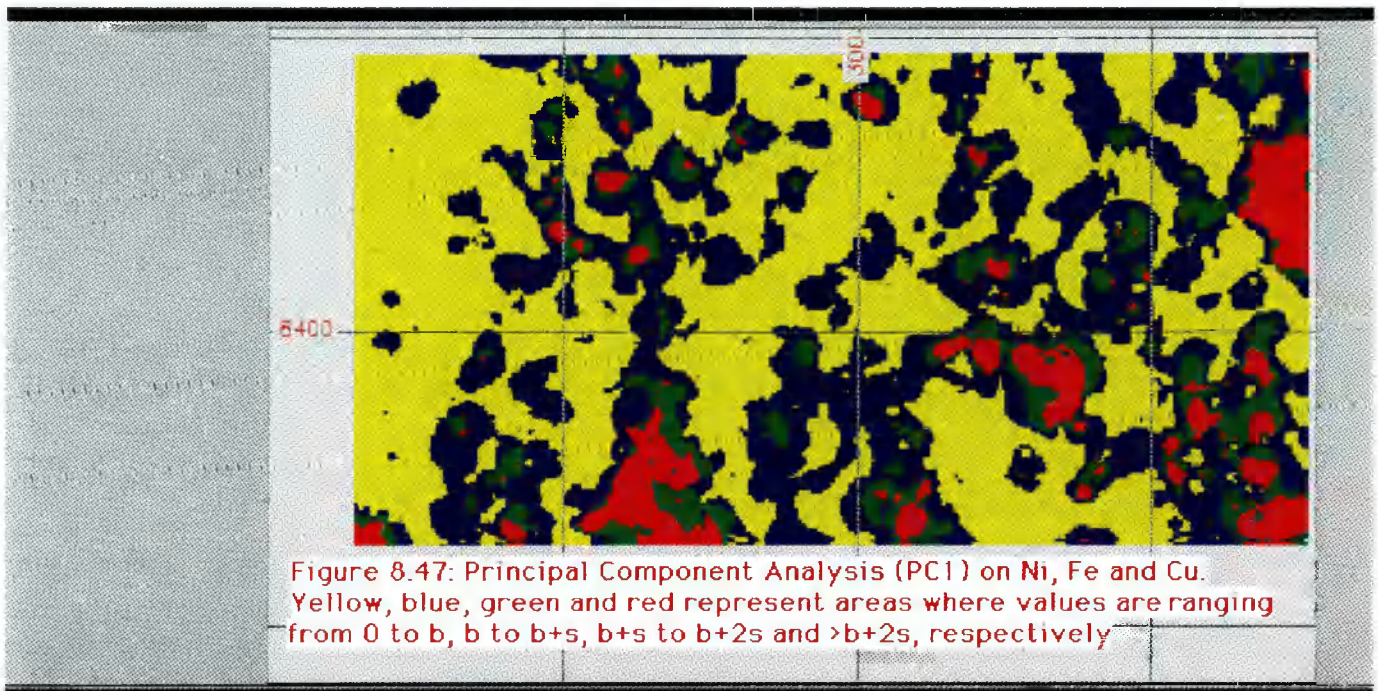


Figure 8.47: Principal Component Analysis (PC1) on Ni, Fe and Cu. Yellow, blue, green and red represent areas where values are ranging from 0 to b, b to b+s, b+s to b+2s and >b+2s, respectively

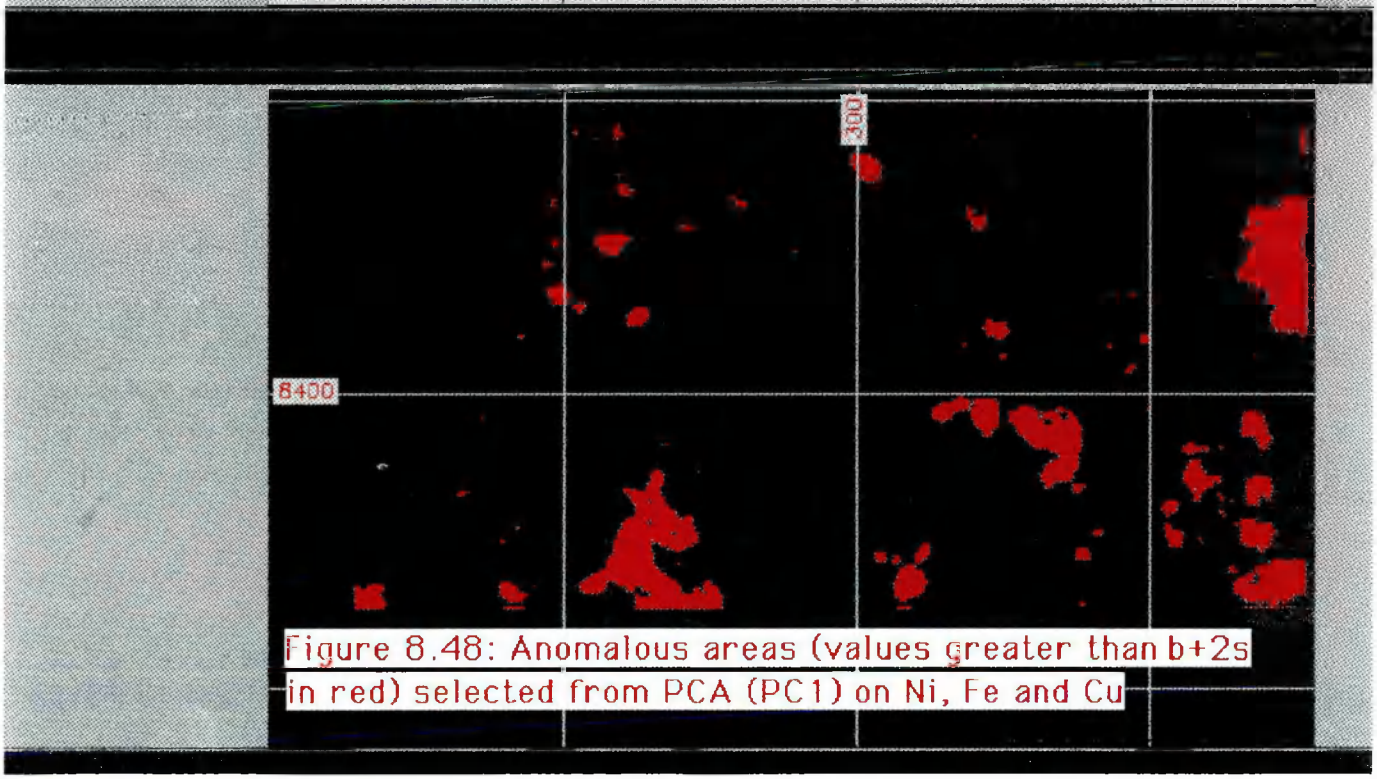


Figure 8.48: Anomalous areas (values greater than b+2s in red) selected from PCA (PC1) on Ni, Fe and Cu

| 1 | 2 | 3 | 4 | 5 | 6 | |
|---|---|---|---|---|---|---|
| 87.04 | 29.1 | 77.1 | 89.4 | 60.4 | 70.9 | 1 |
| | 81.26 | 7.0 | 12.3 | 7.6 | 6.0 | 2 |
| | | 135.32 | 126.1 | 120.4 | 125.1 | 3 |
| | | | 161.50 | 94.0 | 129.7 | 4 |
| | | | | 139.40 | 104.8 | 5 |
| | | | | | 147.56 | 6 |

**Table 8.12**: *Areas (in km2) of overlapping between the element association. 1)Fe-Cu-As-Pb; 2)Fe-Ba-As-Pb; 3)Fe-As-Cr-V-Ba-Cu; 4)Fe-Cu-Co-As; 5)Fe-Mg-Ti-Cu; 6)Ni-Fe-Cu*

The other anomalous areas could be related to true anomalies because they focus attention on the same location. Screening the geochemical data using lithological, structural information derived from existing maps and interpretation of remotely sensed data and airborne geophysical data requires a more sophisticated approach involving increased dimensionality and advanced GIS techniques. This enables the exploration to incorporate more detailed models to mineralisation process than statistical consideration of empirical geochemical data.

# CHAPTER 9: DATA FUSION

## 9.1 Introduction

For many years multidisciplinary data have been integrated using diverse approaches as an aid to solving geological problems. The best known integration method is through manual overlay operations where the final result is presented as a single aggregate of several bits of data.

Although GIS relies on overlay operations, the use of sophisticated arithmetical and logical operations produces maps and reports which no longer necessarily represent a single integration. In fact the results of GIS operations represent a fusion of information. This fusion generates maps and reports which will support the decisions to be made. However, the data base which was exhaustively manipulated for gold exploration, remains ready for new user specifications for other metal ventures and for general survey purposes.

In data integration towards a specific scenario, such as an exploration model, it is sometimes difficult to avoid redundancy. Data fusion procedures can select parts of the

scenario, perform mathematical interactions and logical connections, therefore being a unique way to suppress redundancy. Only in a GIS environment is it possible to achieve data fusion. Computer facilities and GIS functions provide the means. In addition to this, a well organised data base is always required.

In this study, the data base consists of three different types of format files: ASCII, binary and raster formats. The ASCII files include locations of faults, fractures, fold axes, mineral occurrences, stream sediment loci, vegetation and soil sites, and icons. The binary or vector files include faults, fractures and fold axes. The raster files include geological, vegetation and soil maps, Landsat TM, radar, magnetic, radiometric and stream sediment images. The computer facilities are Sun 3/160 C workstation model and peripherals such as a digitising tablet, laser writer and colour laser printer.

Before implementing data fusion it is necessary to expand some fundamental meanings and concepts dealing with such ideas as category, weighted values, preliminary target areas (PTA) and target areas.

A **category** may be referred to as either general or specific. When considered without regard to location, shape or size, a category is a general notion. Thus we can understand that in any one Archaean greenstone belt, volcanic and volcanoclastic rocks are important hosts for gold, no matter what the tangible boundary or particular locality. However, as soon as we recall a real section of an Archaean greenstone belt, such as the Contendas-Mirante Belt, we begin to be more specific by

defining a part of the geotectonic environment, with a geographical location. Therefore a specific category has to be placed in a particular context relative to its surroundings, and to discrete boundaries. Every part of the greenstone belt may be classified in this way. For different purposes different categories tend to dominate our awareness of certain class characteristics. To target gold, its presence is obviously the most important category, but also the geochemical and magnetic anomalies, particular lithologies, presence of sheared zones and granites are also important. Therefore the categories should be divided into hierarchical levels according to their relative importance.

**PTA** has come to mean defining areas which contain an aggregate of categories which properly belongs to the same hierarchical rank in a defined geographical location. This requires that a minimum number of categories should be found together to define a PTA. *Bonham-Carter et al* (1988) suggest that the spatial relationship of the following factors to known gold occurrences: multi-element lake sediment geochemistry, lithology, distance to formation contacts, and distance to anticlinal fold axes. From my own experience and the information contained in Chapter 5, areas of coincidence of geochemical and magnetic anomalies, and favourable lithologies form potential factors for consideration in PTA.

Weighted values represent values assigned to either one category or element of interest or as a category derived from some mathematical operation. In this study an integer power of two ($2^0$, $2^1$, $2^2$,...,$2^n$) was assigned as a weight to each element of interest, the higher the more important, to avoid ambiguities, and a summation of the elements' weights was

performed. This means that all possible combinations of elements result in a unique number. The use of a simple continuous series of numbers as weight can result in the same summed weight for several different possibilities. If random numbers are assigned and a multiplication is performed, the resulting weighted values may represent the false existence of thousands of new categories.

**Target areas** refer to particular portions of PTA which have reached weighted values above a specific level or threshold. In this study the minimum weighted value to be found in any single target area is 52 points which represents the sum of values assigned to geochemical and magnetic anomalies, and favourable lithologies.

In this chapter, I present the result of weight and overlay operations performed either on final results derived from previous Chapters or from the original data base. I also present the main characteristics of the targeted areas for gold found in the study area.

## 9.2 Rationale

To undertake a data fusion the strategy used in this study was:

a) to define the elements of interest according to the chosen decision model;

b) to establish levels of priority among them;

c) to define adequate GIS functions, and

d) to formulate geological scenarios for areas with potential for gold.

The elements of interest represent the nomination of the most important geological characteristics which are common in

Archaean gold deposits. The selected elements of interest from the existing data base were:

a) mineral occurrences,

b) geochemical anomalies;

c) lithological units;

d) mapped structural features;

e) magnetic anomalies;

f) intrusive rocks;

g) interpreted structures.

The chosen area to test the PTA, which is located in the southern part of the study area, has an area of 492,000.00 ha. The reported mineral occurrences reported include: gold (7), baryte (2) copper (1), graphite (1), iron (2), titanium (1) kyanite (2), talc (13), emerald (3), beryl (1), marble (2), vermiculite (7) and asbestos (8). The location of each mineral occurrence will be presented when overlay operations are performed (see Figures 9.4, 9.9 and 9.12).

The geochemical anomalies were grouped into two categories:

a) the very well correlated elemental association, and

b) the uncorrelated element association.

Chapter 8 demonstrated that the well correlated associations are represented by the following element associations: Fe-Cu-Co-As, Fe-As-Cr-V-Ba-Cu, Fe-Ni-Cu, Fe-Mg-Ti-Cu and Fe-Cu-As-Pb. The coincident areas of their mutual occurrences represent the element of interest and hereafter is termed **anomaly one**. The element association represented by Fe-Ba-As-Pb is called **anomaly two**.

Chapter 4 and 5 provided the instruments for the definition of favourable rock units. The chosen lithological units were

those which represent the base of the Lower Unit of the Contendas-Mirante Belt, which consists of volcanic, volcanoclastic rocks and chemical sediments of the Jurema-Travessao Subunit (JTS), and those defined by mafic-ultramafic rocks.

The mapped structural features consist of proximity analysis undertaken on faults, fractures and fold axes which have been confirmed during field work or determined from previous geological maps.

The magnetic anomalies include areas where high magnetic fields (>b +2s) were found, as defined in Chapter 7.

The intrusive rocks consist of granitic bodies: both existing mapped bodies or radiometric anomalies. Granites could represent sources of heat and/or fluids involved in hydrothermal circulation.

The inclusion of radiometric anomalies in the final product is warranted by to the capability of the radiometric method in separating different granitic bodies (Chapter 7, section 7.6.1). Furthermore, there is a high correlation between the radiometric survey and mapped granites.

Figure 9.1 shows in red the radiometric anomalies, in green the existing granitic bodies, and in yellow areas of coincidence between mapped granites and radiometric anomalies.

The interpreted structural features represent those which were collected from Landsat TM, radar and magnetic images. Chapter 6 provided the interpretation of the remotely sensed data and Chapter 7 the interpretation of magnetic images. These data, termed interpreted structures, were compiled into a single map and a proximity analysis was carried out.

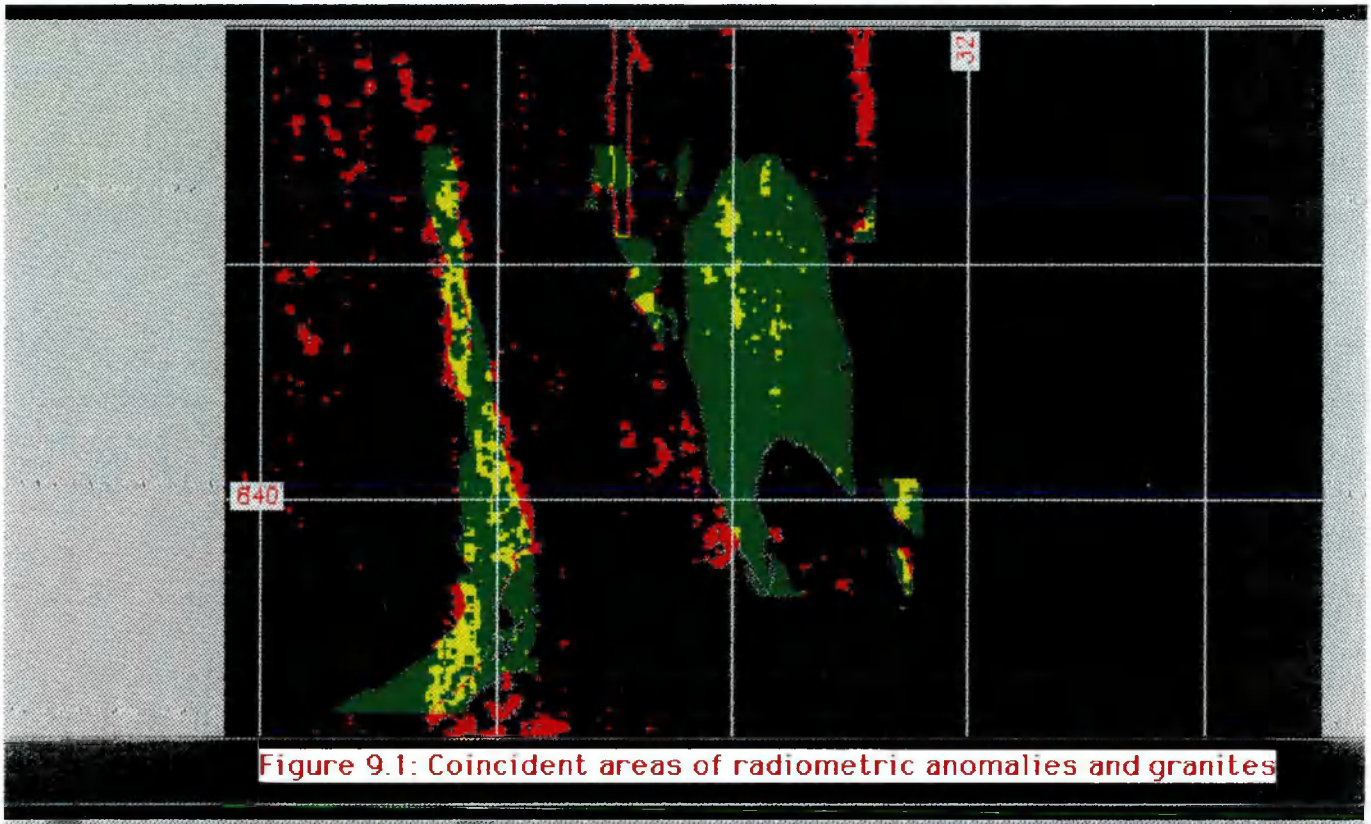


Figure 9.1: Coincident areas of radiometric anomalies and granites

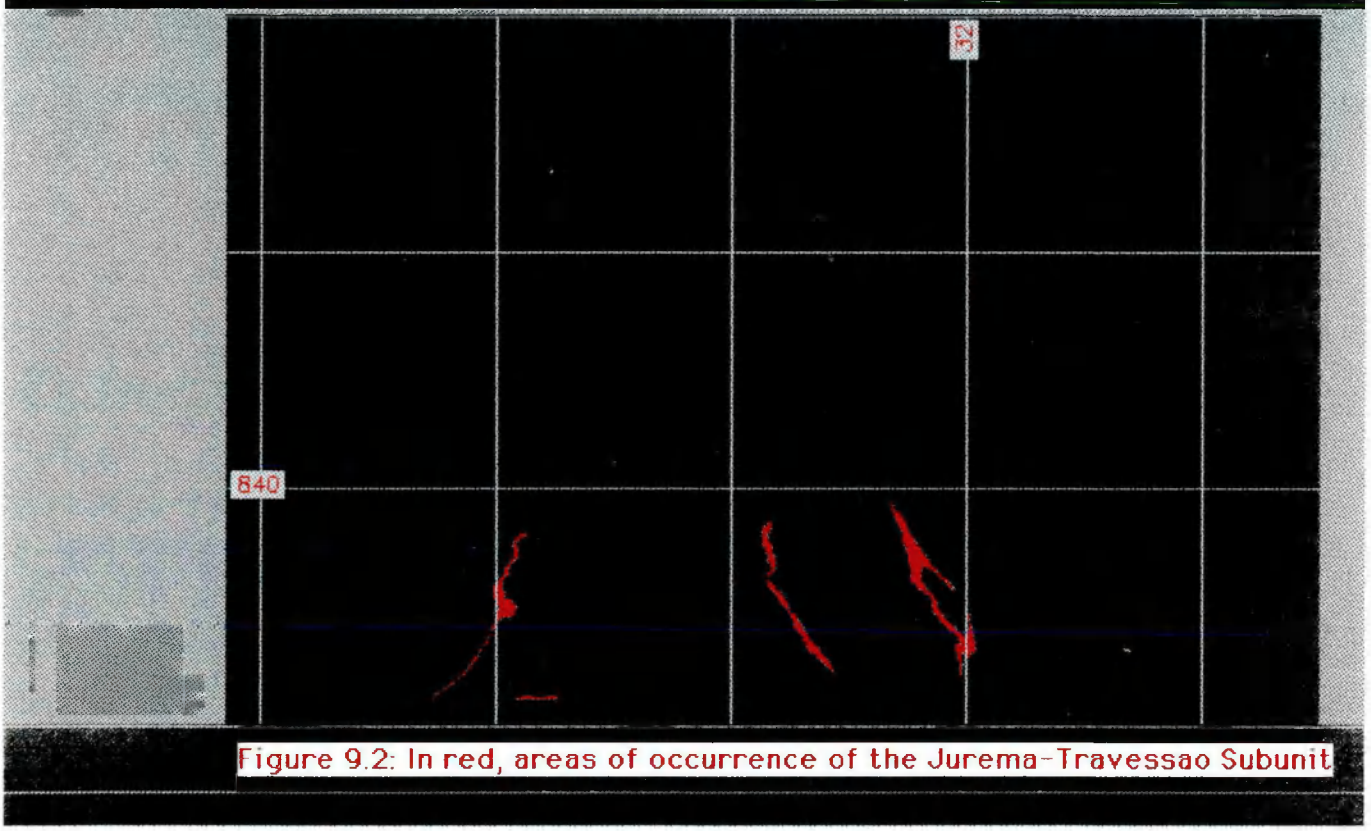


Figure 9.2: In red, areas of occurrence of the Jurema-Travessao Subunit

The proximity analyses was performed taking into consideration the minimum spatial resolution of the data set and the average width of sheared zones observed from field work. Thus, 100 m either side of faults was defined to be the potential width of influence.

The elements of interest were carefully analysed, and weighted according to their importance. The assignment of values to land characteristics allows a comparison of information from different sources, and also provides a hierarchical method for a quick and convenient means of data access.

In this study the assigned weights are shown in Table 9.1. This implies that the minimum value for the preliminary target areas (PTA) is 52 points. The higher the value reached by the PTA, the more important it becomes. To avoid bias in the definition of the levels of priorities of the chosen targets, the percentage of each coincident area of element of interest was multiplied by its corresponding assigned weight. Thus, the level of priority of a particular target, is a sum of the assigned weights of the elements of interest present plus the weights of the coincident areas.

The selected GIS functions are those described in Chapter 3, and so need not be discussed further here.

Three scenarios were established according to either the coincidence or the proximity of a minimum of three elements of interest.

a) Scenario one consists of the presence of gold, anomaly one, JTS and magnetic anomalies,

b) Scenario two consists of the presence of gold, anomaly one, mafic-ultramafic rocks (MUR) and magnetic anomalies, and

c) Scenario three includes anomaly two, MUR and magnetic anomalies.

| ELEMENTS OF INTEREST | WEIGHTS |
|---|---|
| Gold occurrences | 128 |
| Iron and/or base metal occurrences | 64 |
| Geochemical anomalies | 32 |
| Lithology | 16 |
| Mapped structures | 8 |
| Magnetic anomalies | 4 |
| Granites | 2 |
| Interpreted structures | 1 |

**Table 9.1**: *Weights assigned to elements of interest of the study area*

### 9.2.1 Scenario one

To select PTAs in scenario one, a methodological approach is presented here. A map containing areas of occurrence of JTS was created (Figure 9.2), and an overlay operation involving JTS, magnetic anomalies, anomaly one and gold occurrences was undertaken (Figure 9.3). The defined areas of occurrence of elements of interest in terms of the total area represent: JTS 0.49%, magnetic anomalies 3.09% and anomaly one (AN1) 0.70%.

Magnetic anomalies are concentrated in the northern part of the chosen area, whereas JTS and AN1 are more conspicuous in the southern part. This possibly means that the geochemical anomalies should be reflecting the chemical characteristics of the JTS, and the magnetic anomalies are representing physical properties of different Units including those with a

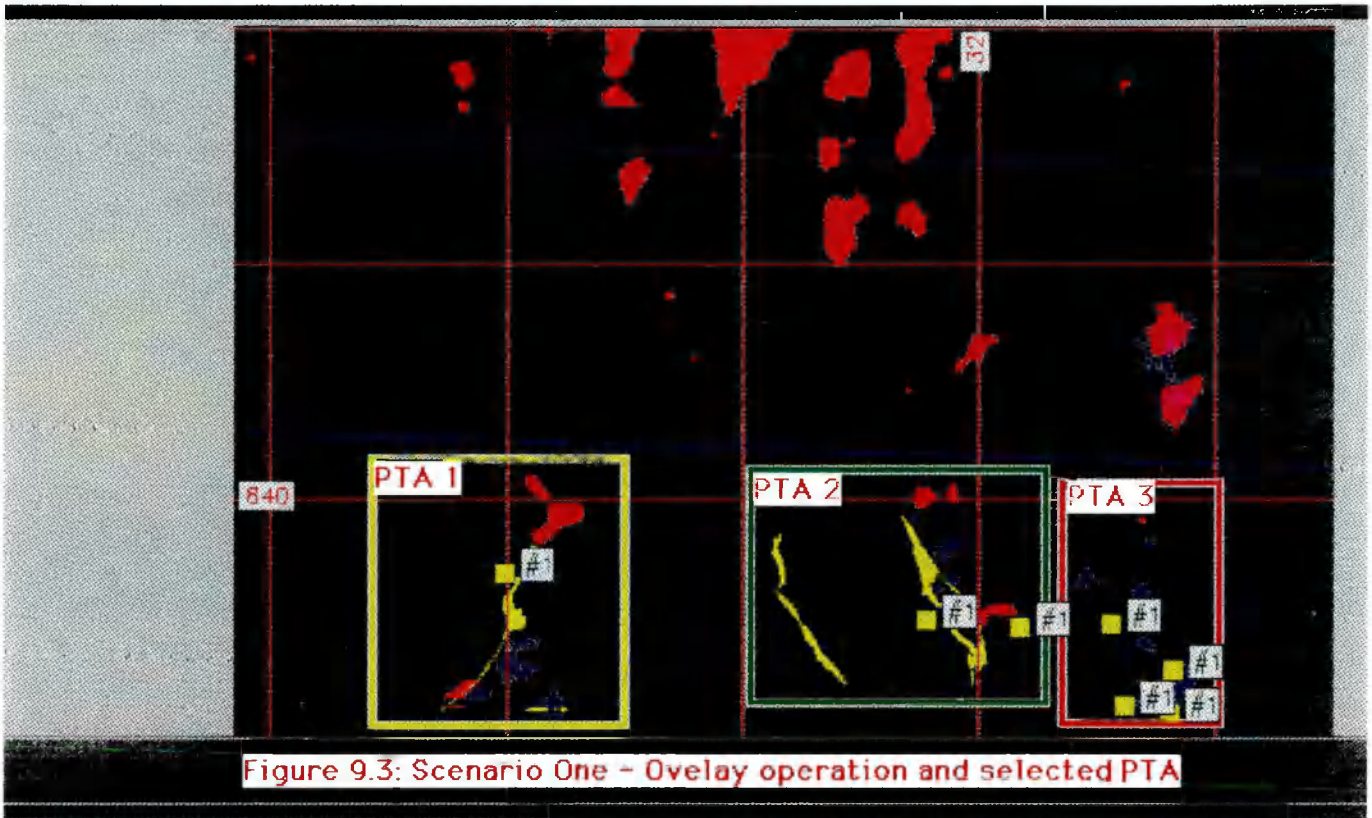


Figure 9.3: Scenario One - Ovelay operation and selected PTA

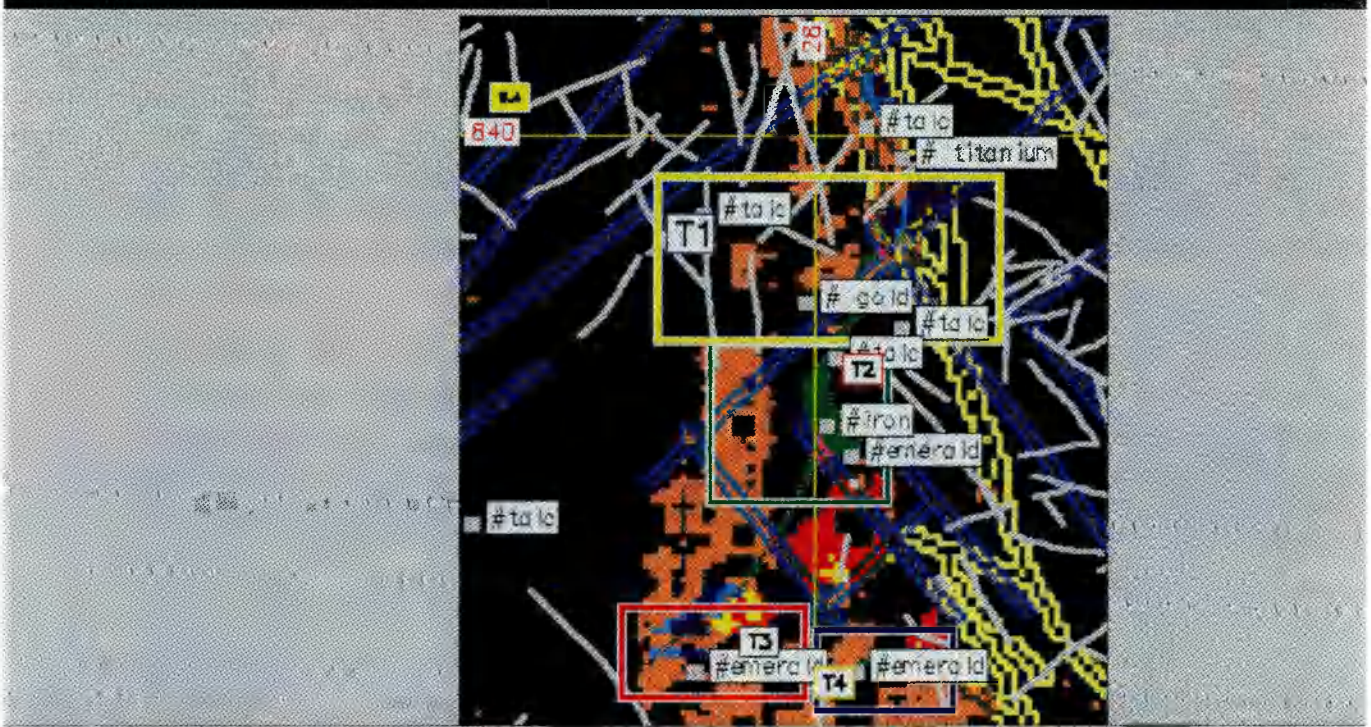


Figure 9.4: Weight operation on Scenario One

particular chemical signature. It is possible that the Barreiro d'Anta and JTS could have the same anomalous magnetite content, but only the JTS seems to have more appropriate geological conditions to suggest anomalous content of base metals, and eventually gold, because of its volcano-sedimentary origin (*Boyle*, 1978). In Figure 9.3, red represents magnetic anomalies (M), JTS appears as yellow and AN1 as blue. In the case of existence of areas with a coincidence of JTS + M, JTS + AN1, AN1 + MAG they are coloured as orange, green magenta and white, respectively. Three PTAs (PTA1, 2 and 3) were selected according to the coincidence of elements of interest (Figure 9.3). Only areas greater than 6.25 ha, which represents the geophysical and geochemical minimum cell size, were considered. The statistical data of the scenario one are presented in Table 9.2.

| ELEMENT OF INTEREST | AREA (ha) |
|---|---|
| MAG. ANOM (M) | 15564.00 |
| JTS | 2491.00 |
| JTS + M | 25.00 |
| ANOM. 1 (AN1) | 3538.00 |
| M + AN1 | 524.00 |
| JTS + AN1 | 80.00 |

**Table 9.2**: *Statistical data of the distribution of elements of interest in Scenario one*

PTA 1 is located in the southeastern part of the study area and has an area of 49754.00 ha, (Figure 9.3). A weight

operation was performed, followed by an overlay of mineral occurrences, faults and fractures the aim being to define target areas. The results of the weight operation is presented in Figure 9.4. A statistical analysis was undertaken to define areas of coincidence of the elements of interest, and the relationship between them. Table 9.3 presents statistical data for areas having more than 50.00 ha.

| CATEGORIES | COLOUR | AREA (ha) | WEIGHT VALUES |
|---|---|---|---|
| INT.STRUCT. (IS) | cyan | 3628.00 | 1 |
| GRANITES (G) | beige | 4721.00 | 2 |
| G + IS | blue greyish | 435.00 | 0.09* |
| MAG. ANOM. (MAG) | dark blue | 573.00 | 4 |
| MAG + IS | brown | 113.00 | 0.04* |
| MAG + G | light blue | 193.00 | 0.08* |
| MAP.STRUC. (MAS) | yellow | 2478.00 | 8 |
| MAS + IS | violet | 313.00 | 0.19* |
| MAS + G | green yellowish | 449.00 | 0.30* |
| MAS + MAG | purple | 267.00 | 0.22* |
| JTS | green | 539.00 | 16 |
| ANOM. 1 (A1) | red | 751.00 | 32 |
| A1 + IS | rose | 120.00 | 0.27* |
| A1 + G | pink | 145.00 | 0.33* |

**Table 9.3:** *Summary of the relationships of the main colours in Figure 9.4 and the statistical data of PTA 1.*

** AREA OF COINCIDENCE*∑WEIGHT/TOTAL AREA OF THE PRESENCE OF ELEMENT OF INTEREST*

Figure 9.4 shows that the mineral occurrences reported in the PTA 1 are: gold (1), talc (6), titanium (1), kyanite (1), beryl (1), iron (1) and emerald (3).

Strictly speaking only iron could be related to gold because this occurrence could be associated with BIF. Kyanite is related to quartz-veins hosted by migmatitic rocks, and the other element and/or minerals could be related to mafic-ultramafic rocks in serpentinized zones (talc), pyroxenite layers (titanium) or contact metamorphism between these rocks and pegmatites (beryl).

The magnetic lineaments strike in two preferred directions: NE and NW. The NW direction shows similarity with mapped structural features. This trend is important because it should represent deep seated features, which are vital in controlling hydrothermal fluid circulation. Although the magnetic lineaments represent the result of the interpretation of magnetic maps, they appear to be very consistent and in some cases they establish a tectonic limit for the JTS (central part of the Figure 9.6). The anomalous radiometric areas are located in the western part, as a continuous belt. On the basis of weighted values, four target areas (T1, T2, T3 and T4) were selected (Figure 9.4).

Target one (Figure 9.5) has an area of 8125.00 ha and reached 225.54 points in the level of importance  The statistical data for areas greater than 6.25 ha of the target one is shown in table 9.4. With the exception of base metals all the elements of interest are present. Apparently there is a straight correlation between gold and granites, magnetic lineaments and JTS. To the northeastern part talc and titanium occurrences are related to magnetic anomalies and sheared zones. This could indicate the presence of mafic-ultramafic rocks.

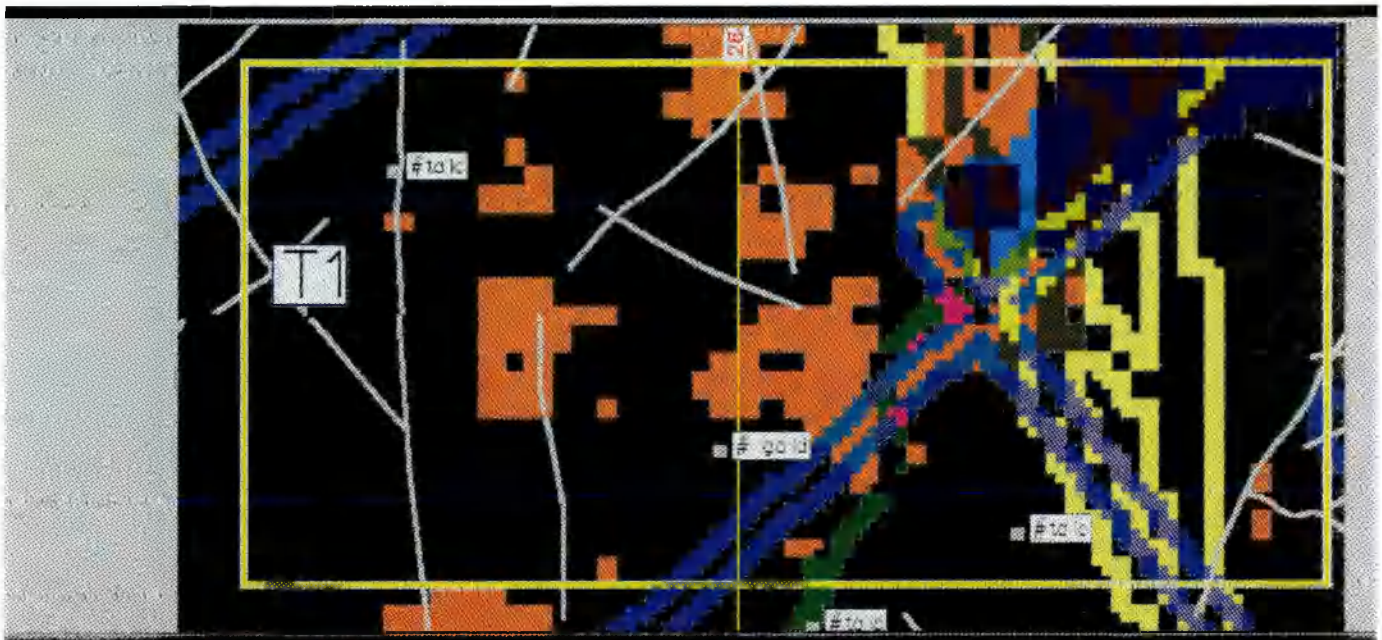


Figure 9.5: Weight operation on Target 1


Figure 9.6: Weight operation on Target 2

Target two (Figure 9.6) has an area of 4875.00 ha and reached 52.16 points in the scale of importance. The statistical data for areas greater than 6.25 ha of the target two is presented in table 9.4. Although no gold occurrence has been reported, the presence of magnetic lineaments, geochemical anomalies, JTS and granites make this a potential target for gold.

Target three (Figure 9.7) has an area of 4000.00 ha and reached 54.22 points in the scale of importance. The statistical data for areas greater than 6.25 ha of target three are presented in Table 9.4. No gold or base metal occurrences have been reported. Although the JTS has a very small area of occurrence, particular geological features are found in that there is a coincidence of magnetic and geochemical anomalies, and granitic rocks.

Target four (Figure 9.8) has an area of 1995.00 ha and reached 60.56 points in the scale of importance. The statistical data for areas greater than 6.25 ha of the target four is presented in Table 9.4. From existing geological information, gold base metal and JTS have not been reported. However, the coincident areas of geochemical anomalies, granites and sheared zones make this a potential target area for gold.

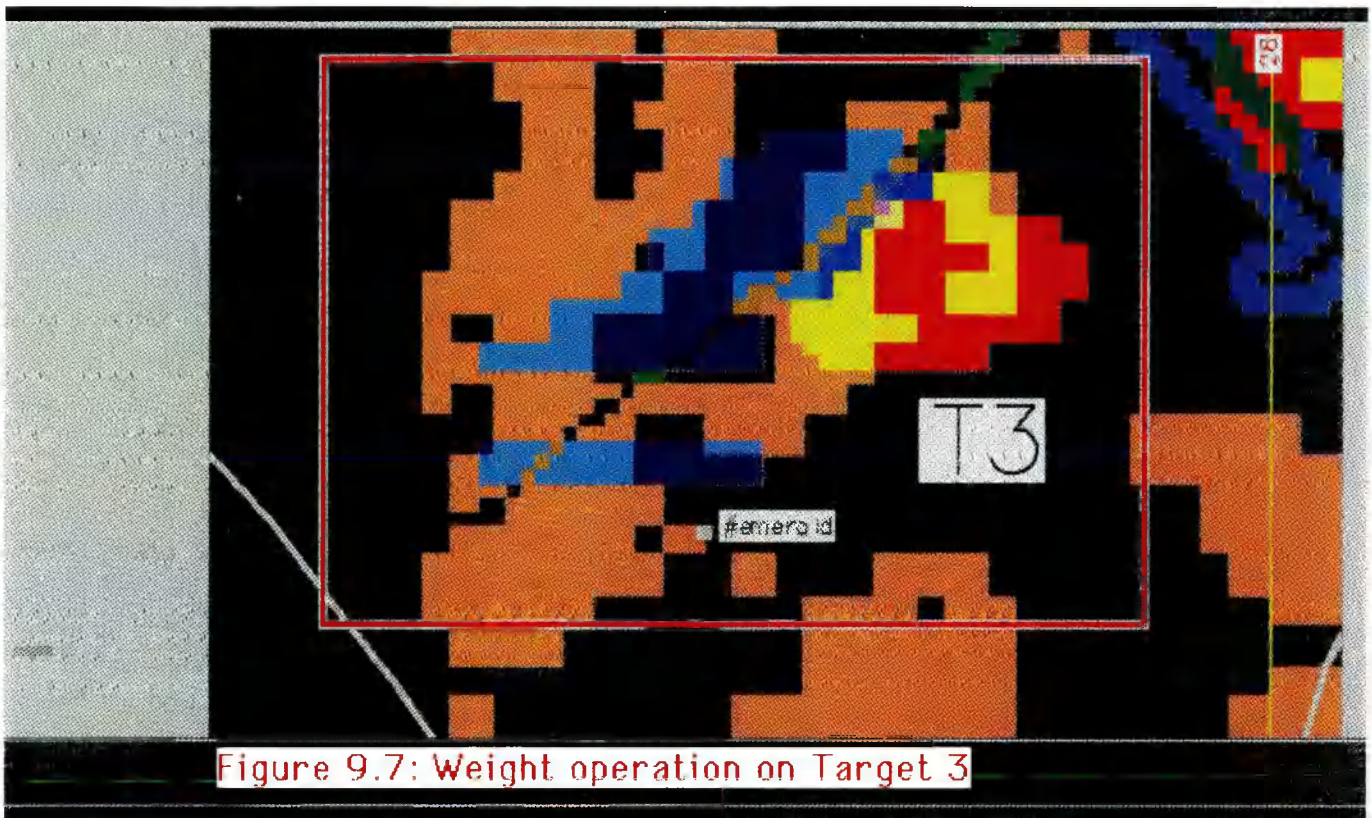


Figure 9.7: Weight operation on Target 3

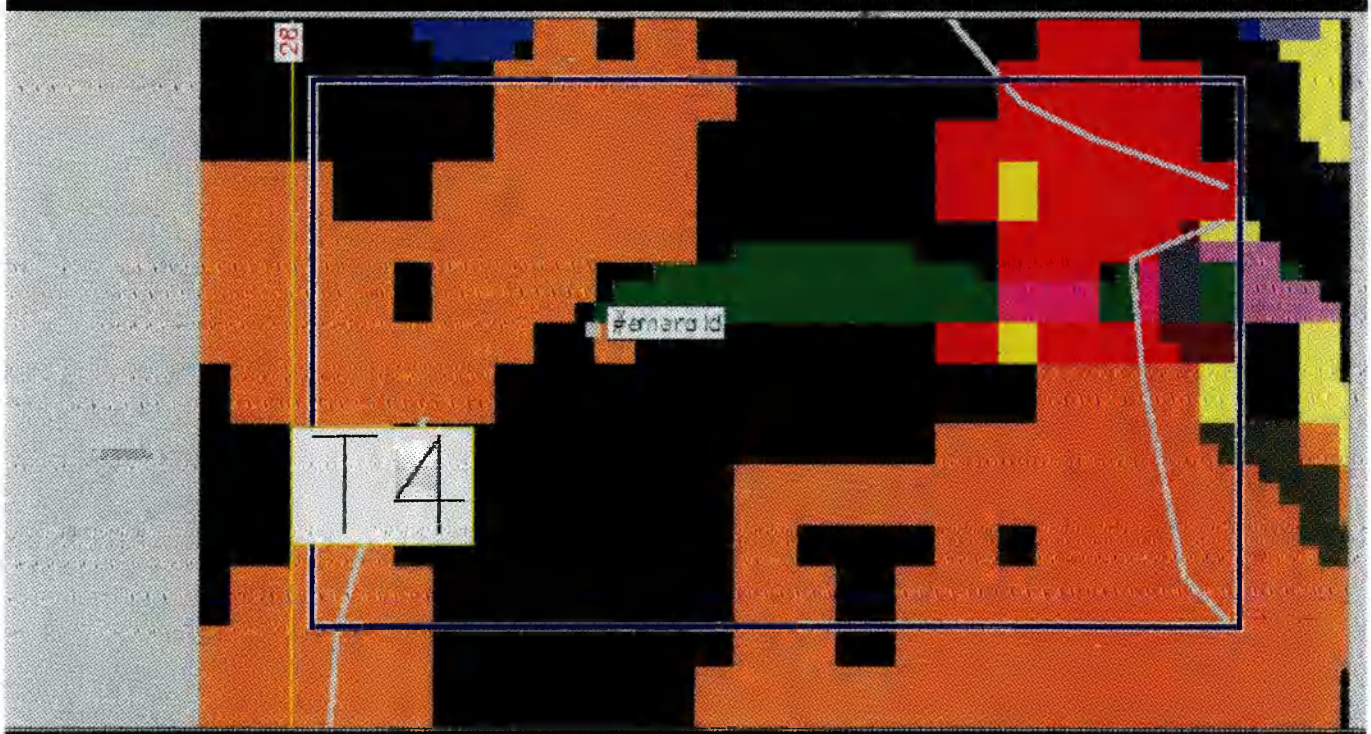


Figure 9.8: Weight operation on Target 4

| EOI | T1 (ha) | WV | T2 (ha) | WV | T3 (ha) | WV | T4 (ha) | WV |
|---|---|---|---|---|---|---|---|---|
| GOLD | - | 128 | - | - | - | - | - | - |
| Fe/BM | - | 64 | - | - | - | - | - | - |
| I | 390.00 | 1 | 332.00 | 1 | 82.00 | 1 | 11.00 | 1 |
| G | 833.00 | 2 | 923.00 | 2 | 998.00 | 2 | 817.00 | 2 |
| I+G | 94.00 | 0.11* | 207.00 | 0.3* | - | - | - | - |
| M | 232.00 | 4 | - | - | 148.00 | 4 | - | - |
| M+I | 89.00 | 0.17* | - | - | - | - | - | - |
| M+G | 33.00 | 0.07* | - | - | - | - | - | - |
| M+G+I | 18.00 | 0.07* | - | - | 119.00 | 0.49* | - | - |
| F | 332.00 | 8 | - | - | - | - | 38.00 | 8 |
| F+I | 120.00 | 0.42* | - | - | - | - | - | - |
| F+G | 94.00 | 0.36* | - | - | - | - | 23.00 | 0.19* |
| F+G+I | 18.00 | 0.05* | - | - | - | - | - | - |
| F+M | 153.00 | 0.71* | - | - | - | - | - | - |
| F+M+I | 29.00 | 0.15* | - | - | - | - | - | - |
| F+M+G | 14.00 | 0.07* | - | - | - | - | - | - |
| V | 70.00 | 16 | 401.00 | 16 | 14.00 | 16 | 76.00 | 16 |
| V+I | 14.00 | 0.09* | 28.00 | 0.23* | - | - | - | - |
| V+G | 26.00 | 0.18* | 7.00 | 0.06 | 17.00 | 0.18 | - | - |
| V+G+I | 12.00 | 0.09* | - | - | - | - | 15.00 | 0.24* |
| A | - | - | 127.00 | 32 | 149.00 | 32 | 146.00 | 32 |
| A+I | - | - | 28.00 | 0.45* | 24.00 | 0.46* | 8.00 | 0.22* |
| A+G | - | - | - | - | 91.00 | 1.8* | 10.00 | 0.29* |
| A+G+I | - | - | 7.00 | 0.12* | - | - | - | - |
| G+M | - | - | - | - | 14.00 | 0.29* | - | - |
| A+V | - | - | - | - | - | - | 13.00 | 0.53* |
| A+V+I | - | - | - | - | - | - | 8.00 | 0.33* |

**Table 9.4**: *Statistical parameters of the target areas of PTA1. (EOI=elements of interest, T=target, WV=weighted values, Fe/BM=iron and/or base metal occurrences, I=interpreted structures, G=granites, M=magnetic anomalies, V=the Jurema-Travessao Subunit, A=anomaly one)*

** AREA OF COINCIDENCE*∑WEIGHT/TOTAL AREA OF THE PRESENCE OF ELEMENT OF INTEREST*

PTA 2 has an area of 54600.00 ha and is located in the central part of the study area (Figure 9.3). A weight operation followed by overlay operations is shown in Figure 9.9.

The mineral occurrences found in this PTA are: gold (2), copper (1), talc (3) and vermiculite (3). Talc and vermiculite should be related to serpentinized ultramafic rocks, and tremolite actinolite schists. There is no correlation at all with copper occurrence and anomaly one.

The magnetic lineaments show a consistent NE direction, sometimes disrupting the JTS. The mapped structures appear as an intricate network striking northwest. Granites occur in contact with JTS and the presence of few magnetic anomalies apparently have no relationship with JTS. On the other hand there is a strong relationship between anomaly one and JTS.

A statistical analysis was undertaken on this PTA and the statistical data for areas greater than 50 ha is presented in Table 9.5.


Figure 9.9: Weight operation on PTA 2


Figure 9.10: Weight operation on Target 5

| CATEGORIES | COLOUR | AREA (ha) | WEIGHT VALUES |
|---|---|---|---|
| FRACTURES | grey | - | - |
| INT. STRUC. (IS) | cyan | 2271.00 | 1 |
| GRANITES (G) | beige | 661.00 | 2 |
| MAG.ANOM (MAG) | dark blue | 483.00 | 4 |
| MAG + G | brown | 89.00 | 0.03* |
| MAP.STRUC. (MAS) | yellow | 12685.00 | 8 |
| MAS + IS | violet | 851.00 | 0.38* |
| MAS + G | green yellowish | 172.00 | 0.08* |
| MAS + MAG | purple | 165.00 | 0.09* |
| JTS | green | 1028.00 | 16 |
| JTS + IS | light brown | 60.00 | 0.05* |
| JTS + MAS | crimson | 598.00 | 0.70* |
| ANOM 1 (A1) | red | 361.00 | 32 |
| A1 + JTS | white | 142.00 | 0.34* |

**Table 9.5**: *Summary of how the main colours in Figure 9.9 are related and the statistical analysis of PTA 2*

** AREA OF COINCIDENCE*∑WEIGHT/TOTAL AREA OF THE PRESENCE OF ELEMENT OF INTEREST*

The selected target area (T 5) reached 193.63 points in the level of importance and has an area of 11475.00 ha. A weight operation was carried out on this target and the results are presented in Figure 9.10. The statistical data of T5 for areas greater than 6.25 ha is presented in Table 9.6. The gold occurrences occupy an area controlled by both magnetic lineaments and mapped faults. The presence of JTS and AN1 nearby the gold occurrences and the structural conditions existing in this target, increases its geological importance.

| ELEMENTS OF INTEREST | T5 (ha) | WEIGHT VALUES |
|---|---|---|
| GOLD | - | 128 |
| I | 612.00 | 1 |
| G | 37.00 | 2 |
| M | 255.00 | 4 |
| F | 2181.00 | 8 |
| F + I | 231.00 | 0.45* |
| F + G | 46.00 | 0.10* |
| F + M | 84.00 | 0.22* |
| V | 614.00 | 16 |
| V + I | 30.00 | 0.11* |
| V + G | 15.00 | 0.06* |
| V + M | 152.00 | 0.66* |
| V + M + I | 20.00 | 0.11* |
| V + M + G | 10.00 | 0.05* |
| A | 174.00 | 32 |
| A + I | 34.00 | 0.25* |
| A + V | 48.00 | 0.50* |
| A + V + I | 11.00 | 0.12* |

**Table 9.6**: *Statistical parameters of the target area T5 (EOI=elements of interest, T=target, WV=weighted values, , I=interpreted structures, G=granites, M=magnetic anomalies, V=the Jurema-Travessao Subunit, A=anomaly one)*

** AREA OF COINCIDENCE*∑WEIGHT/TOTAL AREA OF THE PRESENCE OF ELEMENT OF INTEREST*

PTA 3 has an area of 30100.00 ha and is located in the southeastern part of the study area (Figure 9.3).The mineral occurrences reported are: gold (4), asbestos (4) and graphite (1) (Figure 9.11). Asbestos should be related to

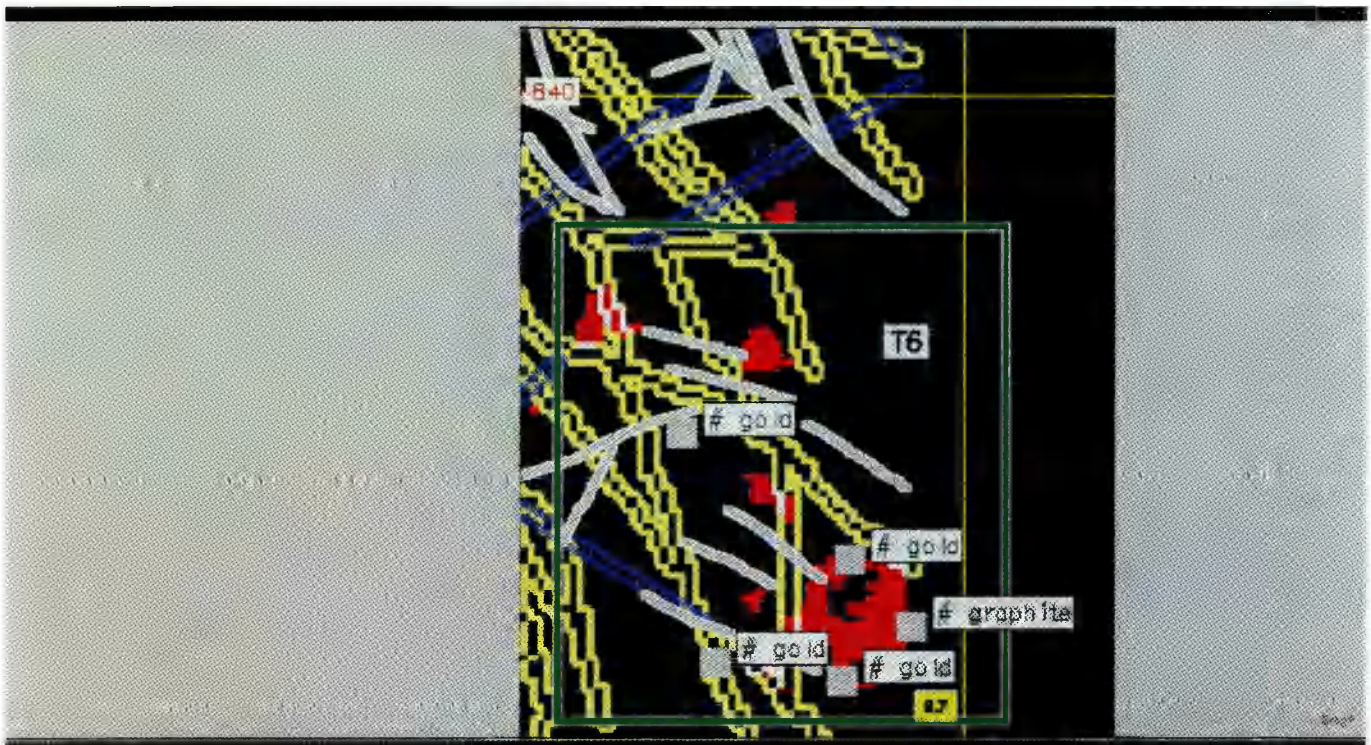


Figure 9.11: Weight operation on PTA 3


Figure 9.12: Weight operation on Target 6

serpentinized ultramafic rocks. Graphite in this area occurs as veins hosted in granulitic rocks. JTS has not been found, however the radiometric survey (see Figure 7.4.4) detected the presence of a lithology with low eTh, eU and K. The radiometric anomalies and the presence of asbestos suggest that non-mapped MUR could be present. Using the same methodology described previously for selecting target areas, one target (T6) was defined (Figure 9.12). T6 has an area of 20147.00 ha and reached 170.73 points in the scale of importance. Table 9.7 presents the statistical data of T6.

| ELEMENT OF INTEREST | COLOUR | AREA (ha) | WEIGHT VALUES |
|---|---|---|---|
| GOLD | grey | - | 128 |
| INT.STRUC. (IS) | blue greyish | 1022.00 | 1 |
| MAP.STRUC. (MAS) | beige | 4552.00 | 8 |
| MAS + IS | dark blue | 289.00 | 0.30* |
| ANOM 1 (A1) | red | 1311.00 | 32 |
| A1 + MAS | white | 202.00 | 1.43* |

**Table 9.7**: *Summary of how the main colours in Figure 9.12 are related and the statistical parameters of the target area (T6)*

** AREA OF COINCIDENCE*∑WEIGHT/TOTAL AREA OF THE PRESENCE OF ELEMENT OF INTEREST*

### 9.2.2 Scenario two

To select PTA in the scenario two the following procedures were carried out:

a) to create a map which displays only the mafic-ultramafic rocks (MUR) (Figure 9.13)

b) an overlay operation using MUR, anomaly one and magnetic anomalies, and

c) weight operations.

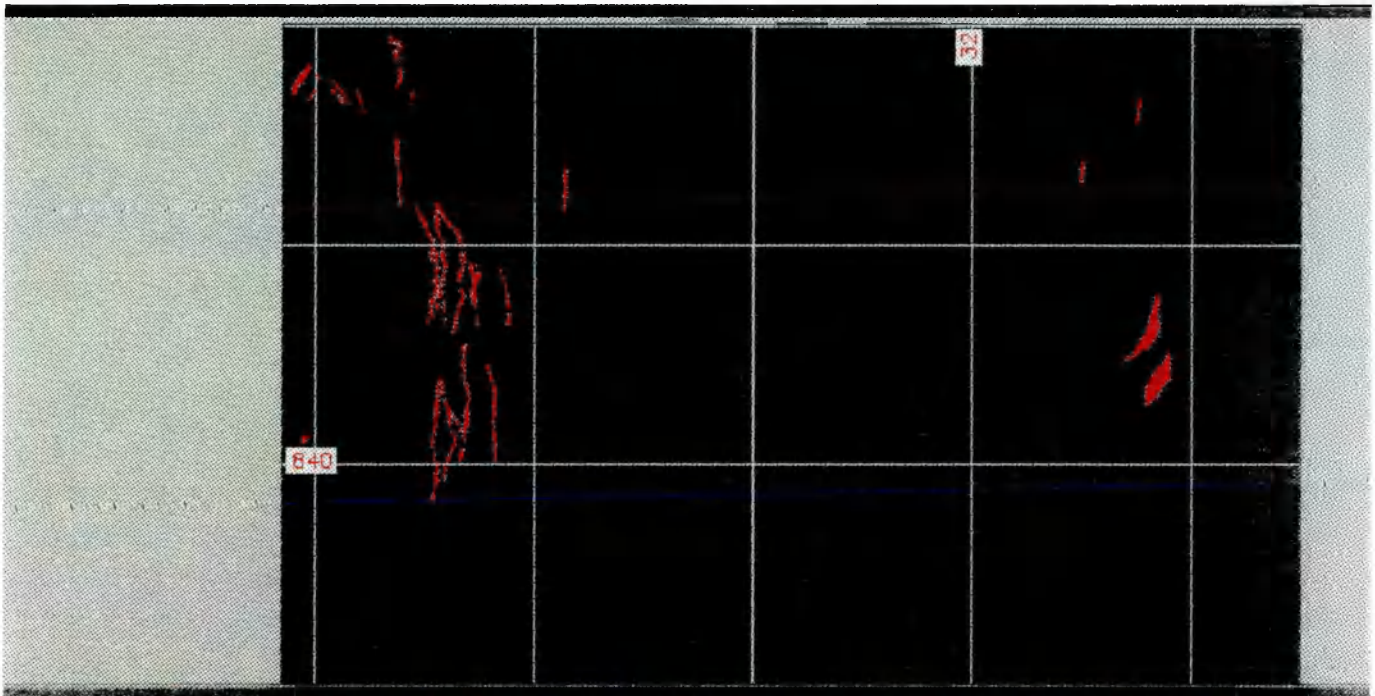


Figure 9.13: In red, areas of occurrence of mafic-ultramafic rocks

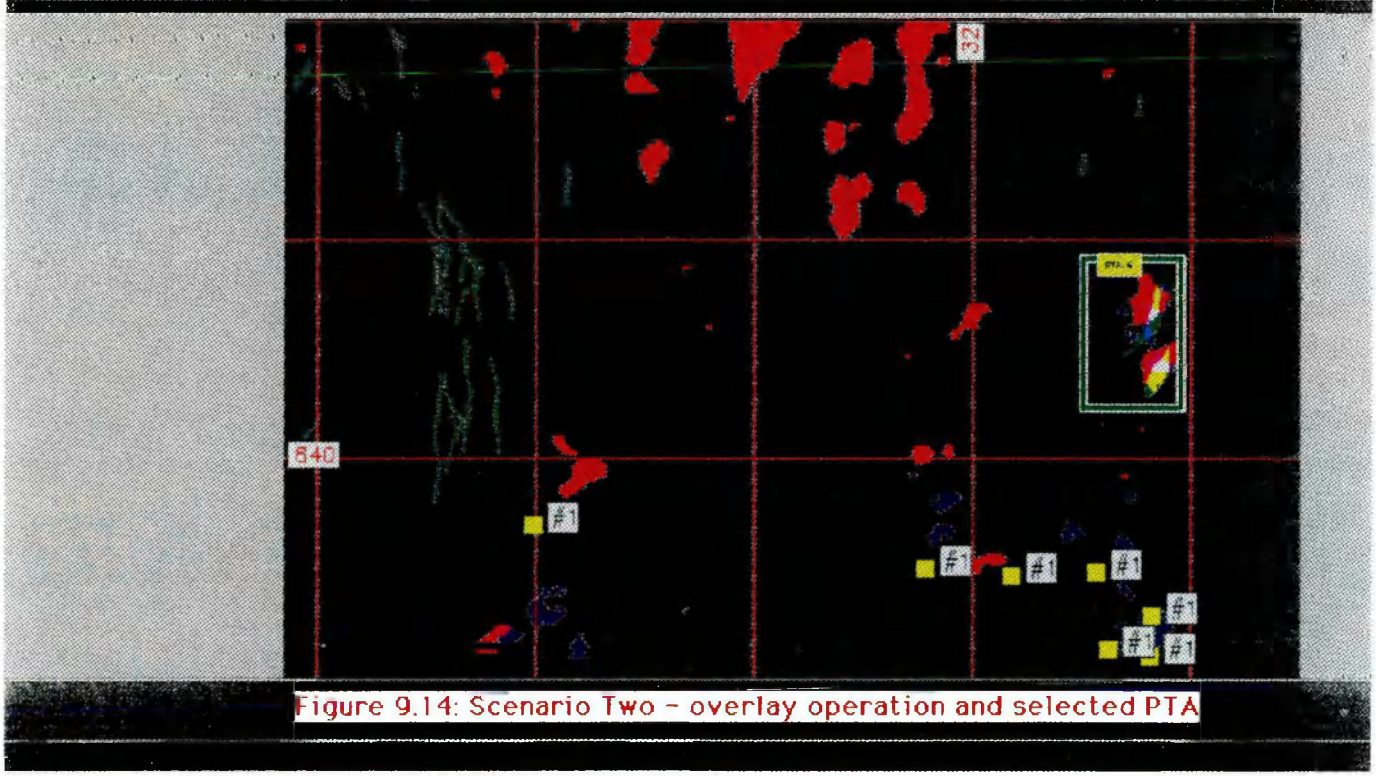


Figure 9.14: Scenario Two - overlay operation and selected PTA

The statistical data of Scenario two are presented in Table 9.8. From the overlaid map (Figure 9.14) one preliminary target area (PTA 4) which in this case represents the proper target area(T 7) was selected. T7 has an area 18000.00 ha, and is located in the central eastern part of the study area. The weight operation on T 7 (Figure 9.15) shows this target reached 68.76 points in the scale of importance.

| ELEMENT OF INTEREST | T7 (ha) | WEIGHTED VALUES |
|---|---|---|
| I | 787.00 | 1 |
| M | 941.00 | 4 |
| M + I | 88.00 | 0.09* |
| F | 925.00 | 8 |
| F + I | 94.00 | 0.21* |
| U | 273.00 | 16 |
| U + M | 333.00 | 1.5* |
| A | 293.00 | 32 |
| A + M | 223.00 | 1.79* |
| A + I | 50.00 | 0.41* |
| A + U | 107.00 | 1.15* |
| A + U + M | 225.00 | 2.61* |

**Table 9.8**: *Statistical parameters of T7. (I=interpreted structures, M=magnetic anomalies, U=mafic-ultramafic rocks, A=anomaly one)*

** AREA OF COINCIDENCE*$\Sigma$WEIGHT/TOTAL AREA OF THE PRESENCE OF ELEMENT OF INTEREST*

Figure 9.13 shows that MUR occupies the eastern and western part of the study area. To the east MUR occurs as thin folded

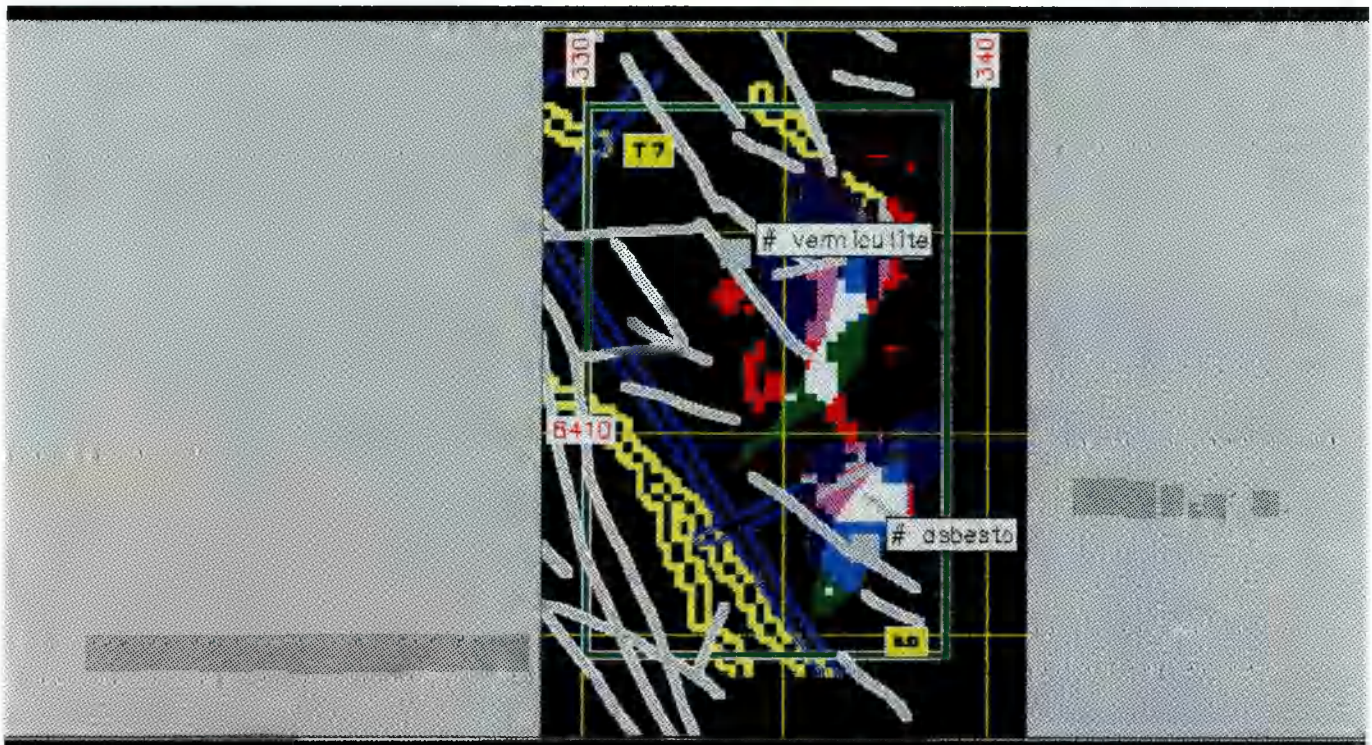


Figure 9.15. Weight operation on target 7

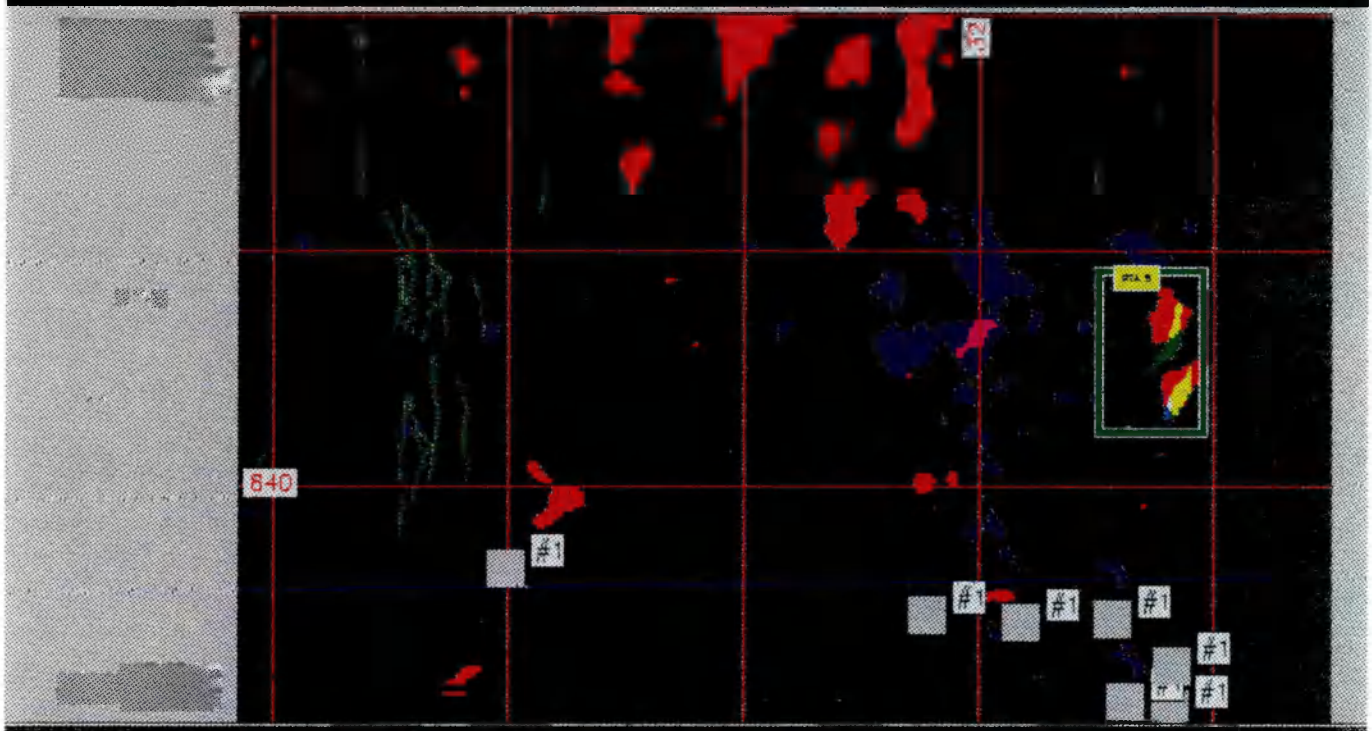


Figure 9.16: Scenario three – overlay operation and selected PTA

stripes with very little correlation with AN1 and magnetic anomalies. To the west MUR occurs as expressive bodies with very strong correlation with anomaly one and magnetic anomalies and in some extent with radiometric anomalies (see Figure 7.4.4). The mineral occurrences present in T 7 are: vermiculite (1) and asbestos (2). The magnetic lineaments show a good relationship with mapped structures, and a particular magnetic lineament forms the tectonic boundary of MUR (Figure 9.15).

### 9.2.3 Scenario three

To select PTA in Scenario three, an overlay operation involving MUR, anomaly two (AN2), mineral occurrences and magnetic anomalies (MAG) was undertaken. Figure 9.16 shows in red MAG, in blue AN2, in green MUR, and their mixes: yellow (MUR + MAG), magenta (MAG + AN2), cyan (MUR + AN2) and white MAG + MUR + AN2), respectively. AN2 has a big area of occurrence, but in a very few places was a coincidence with other elements of interest found. The selected PTA5 has the same area of the chosen target area (T 8) and reached 63.70 points in the scale of importance(Figure 9.16). T7 occupies the same geographical location of the T8 (Figure 9.8).

In terms of the geological characteristics, both target areas are very much the same. However, there are differences between coincidence areas of the elements of interest. AN2 has very little area of coincidence with the other elements of interest. There is a good correlation between AN2 and some occurrences of baryte. The statistical data of the Scenario three is presented in Table 9.9 and the result of a weight operation is shown in Table 9.10.

| ELEMENTS OF INTEREST | T8 (ha) |
|---|---|
| MAG. ANOM. (M) | 15032.00 |
| MUR | 3228.00 |
| MUR + M | 553.00 |
| AN2 | 11102.00 |
| M + AN2 | 496.00 |
| MUR + AN2 | 48.00 |
| MUR + AN2 + M | 38.00 |

**Table 9.9**: *The statistical data of the elements of interest in the Scenario three*

| ELEMENTS OF INTEREST | AREA (ha) | WEIGHT VALUES |
|---|---|---|
| I | 899.00 | 1 |
| M | 1141.00 | 4 |
| M + I | 138.00 | 0.14* |
| F | 1015.00 | 8 |
| F + I | 116.00 | 0.22* |
| M + F | 88.00 | 0.22* |
| U | 349.00 | 16 |
| U + M | 520.0 | 2.12* |
| AN2 | 360.00 | 32 |

**Table 9.10**: *Statistical parameters of T8 (I=interpreted structures, M=magnetic anomalies, U=mafic-ultramafic rocks, AN2=anomaly two).*

** AREA OF COINCIDENCE*∑WEIGHT/TOTAL AREA OF THE PRESENCE OF ELEMENT OF INTEREST*

## 9.3 Discussion of the results

Overlay and weight operations were revealed to be extremely useful for selecting both preliminary target areas (PTA), and target areas. Before appling GIS functions it is important to establish carefully the elements of interest and assign values to each of them. The values must avoid any possibility of ambiguity, thus an integer power of two is the recommended weight.

The Contendas-Mirante belt appears to have a certain potential for gold, especially in the southern part of the study area where a particular target area (T 5) was demonstrated to be a convergence of a series of geological conditions.

A comparison of preliminary target areas and target areas is presented in Table 9.11

| PTA | AREA (ha) | % | TARGET | AREA (ha) | % | POINTS |
|---|---|---|---|---|---|---|
| 1 | 49754.00 | 32.6 | 1 | 8125.00 | 13.0 | 225.54 |
| | | | 2 | 4875.00 | 6.5 | 52.16 |
| | | | 3 | 4000.00 | 3.8 | 54.22 |
| | | | 4 | 1995.00 | 2.5 | 60.56 |
| 2 | 54600.00 | 35.8 | 5 | 11475.00 | 17.00 | 193.63 |
| 3 | 30100.00 | 19.7 | 6 | 20147.00 | 67 | 170.73 |
| 4 | 18000.00 | 11.9 | 7 | 18000.00 | 100 | 68.76 |
| 5 | 18000.00 | * | 8 | 18000.00 | * | 63.70 |

* The target areas T7 and T8 have the same geographical position.

**Table 9.11**: *A comparison of PTA and Target areas of the study area.*

Although all the selected target areas should be investigated in more detail, further exploration in the T 5 should be addressed to gold related to both shear zones (*Clark et al* 1986; *Hamilton* and *Hodgson*, 1986; *Groves et al*, 1985; and *Forster* and *Wilson*, 1984) and lithological favour gold deposits (*Siems*, 1984; *Groves et al*, 1985). Targets 1, and 6 show geological characteristics and any further exploration should emphasize structural models. Targets 2,3,7 and 8 presented a minimum of importance. Therefore further investigations depend very much on the results obtained from the exploration on T1, T5, and T6.

# CHAPTER 10: CONCLUSIONS AND RECOMMENDATIONS

The Contendas-Mirante Belt is a volcanic-sedimentary sequence which is located between two cratonic blocks. It is divided into two distinct units. A mainly volcanogenic Lower Unit consisting of the Jurema-Travessao and Barreiro d'Anta Subunits, and an essentially clastic Upper Unit that includes the Mirante, Rio Gaviao and Areiao Subunits. The regional granitoid intrusions exhibit geochemical characteristics compatible with a continent-continent collision, although more structural and geochemical studies are needed.

Although the absence of gravity data, full geochemical analysis rather than reduced data, digital aeromagnetics and radiometrics for the whole area, the amount of available data was considered a satisfactory data set for our purposes. This data set included: topographic and geological maps, mineral occurrences, stream sediment reconnaissance, airborne magnetic and radiometric surveys, Landsat TM imagery and radar mosaics. They were derived from different sources, with different

scales and for different purposes, therefore, a special technique is needed to integrate such data sets.

The most suitable way for dealing with such huge amounts of data, is via a Geographical Information Systems (GIS). The core of the system is a very well organised data set which should be divided into files having different format, being essential ASCII, binary and raster format files. The generation of these files is one the most crucial and also time-consuming steps to be taken. This included manual and automatic digitization, reading digital tapes with different formats and the generation of UTM geometric corrected files.

The relationship between the format files should be very well established. Transformations which include interpolation, raster to vector or vice-versa and binary to raster, must be very well defined. Magnetic, radiometric and geochemical scattered data were gridded using a minimum tension surface method with satisfactory results.

As a test, the scattered soil and vegetation data were gridded using kriging and weighting moving average, respectively. The methodologies were acceptable; however, the raw data were not sufficiently complete to result in comprehensible products to be integrated with other data sets.

It is fundamental to formulate a decision model prior to implementing a GIS. The decision model leads to the definition of the GIS functions to be used. The gold-oriented GIS strategy was:

a)to define lithological units in the Contendas-Mirante belt which contain mafic volcanics, ultramafic rocks and chemical sediments, especially BIF;

b)to extract structural information and location of anomalous lithologies from existing geological maps, radiometrics magnetic and remotely sensed data;

c)to establish elemental associations that can be found in close relation with gold;

d)by using radiometric data to map granitoid intrusions.

The research led to a necessary evaluation of GIS functions without which economical useful exploration targetting is impossible.

The most important GIS functions which should be incorporated in any software for mineral exploration are:

i)scaling or rotation of reference for "best fit" projection overlays and changes;

ii)conversion from vector data to raster data and vice versa;

iii)fast update ability: changing or adding; open system: the user can input new on-line library;

iv)projection accuracy assessment, data independency and non-redundancy;

v)multiple user environment;

vi)multiple interactions between compatible data bases;

vii) great range of display techniques in 2D or 3D;

viii)easy menu-driven capabilities;

ix)retrieval of one or more data elements from a data file;

x)transformation or manipulation of the values in the data elements via logical and mathematical operations;

xi)store the new data elements created by any analysis as a new file;

xii)searching, identifying or routing a variety of different data items and score these values with assigned weighted values;

xiii) performing geometrical correction using different resampling algorithms;

xv) performing basic statistical and multivariate analysis, displaying and reporting;

xvi) performing interpolation by using different methods;

xvii) measuring area, distance and comparing the results;

xviii) perform, at a minimum, image processing techniques such as contrast stretching, FCC and filtering;

xix) be capable of modelling and simulation, developing scenarios to predict a future events.

The fundamental requirements leading to the generation of an Archaean gold deposits are:

a) source of fluid and gold;

b) a conduit to permit focussed transportation; and

c) a mechanism to induce localised deposition and concentration of gold.

There are many different environments for occurrences of Archaean gold deposits. They include discrete quartz-veins, pervasive microveining, sulphidic haloes to veins, and tabular sulphide disseminations. Host lithologies include virtually every rock type of greenstone terraines. Intravolcanic felsic intrusions are present, or very close to at most gold deposits, and have variable compositions. Gold deposits occur within linear tectonic zones in which relatively high strain magnitudes and available kinematic indicators attest to shearing in transcurrent or thrust systems.

In densely vegetated and poorly exposed areas such as the Contendas-Mirante region, the direct use of spectral reflectance data such as Landsat Thematic Mapper in

lithological mapping is restricted by the vegetation cover. Many image processing techniques were carried out, such as principal component analysis, decorrelation stretching and ratioing aimed at lithological discrimination, but very little could be added to the existing geological maps. However, the great contribution of TM data was, via edge enhanced images, to provide information on regional structures. The structural interpretation added around 20% to the number of known lineaments. The radar data was also useful for structural analysis. The interpretation of enhanced radar data added around 15% to the number of known lineaments either from available geological maps or TM data.

As part of future work, it is ssuggested that Landsat data be used in searching for geochemically stressed vegetation at a different time of year.

The Lepeltier method for establishing background and threshold has proved to be very useful in reducing lognormally distributed aeromagnetic data. The magnetic data reduction method (MDRM) presented here was able to define precisely areas with magnetite-rich zones. The most impressive example is related to the Rio Jacare sill. This sill is 40 km long and 1 km wide, but only five places were defined as anomalous areas, one of them is located at a Ti-V-PGE mine (Maracas Mine). The four other target areas open new perspectives for seeking other Ti-V pipe-like deposits. Another expressive example was the definition of an anomalous magnetic zone in close association with a gold target in development hosted in BIF.

The interpretation of the magnetic lineaments from enhanced images has improved the existing structural framework, especially revealing NE-SW trends, which may have greater controls over hydrothermal circulation than the bulk of fractures and faults mapped at the surface.

The airborne radiometric data has been proved to be an important tool for lithological discrimination. Such a geophysical survey should be carried out at large scales using more sensitive spectrometers, and closer line-spacing. The radiometric data has been demonstrated to separate four different granite types. The fact that granites show different radiometric response, indicates that radiometrics may be revealing subtle differences in granite geochemistry perhaps important in mineral exploration, especially for gold exploration, because there is a close spatial association between some granitoids and Archaean gold deposits. Moreover, there may be more granites than have been mapped.

From the geochemical data set the following parameters should be determined: background, standard deviation, threshold, correlation coefficients, hierarchical levels and elemental associations. The most suitable way of interpreting stream sediment surveys is via raster files because they can easily be integrated with other data sets. Ideally image files should be generated using raw data, but in this case they were not available. Compressed data were used instead, and the results were satisfactory in revealing anomalous areas. However, potentially useful techniques, such as PCA and inter-element ratioing, were not very successful.

In general the elements released by either chemical or mechanical weathering of mineralised zone will be found in the acid soluble fraction. The acid soluble fraction is defined as the minor fraction (usually less than 80 mesh) which contains sulphides, Fe-Mn oxides, sulphates, carbonates, etc. This is because during secondary dispersion most elements which are moved, are in the form of ore minerals, secondary minerals or hydromorphically dispersed. The greatest variations in the amount of acid soluble materials in stream sediments are attributed to geological factors. Due to climate, mechanical weathering is predominant and the most of the surficial dispersion in the study area occurs during the occasional flash flood.

To achieve consistent results from stream sediment surveys the stream-sediment samples must be collected only from small channels draining catchment areas typically in the range of 2 to 5 $km^2$.

When the element associations are very well correlated a multivariate analysis such as the principal component transformation is the most suitable tool for a proper understanding of their relationships.

A set of very well correlated element associations.was defined: Fe-Cu-Co-As, Fe-As-Cr-V-Ba-Cu, Fe-Ni-Cu, Fe-Mg-Ti-Cu and Fe-Cu-As-Pb. These element associations have a close relationship with the volcanic, volcanoclastic and chemical sediments of the base of the Lower Unit. This result should encourage companies to carry out a survey for other gold pathfinder elements such as Bi, Ag and Sb, and also to determine Au panning results on selected areas.

The element association Fe-Ba-As-Pb is very much related to the occurrences of baryte veins. Thus, it has not been effective in the selection of preliminary target areas.

Data fusion rather than data integration is the final product derived from the implementation of a GIS. This implies that the final product is far more sophisticated than a single integration. The data fusion strategy used was: to determine elements of interest and establish levels of priority among them, to define adequate GIS functions and to formulate geological scenarios for areas with potential for gold.

Overlay operations involving the Jurema-Travessao Subunit, geochemical and magnetic anomalies have been demonstrated to be very effective for the selection of preliminary target areas. The weight operations have been shown to be the most powerful tool for establishing target areas and their level of relative importance. These methods have narrowed targets to small areas within a very large one, therefore being adequate for mineral-oriented GIS.

Three geological scenarios were formulated and eight target areas were defined. From those, only four target areas for gold which represent 12% or 58500 ha of the total study area were determined. Due to the convergent geological factors, they are potential targets for gold. It is recommended that further geological investigations should be done.

The assembled data are also appropriate for other uses, such as base metals, baryte, industrial minerals.

# REFERENCES

**Adams, J.A.S.** (1968): Total and Spectrometric Gamma-ray Surveys from helicopters and Vehicles. Symp. on Nuclear Tech. and Min. Res. Buenos Aires Int. Atom. Energy Ag pp:147-161

**Adams, J.A.S and Gasparini, P.** (1970): Gamma-ray spectrometry of Rocks. Elsevier Publishing Co. New York

**Almeida, F.F.M** (1967): Origem e Evolucao da Plataforma Brasileira. *Dep. Nac. Prod. Min. Div. Geol. Mineral.* Bol.241:36 pp

**Almeida, F.F.M., Amaral, G., Cordani, U.G. and Kawashita, K.** (1973): The Precambrian Evolution of the South America Cratonic Margin South of the Amazon River. In: A.E.M. Nairn and F.G. Stechli (Ed) *The Ocean Basins and Margins, 1.* The South Atlantic Plenum Press N.Y. pp:411-446

**Almeida, F.F.M and Hasui, Y** (1984): O Pre-Cambriano no Brasil. In: *O Pre-Cambriano no Brasil* Almeida, F.F.M. and Hasui, Y (Eds) Ed. Edgard Blucher ltd Sao Paulo, Brazil pp:1-5.

**Almeida, F.F.M, Hasui, Y, Brito Neves, B.B. and Fuck, R.A.** (1981): Brazilian Structural Provinces: an Introduction. In: J.M. Mabesoone, B.B. de Brito Neves and A. Sial (Eds) *The Geology of Brazil. Earth Sci. Rev.* 17:1-19

**Andrews, A.J.** (1983): Alteration, Metamorphism and Structure associated with Archaean Volcanic-hosted Gold Deposits, Red Lake District In: Mood, J., White, O.L., Barlow, R.B. and Colvine, A.C. (Eds). Summary of Field work 1983. Ontario Geological survey, Misc. Paper 116

**Andrews, A.J., Hugon, H., Durocher, M. Corfu, F. and Lavigne, M.J.** (1986): The Anatomy of Gold-bearing Greenstone Belt: Red Lake, Northwestern Ontario, Canada. *Proceedings of Gold '86* An Int. Symp. of the Geology of Gold. A.J. Macdonald Ed., Konsult Int. Inc. Toronto pp:3-22.

**Aronoff, S.** (1989): Geographical Information systems: a Management perspective. WDL Publications, Otawa, Canada

**Aronoff, S. and Jones, G.F.** (1985): From Data to Image Action. IEEE Spectrum. *Institute of Electrical and Electronics Engineering* pp:45-52

**Archibald, N.J.** (1982): Structure, Lithological Association Units and Gold Mineralisation, Mount Magnet Area. In:Baxter J.L. Ed. Archaean Geology of the Southern Murchison. *Geol. Soc. Australia* W. Australia. Div. Excursion Guide. pp:15-27

**Asmus, H.E.** (1975): Controle Estrutural da Deposicao Mesozoica das Bacias da Margem Continental Brasileira. *Rev. Bras. Geoc.* 5:160-175

**Barbosa, J.S.F.** (1986): Constituition Lithologique et Metamorphique de la Region Granulitique du Sud de Bahia, Bresil. *Unpb. Doctorat Thesis.* Univ. of Paris VI (no. de ordre 86-34)

--- (1988): Principais Geobarometros Utilizados em Granulitos: Analise dos Resultados de um Exemplo do Sul da Bahia, Brasil. Rev. Bras. de Geoc. 18(2):162-169

--- (1989): The Granulites of the Jequie Complex and Atlantic Mobile Belt, Southern Bahia, Brazil: an Expression of Archaean/ Early Proterozoic Plate Convergence (in press)

**Barbosa, O.** (1966): Tectonica do Nordeste. *XX Cong. Bras. de Geol.* Rio de Janeiro. Publ. no. 1 Nucleo do Rio de Janeiro

**Barbosa, J.S.F. and Fonteilles, M.** (1989): Caracterizacao dos Protolitos da Regiao Granulitica do Sul da Bahia. *Rev. Bras. de Geoc.* 18(2):170-179

**Barley, M.E.** (1982): Phorphyry-style Mineralization Associated with Early Archaean Calc-alkaline Igneous Activity, Eastern Pilbara, Western Australia. *Econ. Geol.* 77, pp:1230-1235

**Barnes, H.L.** (1979): Geochemistry of Hydrothermal Ore Deposits. 2nd Ed.

**Batteham, J.C., Bullock, S.J. and Hopgood, D.N.** (1983): Tanzania Integrated Aeromagnetic and Radiometric Maps for Mineral exploration. Trans. Inst. Min. Metall. b 92 B83-92

**Bernasconi, A.** (1987): The Major Precambrian Terranes of Eastern South America: a Study of their Regional and Chronological Evolution. *Precambrian Res.* no.27 pp:107-124

**Blanchard, B.J.** (1979): Some confusion factors in radar image interpretation. In:Radar geology: an assessment report of the radar workshop Snowmass, Colorado. pp:223-232

**Bonham-Carter,G.F., Agterberg, F.P. and Wright, D.F.** (1988); Integration of Geological Datasets for Gold Exploration in Nova Scotia. *Photog. Eng. and Rem. Sen.* Vol.54, no.11, pp:1585-1592

**Boyle, R.W.** (1974): Elemental Associations in Mineral Deposits and Indicator Elements of Interest in Geochemical Prospecting. Geochemica Survey of Canada. Dept. of Energy Mines and Resources, Ontario Paper 74-45

--- (1979: The Geochemistry of Gold and its Deposits, *Survey of Canada* Bull. 280 584p

**Bridgewater, D., McGregor, V.R. and Windley, B.F.** (1976): Stages in the Development of the Early Precambrian Crust in Greenland. *Spec. Publ. Geol. Soc. S. Africa* 3:475-477

**Brito Neves, B.B et al** (1980): Evolucao Geocronologica do Pre-Cambriano no Estado da Bahia. In: Inda, H.A.V and Duarte, F.B. Coord.Geol. e Recursos Minerais no Estado da Bahia; textos basicos. Salvador SME/CPM Vol.3, pp:1-101

**Bohmke, I. and Varnells, J.** (1896): Gold in Granulites at Renco Mine, Zimbabwe. In: Anhauesser and Mask (Eds). Mineral Deposits of Southern Africa Part 1. Geol. Soc. of South Africa

**Burke, K.C., Kidd, W.S.F., Turcotte, D.L., Dewey, J.F, Mouginis-Mark, P.J., Parmentier, E.M., Sengor, A.M. and Tapponier, P.E.** (1981): Tectonics of Basaltic Volcanism. In:Basaltic Volcanism on the Terrestrial Planets. Pergamon, N.Y. pp:803-898

**Brito, R.S.C.** (1981): Projeto Fazenda Gulcari. Open File Report. Companhia Baiana de Pesquisa Mineral. Convenio CBPM/SME

**Burrough, P.A.** (1985):Principles of Geographical Information Systems for Land Resources Assessment. Clarendon Press Oxford. Monographs on Soil and Resource Surveys

**Burrough, P.A., Brown, L. and Morris, E.C.** (1977): Variations in Vegetation and Soil Pattern across the Hawkesbury Sandstone Plateau from Barren Grounds to Fitzroy Falls, New South Wales *Aust. J. Ecol.* 2 pp:137-159

**Burrows, D.R. and Spooner, E.T.C.** (1986): The McIntyre Cu-Au Deposit, Timmins, Ontario, Canada. *Proceedings of Gold '86.* an Int. Symp. on the Geol. of Gold. A.J. Macdonald Ed. Konsult Int. Inc. Toronto, pp:23-39

**Canas, A.A.D. and Barnett, M.E.** (1985): Generation and Interpretation of False-colour Composite Principal Composite Analysis. *Rem. Sen.* vol.6, no.6, pp:867-881

**Chatfield, C.** (1980): The Analysis of Time Series. Chapman and Hall, London

**Chavez, Jr., P.S.** (1975): Atmospheric, Solar and MTF Corrections for ERTS Digital Imagery. Amer. Soc. of Photog. Proc. of Annual Meeting, Arizona

**Chavez JR, P. and Bauer, B.** (1982): An Automatic Optimum Kernel-Osize Selection Techniques for Edge Enhancement *Rem. Sen. of Env.* 12, pp:23-38

**Cherry, M.E.** (1983): Association of Gold and Felsic Intrusions - Examples from the Abitibi Belt. In: The Geology of Gold in Ontario. Ontario Geol. Survey Misc. Paper 110, pp:48-55

**Clark, K.C.** (1986): Advances in Geographical Information Systems. *Computer Environment and Urban Systems*. Vol.10, pp:175-184

**Clark, M.E., Archibald, N.J. and Hodgson, N.** (1986): The Structural and Metamorphical Setting of the Victoria Gold Mine, Kambalda Western Australia. *Proceedings of Gold '86*. An Int. Symp. of Gold A.J. Macdonald Ed. Konsult Int. Inc. Toronto pp:243-254

**Colvine, A.C., Andrews, A.J., Cherry, M.E., Durocher, M.E., Fyon, A.J. Lavigne, M.J., Macdonald, A.J., Marmont, s., Pousen, K.H., Springer, J.S. and Troop, D.G.** (1984): An Integrated model for the Origin of Archaean Lode Gold Deposits. *Ont. Geol. Surv. Open File* Report 5524 98p

**Colvine, A.C., Fyon, J.A., Heather, K.B., Marmont, S., Smith, P.M. and Troop, D.G.** (1988): Archaean Lode Gold Deposits in Ontario. Mines and Mineral Division Ontario *Geological Survey Miscellaneous Paper* 139

**Corfu, F. and Andrews, A.J.** (1987): Geochronological Constraints on the Timing of Magmatism, Deformation and Gold Mineralisation in the Red Lake Greenstone Belt, Northwestern Ontario. *Can. Jour. of Earth Sci.* Vol.24 pp:1302-1320

**Cordani, U.G.** (1973): Evolucao Geologica Pre-Cambriana da Faixa Costeira entre Salvador e Vitoria. Instituto de Geociencias da USP. Tese livre Docencia

--- (1975):The Geological Evolution of The Brazilian Continental Margin between Recife and Vitoria and the Correlation with its African Counterpart. *Int. Sym. Continental Margins of Atlantic Type.* Sao Paulo Abstract pp:1-4

**Cordani, U.G. and Brito Neves, B.B.** (1982): The Geologic Evolution of South America During the Archaean and Early Proterozoic. In:Int. Symp. of Archaean and Early Proterozoic Geol. Evolution and Metallogenesis. *Rev. Bras. Geoc.* 12 pp:78-188

**Cordani, U.G. and Iyer, S.S.** (1978): Geochronological Investigation on the Precambrian Granulitic Terrains of Bahia, Brazil. *Precambrian Research* 9:255-274

**Cordani, U.G., Sato, K.and Marinho, M.M.** (1985):The Geologic Evolution of the Ancient Granite-Greenstone Terrane of Central Southern Bahia, Brazil. Precambrian Research 27:187-213

**Cordani, U.G., Teixeira, W., Tassinari, C.C.G., Kawashita, K. and Sato, K.** (1988): The Growth of the Brazilian Shield. *Episodes* 11:163-167

**Costa, L.A.M. and Inda, H.A.V.** (1982): O Aulacogeno do Espinhaco. *Ciencias da Terra* 2:13-18

**Costa, L.A.M. and Mascarenhas, J.F.** (1982): The High-grade Metamorphic Terrains in the Interval Mutuipe-Jequie: Archaean and Lower Proterozoic of East-central Bahia. In: *Int. Symp. of Archaean and Early Proterozoic.* pp:19-37

**Coward, M.P.** (1984): Major Shear Zones in the Precambrian Crust; Examples from NW Scotland and Southern Africa and their Significance. Tect. Illust. A. Kroner and R. Greiling Eds. E. Schweizerbart'che Verlagstuchlandlung, Stuttgart pp:207-236

**Crosta, A.P.** (1990): Mapping of Residual soils by Remote Sensing for Mineral Exploration in SW Minas Gerais State, Brazil. PhD Thesis Centre for Remote Sensing, Imperial College of Science, Technology and Medicine. University of London

**Crosta, A.P. and Moore, J. McM.** (1989): Geological Mapping Using Landsat Thematic Mapper Imagery in Almeria Province, Southeast Spain. *Int. J. Rem. Sen.*, vol.10, no.3, pp:505-514

**Cruz, M.J.** (1989): Le Massif de Rio Piau: Une Intrusion de Nature Gabbroique et Anortosique dans le Terrains Granulitiques du Noyau Jequie, Bahia, Bresil. Unpub. Doctorat Thesis. University of Paris VI (No. de ordre 89-4)

**Cudjoe, J.E.** (1970): Progress in Mineral Exploration in Ghana During the Past Half Century (1913-63). In: Symp. 50th Anniversary Ghana Geol. Surv. 1913-63 Ccol. Surv. Ghana Bul.38, pp:1-10

**Cunha, J.C., Bastos, C.A.M., Cavalcanti, J.C.C and Souza, W.S.T.** (1981): Projeto Jurema-Travessao. Companhia Baiana de Pesquisa Mineral. Open file report. Vol.1, 111p

**Cunney, M., Sabate, P., Vidal, P., Marinho, M.M. and Conceicao, H.** (:1989): The Peralluminous Magmatism on the Jacobina-Contendas-Mirante Belt (Bahia, Brazil): a Signature of an Early Proterozoic Continental Collision (in prep.)

**Debon, F. and Le Fort, P.** (1982): A chemical-mineralogical classification of Common Plutonic Rocks and Associations. Trans. Roy. Soc. Edinburgh: *Earth Sci.* 73:135-149

**Drury, S.A** (1982): A Regional Tectonic Study of the Archaean Chitradurga Greenstone Belt, Karnataka, Based on Landsat Interpretation. *J. Geol. Soc. India* 24 pp:167-184

--- (1984): Applications of Digital Image Enhancement in Regional Tectonic Mapping of South India 18th Int. Symp. on Rem. Sen. of the Env. pp:1895-1903

--- (1985): Applications of Digital Image Enhancement in Regional Tectonic Mapping of South India. Proc. XVII Int. Symp. Rem. Sen. of Env. Paris Oct. 1984, Enviroomental Research Institute of Michigan, Ann Arbor, pp:1895-1904

--- (1986): Remote Sensing of Geological Structure in Temperate Agricultural Terrains. *Geol. Mag.* 123, pp:113-121

--- (1987): Image Interpretation in Geology. Allen & Unwin Publ. ltd 243p

**Drury, S.A. and Hunt G.A.** (1989): Geological Uses of Remotely Sensed Reflected and Emitted Data over Laterised Terrains in Western Australia. *Int. Journ. Rem. Sen.* 10 (3) pp:475-497

**Drury, S.A. and Walker, A.S.D.** (1987): Display and Enhancement of Gridded Aeromagnetic Data of the Solway Basin. *Int. J. Rem. Sen.* vol.8, no.10, pp:1433-1444

**Drury, S.A. and Walker, A.S.D.** (1988): Integration of Geological, Geophysical and Remotely Sensed Data for the Solway Basin, England. In: Proc. IGARRS Symp. Edinburgh, Scotland, pp:1663-1666

**Einaudi, M.T., Meinert, L.D. and Newberry, R.J.** (1981): Skarn Deposits *Econ. Geol.* 75th Ann. vol. pp:317-391

**Ermanovics, I., Gibb, R.A., Whitaker, S.H. and Raven, K.** (1984): Advances in Geoscience Surveys at the East Bull Lake Research Area (RA-7) near Massey Ontario. In: Proc. of the 16th Inf. Mtg. on the Nuclear Fuel Waste Manag. Prog. Atomic Energy of Canada Lted. Tech. Rep. TR-218 pp:51-73

**Foster, R.P., Mann, A.G., Stowe, C.W. and Wilson, J.F.** (1986): Archaean Gold Mineralization in Zimbabwe. In: Anhaeuser, C.R. and Maske, S (Eds) Mineral Deposits of Southern Africa Vol.1 Johannesburg, Geol. Soc. of South Africa pp:43-112

**Foster, R.P and Wilson,J.F.** (1984): Geological Setting of Archaean Deposits in Zimbabwe. Proceedings of Gold' 82 The Geology, Geochemistry and Genesis of Gold Deposits. R.P. Foster Ed. *Geological Society of Zimbabwe Sp. Publ. 1* pp:521-551

**Freeman, H.** (1974): Computer Processing of Line-drawing Images *Com. Surv. 6,* pp:54-97

**Fyon, J.A. and Crocket, J.H.** (1981): Volcanic Environment, Carbonate Alteration and Stratiform Gold Mineralization, Timmins. In: Genesis of Archaean Volcanic-hosted Gold Deposits. Symp. held at the Univ. of Waterloo. Ontario Geological Survey. Misc. Paper 97, pp:47-58

**Fyon, J.A. and Lane, L.** (1985): Structural Geology and Alteration Patterns Related to Gold Mineralisation in the Confederation Lake Area. Summary of Filed Work and Other Activities Ontario, Geological Survey. J. Wood, O.L. White, R.B. Barlow and A.C. Colvine Eds. Ontario Geological Survey Miscellaneous paper 126, 351p.

**Galvao, C.F.** et al (1987) Projeto Rio Jacare. Open file report. Companhia Baiana de Pesquisa Mineral. Convenio SME/CBPM

**Garrels, L.M. and Mackenzie, F.T.** (1971): Evolution of Sedimentary Rocks. N.Y. Norton Inc. 307p.

**Gee, R.D., Myers, J.S. and Trendall, A.F.** (1986): Relation between Archaean High-grade Gneiss and Granite-greenstone Terrain in Western Australia. *Precambrian Res.* 33 pp:87-102

**Gillespie, A.B., Kahle, A.B. and Walker, R.E.** (1986): Colour enhancement of highly correlaed images. I. Decorrelation and HSI contrast stretches. *Rem. Sen. of Env.* 20 pp:209-235

**Gibbs, A.K., Montgomery, C.W., O'Day, P.A. and Erslev, E.A.** (1986): The Archaean-Proterozoic Transition: Evidence from the Geochemistry of Metasedimentary Rocks from Guyana and Montana. Geoch. Cosm. Acta 50:2125-2141

**Glikson, A.Y. and Lambert, I.B.** (1976): Vertical Zonation and Petrogenesis of the Early Precambrian Crust in Western Australia. *Tectonoph.* No.30, pp:55-89

**Goetz, A.F.H and Rock, B.N.** (1973): Remote sensing for exploration: an overview. *Econ. Geol.* vol.78, no4, pp:573-591

**Gorman, B.E., Kerrich, R. and Fyfe, W.S.** (1981): Geochemistry and Field Relationships of Lode Gold Deposits in Felsic Igneous Intrusion - Porphyries of the Timmins District. In: Geoscience Research Grant Program. Summary of Research 1980-1981 Ed. by E.G. Pye Ontario Geol. Survey, Misc. Paper 98, pp:108-124

**Grant, F.S.** (1985): Aeromagnetics, Geology and Ore environments I.Magnetite in Igneous, Sedimentary and Metamorphic Rocks: an Overview. II.Magnetite and Ore Environments. Geoexploration (in press)

**Gregory, A.F. and Horwood, J.L.** (1963): A Spectrometric Study of the Attenuation in Air of Gamma-rays from Mineral Resources. US Atomic Energy Commission Report CEX-60-3 Washington DC

**Groves, D.I. and Batt, W.D.** (1984): Spatial and Temporal Variations of Archaean Metallogenetic Associations in Terms of Evolution of Granitoid-Greenstone Belt Terrains with Particular Emphasis on the Western Australia Shield. In:*Archaean Geochemistry.* Kroner Ed. pp:73-98

**Groves, D.I. and Phillips, G.N.** (1987): The Genesis and Tectonic Control on Archaean Gold Deposits of the Western Australia Shield - a Metamorphic Replacement Model. *Ore Geology Reviews.* Vol.2, pp:287-322

**Groves, P.I., Phillips, G.W., Ho, S.E., Henderson, C.A., Clark, M.E. and Wood, G.M.** (1984): Controls Distribution of Archaean Hydrothermal Gold Deposits in western Australia. In: Proc. Symp. Gold '82 Geol. Soc. of Zimbabwe Spec. Publ. 1 A.A. Balkema Rotterdam, The Netherlands

**Groves, D.I., Phillips, G.N., Ho, S.E. and Houstoun, S.M.** (1985): The Nature, Genesis and Regional Controls of Gold Mineralisation in Archaean Greenstone Belts of the Western Australian Shield: a Brief Review. *Trans. Geol. Soc. S. Afr.* 88 pp:135-148

**Groves, D.I., Ho, S.E., Houstoun, S.M. and Phillips, G.N.** (1986): A review of Gold Deposits in the Archaean Greenstone Belts of Western Australia. In: Berkman, D.A. Ed. Publ. of the 13th CMMI Congress, Vol.2, Geology and Exploration, pp:243-250

**Groves, D.I., Phillips, N., Ho, S.E., Houstoun, S.M and Standing, C.** (11987): Craton-scale Distribution of Archaean Greenstone Gold Deposits: Predictive Capacity of the Metamorphic Model. *Econ. Geol.* Vol.82, pp:1045-2058

**Guimaraes, D.** (1951): Arqui-Brasil e sua Evolucao Geologica. *B. Div. Fom. Prod. Min. Dep. Nac. Prod. Min.* Rio de Janeiro, no.88, 314p

**Hamilton, J.V. and Hodgson, C.J.** (1986): Mineralisation and Structure of the Kolar Gold Field, India. In: Proceedings of Gold '86. An Int. Symp. of the Geology of Gold. A.J. Macdonald Ed. Konsult Int. Inc. Toronto. pp:270-283

**Harris, R.** (1987): Satellite Remote Sensing. An Introduction. Routledge & Kegan Paul Inc. 220pp

**Harris, J.R. and Murray, R.** (1990): IHS transform for integration of radar imagery with other remotely sensed data. *Photog. Engin. & Rem. Sen.* vol.56, no12, pp:1631-1641

**Hasui, Y.** (1975): The Ribeira Folded Belt. *Rev. Bras. Geoc.* No.5,pp:257-266

**Henley, R.W., Hedenquist, J.W. and Roberts, P.J.** (1986): Guide to Active Epithermal (Geothermal) Systems and Precious Metal Deposits of New Zealand. Berlin-Sttutgart Gebruder Borntraeger Mon. Ser. Min. Dep. 26, 212p

**Higgins, M.W.** (1971): Cataclastic Rocks. Washington US Government Printing Office. Geological Survey Professional Paper, 687. 97p

**Hodgson, C.J. and MacGeehan, P.J.** (1982): A Review of the Geological characteristics of "Gold only" Deposits in the Superior Province of the Canadian Shield. Geology of Canadian Gold Deposits CIM Special Vol.24 pp:211-228

**Hood, P., Irvine, J. and Hansen, J.** (1982): The Application of the Aeromagnetic Gradiometer Survey Technique to Gold Exploration in the Val d'Or Mining Camp, Quebec. *Can. Min. J.* 106

**Hunt, G.A.** (1988): Improvement in the forward and Inverse Principal Component Transformations for Geological Mapping in Semi-arid Terrains. Proc. of IGARSS '88 Edinburgh ESA SP-284 pp:1061-1062

**Hunt, G.H. and Ashley, R.P.** (1979): Spectra of Altered rocks in the Visible and Near Infrared. *Econ. Geol.* Vol.74, pp:1613-1629

**Hunt, G.H., Salisbury, J.W. and Lenhoff, C.J.** (1974): Visible and Near Infrared Spectra of Minerals and Rocks. IX Basic and Ultrabasic Igneous Rocks. *Modern Geology* vol.5, pp:15-2

--- Visible and Near Infrared Spectra of Minerals and Rocks. VII Acidic Igneous Rocks. *Modern Geology* vol.4, pp:217-224

**Inda, H.A.V. and Barbosa, J.F.** (1978): Texto Explicativo para o Mapa Geologico da Bahia, Esc. 1:1000000 Sec. Minas e Energia, CPM, 137p

**Jardim de Sa, E.F., McReath, I, Neves, B.B.B., Bartels, R.L. and Kawashita, K.** (1978): Reconnaissance Geochronology of the Infrastructure of Part of the Sao Francisco Craton in the State of Bahia, Brazil. Vol. D. Guimaraes. *Jornal de Mineralogia*, vol.7, pp:87-96

**Jensen, H.** (1965): Instrument Details and Application of a New Airborne Magnetometer. *Geophysics* vol.30, pp:875-882

**Kaufmann, H.** (1989: Image Processing Startegies for Mineral Exploration in Arid Areas by Use of TM data. Proc. of the Workshop on Earthnet Pilot Project on Landsat TM applications, Frascati, Italy. ESA SP-1102, pp:111-125

**Kazmin, V., Shifferaw, A. and Balcha, T.** (1978): The Ethiopian Basement Stratigraphy and Possible Manner of Evolution. *Geol. Runchau*, 67, pp:531-546

**Keays, R.R.** (1984): Archaean Gold Deposits and their Source rocks: the Upper Mantle Connection. In: Foster R.P. (Ed) Gold '82: The Geology, Geochemistry and Genesis of Gold Deposits. A.A. Balkema, Rotterdam, pp:17-51

**Kennedy, W.Q.** (1964): The Structural Differentiation of Africa in the Pan-African (±500 m.y.) Tectonic Episode. *Res. Inst. Afr. Geol.* 8th Ann. Rep. Univ. Leeds, pp:48-49

**Kerrich, R.** (1984): Geochemistry of Gold Deposits in the Abitibi Greenstone Belt. Can. Inst. Min. Met. Spec. Vol.27 pp:1-75

**Kerrich, R. and Hodder, R. W.** (1982): Archaean Lode Gold and Base Metal Deposits: Evidence for Metal Separation into Independent Hydrothermal Systems. In: R.W. Hodder and W. Petruk (Eds.) Gold Deposits, CIM Spec. Vol.24 pp:144-160

**Kerswill, J.A.** (1983):_The Lupin Gold Deposits, Contwoyto Lake Area, N.W.T.; Styles of Gold Distribution and Possible Genetical Models. In: Programs with Abstracts Vol9, GAC/MAC Ann. General Meeting

**Kesse, G.O.** (1984): The occurrence of Gold in Ghana. In: Proc. Symp. Gold '82. Geol. Soc. of Zimbabwe Spec. Publ. 1 A.A. Balkema Rotterdam, The Netherlands

**Kimbell, G.S., Burley, A.J., Parker, M.E., Pease, S.F. and Barton, K.J.** (1984): The Gravity Survey of the Molopo Farms Area, Southern Botswana. Bull. 30 Geol. Survey Dept. Botswana

**King, L.C.** (1956): Geomorfologia do Brasil Oriental. Rev. Bras. Geog. Rio de Janeiro 18 (2):147-263

**Kokesh, F. P.** (1951): Gamma-ray logging. Oil and Gas Journal. 50, 284

**Kroner, A.** (1975): Late Precambrian Formations in the Western Richtersveld, Northern Cape province. *Trans. R. Soc. Afr.* 41 pp:375-423

--- (1976): Proterozoic Crustal Evolution in Parts of Southern Africa and Evidence for Extensive Sialic Crust since the End of Archaean *Phylos. Trans. R. Soc. London*, A280, pp:541-553

--- (1977): The Precambrian Geotectonic Evolution of Africa: Plate Accretion Versus Plate Destruction. *Precamb. Res.* 4, pp:163-213

**Lavreau, J.** (1984): Vein and Stratabound Gold Deposits of Northern Zaire. Mineralline Deposita Vol.19, pp:158-165

**Lam, N.S.** (1983): Spatial Interpolation Methods: a Review. *Am. Cart.* 10, pp:129-149

**La Roche, H de** (1968): Comportement Geochemique Differentiel de Na, K et Al dans les Formations Volcaniques et Sedimentaires. Un Guide pour l'Etude des Formations Metamorphique et Plutoniques. C.R. Acad. Sc. Paris D, 267:39-42

**Leblanc, M.** (1981): The Late Proterozoic Ophiolites of Bon Azzer (Morocco): Evidence for Pan-African Plate Tectonics. In: A. Kroner Ed. Precambrian Plate Tectonics. Elsevier, Amsterdam, pp:435-451

**Lepeltier, C.** (1969): A simplified Statistical Treatment of Geochemical Data by Graphical Representation. *Econ. Geol.*, vol.14, pp:538-550

**Levinson, A.A.** (1980): Introduction to exploration geochemistry 2nd ed. Applied Publishing

**Lillesand, T.M. and Kiefer, R.W.** (1979): Remote Sensing and Image Interpretation. John Wiley Publ

**Lima, J.A.D., Oliveira, J.E., Costa, I.V.G.m, Bonfim, L.F.C., Barral, N.M. and Santos, R.A.** (1981): Projeto Aracatu. Companhia de Pesquisa de Recursos Minerais. Convenio CPRM-DNPM, Salvador. Rel. Final Inedito, vol1, 393p

**Macdonald, A.J.** (1983): The Iron-formation-gold Association: Evidence from the Geraldton Area. The Geology of Gold in Ontario. A.C. Colvine Ed. Ontario Geological Survey Miscellaneous paper 110, pp:75-83

**Marinho, M.M., Costa, P.H., Silva, E.F.A. and Torquato, J.R.F.** (1978): A Sequencia Vulcano-sedimentar Contendas-Mirante, uma Estrutura do Tipo "Greenstone Belt". XXX Congr. Bras. Geol. Recife 1:291

**Marinho, M.M., Costa, P.H., Silva, E.F.A. and Soares, J.V.** (1979): Projeto Contendas-Mirante. Companhia Baiana de Pesquisa Mineral. Open file report, vol.1, 225p

**Marinho, M.M.M., Silva, E.F.A., Lopes, G.A.D.C, Soares, J.V. and Cruz, M.J.M.** (1980):Projeto Anaje-Caldeirao. Companhia Baiana de Pesquisa Mineral. Relatorio Final Inedito. Vol.1, 203p

**Mark, D.M. and Lauzon,** J.P. (1984): Linear Quadtrees for Geographical Information Systems. In: Proc. IGU Int. Symp. on Spatial Data Handling, Zurich, pp:412-431

**Marinho, M.M. and Sabate, P.** (1982): The Contendas-Mirante Volcano-sedimentary Sequence and Its Granitic-migmatitic Basement. In: *Int. Symp. of Archaean and Early Prot. Geol. Evol. and Metallog.* CPM/SME. Bahia, Salvador, Brazil. Abstracts and Excursions, vol.1, pp:139-184

**Marmont, S. and Corfu, F.** (1988): Timing of Gold Introduction in the Late Archaean Tectonic Framework of the Canadian Shield. Evidence from U-Pb Zircon Geochronology of the Abitibi Subprovince. Extended Abstract in Proc. of Gold '88, Melbourne

**Mascarenhas, J.F.** (1973): A Geologia do Centro-leste do Estado da Bahia. In: XXVII Cong. Bras. Geol. Aracaju, pp:35-66

--- (1979): Estruturas do Tipo Greenstone Belt no Leste da Bahia. IN: Inda, H.A.V. and Duarte, F.B. Eds. *Geol. e Rec. Min. do Estado da Bahia.* Textos Basicos. SME/CPM, vol.2, pp:23-53

**Mascarenhas, J.F., Pedreira, A.J., Misi, A. Motta, A.C. and Sa, J.H.S.** (1982): Provincia Sao Francisco. In: Almeida, F.F.M. and Hasui, Y. Eds. Precambriano no Brasil

**Matheron, G.** (1971): The Theory of Regionalised Variables and Its Application. Les Cahiers du Centre de Morphologie Matematique de Fontainebleau. Ecole Nationale Superieure des Mines et Energie

**Maxwell, E.M.** (1876): Multivariate System Analysis of Multispectral Imagery. *Photog. Eng. and Rem. Sen.* 42:1173-1186

**Menezes, J.S.** (1980): Aspectos Geoquimicos do Complexo Contendas-Mirante (Area de Contendas do Sincora). Dissert. de Mestrado. Univ. Federal da Bahia

**Menhert, K.R.** (1968): Migmatites and the Origin of Granitic Rocks. Amsterdam, Elsevier. 393p

**Narayanan, K.A. and Rosenfeld, A.** (1981): Image Smoothing by Local Use of Global Information. IEEE *Transactions on Systems, Man and Cybernetics.* Vol.SMC-11, no.2, pp:826-831

**Newhouse, W.H.** (1940): Openings Due to Movement along a Curved or Irregular Fault Plane. Econ. Geol. Vol.35, pp:444-464

**Niblack, W.** (1986): An Introduction to Digital Image Processing. Prentice Hall International UK Lted, 215p

**O'Driscoll, E.S.T.** (1981): A Broad-scale Structural Characteristic of Major Nickel Sulphide Deposits of Western Australia. *Econ. Geol.* 76 pp:1364-1372

**Patterson, N.R.** (1983): New Geophysical Guides to Ore Exploration. In: New paths to Mineral Exploration. Proc. of 3rd Int. Symp. Hannover, Fed. Rep. of Germany. Bender F Ed. Fed. Inst. for Geosciences and Min. Res. Hannover pp:155-168

**Patterson, N.R. and Reeves, C.V.** (1985): Applications of Gravity and Magnetic Surveys: the State-of-the-Art in 1985. *Geophysics* vol.50, no..12, pp:2558-2594

**Pavlidis, T.** (1982): Algorithms for Graphics and Image Processing. Springer-Verlag, Berlin

**Pearce, T.M., Gorman, B.E. and Birkett, T.C.** (1975): The $TiO_2$-$K_2O$-$P_2O_5$ Diagram: a Method of Discriminating between Oceanic and Non-oceanic Basalts. *Earth Planet. Sci. Lett.* 24:419-426

--- (1977): The Relationship between Major Element Chemistry and Tectonic Environment of Basic and Intermediate Volcanic Rocks. *Earth. Planet. Sci. Lett.* 36:121-132

**Pedreira, A.J., Oliveira, J.E., Silva, B.C.E. and Pedrosa, C.J.** (1975): Projeto Bahia (Geologia da Bacia do Rio de Contas) Companhia de Pesquisa de Recursos Minerais. Convenio CPRM-DNPM, Salvador. Rel. Final Inedito, vol.3, 233p

**Pedreira, A. J. and Marinho, M.M.** (1981): Precambrian Geology of Eastern Bahia, Brazil. In: *Seminar on Mineral Research in Precambrian Areas Clausthal-Zellerfeld, West Germany*. Unpub. Lect. of Part., 59p

**Petijohn, F.J.** (1975): Sedimentary Rocks. 3th Ed. N.Y. Harper and Row, 628p

**Peuquet, D.** (1984): A Conceptual Framework and Comparison of Spatial Data Models. *Cartographica* 21(4):66-113

**Pflug, R.** (1965): A Geologia da Parte Meridional da Serra do Espinhaco e Zonas Adjacentes, Minas Gerais. *B. Div. Geol. Min. Dep. Nac. Prod. Min.* Rio de Janeiro, no.226, 55p

**Pflug, R. et al.** (1969): Contribuicao a Geotectonica do Brasil Oriental. Recife, Sudene. Ser. Esp. no.9, 59p

**Phillips, G.N.** (1985): Archaean Gold Deposits of Australia. Inf. Circ. Econ. Geol. Res. Unit. Univ. Witwatersrand, Johanesburg 175, 41p

**Phillips, G.N., and Groves, D.I.** (1984): Fluid Access and Fluid-wall Rock Interaction in the Genesis of the Archaean Gold-quartz Vein Deposit in Hunt Mine, Kambalda, Western Australia. In: Proc. Symp. Gold '82 Geol. Soc. of Zimbabwe, A.A. Balkema Rotterdam, The Netherlands

**Phillips, G.N., Groves, D.I. and Martyn, J.E.** (1984): An Epigenetic Origin for Archaean Banded Iron-formations Hosted Gold Deposits. *Econ. Geol.* Vol.79 pp:102-171

**Pichavant, M., Kontak, D.J., Brique, L., Herrera, J.V. and Clark, A.H.** (1988a): The Miocene-Pliocene Macusani Volcanics, SE Peru II. Geochemistry and Origin of a Felsic Peraluminous Magma. *Cont. Min. Ptrog.* 100:325-338

--- (1988b): The Miocene-Pliocene Macusani Volcanics, SE Peru I Mineralogy and Magmatic Evolution of Two Mica Aluminossilicate-bearing Ignimbrite suite *Cont. Min. Ptrog.* 100:300-324

**Piper, J.D.A.** (1982): The Precambrian Paleomagnetic Record: the Case for the Proterozoic Supercontinent. *Earth Planet. Sci. Lett.* 59, pp:61-89

**Piper, J.D.A., Briden, J.C. and Lomax, K.** (1973): Precambrian Africa and South America as a Single Continent. *Nature* 245, pp:244-248

**Porada, H.** (1979) : The Damara-Ribeira Orogen of the Pan-African/Brasiliano Cycle in Namibia (South West Africa) and Brazil as Interpreted in Terms of Continental Collision. *Tectonophysics* 55, pp:237-265

--- (1985): Stratigraphy and Facies in the Upper Proterozoic Damara Orogen, Namibia Based on a Geodynamic Model *Precam. Res.*, no.29, pp:325-624

--- (1989): Pan-African Rifting and Orogenesis in Southern to Equatorial Africa and Eastern Brazil. *Precam. Res.* 44, pp:103-136

**Pratt, W.K.** (1975): Digital Image Processing New York, Willey

**Reeves, C.V.** (1985): The Kalahari Desert, Central Southern Africa: a Case History of Regional Gravity and Magnetic Exploration. In: Hinze, M.J. (Ed). The Utility of Regional Gravity and Magnetic Anomaly maps. Soc. Exp. Geophy.

**Reeves, C.V.** (1985): Airborne Geophysics for Geological Mapping and Regional Exploration *ITC Journal* 3 pp:147-161

**Richards, D.J. and Walraven, F.** (1975): Airborne Geophysics and ERTS Imagery. *Min. Sci. Eng.* vol.7, no.3, pp:234-278

**Ripley, B.** (1981): Spatial Statistics. Willey, New York

**Roberts, R.G.** (1987): Ore Deposits Model, Number 11: Archaean Lode Gold Deposits. *Geoscience*, Canada, vol.14, pp:37-52

**Rose, A.W, Hawkes, H.E. and Webb, J.S.** (1979): Geochemistry in mineral exploration. Academic Press London

**Rothery, D.A.** (1987): Decorrelation Stretching as an Aid to Image Interpretation. *Int. Journ. Ren. Sen.* 8 pp:1253-1254

--- (1987): Improved Discrimination of Rock Units Using Landsat Thematic Mapper Imagery of the Oman Ophiolite. J. of the Geol. Soc. of London, 144 pp:587-597

**Rothery, D.A. and Hunt. G.A.** (1990): A Simple Way to Perform Decorrelation Stretching and Related Techniques on Menu-driven Image Processing Systems. *Int. Jour. Rem. Sen.* vol.11, no.1, pp:133-137

**Roux, A.T.** (1970): The Application of Geophysics to Gold Exploration in South Africa. In: Morley L.W. (Ed). Min. and Groundwater Geop. Geol. Surv. Can. Econ. Geol. Rep. 26, pp:425-438

**Royer, G.** (1967): Two Years Survey with the Caesium Vapour Magnetometer. *Geophysics* Prospect. vol.15, pp:174-193

**Saager, R. Oberthur, T. and Tomschi, T.** (1987): Geochemistry and Mineralogy of Banded Iron-Formation-Hosted Gold Mineralisation in the Gwanda Greenstone Belt, Zimbabwe. *Econ. Geol.*, vol.82, pp:2017-2032

**Sa, E.F.J.** (1981): A Chapada Diamantina e a Faixa Santo Onofre: um Exemplo de Tectonica Intraplaca no Proterozoico Medio do Craton Sao Francisco. In: Inda, H.A.V, Marinho, M.M. and Duarte, F.B. Eds. Geol. e Recursos Minerais do Estado da Bahia. *Textos Basicos* 4, pp:111-120

**Sabate, P., Machado, G.V.M.S. and Souza, M.Z.A.** (1980): Donnes Structurales des Formations Precambriennes Epimetamorphique du Complexe Contendas-Mirante, Bahia, Bresil. Cahiers ORSTOM, Paris, Ser. Geol. t. XI, 1:18-24

**Sabate, P. and Marinho, M.M.** (1982):The Contendas-Mirante Volcano-sedimentary Sequence and Its Granitic-migmatitic Basement. ISAP. Abstract Excursions. Salvador, Bahia, Brazil

**Sabate, P. Gomes, L.C.C and Anjos, J.A.A** (1988): Nota Explicativa do Mapa Tematico "Granitogenese da Bahia - Folha 1:25000, Vitoria da Conquista". SGM/SME, Bahia, Brazil

**Sabate, P., Marinho, M.M, Vidal, P. and Caen-Vachette, M.** (1990): Continental Collision Affinities of the Lower Proterozoic Peraluminous Granitic Line of the Sao Francisco Craton, Brazil (in prep)

**Sabins, F.F.** (1978): Remote Sensing: Principles and Interpretation. Freeman Publ.

**Sabins, F.F., Blom, R and Elachi, C.** (1979): Expression of San Andreas Fault on Seasat Radar Image. In Radar Geology: an assessment. Report of the Radar Geology Workshop Snowmass, Colorado pp:64-74

**Sangster, D.F.** (1969): The Contact Metasomatic Magnetite Deposits of Southwestern British Columbia Can. Geol. Surv. Bull. 172, 85p

**Samet, H., Rosenfeld, A., Schaffer, C.A. and Weber, R.E.** (1984): Use of Hierarchical Data Structures in Geographical Information Systems. In: Proc. IGU Inst. Symp. on Spatial Data Handling, Zurich, pp:392-411

**Shackleton, R.M.** (1977): Possible Late-Precambrian Ophiolites in Africa and Brazil *Ann. Rep. Res. Inst. Afr.* Geol. Univ. of Leeds 20 pp:3-7

**Sheffield, C.** (1985): Selecting Band Combinations from Multispectral Data *Photog. Eng. and Rem. Sen.* 51, pp:681-687

**Showengerdt, R.A.** (1983): Techniques for Image Processing and Classification in Remote Sensing. Academic Press

**Sial, A.N., Pessoa, D.R.and Kawashita, K.**(1976): New Potassium-Argon Ages, Strontium Ratio Measurements and Chemistry of Mesozoic Basalts, State of Maranhao, Northeast Brazil. *Bol. Mineral*, Recife, Brazil 4:59-72

**Siegal, B.S. and Gillespie, A.R.** (1980): Remote Sensing in Geology. John Wiley Publ.

**Silva, A.B.** (1984): Projeto Sete Varzeas. Convenio SME/CBPM Open file report.

--- (1985): Projeto Jurema Oeste. Convenio SME/CBPM Open file report.

--- (1987): Banded Iron-Formation Gold Deposits and Lithological Interpretation of Landsat TM Data In Bahia State, Brazil. MSc Thesis Imperial College of London

**Silveira, W.P., Lopes, G.A. and Toledo, L.A.A.** (1980): Projeto Umburanas. Companhia Baiana de Pesquisa Mineral. Convenio SME/CBPM. Salvador. Rel. Final Inedito, vol.1, 150p

**Siems, P.L.** (1984): Hydrothermal Alteration for Mineral Exploration-Workshop. Dept. of Geology, College of Mines and Earth Resources Idaho Mining and Mineral Resources Institute and University Continuing Education. University of Idaho

**Simpson, C.** (1986): Determination of Movement Sense in Mylonites. *Jour. of Geol. Educ.* Vol.34, pp:246-260

--- (1987): Earthquake Rupturing as a Mineralisation Agent in Hydrothermal Systems. *Geology*, vol.15, pp:701-704

**Singh, P. and Rao, A.** (1980): Gold Mineralisation and Geology Around Chinmulgund Area, Dharwar District, Karnataka State. *Geol. Survey of India*, vol.113, part 5, pp:32-45

**Slaney, V.R.** (1985): Landsat MSS and Airborne Geophysical Data Combined for Mapping Granite in Southwest Nova Scotia. Machine Processing of Remotely Sensed Data Symp. pp:198-205

**Smith, J.J, Cloke, P.L and Kesler, S.E** (1984): Geochemistry of Fluid Inclusions from the McIntyre-Hollinger Gold Deposits. Timmins Ontario Canada. *Econ. Geol.* Vol.79, pp:1265-1285

**Soha, J.H. and Schwartz, A.A.** (1978): Multispectral Histogram Normalization Contrast Enhancement. 5th Canadian Symp. on Rem. Sen. Proc. pp:86-103

**Stott, G.M. and Smith, P.M.** (1988): Development of Gold-bearing Structures in the Archaean: the Role of Granitic Plutonism. Proceeding of Gold '88, Melbourne

**Streickeisen, A.** (1976): To Each Plutonic Rock Its Proper Name. *Earth Sci. Rev.* Amsterdam, 12(1):1-33

**Taylor, S.R. and McLennan, S.M.** (1985): The Continental Crust: Its Composition and Evolution. Blackwell, Oxford, 312p

**Telford, W.M., Geldart, L.P., Sheriff, R.E. and Keys, D.A.** (1982): Applied Geophysics. Press Syndicate of the University of Cambridge, 860p

**Tihor, L.A. and Crocket, J.M.** (1976): Origin and Distribution of Gold-bearing Carbonate Zones of Kirkland Lake-Larder Lake Areas. Ontario Geol. Surv. of Canada Paper 1976-1A pp:407-408

**Tomlinson, R.F.** (1972): Geographical Data Handling. IGU Commision on Geographical Data Sensing and Processing, Otawa, Canada

**Torquato, J.R.** (1975): Geotectonic Correlation between SE Brazil, SW Africa. *An. Acad. Brazil Cien.* 48 (supl), pp:353-363

--- (1977): Geotectonic Outline of Angola. Cah. ORSTOM Ser. Geol. 9:15-34

**Torquato, J.R. and Cordani, U.G.** (1981): Brazil-Africa Geological Links. *Earth Sci. Rev.* no.17, pp:155-176

**Travis, G.A., Woodwall, R. and Bartram, G.D.** (1971): The Geology of the Kalgoorlie Goldfield. Geol. Soc. of Australia Spec. Publ. Vol.3, pp:175-190

**Trefois, P.** (1988): Correlation Analysis and Principal Component Imagery of a Thematic Mapper Scene as an Aid to Geological Interpretation in the Karema Region (Western Tanzania). In: Lavreau, J. Bardinet, C. (eds)., Image Analysis Geological control and radiometric survey of Landsat TM data in Tanzania. The UNESCO/IUGS/GARS Program in Africa. Musee Royal de l'Afrique Centrale, Tervuren, Belgique. Annales, Serie IN-9, 96:149-156

**Tucker, D.H., Anfillof, V. and Luyendick, A.** (1985): New Large and Standard Format Magnetic Pixel Maps of Australia *Exp. Geoph.* Vol.16 pp:294-299

**Vignol, L.M.** (1987): Etudes Geoquemiques des Granulites du Bresil et de la Zone d'Ivrea: les Elements (K, Rb, Sr, Sm, Nd) et les Isotopes Radiogeniques (Sr et Nd) Unpub. DEA Thesis, Paris VIII Institute de Physique du Globe

**Viljoen, M.J.** (1982): The Nature and Genesis of Archaean Gold Mineralisation in Southern Africa. *Rev. Bras. Geosc.* 12(1-3) *pp:522-530*

--- (1984): Archaean Gold Mineralization and Komatiites in Southern Africa. In: Proc. Symp. Gold '82. Geol. Soc. of Zimbabwe Spec. Publ. 1. A. A. Balkema Ed. Rotterdam, The Netherlands

**Vincent, R.K, McKeon, J.B. and Scott, G.N. (1979)**: Mineral Exploration with Lansat and Radar Data in the Los Andes Region, Venezuela. Abstract only. Proc. of the *Am. Soc. of Photog.* 45th Annual Meeting, Washington DC.

**Vincelette, R.R. and Soeparjadi, R.A. (1976)**: Oil-bearing Reefs in Salwati Basin of Irian Jaya, Indonesia. AAPG Bul. Vol.160, pp:1448-1462

**Waugh, T.C.** (1986): A Response to Recent Papers and Articles on the Use of Quadtrees for Geographical Information Systems. In: Proceedings of the 2th Int. Symp. on Spatial data handling. *Int. Geogr. Union.* Williamsville, N.Y. pp:33-37

**Waters, G.S and Phillips, G.** (1956): A New Method of Measuring the Earth's Magnetic Field. *Geophysics* Prospect. vol.4, pp:1-9

**Webster, R.** (1984): Elucidation and Characterization of Spatial Variation in Soil Using Regionalised Variable Theory. In:*Geostatistics for Natural Resources Characterization* G. Verly et al Ed. Part 2, pp:903-913, Reidel, Doordrecht

**Wilson, N. (1987)**: Combined Sm-Nd, Pb/Pb and Rb-Sr Geochronology and Isotope Geochemistry in Polymetamorphic Precambrian Terrains: Examples from Bahia (Brazil) and Channel Islands (UK). Master of Sciences Thesis, Oxford University, UK

**Wilson, N., Moorbaath, S., Taylor, P.N. and Barbosa, J.S.F** (1988): Archaean and Early Proterozoic Crustal Evolution in the Sao Francisco Craton, Bahia, Brazil. *Chemical Geol.* Vol.70, (1-2) pp:1-46

**Woodwall, R.** (1979): Gold-Australia and the World 1-34 In: Glover J.E and Groves, D.I. Eds. Gold Mineralisation Univ. West Aust. Geol. Dept. & Extension Service Publ. 3, 106p

**Wyckoff, R.D.** (1948): The Gulf Airborne Magnetometer. *Geophysics* vol.13, pp:182-208

# APPENDIX A

# APPENDIX A

## Acronyms and abbreviations used in this work

ACP - Anage-Caldeirao Project

AFM- A=$K_2O$ + $Na_2O$, F=FeO + 0.9*$Fe_2O_3$, M=MgO

AGRS - Airborne Gamma-Ray Spectrometry

AM-FM - Automated Mapping and Facility Management

AS - Areiao Subunit

ASCII - American Standard Code for Information and Interchange

BAS - Barreiro d'Anta Subunit

BGS - British Geological Survey

BIF - Banded Iron-Formation

BIL - Banded Interleaved by Line

BIP - Banded Interleaved by Pixel

BLUE - Best Linear Unbiased Estimate

BO - Boolean Operation

BSQ - Band Sequential

BURP - Basic-Ultrabasic Rocks Project

CAD - Computer Aided Design

CCS - Cartesian Coordinate System

CBPM - Bahian Company for Mineral research

CMB - Contendas-Mirante belt

cgs - Centimetre, gramme, second

CMP - Contendas-Mirante Project

cps - Count per second

CPU - Central Processing Unit

CRC - Colour Ratio Composite

CRT - Cathode Ray Tube

CS - Coordinate System

CV - Convolution Mask

DBMS - Data Base Management System

DN - Digital Number

DRMM - Data Reduction Magnetic Method

EE - Edge Enhancement

eTh - Equivalent Thorium

eU - Equivalent Uranium

eV - Electron Volt

ERTS - Earth Resources Technology Satellite

FCC - False Colour Composite

FS - Fourier Series

GIS - Geographic Information System

GRASS - Geographic Resources Analysis Support System

HOM - Hotine Oblique Mercator

IBP - Itaberaba-Belmonte project

IDS - Image Display Subsystem

IFOV - Instantaneous Field of View

IHS - Intensity, Hue and Saturation

INPE - Brazilian Space Research Institute

IS - Interpreted Structures

ISM - Interactive Surface Modelling

ISN - Image Storage Node

JTS - Jurema-Travessao Subunit

LUT - Look UP Table

MAS - Mapped Structures

MDRM - Magnetic Data Reduction Method

MeV - Megaelectron Volt

MS - Mirante Subunit

MSS - Multi-Spectral Scanner

MUR - Mafic-ultramafic rocks

μm - Nanometre ($10^{-6}$ m)

NIR - Near Infrared

PA - Proximity Analysis

PC - Principal Component

PCA - Principal Component Analysis

PCT - Principal Component Transformation

ppm - parts per million

PT - Pressure and Temperature

PTA- Preliminary Target Areas

QDM - Quadtree Data Model

RAM - Random Access Memory

RBV - Return Beam Vidicon

RDM - Raster Data Model

REE - Rare Earth Element

RGB - Red, Green and Blue

RGS - Rio Gaviao Subunit

RLEM - Run-Length Encoding Model

RM - Raster Model

ROM - Read Only Memory

RSI - Remote Sensed Imagery

SDM - "Spaghetti" Data Model

SF - Smoothing Filter

SI - Systhéme Internacionale

SIR-A - Shuttle Imaging Radar

Slar - Side-Looking Airborne Radar

SME - Secretariat of Mining and Energy

SNLCS - Brazilian System of Soil Classification

SOM - Space Oblique of Mercator

SP - Spatial Filtering

SR - Spatial Resolution

SSS - Stream Sediment Survey

SWIR - Short-Wave Infra Red

TDM - Topological Data model

TCP - Triunfo-Contendas Project

TINM - Triangular Irregular Network Model

TM - Thematic Mapper

TP - Thiessen Polygons

TSA - Trend Surface Analysis

UNIRAS - Universal Raster System

USACERL - United States Army Construction Engineering Research Laboratory

UTM - Universal Traverse Mercator

VM - Vector Model

VNIR _ Very Near Infrared

VPEM - Value Point Encoding Model

WMA - Weighting Moving Average

# APPENDIX B

# APPENDIX B

**Program to convert ASCII files into GRASS dig_att files (AREAS) written in PASCAL and FORTRAN. Run on VAX, PC or SUN**

```
PROGRAM format ( input,output );
{+
COMPONENT:
PROGRAM DESCRIPTION:
AUTHOR: A. BARROS
CREATION DATE: tbs]%
DESIGN ISSUES:
MODIFICATION HISTORY:
      Date      |   Name   | Description
----------------+----------+-------------------
This program Re formats the geological data
-}
VAR
    first, second: REAL;
    I,j,m,n :integer;
    datafile,newfile:text;
    filename,line:packed ARRAY [1..80] OF char;
BEGIN
write ('Enter file name: ');
readln(filename);
OPEN( FILE_VARIABLE     := datafile,
      FILE_NAME         := filename,
      HISTORY           := OLD );
```

```
write ('Enter new file name: ');
readln(filename);
OPEN( FILE_VARIABLE     := newfile,
      FILE_NAME         := filename,
      HISTORY           := NEW );
reset(datafile);
rewrite(newfile);
readln(datafile,line);
while not eof(datafile) do
BEGIN
readv(line,first,second,i,j,m,n);
first := first* 1000;
second := second* 1000;
writeln(newfile,'    ',first:10:3,'    ',second:11:3,' ',j:3,'
',n:2);
readln(datafile,line);
END
END.
```

**ORIGINAL FILE:**

```
8484.91400   282.84600   1 3
8485.11000   282.73103   2 3
8485.19300   282.59100   3 3
8485.32500   282.47600   4 3
8484.91400   282.84600   5 3
```

**FIRST STEP:**

```
8484914.000   282846.000    3
8485110.000   282731.031    3
8485193.000   282591.000    3
8485325.000   282476.000    3
8484914.000   282846.000    3
```

```
      PROGRAM strip
C        Reformats data file
      REAL*4 east,north
      INTEGER cat
      CHARACTER*30 FILENAME,NEWFILE
      write (6,*)'What file do you want to change?'
      read(5,15)filename
      write (6,*)'What is the new file name?'
      read(5,15)newfile
```

```
15    FORMAT(A30)
C
      OPEN (
      1 UNIT=10,
      1    FILE = FILENAME,status='old')
      OPEN (
      1 UNIT=20,
      1    FILE = newfile,status='new')
C assumes file has max 25000 lines of data
      do 100 i=1,25000
      read (10,300)east,north,cat
      write(20,400)east,north,cat
100   continue
300   format(4x,f10.3,3x,f11.3,5x,i2)
400   format('A',5x,f9.2,4x,f10.2,9x,i2)
      END
```

**FINAL GRASS dig_att FILE (AREA):**

```
A 282846.0000000 8484914.000000       3
A 282731.0310000 8485110.000000       3
A 282591.0000000 8485193.000000       3
A 282476.0000000 8485325.000000       3
A 282846.0000000 8484914.000000       3
```

**To convert ASCII files into GRASS dig_ascii files (AREAS) written in PASCAL and FORTRAN. Run on VAX, PC or SUN:**

```
PROGRAM format ( input,output );
{+
COMPONENT:
PROGRAM DESCRIPTION:
AUTHORS:A. BARROS
CREATION DATE: tbs]%
DESIGN ISSUES:
MODIFICATION HISTORY:
      Date      |   Name   | Description
--------------+---------+-------------
This program Re formats the geological data
-}
VAR
    first, second: REAL;
    I,j,m,n :integer;
    datafile,newfile:text;
```

```
    filename,line:packed ARRAY [1..80] OF char;
BEGIN
write ('Enter file name: ');
readln(filename);
OPEN( FILE_VARIABLE     := datafile,
      FILE_NAME         := filename,
      HISTORY           := OLD );
write ('Enter new file name: ');
readln(filename);
OPEN( FILE_VARIABLE     := newfile,
      FILE_NAME         := filename,
      HISTORY           := NEW );
reset(datafile);
rewrite(newfile);
readln(datafile,line);
while not eof(datafile) do
BEGIN
readv(line,first,second,i,j,m,n);
first := first* 1000;
second := second* 1000;
writeln(newfile,'    ',second:11:3,'   ',first:10:3,' ',j:3,'
',n:1);
readln(datafile,line);
END
END.
```

**ORIGINAL FILE:**

```
8484.91400   282.84600   1 3
8485.11000   282.73103   2 3
8485.19300   282.59100   3 3
8485.32500   282.47600   4 3
8484.91400   282.84600   5 3
```

**FIRST STEP:**

```
8484914.000   282846.000    3
8485110.000   282731.031    3
8485193.000   282591.000    3
8485325.000   282476.000    3
8484914.000   282846.000    3
```

```
     PROGRAM strip
C       Reformats data file
```

```
      REAL*4 east,north
      INTEGER cat
      CHARACTER*30 FILENAME,NEWFILE
write (6,*)'What file do you want to change?'
      read(5,15)filename
      write (6,*)'What is the new file name?'
      read(5,15)newfile
15    FORMAT(A30)
C
      OPEN (
      1 UNIT=10,
      1    FILE = FILENAME,status='old')
      OPEN (
      1 UNIT=20,
      1    FILE = newfile,status='new')
C assumes file has max 25000 lines of data
      do 100 i=1,25000
      read (10,300)east,north,cat
      write(20,400)east,north,cat
100   continue
300   format(4x,f11.3,3x,f10.3,1x,i3)
400   format(1x,f12.2,1x,f12.2,4x,i3)
      END
```

**SECOND STEP:**

```
8484914.000   282846.000    1
8485110.000   282731.031    2
8485193.000   282591.000    3
8485325.000   282476.000    4
8484914.000   282846.000    5
PROCEDURE integers
local     find_one,
      start,
      last,
      intg,
      lpcnt,
      selst,
      curlin;
on_error
      if error = TPU$_STRNOTFOUND then
      position (end_of (current_buffer));
```

```
        find_one := mark (none);
        return;
        else
        abort;
      endif;
endon_error;
loop
    find_one := search ("      1", forward, exact);
    position (find_one);
    position (line_end);
    erase_character (-1);
    copy_text ("x");
    position (line_begin);
    split_line;
    move_vertical (-1);
    copy_text ("L");
    start := mark (none);
    find_one := search ("      1", forward, exact);
    position (find_one);
    move_vertical (-1);
    position (line_begin);
    last := mark (none);
    position (line_end);
    lpcnt := 0;
    loop
     lpcnt := lpcnt + 1;
     move_horizontal (-1);
     exitif current_character = " ";
    endloop;
    selst := select (none);
    move_horizontal (lpcnt);
    intg := select_range;
    position (start);
    copy_text (intg);
    selst := 0;
    move_vertical (1);
    loop
     position (line_end);
     loop
         move_horizontal (-1);
         exitif current_character = " ";
```

```
        erase_character (1);
      endloop;
      position (line_begin);
      curlin := mark (none);
      exitif curlin = last;
      move_vertical (1);
    endloop;
    move_vertical (1);
    curlin := mark (none);
    exitif curlin = end_of (current_buffer);
endloop;
endprocedure;
```

**FINAL GRASS dig_ascii file (AREA):**

```
A 5
8484914.00    282846.00    1
8485110.00    282731.03    2
8485193.00    282591.00    3
8485325.00    282476.00    4
8484914.00    282846.00    5
```

**Program to convert ASCII file into GRASS site list file written in PASCAL and FORTRAN. Run on VAX, PC or SUN:**

```
PROGRAM format ( input,output );
{+
COMPONENT:
PROGRAM DESCRIPTION:
AUTHORS:A. BARROS
CREATION DATE: tbs]%
DESIGN ISSUES:
MODIFICATION HISTORY:
      Date      |   Name   | Description
--------------+---------+-------------
This program Re formats the geochemical data
-}
VAR
    first, second: REAL;
    I,j,m,n :integer;
    datafile,newfile:text;
    filename,line:packed ARRAY [1..80] OF char;
```

```
BEGIN
write ('Enter file name: ');
readln(filename);
OPEN( FILE_VARIABLE     := datafile,
      FILE_NAME         := filename,
      HISTORY           := OLD );
write ('Enter new file name: ');
readln(filename);
OPEN( FILE_VARIABLE     := newfile,
      FILE_NAME         := filename,
      HISTORY           := NEW );
reset(datafile);
rewrite(newfile);
readln(datafile,line);
while not eof(datafile) do
BEGIN
readv(line,first,second,i,j,m,n);
first := first* 1000;
second := second* 1000;
writeln(newfile,'    ',first:10:3,'    ',second:11:3,' ',j:3,'
',n:1);
readln(datafile,line);
END
END.
```

**ORIGINAL FILE:**

```
259.359985   8400.370117  0     1 0 2
280.690002   8399.040039  0     2 0 2
289.869995   8399.089844  0     3 0 2
292.889984   8399.549805  0     4 0 2
293.699982   8398.939453  0     5 0 2
```

**FIRST STEP:**

```
259359.985   8400370.117  2
280690.002   8399040.039  2
289869.995   8399089.844  2
292889.98    8399549.805  2
293699.98    8398939.453  2
```

```
PROGRAM strip
C       Reformats data file
REAL*4 east,north
```

```
      INTEGER cat
      CHARACTER*30 FILENAME,NEWFILE
      write (6,*)'What file do you want to change?'
      read(5,15)filename
      write (6,*)'What is the new file name?'
      read(5,15)newfile
15    FORMAT(A30)
C  OPEN (
      1 UNIT=10,
      1   FILE = FILENAME,status='old')
      OPEN (
      1 UNIT=20,
      1   FILE = newfile,status='new')
C assumes file has max 4000 lines of data
      do 100 i=1,4000
      read (10,300)east,north,cat
      write(20,400)east,north,cat
100   continue
300   format(4x,f10.6,3x,f11.6,5x,i1)
400   format(f9.2,'|',f10.2,'|','#',i1)
      END
```

**FINAL GRASS SITE LIST FILE:**

```
259359.98|8400370.11# 2
280690.00|8399040.03# 2
289869.99|8399089.84# 2
292889.98|8399549.80# 2
293699.98|8398939.45# 2
```

**Program to convert profiles into scattered data points written in PASCAL. Run on VAX, PC or SUN**

```
PROGRAM Adjust_profile (INPUT, OUTPUT);

CONST
cps_per_km = 160;

TYPE

  coord_pair_type        = RECORD
                      x   : REAL;
                      y   : REAL
```

```
                                END;
file_name_type          = VARYING [256] OF CHAR;
VAR
  baseline_file          : TEXT;
  profile_file           : TEXT;
  output_file            : TEXT;
  baseline_file_name     : file_name_type;
  profile_file_name      : file_name_type;
  output_file_name       : file_name_type;
  slope_point            : ARRAY [1..2] OF coord_pair_type;
  cps                    : REAL;
  slope                  : REAL;
  intercept              : REAL;
  extrapolating          : BOOLEAN := FALSE;
  reversing_input        : BOOLEAN := FALSE;
  reversing_output       : BOOLEAN := FALSE;
  answer                 : VARYING [3] OF CHAR;
(* ----------------------------------------*)
PROCEDURE Open_files;
  BEGIN (* Procedure *)
  WRITE ('Enter baseline file name > ');
  READLN (baseline_file_name);
  OPEN (FILE_VARIABLE     := baseline_file,
        FILE_NAME         := baseline_file_name,
        HISTORY           := READONLY);
  RESET (baseline_file);
  WRITE ('Enter profile file name > ');
  READLN (profile_file_name);
  OPEN (FILE_VARIABLE     := profile_file,
        FILE_NAME         := profile_file_name,
```

```
        HISTORY             := READONLY);
  RESET (profile_file);
  WRITE ('Enter output file name > ');
  READLN (output_file_name);
  OPEN (FILE_VARIABLE      := output_file,
        FILE_NAME          := output_file_name,
        HISTORY            := NEW);
  REWRITE (output_file);
  WRITE ('Do you want the output file to show coordinates as
(Y,X) [No] >');
  READLN (answer);
  IF (answer <> '')
    THEN
      IF (answer[1] IN ['y','Y'])
     THEN
       reversing_output := TRUE;
  WRITE ('Do the input files show coordinates as (Y,X) [N]
>');
  READLN (answer);
  IF (answer <> '')
    THEN
      IF (answer[1] IN ['y','Y'])
     THEN
       reversing_input := TRUE;
  END; (* Procedure : Open_files *)

(* ---------------------------------- *)
PROCEDURE Read_coord_pair (VAR this_file  : TEXT;
                           VAR coord      : coord_pair_type);
  BEGIN (* Procedure *)
  IF (reversing_input)
```

```
    THEN
      READLN (this_file, coord.y, coord.x)
    ELSE
      READLN (this_file, coord.x, coord.y)
  END; (* Procedure : Read_coord_pair *)

(* ---------------------------------- *)
PROCEDURE Write_coord_pair (VAR this_file   : TEXT;
                                coord       : coord_pair_type;
                        cps         : REAL);
  BEGIN (* Procedure *)
  IF (reversing_output)
    THEN
      WRITE (this_file, coord.y:24:6, coord.x:24:6)
    ELSE
      WRITE (this_file, coord.x:24:6, coord.y:24:6);
  WRITELN (this_file, cps:24:6);
  END; (* Procedure : Read_coord_pair *)

(* ------------------------------------- *)
PROCEDURE Find_equation;
  BEGIN (* Procedure *)
  slope_point[1] := slope_point[2];
  IF (EOF (baseline_file))
    THEN
      extrapolating := TRUE
    ELSE
      BEGIN
      Read_coord_pair (baseline_file, slope_point[2]);
      slope := (slope_point[1].y - slope_point[2].y) /
(slope_point[1].x - slope_point[2].x);
```

```
      intercept := slope_point[1].y - slope * slope_point[1].x
      END
  END; (* Procedure : Find_equation *)

(* ------------------------------------ *)
PROCEDURE Adjust_y_values;
  VAR
    current_point     : coord_pair_type;
    output_point      : coord_pair_type;
  BEGIN (* Procedure *)
  WHILE (NOT (EOF (profile_file))) DO
    BEGIN
    Read_coord_pair (profile_file, current_point);
    IF (current_point.x > slope_point[2].x) AND (NOT
(extrapolating))
      THEN
        Find_equation;
    output_point.x := current_point.x;
    output_point.y := slope * current_point.x + intercept;
    cps            := (output_point.y - current_point.y) *
cps_per_km;
    Write_coord_pair (output_file, output_point, cps);
    END;
  END; (* Procedure : Adjust_y_values *)

(* ------------------------------------ *)
BEGIN (* Program *)
Open_files;
Read_coord_pair (baseline_file, slope_point[2]);
Find_equation;
Adjust_y_values;
```

```
END. (* Program : Adjust_profile *)
```

**ORIGINAL BASE-LINE FILE**

```
334.742004    8368.765625  1      1 0 1
334.796021    8374.995117  1      2 0 1
334.786011    8379.967773  1      3 0 1
334.832001    8384.981445  1      4 0 1
335.076019    8390.015625  1      5 0 1
335.237030    8393.778320  1      6 0 1
335.003021    8396.393555  1      7 0 1
```

**ORIGINAL PROFILE**

```
334.432007    8368.737305  1      1 0 1
334.496002    8368.843750  1      2 0 1
334.359009    8369.173828  1      3 0 1
334.443024    8369.311523  1      4 0 1
334.402008    8369.667969  1      5 0 1
334.485016    8369.774414  1      6 0 1
334.354004    8369.956055  1      7 0 1
334.407013    8370.008789  1      8 0 1
334.409027    8370.235352  1      9 0 1
```

**FINAL FILE**

```
334.741760    8368.737305    49.560547
334.742676    8368.843750    39.467773
334.745544    8369.173828    61.845703
334.746735    8369.311523    48.593750
334.749817    8369.667969    55.649414
334.750763    8369.774414    42.519531
334.752319    8369.956055    63.730469
334.752777    8370.008789    55.322266
334.754761    8370.235352    55.317383
```